Theory and numerics of three-dimensional strong discontinuities at finite strains

vom Fachbereich Maschinenbau und Verfahrenstechnik
der Technischen Universität Kaiserslautern
zur Verleihung des akademischen Grades
Doktor-Ingenieur (Dr.-Ing.)
genehmigte Dissertation

von
Dipl.-Ing. Philippe Jäger
aus
Hattingen

Hauptreferent:	Prof. Dr.-Ing.	P. Steinmann
Korreferenten:	Prof. Dr.-Ing.	E. Kuhl
	Prof. Dr.-Ing.	L.J. Sluys
	JP Dr.-Ing.	J. Mergheim
Vorsitzender:	Prof. Dr.-Ing.	P. Geiß
Dekan:	Prof. Dr.-Ing.	S. Ripperger

Tag der Einreichung:	22.04.2009
Tag der mündlichen Prüfung:	12.06.2009

Kaiserslautern, Juni 2009

D 386

Vorwort

Die vorliegende Arbeit entstand in den Jahren 2005-2009 während meiner Zeit am Lehrstuhl für Technische Mechanik der TU Kaiserslautern. Dort war ich erst als Stipendiat im Rahmen der zweiten Phase des Graduiertenkollegs: *Ingenieurmaterialien auf verschiedenen Skalen: Experiment, Modellierung und Simulation GRK814* und später als wissenschaftlicher Mitarbeiter tätig. Die finanzielle Unterstützung der DFG im Rahmen des Graduiertenkollegs war somit die Basis und hat diese Arbeit erst möglich gemacht.
Mein herzlicher Dank gilt Herrn Prof. P. Steinmann für seine Förderung sowohl im Rahmen meiner Arbeit als auch darüber hinausgehend. Herr Prof. P. Steinmann hat mich von Anfang an motiviert und unterstützt und mir die Möglichkeit gegeben, meine Arbeit in einem kreativen Umfeld weiter zu entwickeln. Mein ganz besonderer Dank gilt außerdem meiner Betreuerin Prof. E. Kuhl. Sie war maßgeblich für die Betreuung meines Projektes verantwortlich und die Zusammenarbeit mit ihr war einer der Hauptgründe für das Gelingen dieser Arbeit.
Weiterhin bedanken möchte ich mich bei Herrn Prof. L.J. Sluys und bei Frau JP J. Mergheim für die Übernahme und die Durchführung des Korreferats sowie bei Herrn Prof. P. Geiß für die Übernahme des Vorsitzes.
Zusätzlich möchte ich mich bei allen Kollegen des LTM für die sehr gute Arbeitsatmosphäre während meiner Zeit in Kaiserslautern bedanken.
Insbesondere hervorheben möchte ich dabei meine Bürokollegen Holger Meier, Patrick Schmidt, Swantje Bargmann und Paul Fischer, deren spezielle Hilfe bei Vortragsvorbereitungen und Diskussionen in erheblichem Masse zum Gelingen diese Projektes beigetragen hat.
Abschließend gilt mein großer Dank meiner ganzen Familie für die Unterstützung während der gesamten Ausbildung sowie meiner Freundin Julia Mattick für ihre viele Geduld während der letzten vier Jahre.

Kaiserslautern, Juni 2009 Philippe Jäger

Zusammenfassung

Brüche und Risse in Ingenieurkonstruktionen jeglicher Art führen zu einer Reduktion der maximal auftretenden Belastbarkeit, die im schlimmsten Fall zu einem totalen Versagen der entsprechenden Konstruktion führt.
Die Analyse von bestehenden Rissen so wie die Beurteilung ihrer Gefährlichkeit als auch die Vorhersage weiterer Rissbildung ist deswegen ein wichtiger Bestandteil im Rahmen der Materialenwicklung und der Auslegung von Ingenieurkonstruktionen. Die Bruch- oder Rissbildung ist grundsätzlich abhängig von der dem betrachteten Material zugrunde liegenden Mikrostruktur. Abhängig von der Homogenität dieser Mikrostruktur in ihrem Atomgitter und der Anzahl der initialen Defekte in diesem Gitter bilden sich bei entsprechender Belastung der Struktur Mikrorisse an hoch belasteten Stellen. Bei weiterer Belastung können sich diese Mikrorisse vereinigen und zu einem sichtbar werdenden, makroskopischen Riss des Materials führen.
Das Ziel dieser Arbeit ist es, auf Basis einer phänomenologischen Ingenieurbetrachtung, ein finite Elemente Programm für die netzunabhängige, dreidimensionale Modellierung von Rissbildung in Festkörpern mit Abbildung der dazugehörigen Strukturantwort zu entwickeln. Dabei wird besonderer Wert darauf gelegt, die Formulierung nicht auf kleine Deformationen zu begrenzen sondern stattdessen beliebig große Verformungen der betrachteten Strukturen zuzulassen.
Für die Simulationen solcher Versagensvorgänge wurden in der jüngeren Vergangenheit schon verschiedene Konzepte vorgeschlagen und untersucht.
Den Anfang machten kontinuierliche Modelle. Bei diesen Ansätzen im Rahmen der Festkörpermechanik wird das Verschiebungsfeld als kontinuierlich angesehen und der komplette entfestigende Versagensvorgang muss vom zugehörigen Materialgesetz beschrieben werden. Grundsätzlich unterliegen solche Materialgesetze dem Prinzip der lokalen Wirkung, d.h. die Materialantwort in einem betrachteten Materialpunkt wird unabhängig von seiner benachbarten Umgebung abgebildet. Deswegen können solche Modelle die Größe der zugehörigen Versagenszone nicht ohne weiteren Aufwand abbilden. Dies führt als weitere Konsequenz zu einer Netzabhängigkeit der entsprechenden Simulation.
Regularisierungstechniken, d.h. die Erweiterung der Konstitutivgesetzte durch nichtlokale Parameter oder gradientenerweiterte Terme, um die Größe der Versagenszone abzubilden, können Abhilfe schaffen und die Netzabhängigkeit verhindern. Allerdings ist weder die Bestimmung der benötigten nicht-lokalen Parameter als auch die Formulierung der notwendigen zusätzlichen Randbedingungen für die gradientenerweiterten Modelle einfach zu handhaben. Aufgrund dessen zieht man im Rahmen der Modellierung von Rissausbreitung diskrete Ansätze vor.
Diskrete Ansätze nutzen Diskontinuitäten im Verschiebungsfeld, um das entsprechende Bruchverhalten realistisch abzubilden. Dabei lassen sich die verschiedenen verfügbaren diskreten Modelle in drei wesentliche Teile gliedern. Der erste Teil im Rahmen der Festkörpermechanik ist die Umsetzung der Diskontinuität bei der Diskretisierung.

Der zweite Teil erfordert die Abbildung des entfestigenden postkritischen Verhaltens, während der dritte Teil die Entstehung und die Rissausbreitungsrichtung sowie die notwendige geometrische Beschreibung der Rissfläche beinhaltet.
Eine Möglichkeit, den ersten Teil zu realisieren, ist die Nutzung der permanenten Neuvernetzung während einer Simulation, *remeshing*. Solche Ansätze erfordern allerdings einen extrem hohen numerischen Aufwand. Zusätzlich werden bei der Nutzung von Plastizitätsmodellen, oder, technisch gesehen, bei der Verwendung von internen Variablen im Rahmen der finite Elemente Methode, Algorithmen benötigt, welche die Positionsänderungen der Integrationspunkte aufgrund der Neuvernetzung berücksichtigen.
Eine weitere Möglichkeit stellen so genannte Grenzelemente, *interface elements*, dar. Bei dieser Technik werden entlang der Elementgrenzen, entweder für einen bestimmtem vordefinierten Risspfad entlang der Elementgrenzen oder für alle möglichen Elementgrenzen, spezielle Grenzelemente positioniert, um den Riss abzubilden. Allerdings ist es offensichtlich, dass bei Anwendung dieser Methode die Berechnung der Rissfortschrittsrichtung entfällt und netzabhängige Risspfade berechnet werden.
Die erste Methode für die wirklich netzunabhängige Berücksichtigung von Diskontinuitäten im Verschiebungsfeld ist die *embedded discontinuouity method*. Basierend auf dem *enhanced assumed strain concept (EAS)* werden dort zusätzlich lokale Elementfreiheitsgrade eingeführt, um das diskontinuierliche Verschiebungsfeld abzubilden. Diese Technik besticht durch ihre Effizienz, da aufgrund der lokalen zusätzlichen Freiheitsgrade das globale Gesamtgleichungssystem nicht beeinflusst wird. Allerdings ist der Nachteil, dass die elementweise eingeführten Rissflächen grundsätzlich immer, d.h. unabhängig von der räumlichen Dimension, diskontinuierlich sind, was zu einer Überbewertung der Materialsteifigkeit führen kann.
Aufgrund dessen wurde die so genannte *extended finite elemente method (XFEM)* auf Basis des *partition of unity concepts* entwickelt. Bei dieser Methode werden globale Elementfreiheitsgrade genutzt, um den Riss bzw. die Rissfläche abzubilden. Diese Methode erlaubt prinzipiell die C^0-stetige Berücksichtigung von beliebig orientierten Rissen bzw. Rissflächen in der Struktur. Während die *XFEM* Sprungfreiheitsgrade als zusätzliche globale Unbekannte einführt, besteht ein weiterer Ansatz darin, den Sprung aus zusätzlichen Verschiebungsfreiheitsgraden zu interpolieren, *phantom-node method*. Diese Technik gehört zu den *discontinuous Galerkin methods* und ist eine Umparametrisierung der *XFEM* Basisfunktionen. Allerdings sollte erwähnt werden, dass die Entscheidung für eine der Parametrisierungen einige Unterschiede hinsichtlich der Modellierung von Rissen auf Elementgrenzen, Rissspitzenelementen oder Übergangselementen mit sich bringt. In dieser Arbeit wird für die Modellierung der letztere Ansatz gewählt.
Um die Möglichkeiten abzuschließen, Diskontinuitäten im Verschiebungsfeld zu realisieren, sollten allerdings noch die Randelementmethode, *boundary element method (BEM)*, und auch die komplett netzfreien Verfahren, *mehsless methods*, erwähnt werden.
Da die zuletzt beschriebenen Methoden jeweils diskrete Ansätze sind, besteht die Möglichkeit, die entfestigende Materialantwort, also den zweiten oben genanten notwendigen Teil, mit der Nutzung des kohäsiven Risskonzepts, *cohesive crack concept*, zu real-

isieren. Bei der Nutzung dieses Konzepts wird angenommen, dass in einer Prozesszone um die aktuellen Rissspitze, abhängig von der Rissöffnung, noch kohäsive Spannungen übertragen werden können. Diese Traktions-Verschiebungsbeziehungen, *traction separation laws*, sind nichts anderes als eine makroskopische oder phänomenologische Berücksichtigung der Defekte auf der nicht aufgelösten Mikrostruktur. Zusätzlich hat die Nutzung dieses Konzepts den Vorteil, dass die Spannungen an der Rissspitze beschränkt werden. Dies ist normalerweise nicht der Fall, d.h. die Spannungsverteilung an der Rissspitze ist gewöhnlich singulär. Diese hat zur Konsequenz, dass die Spannungen vor der Rissspitze in numerischen Simulationen von der Elementgröße abhängen und deswegen als Fehlerkriterium ungeeignet sind.
Im Rahmen der linear elastischen Bruchmechanik, *linear elastic fracture mechanics (LEFM)*, schafft das Berechungskonzept der Spannungsintensitätsfaktoren *(SIF)* auf der Basis von wegunabhängigen Energieintegralen Abhilfe. Allerdings ist dies nicht nutzbar bei nichtlinearen Simulationen. Außerdem ist dieses Konzept im Gegensatz zum kohäsiven Risskonzept auf Prozesszonen beschränkt, die wesentlich kleiner sind als die zu analysierende Struktur. Die Beschreibung des zweiten benötigten Teils abschließend kann man sagen, dass das kohäsive Risskonzept in Verbindung mit einem diskreten Ansatz für das Verschiebungsfeld sehr gut geeignet ist um das postkritische Entfestigungsverhalten bei Strukturen mit großen Deformationen abzubilden.
Als nächsten wird der Fokus auf den dritten benötigten Teilabschnitt gelegt.
In Rissfortschrittsimulationen mit Berücksichtigung des diskontinuierlichen Verschiebungsfeld ist grundsätzlich die Ermittlung des Fehlerursprungs als auch die Bestimmung der aktuellen Rissrichtung notwendig. Im Rahmen der linear elastischen Bruchmechanik existieren viele verschieden Kriterien auf der Basis der genannten Spannungsintensitätsfaktoren.
Das generelle Konzept der Konfigurations- oder Materiellen Kräfte, *material force method*, stellt eine Alternative für den betrachteten nichtlinearen Fall dar. Allerdings ist es für spröde Materialien üblich, die Rissentstehung als auch die Rissfortschrittsrichtung anhand eines Hauptspannungskriteriums zu bestimmen.
Es muss betont werden, dass für zweidimensionale Simulationen die Berechnung der Rissrichtung, als Rissnormalenvektor oder als Risstangentenvektor, ausreichend ist für die $\mathcal{C}_0$-stetige Verfolgung des Risspfades. Obwohl die meisten algorithmischen Details sich aufgrund der allgemeinen Tensor Notation beim Übergang zum dreidimensionalen Raum nicht ändern, erfordert die genannte Verfolgung des Risspfades im Dreidimensionalen weitere Betrachtungen, da die $\mathcal{C}^0$-Stetigkeit nicht eindeutig gegeben ist. Algorithmen zur Berechnung des Risspfades im Dreidimensionalen können grundsätzlich in drei Kategorien eingeteilt werden: lokale, nicht-lokale und globale Algorithmen. Im Rahmen dieser Arbeit werden die verschiedenen verfügbaren Ansätze aus der Literatur diskutiert.
Im Detail wird eine lokale Methode vorgestellt, bei der die $\mathcal{C}^0$-Stetigkeit in der Rissfläche in Abhängigkeit der gerissenen Nachbarelemente gesichert wird. Weiterhin wird eine nichtlokale Methode vorgestellt, bei der die Rissfläche abhängig von einer nicht-lokalen Nachbarschaft mit der Methode der kleinsten Fehlerquadrate geglättet wird. Zusätzlich wird basierend auf impliziten Funktionen die *level set method* vorgestellt. Im Dreidimensionalen werden bei diesem Konzept die Rissfläche sowie die Riss-

front durch konstante Werte einer skalarwertigen Funktion beschrieben. Da die Funktionen abhängig von der Geschwindigkeit der Rissfront formuliert werden, können die unbekannten Funktionswerte durch Lösung von *Hamilton-Jacobi* Gleichungen bestimmt werden. Die *Hamilton-Jacobi* Gleichungen werden dann nur in einer Umgebung um die entsprechende Rissfront gelöst und die *level set method* kann deshalb im Dreidimensionalen den nicht-lokalen Methoden zugeordnet werden.
Eine Alternative stellt das so genannte *global tracking* dar. Im Rahmen dieser Methode wird ebenfalls eine implizite Definition der Rissfläche genutzt. Allerdings werden die unbekannten Funktionswerte, basierend auf einer zusätzlichen partiellen Differentialgleichung, für das gesamte Gebiet bestimmt.
Nach der Ausarbeitung und der Bewertung der Rissverfolgungsalgorithmen und damit der Vollendung des dritten notwendigen Teilabschnitts wird das entwickelte finite Element Programm abschließend anhand von Experimenten und Benchmarks aus der Literatur verifiziert.

Nomenclature

$\mathcal{B}_0$	reference configuration	p. 7
$\mathcal{B}_t$	current configuration	p. 7
$\boldsymbol{X}$	referential placement vector	p. 7
$\boldsymbol{x}$	spatial placement vector	p. 7
$\boldsymbol{\varphi}$	spatial motion map	p. 7
$\boldsymbol{\Phi}$	material motion map	p. 8
$\boldsymbol{F}$	deformation gradient	p. 8
$\boldsymbol{f}$	inverse deformation gradient	p. 8
J	JACOBIAN	p. 8
j	inverse JACOBIAN	p. 8
$\mathrm{d}V$	infinitesimal referential volume element	p. 9
$\mathrm{d}v$	infinitesimal spatial volume element	p. 9
$\boldsymbol{N}$	referential normal vector	p. 9
$\boldsymbol{n}$	spatial normal vector	p. 9
$\mathrm{d}A$	infinitesimal referential area element	p. 9
$\mathrm{d}a$	infinitesimal spatial area element	p. 9
$\boldsymbol{R}$	rotation tensor	p. 9
$\boldsymbol{U}$	referential stretch tensor	p. 9
$\boldsymbol{u}$	spatial stretch tensor	p. 9
$\boldsymbol{C}$	left CAUCHY-GREEN strain tensor	p. 9
$\boldsymbol{b}$	right CAUCHY-GREEN strain tensor	p. 9
$\boldsymbol{E}$	GREEN-LAGRANGE strain tensor	p. 9
$\boldsymbol{e}$	EULER-ALMANSI strain tensor	p. 9
$\boldsymbol{I}$	second order unit tensor	p. 9
$\boldsymbol{T}$	PIOLA traction vector	p. 10
$\boldsymbol{t}$	CAUCHY traction vector	p. 10
$\boldsymbol{P}$	PIOLA stress tensor	p. 11
$\boldsymbol{\sigma}$	CAUCHY stress tensor	p. 11
$\boldsymbol{S}$	PIOLA-KIRCHHOFF stress tensor	p. 11
$\boldsymbol{v}$	spatial velocity	p. 12
$\boldsymbol{a}$	spatial acceleration	p. 12
ρ_0	referential mass density	p. 12
ρ_t	spatial mass density	p. 12
m	mass	p. 12
$\boldsymbol{p}$	linear momentum vector	p. 13
$\boldsymbol{B}_0$	referential body force vector	p. 13
$\boldsymbol{b}_t$	spatial body force vector	p. 13
$\boldsymbol{l}$	angular momentum vector	p. 14
$\boldsymbol{r}$	position vector	p. 14

$\overset{3}{\boldsymbol{e}}$	third order permutation tensor	p. 15
W_p	referential stress power	p. 16
w_p	spatial stress power	p. 16
$\mathcal{D}_o$	referential dissipation	p. 17
ψ_0	HELMHOLTZ/free energy density	p. 17
λ, μ	LAMÉ parameters	p. 18
$\mathbb{L}$	referential elasticity tensor	p. 18
$\mathbb{A}$	two point elasticity tensor	p. 19
$\mathbb{E}$	spatial elasticity tensor	p. 19
$\mathbb{I}^{sym}$	fourth order identity tensor	p. 19
$\boldsymbol{\eta}$	vector valued test function	p. 37
$\delta\boldsymbol{\varphi}$	virtual spatial deformation map	p. 22
$\delta\mathcal{W}$	total virtual work	p. 22
$\delta\mathcal{W}^{int}$	internal virtual work	p. 22
$\delta\mathcal{W}^{ext}$	external virtual work	p. 22
n_{el}	number of elements	p. 24
n_{en}	number of element nodes	p. 24
$\mathcal{B}_0^{el}$	element domain	p. 24
N	LAGRANGIAN shape function	p. 24
$\mathcal{B}_\diamond^{el}$	element unit domain	p. 24
$\overset{n_{el}}{\underset{e=1}{\mathbf{A}}}$	element assembly operator	p. 24
$\mathbf{R}$	vector valued residual	p. 25
$\mathbf{R}^{int}$	internal residual contribution	p. 25
$\mathbf{R}^{ext}$	external residual contribution	p. 25
n_{np}	total number of node points	p. 25
$\mathbf{K}_{IJ}$	tangent stiffness matrix	p. 26
Γ	referential discontinuity surface	p. 28
$[\![\boldsymbol{\varphi}]\!]$	jump term of spatial motion map	p. 28
$\bar{\gamma}^+, \bar{\gamma}^-$	spatial discontinuity surfaces	p. 29
$\mathcal{H}$	HEAVISIDE function	p. 29
δ_Γ	DIRAC delta-distribution	p. 30
$[\![\delta\boldsymbol{\varphi}]\!]$	virtual jump term of spatial motion map	p. 33
$\boldsymbol{\xi}$	local element coordinates	p. 37
$\mathcal{B}_\diamond^{el}$	local unit element configuration	p. 37
$V_\diamond^{el}$	local unit volume	p. 37
$\boldsymbol{\eta_i}$	local element sub-coordinates	p. 37
$\mathcal{B}_\triangle^{subel}$	local sub-unit element configuration	p. 37
$V_\triangle^{subel}$	local sub-unit volume	p. 38
α	GAUSS quadrature point	p. 38
n_{gp}	number of GAUSS quadrature points	p. 38
V_{tet}^{el}	tetrahedral element volume	p. 38
V_{wedge}^{el}	wedge element volume	p. 38
$\boldsymbol{X}_{\text{tip}}^{P_1}, \boldsymbol{X}_{\text{tip}}^{P_2}$	referential crack front placement	p. 42
$\boldsymbol{X}_{\text{tip}^*}^{Q_1}, \boldsymbol{X}_{\text{tip}^*}^{Q_2}$	referential crack front assumed values	p. 42

E	YOUNG'S modulus	p. 43
ν	POISSON'S ratio	p. 43
$\bar{\gamma}$	fictitious spatial discontinuity surface	p. 49
$\bar{\boldsymbol{\varphi}}$	average spatial motion map	p. 49
$\bar{\boldsymbol{F}}$	average deformation gradient	p. 49
$\bar{\boldsymbol{n}}$	fictitious spatial normal vector	p. 49
$\bar{\boldsymbol{T}}^c$	cohesive PIOLA traction vector	p. 50
$\bar{\boldsymbol{t}}^c$	cohesive CAUCHY traction vector	p. 50
$\delta\mathcal{W}_{coh}$	cohesive virtual work	p. 50
β	area ratio	p. 52
$\bar{\psi}_0^c$	referential cohesive interface potential	p. 52
$\mathcal{D}_0^c$	referential cohesive interface dissipation	p. 52
$[\![\boldsymbol{\varphi}_n]\!]$	divergent jump term contribution	p. 53
$[\![\boldsymbol{\varphi}_t]\!]$	relative jump term contribution	p. 53
$\overset{3}{\boldsymbol{G}}$	derivative provisional result	p. 54
$\boldsymbol{H}$	derivative provisional result	p. 54
$\boldsymbol{T}_n$	cohesive tangent operator	p. 55
$\boldsymbol{T}_\varphi$	cohesive tangent operator	p. 55
$\bar{N}\vert_p^\Gamma$	shape function set	p. 56
$\boldsymbol{L}_\Gamma^p$	gradient shape function set	p. 56
$\mathbf{R}_{coh}$	cohesive residual contribution	p. 56
$\mathbf{K}_{IJ}^{coh}$	cohesive tangent stiffness matrix	p. 57
f_t	tensile strength	p. 58
G_f	cohesive fracture energy	p. 58
p, q	numerical softening parameter	p. 60
E_t	tangential interface stiffness	p. 61
E_c	contact interface stiffness	p. 62
L_0^{el}	referential finite element length	p. 62
l_t^{el}	spatial finite element length	p. 62
V_0^{el}	referential finite element volume	p. 62
$\boldsymbol{\delta}^c$	general cohesive jump measure	p. 64
$\vert\boldsymbol{\delta}_{max}^c\vert$	cohesive history variable	p. 64
κ^c	cohesive loading function	p. 64
$\bar{\Gamma}_\square^{el}$	local unit element area domain	p. 64
λ^σ	eigenvalue of CAUCHY stress tensor	p. 65
$\boldsymbol{n}^\sigma$	eigenvector of CAUCHY stress tensor	p. 65
f_c	compression strength	p. 77
$\boldsymbol{n}^{\sigma_{max}}$	maximal principal stress direction	p. 77
$\boldsymbol{n}^{crk}$	spatial crack surface normal vector	p. 77
$\boldsymbol{N}^{crk}$	referential crack surface normal vector	p. 77
$\boldsymbol{X}^{crk}$	single crack surface description point	p. 78
n_{ed}	number of cracked neighboring edges	p. 78
$\boldsymbol{X}^{ed}$	midpoint of cracked neighboring edge	p. 78
R^σ	radius of referential sphere around the crack tip	p. 79
ip	integration point	p. 79

R^{ip}	distance between integration point and crack tip	p. 79
V^{ip}	referential element volume related to integration point	p. 79
n_{ip}	number of integration points within the sphere	p. 80
$\mathcal{I}$	set of sphere integration points	p. 80
$\mathcal{I}^{\sigma}$	uncracked related sphere integration points	p. 80
$\mathcal{I}^{n}$	cracked related sphere integration points	p. 80
n_{σ}	cardinality for set of uncracked integration points	p. 80
n_{n}	cardinality for set of cracked integration points	p. 80
$\widetilde{\boldsymbol{\sigma}}$	non-local CAUCHY stress tensor	p. 80
$\widetilde{\boldsymbol{n}}^{\widetilde{\sigma}_{max}}$	average maximal principal stress direction	p. 80
$\widetilde{\boldsymbol{n}}^{n}$	average crack surface normal vector	p. 80
θ^{crk}	crack extension deviation angle	p. 81
θ^{crit}	critical crack extension deviation angle	p. 81
n_{tip}	number of crack tip elements	p. 81
cp	element crack surface cut point	p. 82
n_{cp}	number of element crack surface cut points	p. 82
$\boldsymbol{X}^{cp}$	element crack surface cut point vector	p. 82
$\boldsymbol{N}^{\sigma_{max}}$	referential maximal principal stress direction	p. 82
$\widetilde{\boldsymbol{N}}^{\widetilde{\sigma}_{max}}$	average referential maximal principal stress direction	p. 83
n_{crk}	total number of crack surface cut points	p. 84
$\{X, Y, Z\}$	global CARTESIAN coordinate system	p. 84
$\boldsymbol{E}_i^c$	global orthonormal base vectors	p. 84
R^c	radius of referential sphere around the crack tip	p. 84
$\mathcal{I}^c$	set of all crack surface cut points	p. 84
R_i^{cp}	distance between crack tip and intersection point	p. 84
n_c	cardinality for set of cut points	p. 84
$\widehat{\boldsymbol{X}}^c$	center of non-local point cloud	p. 84
$\{\widehat{X}, \widehat{Y}, \widehat{Z}\}$	local CARTESIAN coordinate system	p. 84
$\widehat{\boldsymbol{E}}_i^c$	local orthonormal base vectors	p. 84
$\boldsymbol{\Sigma}^c$	covariance tensor	p. 84
λ^{Σ^c}	eigenvalue of covariance tensor	p. 84
$\widehat{\boldsymbol{X}}_i^{cp}$	local crack surface corner points	p. 85
$\boldsymbol{Q}^c$	orthogonal transformation tensor	p. 85
$\widehat{Z}^c$	crack surface function	p. 85
a_i	crack surface function coefficients	p. 85
Φ^c	least square function	p. 85
$\widehat{\boldsymbol{T}}_{\widehat{X}}^c$	crack surface tangent vector	p. 85
$\widehat{\boldsymbol{T}}_{\widehat{Y}}^c$	crack surface tangent vector	p. 85
$\mathcal{I}^{\phi}$	set of crack surface level contours	p. 86
ϕ	crack surface level contour	p. 86
$\boldsymbol{T}_2^{crk}$	referential crack surface tangent vector	p. 87
$\boldsymbol{T}_3^{crk}$	referential crack surface tangent vector	p. 87
$\boldsymbol{t}_2^{crk}$	spatial crack surface tangent vector	p. 87
$\boldsymbol{t}_3^{crk}$	spatial crack surface tangent vector	p. 87

$\boldsymbol{J}$	referential crack tracking flux vector	p. 87
$\boldsymbol{D}$	anisotropic constitutive crack tracking tensor	p. 88
$\delta\phi$	virtual crack surface level contour	p. 89
$\delta\mathcal{W}_0^{\phi}$	global tracking virtual weak form formulation	p. 89
R_I^{int}	scalar-valued internal tracking residual	p. 89
R_I^{ext}	scalar-valued external tracking residual	p. 89
K_{IJ}	global tracking solution matrix	p. 89
F_I	global tracking solution vector	p. 89
$\bar{\phi}^{initial}$	initial crack surface values	p. 90
$\boldsymbol{X}^{\Gamma}$	referential crack placements	p. 92
ϕ	crack surface level set function	p. 92
χ	crack front level set function	p. 92
$\mathcal{I}^{\phi}$	set of crack surface level contours	p. 92
$\mathcal{I}^{\chi}$	set of crack front level contours	p. 92
$\boldsymbol{X}_s^{\Gamma}$	referential crack surface placements	p. 93
$\boldsymbol{X}_f^{\Gamma}$	referential crack front placements	p. 93
$\mathcal{I}^{upd}$	level set sub-domain	p. 93
$\boldsymbol{N}^{\phi}$	unit crack surface normal vector	p. 94
$\boldsymbol{N}^{\chi}$	unit crack front normal vector	p. 94
$\boldsymbol{T}^{t}$	unit crack front tangent vector	p. 94
$\boldsymbol{V}^{\Gamma}$	crack front velocity	p. 94
V^{ϕ}	crack front velocity normal field	p. 94
V^{χ}	crack front velocity tangent field	p. 94
Δt	critical time step	p. 97

Contents

1. Introduction

1.1. Motivation

Fracture in engineering structures is usually accompanied by downgrading load-capacities and eventually with the complete breakdown of the considered structure. Therefore, the reliable prediction of crack formation and propagation in structures is an integral part in material design and structural analysis.
Crack formation is usually determined by the underlying micro-structure of the material, i.e., the homogeneity of the material and the amount of initial defects. Based on this micro-structure, the first crack onset is given by the nucleation of certain micro-separations. These irreversible micro separations can be treated as small micro cracks which usually occur in a small zone (process zone) around a current existing macro crack or cut-out (notch) of the considered material. Then, by raising the applied loading on the considered structure these micro-cracks grow, leading to larger defects which eventually coalesce and result in a visible macroscopic crack.
For phenomenological considerations in the framework of engineering continuum considerations these irreversible processes reduce the strength and the stiffness of the considered material. Additionally, the irreversibility of the crack formation is represented by energy dissipation. The prediction of this macroscopic failure load with its complete corresponding post-peak behavior requires robust and stable computational algorithms. Especially in a large deformational continuum mechanics setting, these algorithms must be capable of dealing with the corresponding highly non-linear set of governing equations.
The main goal of this thesis is therefore the prediction of the connected macroscopic failure load with its corresponding post-peak behavior and associated failure surface in a three-dimensional finite element setting for finite strains.

1.2. State of the art review

Based on the general concept of finite elements, the first recommended approaches account for material failure in a smeared sense, i.e., continuous smooth failure was attributed to strain softening equations in the form of damage or plasticity on the element level, see, e.g., OLIVER [147, 148] and DE BORST [41] for smeared crack models or SIMO & JU [180, 181] for damage formulations. Since these formulations do not account for a real discontinuity in the considered field variable, i.e., a discontinuity in the spatial motion map for continuum mechanics solid problems, this procedure leads to large deformation gradients which localize in a narrow band in the considered process zone. However, in the chosen continuous mechanical setting the material response at a certain point, i.e., the stress-strain relation, depends only on the corresponding state variables of the considered point. Consequently, all material failure tends to con-

centrate on one material point. Therefore, the width of the narrow band can not be captured by the finite element solution itself and instead the width of the failure band depends on the chosen finite element size. This can lead to an ill-posedness of the complete problem.
One possibility to circumvent this ill-posedness is the consideration of non-local or higher gradient terms in the constitutive equations (regularization), compare, e.g., JIRÁSEK et al. [104], GRASSL & JIRÁSEK [79], PATZAK & JIRÁSEK [156], LIEBE [115], WELLS et al. [207], OLIVER [146] or DE BORSTet al. [43, 45]. However, all of these regularization techniques require a sufficiently large mesh-resolution of the process zone which leads to a high numerical effort. In addition, the consideration of higher gradient terms demands the formulation of additional boundary conditions, whereas non-local regularization techniques require the determination of the particular non-local material parameters.
Accordingly, it seems reasonable to account for so called discrete fracture models. Most of these discrete failure models consist of three main building blocks. The first building block regards the real description of propagation discontinuities in a continuum mechanic finite element setting. The second building block takes into account the connected softening material response, whereas the third building block includes the computation of the crack propagation direction with the corresponding geometrical description of the failure surface.
One possibility to realize the first building block is a kinematical crack representation and its evolution by permanent remeshing processes, see, e.g., ASKES et al. [12] or SWENSON & INGRAFFEA [196]. However, this procedure leads to high numerical effort and requires update schemes regarding constitutive relations with internal variables, i.e., plasticity or damage formulations.
Another alternative is the use of so called interface elements. Applying this method, a priori defined interfaces are introduced between either predefined inter-element boundaries, or, alternatively, each inter-element boundary, see, e.g., NEEDLEMAN [141], XU & NEEDLEMAN [212, 213, 214], SIMONE [183] or SCHELLEKENS & DE BORST [174]. Obviously, using this approach leads inherently to mesh dependent crack paths and therefore supersedes the third building mentioned block.
The first method to truly simulate mesh-independent discrete failure surfaces was the embedded discontinuity technique. Motivated by the assumed enhanced strain concept (EAS), additional degrees of freedom were introduced locally on the element level to characterize the failure plane, see, e.g., DVORKIN [56], OLIVER et al. [149, 151, 150, 152], ARMERO & GARIKIPATI [10], ARMERO & LINDER [11], MOSLER [139], BOLZON et al. [23, 23], SCHRÖDER& LÖBLEIN [177], or JIRÁSEK [105], [106]. This technique convinces through its computational efficiency: Due to the local nature of the enhancement, the size of the related global system of equations was not affected by the adaptively introduced failure surface. An obvious drawback of this local crack representation, however, was the general discontinuous nature of the introduced failure surfaces that was soon found to introduce stress locking associated with an over-estimation of the corresponding structural stiffness.
To overcome this deficiency BELYTSCHKO and co-workers introduced the extended finite element method (XFEM) based on the partition of unity approach of BABUSKA &

MELENK [13], see, e.g., BELYTSCHKO & BLACK [17], BELYTSCHKO et al. [18] or DOLBOW [48]. At the additional cost of global degrees of freedom, smooth discrete cracks could be finally modeled anywhere in the domain, see likewise SUKUMAR et al. [195] or HUANG et al. [94].
While the XFEM uses the jump in the considered field variable, i.e., the jump in the spatial motion map for a solid mechanic problem, as additional unknowns, the method proposed by HANSBO & HANSBO [87, 86, 85], based on the idea of NITSCHE [142], works exclusively with deformation degrees of freedom. We emphasize that this latter technique can be understood as a reparametrization of the XFEM basis functions and vice versa, see, e.g., AREIAS & BELYTSCHKO [6]. However, by applying one parametrization there are some assets and drawbacks concerning crack neighboring elements, enrichment of special crack tip elements and crack paths on inter-element edges (2d) or surfaces (3d).
To complete the description of available approaches, we mention complete meshless methods and the boundary method which have also been applied successfully to model crack propagation, see, e.g., KOLK & KUHN [110, 109], CITARELLA & PERELLA [35], FRANGI [64], for the boundary element method (BEM) and RABCZUK & BELYTSCHKO [159], or RABCZUK et al. [161] for completely meshfree methods.
Since all these latter introduced approaches are discrete in nature, the dissipative softening behavior caused by the fracture process is characterized in terms of cohesive surface tractions depending at least on the jump in the spatial motion map. Accordingly, the bulk material can be captured by usual continuum mechanics constitutive equations.
The cohesive crack has originally been proposed by DUGDALE [53, 65] and BARENBLATT [15]. It was further elaborated for concrete materials by HILLERBORG [90]. The key assumption of the cohesive crack concept is that the introduced discrete crack surfaces are able to transfer stresses within the process zone of propagating cracks. Therefore, the cohesive crack concept is a very elegant tool to merge all mentioned irreversible failure mechanisms into an arbitrary traction separation relation.
In addition, the cohesive crack concept enables the computation of bounded crack tip stresses. Usually the stress distribution at a mathematical sharp crack tip is singular. As a consequence the stress computation in numerical simulations depends on the mesh size and can not be used for the determination of crack growth. In the case of linear elastic fracture mechanics this can be circumvented by applying IRVINS's successful concept of the stress intensity factors, see, e.g., HAHN [83], GROSS & SEELIG [81] or KUNA [113] for an overview. However, this concept is only applicable for the linear elastic case which is not compliant with the aims of this work. Furthermore, in contrast to the cohesive crack concept, this concept is only applicable for process zone dimensions much smaller than the considered structural ones, see, e.g., REMMERS [163] for a more detailed explanation.
In summary, the cohesive crack concept in conjunction with discrete fracture models leads to a sufficient approach to model the softening behavior for large deformational analysis. It has been adopted by several authors to capture brittle as well as ductile failure, see, e.g., MERGHEIM et al. [127, 129], RUIZ et al. [168], ORTIZ [155], GASSER & HOLZAPFEL [71, 70, 73], DE BORST et al. [42, 44], WELLS & SLUYS [205] or AREIAS &

RABCZUK [8].
Finally we point our attention to the third building block. In crack propagation simulations the chosen discrete crack model requires the computation of the onset of failure as well as the crack propagation direction.
For analyses with restrictions to linear elasticity many crack propagation criteria are available based on stress intensity factors computed with the help of boundary potential energies, see, e.g., GOSZ [77, 78], HUBER et al. [95], RICHARD et al. [167] and BAKKER [14] for three-dimensional applications, or KUNA [113] for an overview.
The general concept of material or configurational forces represents an alternative for the large deformation setting, see, e.g., STEINMANN [189], DENZER [46], DENZER et al. [47] in general or HEINTZ [89], FAGERSTRÖM [60], CONSTANZO [39], MIEHE & GÜRSES [131] or GÜRSES [82] for crack propagation analysis.
However, for brittle materials in the framework of large deformations, the crack propagation direction is usually determined by a principal stress based RANKINE criterion, see, e.g., WELLS [204], MOSLER [138], MERGHEIM [125] or DUMSTORFF AND MESCHKE [55] for an overview.
We emphasize that for two-dimensional formulations the information of the crack onset and the crack propagation direction, either as the crack normal vector or alternatively as the crack tangent vector, is sufficient for a unique tracking of the crack path. The extension from two to three-dimensional crack propagation is, however, not straightforward. Most algorithmic changes concerning the failure and the crack propagation criterion are of minor concern because of the general tensorial framework. However, especially tracking the crack path in a unique $\mathcal{C}^0$-continuous way and the description of the corresponding failure surface deserve additional attention in a three-dimensional setting.
By refraining from pre-defining the crack path, which is referred to as fixed tracking, existing crack tracking strategies can basically be subdivided into local, non-local or global tracking methods.
A local tracking strategy is proposed by AREIAS & BELYTSCHKO [4]. They introduce a local tracking algorithm which provides the actual discrete element failure surface based on the failure criterion and the direct neighboring elements.
Further approaches have been documented by GASSER & HOLZAPFEL [71, 72, 73, 69]. Starting with a total crack surface description, which is inherently discontinuous due to the applied finite element formulation, they introduce a technique to minimize the discontinuities in the total crack surface based on a non-local neighborhood of the considered crack tip.
A further non-local alternative is the use of the level set method. Here the crack path (2d) or crack surface (3d), respectively, is given by implicit (level set) functions. This means that the geometrical description of the crack is given by constant values of a function which is one dimension higher than the desired crack surface description, see, e.g., SETHIAN [178] for a general overview. This concept is applied successfully in two-dimensional crack propagation analysis since the level set values can be easily and uniquely extended in a non-local neighborhood around the current crack tip, see, e.g., BELTYSCHKO et al. [19], CHESSA & BELYTSCHKO [33], STOLARSKA et al. [192], BORDAS & MORAN [25], DUFLOT [51] or VENTURA et. al [201, 202]. In addition

this concept is also applied for tracking the crack path in three-dimensional analysis, however, with increasing computational effort. In contrast to the two-dimensional case where the computation of the level set values is rather straightforward, in three-dimensional analysis the level set values have to be computed by solving HAMILTON-JACOBI equations in a non-local neighborhood around the current crack tip, see, e.g., MOËS et al. [134], GRAVOUIL et al. [80], BURCHARD et al. [29], DUDU et al. [50], CECIL & MARTHALER [31], or SUKUMAR et al. [194, 193].
Whereas the HAMILTON-JACOBI equations are only formulated for a non-local neighborhood, OLIVER et al. [153, 152] and SAMANIEGO [169] have proposed the so called global tracking algorithm. It also uses an implicit crack surface description similar to the foregoing approach. However, the corresponding level set values are computed by solving an additional partial differential equation for the complete considered structure. This concept is, as far as we know, also applied successfully by CERVERA & CHIUMENTI [32], CHAVEZ [57] and FEIST & HOFSTETTER [61, 62].
To complete the third required building block we also mention the tracking strategies or the kind of crack surface description for the boundary element method, see, e.g., KOLK & KUHN [109] or the complete meshless techniques, see, e.g., RABCZUK & BELYTSCHKO [159], or RABCZUK et al. [161].

1.3. Outline

This thesis is organized at follows:

Chapter 2 (*Continuous solid mechanics)*. The basics of continuum solid mechanics and finite elements are briefly introduced as a basis and a reference for the complete work. According to the aims of this thesis, focus is placed on expressing the governing equations in the framework of finite deformations.

Chapter 3 (*Discontinuous solid mechanics*). The continuous situation of the former chapter is extended to discontinuous considerations. Accordingly, the corresponding governing equations and the required finite element formulation for the modeling of strong discontinuities in non-linear solid mechanics are presented. However, this chapter is restricted to stationary cracks and their mesh-independent realization.

Chapter 4 (*The cohesive crack concept*). Within this chapter the general modeling of cohesive cracks based on the mesh-independent finite element discretization scheme of the forgoing chapter is motivated and provided. Different cohesive traction separation laws are illustrated and, finally, the propagation of cohesive cracks along predefined crack paths in three-dimensional domains is presented.

Chapter 5 (*Crack path tracking strategies*) By refraining on the use of predefined crack paths, this chapter deals with the description and the computation of the current crack surface, based on the actual status of the considered structure. We present five of the most common approaches to track crack surfaces within a three-dimensional finite element setting. Thereby, we compare the particular approaches by means of common quality measures such as robustness, stability, efficiency, computational cost and crack surface continuity.

Chapter 6 (*Representative numerical examples*). Within this chapter representative numerical examples for brittle fracture in solids are illustrated. As a basis, we consider brittle fracture in concrete to validate the elaborated finite element tool by experimental benchmark problems. Afterwards we focus on the modeling of brittle fracture in folding rocks which obviously requires the presented non-linear formulation.

Chapter 7 (*Discussion*). Concluding this work, we summarize and discuss the results, and we present a preview of possible future extensions and applications.

2. Continuous solid mechanics

2.1. Motivation

This first chapter briefly introduces the basics of continuum mechanics and finite elements as a basis and a reference for the complete work. By virtue of the formulated aims of this thesis importance is attached to express the governing equations of continuum mechanics in the settings of finite deformations. In detail, the continuum mechanics part of this chapter starts with the kinematics, then introduces the concept of stress and elaborates the necessary balance equations. Afterwards, hyperelastic constitutive relations are considered in a thermodynamical, general framework and the governing equations of the boundary value problem for non-linear solid mechanics are provided. This part is mainly based on HOLZAPFEL [93], ALTENBACH & ALTENBACH [2], STEIN & BARTHOLD [188], while OGDEN [145] and SPENCER [185] are referred for some particular aspects.
The second part of this chapter deals with the formulation of the governing equations of continuum solid mechanics in a finite element framework. This part starts with a formulation of the weak form of the boundary value problem. Further on, the discretization of the governing equations is provided and an incremental solution procedure is discussed. This part is mainly based on WRIGGERS [210], BELYTSCHKO et al. [197], whereas ZIENKIEWICZ [217], ALTENBACH & SACHAROV [3] and BATHE [16] are referred in some cases. This chapter makes no claim to be complete. Instead, this chapter attempts to explain the necessary background which is required for the understanding of the following parts of the thesis.

2.2. Kinematics

Kinematics is the part of mechanics which takes into account the changes of geometry of an object during motion without consideration of the circumstances leading to this motion. In this section, we discuss the kinematics of homogeneous bodies $\mathcal{B}$ in the three-dimensional EUCLIDIAN vector-space which in accordance with the theory of continuum mechanics can be considered as composition of a set of particles. Placements $\boldsymbol{x}$ of particles occupying the body $\mathcal{B}$ at a certain time $t \in \mathbb{R}^+$ are defined as the spatial or current configuration $\mathcal{B}_t$. Placements $\boldsymbol{x} = \boldsymbol{X}$ of particles occupying the body B at a known initial time t_0 are defined as the material or reference configuration $\mathcal{B}_0$. Now, we define a non-linear spatial motion map $\boldsymbol{\varphi}(\boldsymbol{X}, t)$ which maps all particles of the body $\mathcal{B}$ from the reference into the spatial configuration, compare figure 2.1. In this motion map we observe a certain particle of the body $\mathcal{B}$ as it moves. This description of motion is often referred to as the material or LAGRANGIAN description because it is characterized with respect to the material coordinates $\boldsymbol{X}$. Furthermore, this deformation map has to be unique, differentiable and continuous.

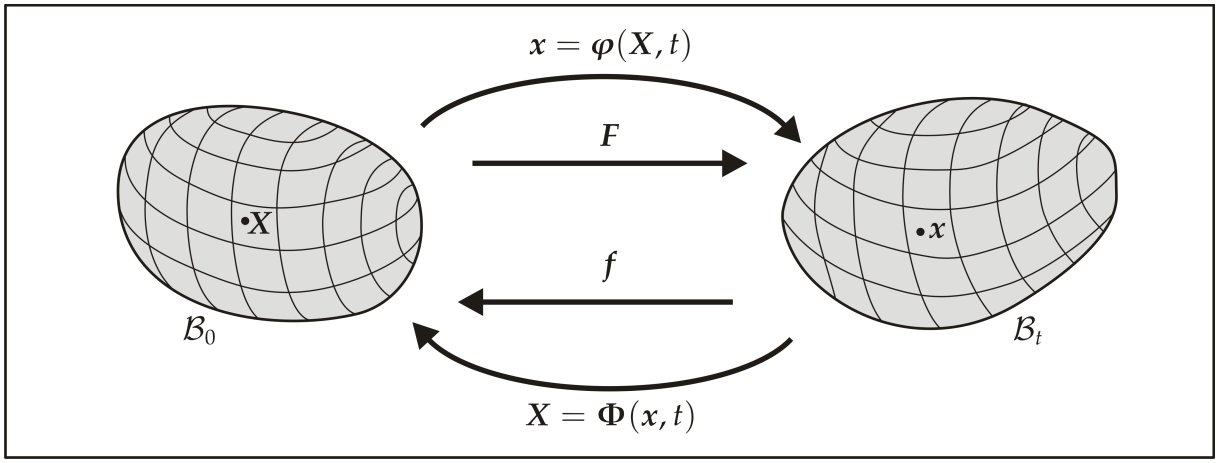

Figure 2.1.: Deformation and inverse deformation map of a body $\mathcal{B}$.

$$\boldsymbol{x} = \boldsymbol{\varphi}(\boldsymbol{X}, t) \quad \boldsymbol{\varphi} : \mathcal{B}_0 \times \mathbb{R}^+ \rightarrow \mathcal{B}_t \tag{2.1}$$

Next, we introduce an inverse non-linear material motion map which maps all particles of the body $\mathcal{B}$ from the spatial into the reference configuration. In this description of motion we focus on a certain point in space and we observe what happens at this point while the time changes. This description is often referred to as the spatial or EULERIAN description.

$$\boldsymbol{X} = \boldsymbol{\Phi}(\boldsymbol{x}, t) \quad \boldsymbol{\Phi} : \mathcal{B}_t \times \mathbb{R}^+ \rightarrow \mathcal{B}_0 \tag{2.2}$$

Then we introduce the deformation gradient $\boldsymbol{F}$ as the tangent map which maps line elements $\mathrm{d}\boldsymbol{X}$ of the referential tangent space $T\mathcal{B}_0$ onto line elements $\mathrm{d}\boldsymbol{x}$ of the spatial tangent space $T\mathcal{B}_t$.

$$\boldsymbol{F} = \frac{\partial \boldsymbol{\varphi}(\boldsymbol{X}, t)}{\partial \boldsymbol{X}} = \nabla_{\boldsymbol{X}} \boldsymbol{\varphi}(\boldsymbol{X}, t) \quad \boldsymbol{F} : T\mathcal{B}_0 \rightarrow T\mathcal{B}_t \tag{2.3}$$

Note that $\boldsymbol{F}$ is a second order two-point tensor, that means, it is associated with both introduced configurations. The deformation gradient is (in general) non-symmetric. Again, we define an inverse map and introduce the inverse deformation gradient $\boldsymbol{f} = \boldsymbol{F}^{-1}$ as the tangent map which maps line elements $\mathrm{d}\boldsymbol{x}$ of the spatial tangent space $T\mathcal{B}_t$ onto line elements $\mathrm{d}\boldsymbol{X}$ of the referential tangent space $T\mathcal{B}_0$.

$$\boldsymbol{f} = \frac{\partial \boldsymbol{\Phi}(\boldsymbol{x}, t)}{\partial \boldsymbol{x}} = \nabla_{\boldsymbol{x}} \boldsymbol{\Phi}(\boldsymbol{x}, t) \quad \boldsymbol{f} : T\mathcal{B}_t \rightarrow T\mathcal{B}_0 \tag{2.4}$$

Thereby, we introduce the determinant of the deformation gradient and the determinant of the inverse deformation gradient $j = J^{-1}$ as the following JACOBIANS:

$$J = \det(\boldsymbol{F}) > 0 \qquad \text{and} \qquad j = \det(\boldsymbol{f}) > 0 \tag{2.5}$$

It is required that the JACOBIANS are not equal to zero to ensure the assumed existence of a unique mapping whereas the conditions $J > 0$ and $j > 0$ ensure that the body $\mathcal{B}$ cannot penetrate itself during the considered deformation.

Now, with the deformation gradient as the first and important measure of deformation during motion, we express the transformation of infinitesimal volume elements and the transformation of infinitesimal area elements. Infinitesimal volume elements are transformed by means of the JACOBIANS,

$$\mathrm{d}v = J\,\mathrm{d}V \qquad \text{and} \qquad \mathrm{d}V = j\,\mathrm{d}v \tag{2.6}$$

whereas we transform the orientation of infinitesimal area elements $\mathrm{d}\boldsymbol{a} = \boldsymbol{n}\,\mathrm{d}a$ and $\mathrm{d}\boldsymbol{A} = \boldsymbol{N}\,\mathrm{d}A$ by applying NANSONS's formula.

$$\mathrm{d}\boldsymbol{a} = J\,\boldsymbol{F}^{-t}\cdot\mathrm{d}\boldsymbol{A} \qquad \text{and} \qquad \mathrm{d}\boldsymbol{A} = j\,\boldsymbol{f}^{-t}\cdot\mathrm{d}\boldsymbol{a} \tag{2.7}$$

Moreover, the deformation gradient is the basis for the following deformation measures of the body $\mathcal{B}$. It is important that the deformation gradient contains rigid body motions as well as the stretch of the body $\mathcal{B}$. Therefore, we apply a polar decomposition of the deformation gradient into pure rotation $\boldsymbol{R}$ and pure stretch $\boldsymbol{U}$ measured in the reference configuration and pure stretch $\boldsymbol{u}$ measured in the spatial configuration.

$$\boldsymbol{F} = \boldsymbol{R}\cdot\boldsymbol{U} = \boldsymbol{u}\cdot\boldsymbol{R} \tag{2.8}$$

Here, $\boldsymbol{R}$ is an orthogonal rotation tensor in the considered configuration and the stretch tensors $\boldsymbol{U}$ and $\boldsymbol{u}$ are positive definite symmetric tensors. Then, we introduce the right and left CAUCHY-GREEN strain tensor.

$$\boldsymbol{C} = \boldsymbol{F}^t\cdot\boldsymbol{F} = \boldsymbol{U}^2 \qquad \text{and} \qquad \boldsymbol{b} = \boldsymbol{F}\cdot\boldsymbol{F}^t = \boldsymbol{u}^2 \tag{2.9}$$

The advantage of using the symmetric left or right CAUCHY-GREEN strain tensor instead of the deformation gradient to measure the deformation of a body $\mathcal{B}$ is given by the fact that $\boldsymbol{C}$ and $\boldsymbol{b}$ reduce to the second order unit tensor $\boldsymbol{I}$ in case of a rigid body motion. Additionally, we can demand that a strain measure should be equal to zero in case of a rigid body motion. Thus, we introduce the referential GREEN-LAGRANGE strain tensor as well as the spatial EULER-ALMANSI strain tensor.

$$\boldsymbol{E} = \frac{1}{2}\left[\boldsymbol{C} - \boldsymbol{I}\right] \qquad \text{and} \qquad \boldsymbol{e} = \frac{1}{2}\left[\boldsymbol{I} - \boldsymbol{b}^{-1}\right] \tag{2.10}$$

These symmetric strain tensors measure the differences between the squares of line elements in the spatial and material configuration, respectively. Both strain tensors vanish in case of a rigid body motion, i.e. $\boldsymbol{E} = \boldsymbol{e} = \boldsymbol{0}$ if $\boldsymbol{C} = \boldsymbol{b}^{-1} = \boldsymbol{I}$. To round off this section about kinematics, we will briefly address the transformation of the introduced vector and tensor quantities from the reference into the spatial configuration. As mentioned before, the deformation gradient is a two-point tensor associated with both explained configurations whereas all other introduced vector or tensor quantities introduced so far are uniquely associated to one of the configurations. Hence, we can transform the considered quantity by multiplication by $\boldsymbol{F}$, $\boldsymbol{F}^t$, $\boldsymbol{f}$ or $\boldsymbol{f}^t$, whereby the particular procedure depends in detail on the considered quantity. These operations are referred to as pull-back as well as push-forward operations, see, e.g., HOLZAPFEL [93] or STEIN & BARTHOLD [188].

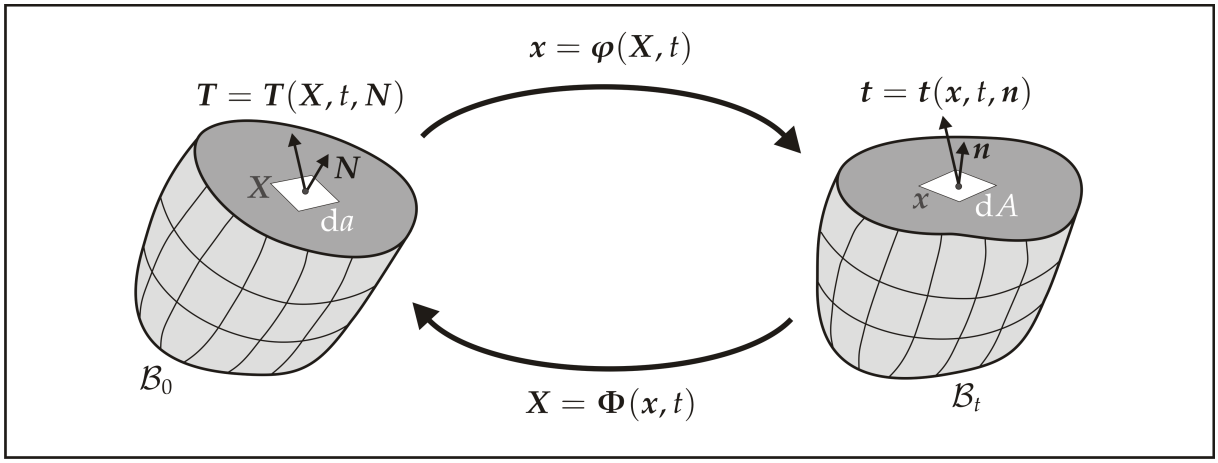

Figure 2.2.: Traction vectors in reference and current configuration acting on infinitesimal surface elements with outward normal vectors.

2.3. Stress

In the sequel, we consider the concept of stress and explain the characteristics of traction vectors and stress tensors which are required within this work. In general, traction vectors are surface force vectors per unit surface areas at a certain point. We introduce a force vector per unit area in the spatial and in the reference configuration, respectively, compare figure 2.2.

$$\boldsymbol{t} = \lim_{\Delta a \to 0} \frac{\Delta \boldsymbol{f}}{\Delta a} = \frac{\mathrm{d}\boldsymbol{f}}{\mathrm{d}a} \qquad \text{and} \qquad \boldsymbol{T} = \lim_{\Delta A \to 0} \frac{\Delta \boldsymbol{f}}{\Delta A} = \frac{\mathrm{d}\boldsymbol{f}}{\mathrm{d}A} \tag{2.11}$$

The first traction vector $\boldsymbol{t}$ is called true traction vector, or likewise CAUCHY traction vector, because the acting force vectors on the current configuration are related to a surface element on the current configuration. The second traction vector $\boldsymbol{T}$ relates the acting force vectors in the current configuration to a surface element in the reference configuration. This traction vector is called nominal stress vector, or likewise PIOLA traction vector. The introduced traction vectors have the same direction, however, they have different magnitudes due to the related area elements, obviously $\boldsymbol{t} = \frac{\mathrm{d}A}{\mathrm{d}a}\,\boldsymbol{T}$. Due to this relation between the area elements, the traction vectors at a certain point depend also on the normal vector describing the orientation of the related area element or tangent plane. This is a difference to standard field quantities depending only on $\boldsymbol{x}$ and t.

$$\boldsymbol{t} = \boldsymbol{t}(\boldsymbol{x}, t, \boldsymbol{n}) \qquad \text{and} \qquad \boldsymbol{T} = \boldsymbol{T}(\boldsymbol{X}, t, \boldsymbol{N}) \tag{2.12}$$

Further on, we imagine that the surfaces in figure 2.2 are imaginary internal surfaces of a separated body $\mathcal{B}$. Then, we apply the CAUCHY-lemma which states that the tractions acting on the opposite sides of the imaginary surface are equal in magnitude, however, they have opposite directions.

$$\boldsymbol{t}(\boldsymbol{x}, t, -\boldsymbol{n}) = -\boldsymbol{t}(\boldsymbol{x}, t, \boldsymbol{n}) \qquad \text{and} \qquad \boldsymbol{T}(\boldsymbol{x}, t, -\boldsymbol{N}) = -\boldsymbol{T}(\boldsymbol{x}, t, \boldsymbol{N}) \tag{2.13}$$

Therefore, it is arbitrary whether we apply the cut of the imaginary internal surface from the not pictured upper side (index u) or the pictured lower side (index l) of the body because $\boldsymbol{n}_u = -\boldsymbol{n}_l$ and $\boldsymbol{N}_u = -\boldsymbol{N}_l$, respectively. Due to this uniqueness of the traction vector at a certain point, we apply the CAUCHY-theorem and consider stress tensors. The CAUCHY-theorem states that the traction vectors follow from a linear map of the particular surface normal with a second order stress tensor. We obtain a true or CAUCHY stress tensor $\boldsymbol{\sigma}$ resulting in the true tractions by contraction with the associated normal vector $\boldsymbol{n}$. Moreover, we consequently obtain the nominal or PIOLA stress tensor resulting in the nominal traction vector by contraction with the associated normal vector $\boldsymbol{N}$.

$$\boldsymbol{t} = \boldsymbol{\sigma} \cdot \boldsymbol{n} \qquad \text{and} \qquad \boldsymbol{T} = \boldsymbol{P} \cdot \boldsymbol{N} \tag{2.14}$$

The true stress tensor is symmetric, $\boldsymbol{\sigma} = \boldsymbol{\sigma}^t$, which will be shown later by the balance of angular momentum. Furthermore, the true stress tensor is associated to the current configuration - remember that the true tractions are force per unit area in the current configuration. The PIOLA stress tensor is neither symmetric nor associated to a single configuration. This means that the PIOLA stress tensor is a two-point tensor just like the deformation gradient. The non-symmetry can be easily shown by applying NANONS'S formula (2.7) and expressing the traction vector $\boldsymbol{T}$ in terms of the CAUCHY-stress tensor.

$$\boldsymbol{T} = \frac{\mathrm{d}a}{\mathrm{d}A}\,\boldsymbol{t} = \frac{\mathrm{d}a}{\mathrm{d}A}\,\boldsymbol{\sigma} \cdot \boldsymbol{n} = J\,\sigma \cdot \boldsymbol{F}^{-t}\,\boldsymbol{N} = \boldsymbol{P} \cdot \boldsymbol{N} \tag{2.15}$$

With these expressions, we obtain the relation $\boldsymbol{P} = J\,\boldsymbol{\sigma} \cdot \boldsymbol{F}^{-t}$ between the true and the PIOLA stress tensor, and, obviously, the latter is non-symmetric for a general non-symmetric $\boldsymbol{F}$. This motivates a pull-back operation of the PIOLA stress tensor to obtain an alternative symmetric tensor which is called PIOLA-KIRCHHOFF stress tensor.

$$\boldsymbol{S} = \boldsymbol{F}^{-1} \cdot \boldsymbol{P} = J\,\boldsymbol{F}^{-1} \cdot \boldsymbol{\sigma} \cdot \boldsymbol{F}^{-t} \tag{2.16}$$

This tensor does not admit a physical interpretation in terms of surface tractions, however, it is symmetric, $\boldsymbol{S} = \boldsymbol{S}^t$, and it is completely associated to the reference configuration.

2.4. Balance equations

Material bodies $\mathcal{B}$ are equipped with physical properties, e.g., mass, linear momentum, angular momentum or energy. For these properties we formulate balance equations and discuss their consequences. These balance equations take into account the temporal change of the particular balanced quantity due to external actions, e.g., loading by forces or heat flux and possible internal production processes. Note that these balance equations can be embedded into a general mathematical format, or master balance law, which has to be adapted for the particularly considered balanced quantity. However, within this work, we abstain from embedding each balance equation into a master balance law to make this section as short and clearly arranged as possible. What remains

for discussing the particular balance equations is to specify the temporal changes of a quantity. We start with a LAGRANGIAN description and consider a material time derivative D_t, that means, we take into account the partial time derivative of a quantity at fixed $\boldsymbol{X}$.

$$D_t = \partial_t \left[[\bullet](\boldsymbol{X}, t) \right] \tag{2.17}$$

By applying this material time derivative on the spatial motion map $\boldsymbol{\varphi}$, we obtain the spatial velocity $\boldsymbol{v}$ as well as the spatial acceleration $\boldsymbol{a}$ of the considered body $\mathcal{B}$.

$$\boldsymbol{v}(\boldsymbol{X}, t) = D_t\, \boldsymbol{\varphi}(\boldsymbol{X}, t) = \dot{\boldsymbol{\varphi}}(\boldsymbol{X}, t) \qquad \text{and} \qquad \boldsymbol{a}(\boldsymbol{X}, t) = D_t\, \dot{\boldsymbol{\varphi}}(\boldsymbol{X}, t) = \ddot{\boldsymbol{\varphi}}(\boldsymbol{X}, t) \tag{2.18}$$

By using the inverse deformation map, recall that $\boldsymbol{X} = \boldsymbol{\Phi}(\boldsymbol{x}, t)$, we can write the spatial velocity in an EULERIAN description.

$$\boldsymbol{v}(\boldsymbol{X}, t) = \boldsymbol{v}(\boldsymbol{\Phi}(\boldsymbol{x}, t), t) = \boldsymbol{v}(\boldsymbol{x}, t) \qquad \text{and} \qquad \boldsymbol{a}(\boldsymbol{X}, t) = \boldsymbol{a}(\boldsymbol{\Phi}(\boldsymbol{x}, t), t) = \boldsymbol{a}(\boldsymbol{x}, t) \tag{2.19}$$

2.4.1. Balance of mass

The mass is assumed to be continuously (or at least piecewise continuously) distributed over the considered body $\mathcal{B}$. We introduce the following scalar mass densities in the particular configurations.

$$\rho_o(\boldsymbol{X}) = \lim_{\Delta V \to 0} \frac{\Delta m}{\Delta V} \qquad \text{and} \qquad \rho_t(\boldsymbol{x}, t) = \lim_{\Delta v \to 0} \frac{\Delta m}{\Delta v} \tag{2.20}$$

It is important that the density ρ_o is not time dependent and inherently associated with the reference configuration. Next, we obtain the mass of the body by integrating the mass densities over the associated volumes. We consider only closed systems, which means, the mass is constant during the considered motion. This leads to the following global form of total mass of the body.

$$m = \int_{\mathcal{B}_0} \rho_0(\boldsymbol{X})\, \mathrm{d}V = \int_{\mathcal{B}_t} \rho_t(\boldsymbol{x}, t)\, \mathrm{d}v = \text{constant} > 0 \tag{2.21}$$

The balance of mass requires that the material time derivative is equal to zero for all times, $D_t\, m = 0$. Clearly, the volume of the body must decrease with increasing density. We notice that (2.21) holds for arbitrary domains and we express the local form of the balance of mass with the help of the JACOBIAN.

$$\rho_0\, \mathrm{d}V = \rho_t\, \mathrm{d}v \quad \Rightarrow \quad \rho_0 = \frac{\mathrm{d}v}{\mathrm{d}V}\, \rho_t = J\, \rho_t \tag{2.22}$$

Finally, we take into account an important expression for tensor fields of any order which holds only for systems with mass conservation.

$$D_t \int_{\mathcal{B}_t} \rho_t(\boldsymbol{x}, t)\, [\bullet](\boldsymbol{x}, t)\, \mathrm{d}v = \int_{\mathcal{B}_t} \rho_t(\boldsymbol{x}, t)\, D_t[\bullet](\boldsymbol{x}, t)\, \mathrm{d}v \tag{2.23}$$

This expression states that for any quantity which should be integrated over the volume of the considered body, the material time derivative does influence only the chosen tensor quantity. This is easily understood because a change of the integration volume has to be balanced by a change of the density to ensure that the mass remains constant. A more detailed exposition can be found, e.g., in ALTENBACH & ALTENBACH [2].

2.4.2. Balance of linear momentum

The balance of linear momentum corresponds to the second axiom of NEWTON which states that the sum of applied forces on the considered body is equal to the temporal changes of the linear momentum $\boldsymbol{p}$. The linear momentum is defined as the product of mass and spatial velocity and is formulated in a reference and a spatial format.

$$\boldsymbol{p} = \int_{\mathcal{B}_0} \rho_0(\boldsymbol{X})\, \boldsymbol{v}(\boldsymbol{X}, t)\, dV = \int_{\mathcal{B}_t} \rho_t(\boldsymbol{x}, t)\, \boldsymbol{v}(\boldsymbol{x}, t)\, dv \tag{2.24}$$

We apply the introduced material time derivative to identify the temporal change in the linear momentum. By doing so, the material time derivative in the spatial format influences only the velocity due to (2.23) although the density ρ_t is time-dependent. Additionally, we introduce body forces $\boldsymbol{b}_t(\boldsymbol{x}, t) = \rho_t(\boldsymbol{x}, t)\, \boldsymbol{g}$ to account for possible gravity loading per unit volume. To express the balance of momentum in a reference format, we also define so called pseudo body forces $B_0(\boldsymbol{X}, t) = \rho_0(\boldsymbol{X})\, \boldsymbol{g}$. The pseudo body forces are connected to the body forces via the particular JACOBIAN, e.g., $\boldsymbol{B}_0 = J\, \boldsymbol{b}_t$. We complete the applied forces by regarding the possible particular tractions $\boldsymbol{t}$ and $\boldsymbol{T}$ on the outer boundary of the body, with $\boldsymbol{n}$ and $\boldsymbol{N}$ being the corresponding outward normal vectors. Then, we can express the balance of linear momentum in the reference as well as the spatial configuration.

$$\begin{aligned} D_t\, \boldsymbol{p} = \int_{\mathcal{B}_0} \rho_0\, D_t\, \boldsymbol{v}\, dV &= \int_{\partial\mathcal{B}_0} \boldsymbol{T}\, \mathrm{d}A + \int_{\mathcal{B}_0} \boldsymbol{B_o}\, \mathrm{d}V \\ D_t\, \boldsymbol{p} = \int_{\mathcal{B}_t} \rho_t\, D_t\, \boldsymbol{v}\, dv &= \int_{\partial\mathcal{B}_t} \boldsymbol{t}\ \mathrm{d}a\ + \int_{\mathcal{B}_t} \boldsymbol{b}_t\, \mathrm{d}v \end{aligned} \tag{2.25}$$

Moreover, we reformulate the integral form of the respective traction term by using the divergence theorem, compare appendix (A.10).

$$\begin{aligned} \int_{\partial\mathcal{B}_0} \boldsymbol{T}\, \mathrm{d}A &= \int_{\partial\mathcal{B}_0} \boldsymbol{P} \cdot \boldsymbol{N}\, \mathrm{d}A = \int_{\mathcal{B}_0} \mathrm{Div}\boldsymbol{P}\, \mathrm{d}V \\ \int_{\partial\mathcal{B}_t} \boldsymbol{t}\ \mathrm{d}a &= \int_{\partial\mathcal{B}_t} \boldsymbol{\sigma} \cdot \boldsymbol{n}\ \mathrm{d}a = \int_{\mathcal{B}_t} \mathrm{div}\boldsymbol{\sigma}\, \mathrm{d}v \end{aligned} \tag{2.26}$$

Thereby, $\mathrm{div}[\bullet] = \nabla_{\boldsymbol{x}}[\bullet] : \boldsymbol{I}$ is applied on spatial quantities whereas $\mathrm{Div}[\bullet] = \nabla_{\boldsymbol{X}}[\bullet] : \boldsymbol{I}$ belongs to reference quantities. Next, substituting (2.26) in (2.25) provides the balance of linear momentum in a global form.

$$\int_{\mathcal{B}_0} (\mathrm{Div}\boldsymbol{P} + \boldsymbol{B}_0 - \rho_0\, \boldsymbol{a})\ \mathrm{d}V = \int_{\mathcal{B}_t} (\mathrm{div}\boldsymbol{\sigma} + \boldsymbol{b}_t - \rho_t\, \boldsymbol{a})\ \mathrm{d}v = \boldsymbol{0} \tag{2.27}$$

Regarding that the expression (2.27) holds for arbitrary domains we obtain the local format of the balance of linear momentum which, in this case, is equivalent to CAUCHY'S first equation of motion.

$$\mathrm{Div}\boldsymbol{P} + \boldsymbol{B}_0 - \rho_0\,\boldsymbol{a} = \mathrm{div}\boldsymbol{\sigma} + \boldsymbol{b}_t - \rho_t\,\boldsymbol{a} = \boldsymbol{0} \tag{2.28}$$

This format is the equilibrium equation to be solved in the case of solid mechanics. Obviously, the reference formulation is connected to the spatial format by a push-forward operation with $\mathrm{Div}\boldsymbol{P} = J\,\mathrm{div}\boldsymbol{\sigma}$ and $\boldsymbol{B}_0 = J\,\boldsymbol{b}_t$.

2.4.3. Balance of angular momentum

The global form of the balance of angular momentum states that the sum of applied torques on a considered body is equal to the temporal change of angular momentum. The angular momentum vector $\boldsymbol{l}$ is defined as the cross product of the position vector $\boldsymbol{r}$ from an arbitrarily chosen origin with the linear momentum vector $\boldsymbol{p}$.

$$\boldsymbol{l} = \int_{\mathcal{B}_o} \boldsymbol{r}(\boldsymbol{X},\boldsymbol{t}) \times [\rho_0(\boldsymbol{X})\,\boldsymbol{v}(\boldsymbol{X},t)]\,\mathrm{d}V = \int_{\mathcal{B}_t} \boldsymbol{r}(\boldsymbol{x},\boldsymbol{t}) \times [\rho_t(\boldsymbol{x},\boldsymbol{t})\,\boldsymbol{v}(\boldsymbol{x},t)]\,\mathrm{d}v \tag{2.29}$$

The applied torques are defined as the cross product of the position vector $\boldsymbol{r}$ with the particular traction vector and the particular body force, respectively. Accordingly, we can express the global balance of angular momentum as follows.

$$\begin{aligned} D_t \int_{\mathcal{B}_0} \boldsymbol{r} \times (\rho_0\,\boldsymbol{v})\,\mathrm{d}V &= \int_{\partial\mathcal{B}_0} \boldsymbol{r} \times \boldsymbol{T}\,\mathrm{d}A + \int_{\mathcal{B}_0} \boldsymbol{r} \times \boldsymbol{B}_0\,\mathrm{d}V \\ D_t \int_{\mathcal{B}_t} \boldsymbol{r} \times (\rho_t\,\boldsymbol{v})\,\mathrm{d}v &= \int_{\partial\mathcal{B}_t} \boldsymbol{r} \times \boldsymbol{t}\,\mathrm{d}a + \int_{\mathcal{B}_t} \boldsymbol{r} \times \boldsymbol{b}_t\,\mathrm{d}v \end{aligned} \tag{2.30}$$

We transform the surface part of the latter equation into a volume part by applying the GAUSSIAN integral-theorem for cross-products, see Appendix (A.10).

$$\begin{aligned} \int_{\partial\mathcal{B}_0} \boldsymbol{r} \times \boldsymbol{T}\,\mathrm{d}A &= \int_{\mathcal{B}_0} [\boldsymbol{r} \times \mathrm{Div}\boldsymbol{P} + \nabla_{\boldsymbol{X}}\,\boldsymbol{r} \times \boldsymbol{P}]\,\mathrm{d}V \\ \int_{\partial\mathcal{B}_t} \boldsymbol{r} \times \boldsymbol{t}\,\mathrm{d}a &= \int_{\mathcal{B}_t} [\boldsymbol{r} \times \mathrm{div}\boldsymbol{\sigma} + \nabla_{\boldsymbol{x}}\,\boldsymbol{r} \times \boldsymbol{\sigma}]\,\mathrm{d}v \end{aligned} \tag{2.31}$$

We emphasize again that the position vector can be chosen arbitrarily. It hence stands to reason to choose $\boldsymbol{r} = \boldsymbol{x}$ because then $\nabla_{\boldsymbol{x}}\,\boldsymbol{r} = \boldsymbol{I}$ and $\nabla_{\boldsymbol{X}}\,\boldsymbol{r} = \boldsymbol{F}$ hold. Substituting (2.31) in (2.30) and regarding the chosen position vector leads to the following format of the angular momentum.

$$\begin{aligned} \int_{\partial\mathcal{B}_0} \boldsymbol{r} \times [\rho_0\,\boldsymbol{a} - \boldsymbol{B}_0 - \mathrm{Div}\boldsymbol{P}]\,\mathrm{d}V &= \int_{\mathcal{B}_0} \boldsymbol{F} \times \boldsymbol{P}\,\mathrm{d}V &&= \int_{\mathcal{B}_0} \overset{3}{\boldsymbol{e}} : [\boldsymbol{F} \cdot \boldsymbol{P}^t]\,\mathrm{d}V \\ \int_{\mathcal{B}_t} \boldsymbol{r} \times [\rho_t\,\boldsymbol{a} - \boldsymbol{b}_t - \mathrm{div}\boldsymbol{\sigma}]\,\mathrm{d}v &= \int_{\mathcal{B}_t} \boldsymbol{I} \times \boldsymbol{\sigma}\,\mathrm{d}v &&= \int_{\mathcal{B}_t} \overset{3}{\boldsymbol{e}} : [\boldsymbol{I} \cdot \boldsymbol{\sigma}^t]\,\mathrm{d}v \end{aligned} \tag{2.32}$$

Thereby, we have used the exposition of the vector cross-product with the third order permutation tensor, $[\bullet] \times [\diamond] = \overset{3}{\boldsymbol{e}} : [[\bullet] \cdot [\diamond]]$. Then we pay attention to the left hand term of (2.32) which consists of the linear momentum balance expression. This has to be zero and if we regard that the latter expression holds for arbitrary domains, we end up with the following local statements of the balance of angular momentum.

$$\overset{3}{\boldsymbol{e}} : [\boldsymbol{F} \cdot \boldsymbol{P}^t] = \boldsymbol{0} \qquad\qquad \overset{3}{\boldsymbol{e}} : [\boldsymbol{I} \cdot \boldsymbol{\sigma}^t] = \boldsymbol{0} \tag{2.33}$$

It can easily be confirmed that to fulfill the spatial format of the balance equation the symmetry of the CAUCHY stress tensor, $\boldsymbol{\sigma} = \boldsymbol{\sigma}^t$, is required. This is the desired result which we have mentioned while introducing the stress tensors. In contrast, the referential format requires that $\boldsymbol{F} \cdot \boldsymbol{P}^t = \boldsymbol{P} \cdot \boldsymbol{F}^t$ holds for the nominal stress tensor and the deformation gradient. This again shows that the nominal-stress tensor is non-symmetric because $\boldsymbol{F}$ is (in general) non-symmetric.

2.4.4. Balance of mechanical energy

Without further detailed explanation, the first law of thermodynamics expresses the conservation of total energy of a body. In general, the notion of energy is not restricted to mechanical energy, that means, it also includes, e.g., thermal or electrical energy. Within this work, we only take into account mechanical energy because this is sufficient for the following. In this special case the balance of energy does not provide an additional statement which must be fulfilled, it is just a consequence of the balance of linear momentum. However, the balance of mechanical energy allows us to define energetically conjugated variables, which is important for the next section about constitutive equations. Therefore, we weight the global balance of linear momentum (2.27) in the reference and spatial format with the spatial velocity $\boldsymbol{v}$.

$$\int_{\mathcal{B}_0} \boldsymbol{v} \cdot [\mathrm{Div}\boldsymbol{P} + \boldsymbol{B}_0 - \rho_0 \, D_t \, \boldsymbol{v}] \, \mathrm{d}V = \int_{\mathcal{B}_t} \boldsymbol{v} \cdot [\mathrm{div}\boldsymbol{\sigma} + \boldsymbol{b}_t - \rho_t \, D_t \, \boldsymbol{v}] \, \mathrm{d}v = 0 \tag{2.34}$$

We focus on the term which results form the multiplication of the divergence terms of the stress tensors with the spatial velocity. By applying the standard rules for the divergence of vector and tensor products (A.9) and with transformation of the volume integral into a surface integral via the divergence theorem, we obtain the following result.

$$\begin{aligned} \int_{\mathcal{B}_0} \boldsymbol{v} \cdot \mathrm{Div}\boldsymbol{P} \, \mathrm{d}V &= \int_{\mathcal{B}_0} [\mathrm{Div}[\boldsymbol{v} \cdot \boldsymbol{P}] - \boldsymbol{P} : \nabla_{\boldsymbol{X}} \boldsymbol{v}] \, \mathrm{d}V = \int_{\partial\mathcal{B}_0} \boldsymbol{T} \cdot \boldsymbol{v} \, \mathrm{d}A - \int_{\mathcal{B}_0} \boldsymbol{P} : \nabla_{\boldsymbol{X}} \boldsymbol{v} \, \mathrm{d}V \\ \int_{\mathcal{B}_t} \boldsymbol{v} \cdot \mathrm{Div}\boldsymbol{\sigma} \, \mathrm{d}v &= \int_{\mathcal{B}_t} [\mathrm{div}[\boldsymbol{v} \cdot \boldsymbol{\sigma}] - \boldsymbol{\sigma} : \nabla_{\boldsymbol{x}} \boldsymbol{v}] \, \mathrm{d}v = \int_{\partial\mathcal{B}_t} \boldsymbol{t} \cdot \boldsymbol{v} \, \mathrm{d}a - \int_{\mathcal{B}_t} \boldsymbol{\sigma} : \nabla_{\boldsymbol{x}} \boldsymbol{v} \, \mathrm{d}v \end{aligned} \tag{2.35}$$

In addition, we take into account that the material gradient of the spatial velocity $\boldsymbol{v}$ is the rate of the deformation gradient $\nabla_{\boldsymbol{X}} \boldsymbol{v}(\boldsymbol{X}, t) = \dot{\boldsymbol{F}}$. Rearranging the term in (2.34), which results by weighting the spatial acceleration with the spatial velocity, provides

the following format of the weighted balance of momentum. This is exactly the definition of the balance of mechanical energy.

$$\begin{aligned} D_t \int_{\mathcal{B}_0} \frac{1}{2}\,\rho_0\,\boldsymbol{v}\cdot\boldsymbol{v}\,\mathrm{d}V + \int_{\mathcal{B}_0} \boldsymbol{P} : \dot{\boldsymbol{F}}\,\mathrm{d}V &= \int_{\partial\mathcal{B}_0} \boldsymbol{T}\cdot\boldsymbol{v}\,\mathrm{d}A + \int_{\mathcal{B}_0} \boldsymbol{B}_0\cdot\boldsymbol{v}\,\mathrm{d}V \\ \underbrace{D_t \int_{\mathcal{B}_t} \frac{1}{2}\,\rho_t\,\boldsymbol{v}\cdot\boldsymbol{v}\;\mathrm{d}v}_{\text{kinetic energy}} + \underbrace{\int_{\mathcal{B}_t} \boldsymbol{\sigma} : \nabla_{\boldsymbol{x}}\,\boldsymbol{v}\,\mathrm{d}v}_{\text{stress power}} &= \underbrace{\int_{\partial\mathcal{B}_t} \boldsymbol{t}\cdot\boldsymbol{v}\;\mathrm{d}a + \int_{\mathcal{B}_t} \boldsymbol{b}_t\cdot\boldsymbol{v}\;\mathrm{d}v}_{\text{external force power}} \end{aligned} \tag{2.36}$$

The first contribution of (2.36) is defined as the kinetic energy. The second contribution is introduced as the stress power, whereas the right hand side is the power of the external mechanical forces. Clearly, the balance of mechanical energy states that a part of the power of the external forces is transformed into kinetic energy whereas the remainder is the stress power.

Remark 2.4.1 (Mechanical and thermal stress power) *The stress power itself can be split into two parts which contribute to the energy balance of the considered body. The first contribution is the part of the external forces which is stored in the considered body. This part is defined as the internal energy (or internal energy density in the local format) of the body. The other contribution is the part of the stress power which is possibly transformed into non-mechanical energy. This process is known as energy dissipation. Dissipation can either increase the non-mechanical energy contributions or dispense non-mechanical energy in the environment, e.g., in form of heat.*

Remark 2.4.2 (Thermodynamically conjugated variables) *As mentioned in the beginning of this section, the balance of mechanical energy allows us to define energetically conjugated variables. The* CAUCHY *stress tensor $\boldsymbol{\sigma}$ is energetically conjugated to the spatial velocity gradient $\nabla_{\boldsymbol{x}}\,\boldsymbol{v}$. The nominal stress tensor $\boldsymbol{P}$ is energetically conjugated to the rate of the deformation gradient $\dot{\boldsymbol{F}}$. We thus can express the material format of the stress power, recall that $\boldsymbol{S} = \boldsymbol{F}^{-1}\cdot\boldsymbol{P}$, and summarize the pairs of energetically conjugated variables in the following local formats of the stress power in the particular configuration.*

$$W_p = \boldsymbol{P} : \dot{\boldsymbol{F}} = \boldsymbol{S} : \dot{\boldsymbol{E}} \qquad\qquad w_p = \boldsymbol{\sigma} : \nabla_{\boldsymbol{x}}\boldsymbol{v} \tag{2.37}$$

Accordingly, the PIOLA-KIRCHHOFF *stress tensor is energetically conjugated to the rate of the* GREEN-LAGRANGE *strain tensor.*

2.5. Constitutive equations

Constitutive equations describe the material behavior of the considered body. A prerequisite for the constitutive modeling is to derive principles to decide whether a material model is physically reasonable. This is the reason why continuum mechanics is considered in a thermodynamical framework, which means that the budget of energy is extended to non-mechanical forms of energy. Within this work, we are only focusing on mechanical energy. However, to understand the formulations of the following

constitutive relations, we will briefly explain the two main statements of thermodynamics, for a detailed derivation see, e.g., ALTENBACH & ALTENBACH [2] or STEIN & BARTHOLD [188]. The first statement of thermodynamics or the first law of thermodynamics is the total balance of energy, including all incorporated forms of energy. This statement describes how one form of the considered energy forms transfers into the others. It is important that the transfer of one particular energy form into another as well as the reverse process is theoretically not limited. However, in nature it can be detected that particular energy transformations, e.g., mechanical to thermic energy are favored. This favored energy transformations are irreversible and the second main statement or second law of thermodynamics ensures that this process of energy transfer runs into this desired direction. Within this work, we neglect any thermal effects for the following constitutive equations. Hence, we abstain from introducing the complete notion of entropy and we express the second law of thermodynamics in the following local referential format of the CLAUSIUS-PLANCK inequality for the dissipation $\mathcal{D}_0$.

$$\mathcal{D}_0 = W_p - D_t\psi_0 \geq 0 \tag{2.38}$$

Here, ψ_0 is the HELMHOLTZ or free energy density function. We present only the material format of the second law of thermodynamics because we focus on solid mechanics and we want to work with referential coordinates and material time derivatives.
Next, we will define this free energy density for hyperelastic materials. Thereby, in addition to the presented laws of thermodynamics, further requirements have to be fulfilled (equipresence, determinism, local action, material objectivity, material symmetry, admissibility) which are described in detail in, e.g., ALTENBACH & ALTENBACH [2], STEIN & BARTHOLD [188]. In this chapter, we will only give a brief comment on the used principles for hyperelastic materials. We indicate that a body $\mathcal{B}$ is called elastic if we consider complete reversible processes, that means, processes with no dissipation. We consider only homogeneous bodies, meaning, we neglect an explicit dependence of the free energy density on $\boldsymbol{X}$. In this way, we can write the mentioned CLAUSIUS-DUHEM inequality as an equation for reversible processes for the energetically conjugated variables $\boldsymbol{P}$ and $\dot{\boldsymbol{F}}$ in the referential format.

$$\mathcal{D}_0 = \boldsymbol{P} : \dot{\boldsymbol{F}} - D_t\psi_0(\boldsymbol{F}) = \left[\boldsymbol{P} - \frac{\partial\psi_0(\boldsymbol{F})}{\partial\boldsymbol{F}}\right] : \dot{\boldsymbol{F}} = 0 \tag{2.39}$$

As a consequence the nominal stress tensor $\boldsymbol{P}$ follows as the derivative of the free energy density function with respect to the deformation gradient. In case of hyperelasticity the free energy density features a total differential and is independent of the state of deformation. In this special case and by further considering only mechanical energy, the introduced HELMHOLTZ energy density is equal to the further mentioned internal energy density. Clearly, the free energy density models only that part of the stress power which should be stored in the body because there is no dissipation.
However, the presented format does not fulfill the principal of material objectivity which states that the material response is independent of the particular observer. This statement technically requires that the free energy density keeps constant for rigid body motions. Therefore, the free energy density is expressed in a general referential format, $\psi_0(\boldsymbol{F}) = \psi_0(\boldsymbol{F}^t \cdot \boldsymbol{F}) = \psi_0(\boldsymbol{C}(\boldsymbol{F}))$. By applying this latter dependence on the

strain energy density we obtain the desired stress tensors as the following derivatives of the free energy density.

$$\begin{aligned} \boldsymbol{P} &= \frac{\partial \psi_0(\boldsymbol{C}(\boldsymbol{F}))}{\partial \boldsymbol{F}} &&= 2\,\boldsymbol{F} \cdot \frac{\partial \psi_0(\boldsymbol{C}(\boldsymbol{F}))}{\partial \boldsymbol{C}} \\ \boldsymbol{S} &= \frac{\partial \psi_0(\boldsymbol{C}(\boldsymbol{F})}{\partial \boldsymbol{E}} &&= 2\,\frac{\partial \psi_0(\boldsymbol{C}(\boldsymbol{F}))}{\partial \boldsymbol{C}} \end{aligned} \tag{2.40}$$

In the chosen case of a referential free energy density, we obtain the spatial CAUCHY stress tensor by applying the following push-forward operation.

$$\boldsymbol{\sigma} = \frac{1}{J}\,\frac{\partial \psi(\boldsymbol{C}(\boldsymbol{F}))}{\partial \boldsymbol{F}} \cdot \boldsymbol{F}^t = \frac{2}{J}\,\boldsymbol{F} \cdot \frac{\partial \psi(\boldsymbol{C}(\boldsymbol{F}))}{\partial \boldsymbol{C}} \cdot \boldsymbol{F}^t \tag{2.41}$$

Now, we restrict ourselves without loss of generality to the NEO-HOOKEAN constitutive equation, see, e.g., WRIGGERS [210] or BELYTSCHKO et al. [197] for a more comprehensive exposition. This constitutive equation is an extension of the classical isotropic HOOKE'S law to large deformation and is a sufficient relation for the following tasks. The associated energy density function is the following, with μ and λ being the LAMÉ parameters.

$$\psi_0(\mathrm{I}_c, \mathrm{III}_c) = \frac{\mu}{2}\,[\mathrm{I}_c - 3] - \mu \ln\left(\sqrt{\mathrm{III}_c}\right) + \frac{\lambda}{2} \ln^2\left(\sqrt{\mathrm{III}_c}\right) \tag{2.42}$$

Since we consider only isotropic materials the energy density is given in terms of invariants, $\mathrm{I}_c = \boldsymbol{C} : \boldsymbol{I}$ and $\mathrm{III}_c = \det(\boldsymbol{C}) = J^2$, see likewise appendix (A.7) or, e.g., SPENCER [185] for a more detailed explanation of invariants. We can specify the PIOLA stress tensor, the PIOLA-KIRCHHOFF stress tensor and the CAUCHY stress tensor for the chosen NEO-HOOKEAN constitutive law.

$$\begin{aligned} \boldsymbol{S} &= \mu\,[\boldsymbol{I} - \boldsymbol{C}^{-1}] + \lambda \ln \sqrt{\mathrm{III}_c}\,\boldsymbol{C}^{-1} \\ \boldsymbol{P} &= \mu\,\boldsymbol{F} - \left[\mu - \lambda \ln\left(\sqrt{\mathrm{III}_c}\right)\right]\,\boldsymbol{F}^{-t} \\ \boldsymbol{\sigma} &= \frac{\mu}{J}\,[\boldsymbol{b} - \boldsymbol{I}] + \frac{\lambda\,\ln\left(\sqrt{\mathrm{III}_c}\right)}{\sqrt{\mathrm{III}_c}}\,\boldsymbol{I} \end{aligned} \tag{2.43}$$

Next, we take into account the incremental form of the constitutive equations. This form provides the constitutive relation between incremental changes in stresses and strains which are referred to as tangent moduli or elasticity tensor, see, e.g., HOLZAPFEL [93] for a more comprehensive explanation. These tangent moduli are given for the referential pair of variables $\boldsymbol{S}$ and $\boldsymbol{E}$ because due to the formulation of the constitutive law in referential coordinates this purely referential format is the frequently used one for the linearization in the following section.

$$\mathbb{L} = \frac{\partial \boldsymbol{S}}{\partial \boldsymbol{E}} = \frac{\partial^2 \psi_0}{\partial \boldsymbol{E}^2} = 4\,\frac{\partial^2 \psi_0}{\partial \boldsymbol{C}^2} = -\left[2\,\mu - 2\,\lambda \ln\left(\sqrt{\mathrm{III}_c}\right)\right]\,\frac{\partial \boldsymbol{C}^{-1}}{\partial \boldsymbol{C}} + \lambda\,\boldsymbol{C}^{-1} \otimes \boldsymbol{C}^{-1} \tag{2.44}$$

Thereby, we make use of the partial derivatives of the invariants as well as the following derivative with $\frac{\partial \boldsymbol{C}^{-1}}{\partial \boldsymbol{C}} = -\frac{1}{2}\left[\boldsymbol{C}^{-1}\overline{\otimes}\boldsymbol{C}^{-1} + \boldsymbol{C}^{-1}\underline{\otimes}\boldsymbol{C}^{-1}\right]$, compare appendix (A.11). For

the sake of completeness we mention that it is also possible to express the elasticity tensor in a two-point description. We obtain an elasticity tensor associated with both configurations for the pair of variables $\boldsymbol{P}$ and $\boldsymbol{F}$ by calculating the second derivative of the strain energy density with respect to the deformation gradient or by applying the following broadly speaking intermediate push-forward operation on the referential elasticity tensor $\mathbb{L}$, see, e.g., WRIGGERS [210] or OGDEN [145].

$$\begin{aligned} \mathbb{A} &= \frac{\partial \boldsymbol{P}}{\partial \boldsymbol{F}} = \frac{\partial^2 \psi_0}{\partial \boldsymbol{F}^2} = [\boldsymbol{F} \overline{\otimes} \boldsymbol{I}] : \mathbb{L} : \left[\boldsymbol{F}^t \overline{\otimes} \boldsymbol{I}\right] + \boldsymbol{I} \overline{\otimes} \boldsymbol{S} \\ \mathbb{A} &= \lambda\, \boldsymbol{F}^{-t} \otimes \boldsymbol{F}^{-t} + \left[\mu - \ln\left(\sqrt{\mathrm{III}_c}\right)\right] \boldsymbol{F}^{-t} \underline{\otimes} \boldsymbol{F}^{-1} + \mu\, \boldsymbol{I} \overline{\otimes} \boldsymbol{I} \end{aligned} \tag{2.45}$$

A complete push-forward operation of the elasticity tensor $\mathbb{L}$ in the referential format leads to the completely spatial tangent modulus $\mathbb{E}$ for the spatial pair of variables $\boldsymbol{\sigma}$ and $\nabla_{\boldsymbol{x}} \boldsymbol{\varphi}$, see, e.g., WRIGGERS [210] for a detailed elaboration.

$$\mathbb{E} = \frac{1}{\sqrt{(\mathrm{III}_c)}} [\boldsymbol{F} \overline{\otimes} \boldsymbol{F}] : \mathbb{L} : [\boldsymbol{F}^t \overline{\otimes} \boldsymbol{F}^t] = \frac{\lambda}{\sqrt{\mathrm{III}_c}}\, \boldsymbol{I} \otimes \boldsymbol{I} + 2 \left[\frac{\mu - \ln\left(\sqrt{\mathrm{III}_c}\right)}{\sqrt{\mathrm{III}_c}}\right] \mathbb{I}^{sym} \tag{2.46}$$

Thereby, $\mathbb{I}^{sym} = \frac{1}{2}\left[\boldsymbol{I} \overline{\otimes} \boldsymbol{I} + \boldsymbol{I} \underline{\otimes} \boldsymbol{I}\right]$ denotes the symmetric fourth order identity tensor. It is important that the referential as well as the spatial elasticity tensor $\mathbb{L}$ and $\mathbb{E}$ are fully symmetric. This means that $[\bullet]_{ijkl} = [\bullet]_{ijlk}$ holds because both of the referential participants $\boldsymbol{S}$ and $\boldsymbol{E}$ as well as both of the spatial participants $\boldsymbol{\sigma}$ and $\nabla_{\boldsymbol{x}} \boldsymbol{\varphi}$ are symmetric. Furthermore, it holds $[\bullet]_{ijkl} = [\bullet]_{klij}$ due to the attribute of the free energy density which features a total differential for hyperelasticity. For the two-point elasticity tensor only the latter symmetry is valid because as mentioned before neither $\boldsymbol{P}$ nor $\boldsymbol{F}$ is symmetric in general.

2.6. Boundary value problem

In this section we formulate the boundary value problem to be solved in the case of solid mechanics. We prefer a LAGRANGIAN description because in solid mechanics the reference configuration is usually known. Accordingly, the main task besides the formulation of practical initial and boundary conditions is to determine the actual spatial deformation map $\boldsymbol{x} = \boldsymbol{\varphi}(\boldsymbol{X}, t)$ based on the known referential configuration and the introduced fundamental equations. This facts also illustrates that we have used a constitutive relation in reference coordinates in the last section without further explanation. Before going into detail of the formulation of the boundary value problem we have to emphasize some crucial aspects.

Remark 2.6.1 (Temporal dependence) *The first aspect concerns the time dependence. This dependence is fundamental to understand the introduced equations, e.g., the balance of energy. Therefore, we have introduced all fundamental equations in a fully time dependent framework. From now on, we neglect the time dependence and consider quasi static circumstances which are acceptable for the following considerations within this work. Accordingly, the formulation of initial conditions for the boundary value problem is thus unnecessary.*

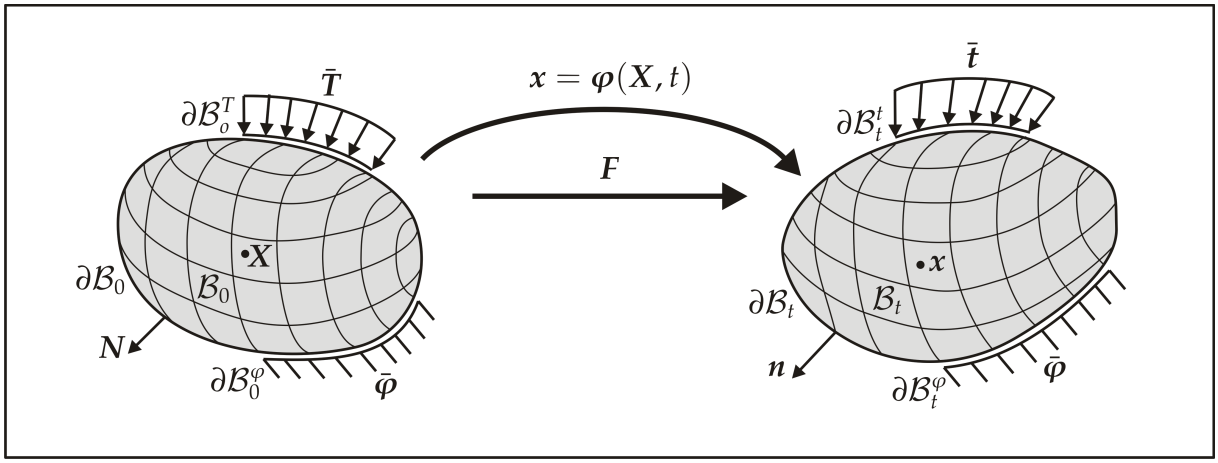

Figure 2.3.: Boundary value problem of body $\mathcal{B}$ with particular boundary $\partial\mathcal{B}_o$ and $\partial\mathcal{B}_t$ on which either DIRICHLET or NEUMANN boundary conditions can be prescribed.

Remark 2.6.2 (Variational vs. virtual work formulation) *The next issue regards the way of introducing the weak form of the boundary value problem. It should be recalled that the constitutive equations can be derived as the total differential of the free or* HELMHOLTZ *energy density in the case of hyperelasticity. If we now presume that the external loads are in addition so called conservative loads, that means, they are also independent of the state of deformation, we can derive the weak form of the boundary value problem by a variational formulation based on the principle of stationary potential energy. This means that we take into account the total potential energy of the body which consists of the mentioned internal energy which is stored in the body by virtue of the actual deformations and the external energy due to the external loads, see, e.g.,* HOLZAPFEL *[93],* STEIN & BARTHOLD *[188] or* OGDEN *[145] for a detailed explanation. However, we will see later in this work that for discontinuous processes with special regards to discontinuous interfaces a consistent variational formulation is not always straightforward. Accordingly, we use the more general way and apply the principal of virtual work for the derivation of the governing equations of the boundary value problem and abstain from expressing the equations additionally in a variational context for the sake of clear arrangement.*

Remark 2.6.3 (Referential vs. spatial format) *Although we use a* LAGRANGIAN *description in referential coordinates, we express all further equations in a referential and a spatial format. On one hand this is done for the sake of completeness. On the other hand, later in this work, we will see that it is useful to model constitutive equations in a spatial setting. This is more physical for both, the present continuous and the later discontinuous solid problem.*

As the basic equations for the boundary value problem we recapitulate the local format of the balance of momentum as well as the constitutive relations of the stresses in the particular configuration, see equation (2.47) and (2.48). We subdivide the boundary of the body into disjoint parts $\partial\mathcal{B}_0 = \partial\mathcal{B}_0^\varphi \cup \partial\mathcal{B}_0^T$ and $\partial\mathcal{B}_t = \partial\mathcal{B}_t^\varphi \cup \partial\mathcal{B}_t^t$ with $\partial\mathcal{B}_0^\varphi \cap \partial\mathcal{B}_0^T = \varnothing$ and $\partial\mathcal{B}_t^\varphi \cup \partial\mathcal{B}_t^t = \varnothing$. Then we add the boundary conditions in terms of primary or DIRICHLET conditions regarding fixed parts of the spatial deformation map as well as secondary or NEUMANN conditions taking into account fixed tractions in the particular

configuration, see equations (2.49), (2.50) or compare figure 2.3.

equilibrium	$\mathbf{0} = \mathrm{Div}\boldsymbol{P} + \boldsymbol{B}_0$	$\mathbf{0} = \mathrm{div}\boldsymbol{\sigma} + \boldsymbol{b}_t$	(2.47)
constitutive equation	$\boldsymbol{P} = 2\,\boldsymbol{F} \cdot \dfrac{\partial \psi}{\partial \boldsymbol{C}}$	$\boldsymbol{\sigma} = \dfrac{2}{J}\,\boldsymbol{F} \cdot \dfrac{\partial \psi}{\partial \boldsymbol{C}} \cdot \boldsymbol{F}^t$	(2.48)
DIRICHLET conditions	$\boldsymbol{\varphi} = \bar{\boldsymbol{\varphi}}$	$\boldsymbol{\varphi} = \bar{\boldsymbol{\varphi}}$	(2.49)
NEUMANN conditions	$\boldsymbol{T} = \boldsymbol{P} \cdot \boldsymbol{N} = \bar{\boldsymbol{T}}$	$\boldsymbol{t} = \boldsymbol{\sigma} \cdot \boldsymbol{n} = \bar{\boldsymbol{t}}$	(2.50)

2.6.1. Principal of virtual work

As a prerequisite for the following principal of virtual work we weight the particular local format of the balance of momentum with an admissible vector valued test function $\boldsymbol{\eta} \in H_0^1$. This test function is required to be arbitrary, infinitesimal, and kinematically admissible, i.e., the test function is equal to zero on the DIRICHLET boundary. We integrate over the particular domain of interest and obtain the following weighted formats of the balance of linear momentum.

$$\int_{\mathcal{B}_0} \boldsymbol{\eta} \cdot \mathrm{Div}\boldsymbol{P}\,\mathrm{d}V + \int_{\mathcal{B}_0} \boldsymbol{\eta} \cdot \boldsymbol{B}_t\,\mathrm{d}V \quad = \int_{\mathcal{B}_t} \boldsymbol{\eta} \cdot \mathrm{div}\boldsymbol{\sigma}\,\mathrm{d}v + \int_{\mathcal{B}_t} \boldsymbol{\eta} \cdot \boldsymbol{b}_t\,\mathrm{d}v = 0 \tag{2.51}$$

Then we reformulate the divergence term by applying integration by parts which provides the following result for the particular configuration.

$$\begin{aligned} \int_{\mathcal{B}_0} \boldsymbol{\eta} \cdot \mathrm{Div}\boldsymbol{P}\,\mathrm{d}V &= \int_{\mathcal{B}_0} \mathrm{Div}[\boldsymbol{\eta} \cdot \boldsymbol{P}]\,\mathrm{d}V - \int_{\mathcal{B}_0} \nabla_{\boldsymbol{X}}\boldsymbol{\eta} : \boldsymbol{P}\,\mathrm{d}V \\ \int_{\mathcal{B}_t} \boldsymbol{\eta} \cdot \mathrm{div}\boldsymbol{\sigma}\,\mathrm{d}v &= \int_{\mathcal{B}_t} \mathrm{div}[\boldsymbol{\eta} \cdot \boldsymbol{\sigma}]\;\mathrm{d}v - \int_{\mathcal{B}_t} \nabla_{\boldsymbol{x}}^{sym}\boldsymbol{\eta} : \boldsymbol{\sigma}\,\mathrm{d}v \end{aligned} \tag{2.52}$$

Next, we focus on the latter result (2.52) and transform the volume integral of the divergence term into a surface integral by applying the divergence theorem, see appendix (A.10).

$$\begin{aligned} \int_{\mathcal{B}_0} \mathrm{Div}[\boldsymbol{\eta} \cdot \boldsymbol{P}]\,\mathrm{d}V &= \int_{\partial\mathcal{B}_0} \boldsymbol{\eta} \cdot \boldsymbol{P} \cdot \boldsymbol{N}\,\mathrm{d}A \\ \int_{\mathcal{B}_t} \mathrm{div}[\boldsymbol{\eta} \cdot \boldsymbol{\sigma}]\,\mathrm{d}v &= \int_{\partial\mathcal{B}_t} \boldsymbol{\eta} \cdot \boldsymbol{\sigma} \cdot \boldsymbol{n}\;\mathrm{d}a \end{aligned} \tag{2.53}$$

At this point, we include the kinematic admissibility of the test function, recall that $\boldsymbol{\eta} = 0\ \forall \boldsymbol{X} \in \partial\mathcal{B}_0^{\varphi}$ and $\boldsymbol{\eta} = 0\ \forall \boldsymbol{x} \in \partial\mathcal{B}_t^{\varphi}$. This means that the just emerging result (2.53) is either equal to zero or matches the particular NEUMANN boundary conditions. By combining the results of (2.52) and (2.53) with (2.51) we obtain the following particular

formats.

$$\begin{aligned} \int_{\mathcal{B}_0} \nabla_{\boldsymbol{X}} \boldsymbol{\eta} : \boldsymbol{P}\, \mathrm{d}V \; - \int_{\partial\mathcal{B}_0} \boldsymbol{\eta} \cdot \bar{\boldsymbol{T}}\, \mathrm{d}A - \int_{\mathcal{B}_0} \boldsymbol{\eta} \cdot \boldsymbol{B}_0\, \mathrm{d}V \; &= 0 \\ \int_{\mathcal{B}_t} \nabla_{\boldsymbol{x}}^{sym} \boldsymbol{\eta} : \boldsymbol{\sigma}\, \mathrm{d}v - \int_{\partial\mathcal{B}_t} \boldsymbol{\eta} \cdot \bar{\boldsymbol{t}}\; \mathrm{d}a \; - \int_{\mathcal{B}_t} \boldsymbol{\eta} \cdot \boldsymbol{b}_t\; \mathrm{d}v \; &= 0 \end{aligned} \tag{2.54}$$

Remark 2.6.4 (Weak form) *Equation* (2.54) *is called weak form because it fulfills the balance of linear momentum in a weak sense. This means that the originally weighted balance of momentum* (2.51) *has to be equal to zero for all possible test functions. This format is equivalent to the local balance of linear momentum. However, the use of integration by parts requires that the test function is at least ordinary differentiable, recall that we have stated* $\boldsymbol{\eta} \in H_0^1$*. Thus, we have restricted the test function and therefore the latter format is called weak form. This final format is the non-linear integral description of the boundary value problem which has to be further discussed in the following.*

We further specify the test function and interpret the test function as a virtual deformation map $\boldsymbol{\eta} = \delta\boldsymbol{\varphi}$. Accordingly, we interpret the weak form (2.54) as a virtual work equation and split the expression into an internal as well as an external virtual work part.

$$\begin{aligned} \delta\mathcal{W} \quad &= \delta\mathcal{W}_{int} - \delta\mathcal{W}_{ext} = 0 \\ \delta\mathcal{W}^{int} \quad &= \int_{\mathcal{B}_0} \nabla_{\boldsymbol{X}} \delta\boldsymbol{\varphi} : \boldsymbol{P}\, \mathrm{d}V = \int_{\mathcal{B}_t} \nabla_{\boldsymbol{x}}^{sym} \delta\boldsymbol{\varphi} : \boldsymbol{\sigma}\, \mathrm{d}v \\ \delta\mathcal{W}^{ext} \quad &= \int_{\partial\mathcal{B}_0} \delta\boldsymbol{\varphi} \cdot \bar{\boldsymbol{T}}\, \mathrm{d}A + \int_{\mathcal{B}_0} \delta\boldsymbol{\varphi} \cdot \boldsymbol{B}_0\, \mathrm{d}V = \int_{\partial\mathcal{B}_t} \delta\boldsymbol{\varphi} \cdot \bar{\boldsymbol{t}}\, \mathrm{d}a + \int_{\mathcal{B}_t} \delta\boldsymbol{\varphi} \cdot \boldsymbol{b}_t\, \mathrm{d}v \end{aligned} \tag{2.55}$$

2.6.2. Linearization of continuous equations

As mentioned above the principle of virtual work is non-linear in the unknown spatial deformation map. Therefore, the next section elaborates the solution of the mentioned non-linear boundary value problem. Analytical or closed-form mathematical solutions of this set of partial differential equations are only known for some special cases. In general numerical solutions are required to solve equation (2.54). One possible and common technique to solve these non-linear equations is the iterative solution with a NEWTON-RAPHSON scheme in conjunction with the finite element method. For this solution technique a consistent linearization of all associated quantities is needed. We apply the directional derivative $\Delta[\bullet](\boldsymbol{X}) = \frac{\mathrm{d}}{\mathrm{d}\epsilon}[\bullet](\boldsymbol{X} + \epsilon\, \Delta\boldsymbol{X})\Big|_{\epsilon=0}$ and express the virtual work equation based on a first order TAYLOR expansion as follows.

$$\delta\mathcal{W}(\boldsymbol{\varphi} + \Delta\boldsymbol{\varphi}) = \delta\mathcal{W}(\boldsymbol{\varphi}) + \Delta\delta\mathcal{W}(\boldsymbol{\varphi}) \tag{2.56}$$

By applying this linearization, the complete non-linear problem is displaced by a sequence of linear problems which are straightforward to solve within an iteration process. Next, we consider the linearization of the mentioned continuous virtual work expressions including the linearization of all required kinematical quantities. We assume that the virtual work of the external forces $\delta\mathcal{W}^{ext}$ is independent on the deformation such that $\Delta\delta\mathcal{W}^{ext} = 0$. What remains is the linearization of the internal virtual work expression. We recall that the introduced constitutive equations are originally given in a purely referential format in terms of $\boldsymbol{S}$ and $\boldsymbol{E}$. Hence, we apply a complete pull-back operation of (2.55) to perform the linearization in the purely referential format. We recall that $\boldsymbol{P} = \boldsymbol{F} \cdot \boldsymbol{S}$ and $\boldsymbol{S} = \boldsymbol{S}^t$ and obtain $\nabla_{\boldsymbol{X}}\delta\boldsymbol{\varphi} : \boldsymbol{P} = \nabla_{\boldsymbol{X}}\delta\boldsymbol{\varphi} : [\boldsymbol{F} \cdot \boldsymbol{S}] = [\nabla^t_{\boldsymbol{X}}\delta\boldsymbol{\varphi} \cdot \boldsymbol{F}]^{sym} : \boldsymbol{S}$. Correspondingly, the purely referential format can be expressed as follows.

$$\delta\mathcal{W}^{int} = \int_{\mathcal{B}_0} \nabla_{\boldsymbol{X}}\delta\boldsymbol{\varphi} : \boldsymbol{P}\,\mathrm{d}V = \int_{\mathcal{B}_0} [\nabla^t_{\boldsymbol{X}}\delta\boldsymbol{\varphi} \cdot \boldsymbol{F}]^{sym} : \boldsymbol{S}\,\mathrm{d}V \tag{2.57}$$

Next, the directional derivative of the deformation gradient $\Delta\boldsymbol{F} = \nabla_{\boldsymbol{X}}\Delta\boldsymbol{\varphi}$ as well as the directional derivative of the GREEN-LAGRANGE strain tensor $\Delta\boldsymbol{E} = [\Delta\boldsymbol{F}^t \cdot \boldsymbol{F}]^{sym}$ allow us to state the incremental relation between this energetically conjugated variables by means of the symmetric referential elasticity tensor $\Delta\boldsymbol{S} = \mathbb{L} : \Delta\boldsymbol{E} = \mathbb{L} : \left[\Delta\boldsymbol{F}^t \cdot \boldsymbol{F}\right]^{sym}$. Now, we express the directional derivative of the complete internal virtual work equation.

$$\Delta\delta\mathcal{W}^{int} = \int_{\mathcal{B}_0} \left[\nabla^t_{\boldsymbol{X}}\delta\boldsymbol{\varphi} \cdot \nabla_{\boldsymbol{X}}\Delta\boldsymbol{\varphi}\right]^{sym} : \boldsymbol{S}\,\mathrm{d}V + \int_{\mathcal{B}_0} \left[\nabla^t_{\boldsymbol{X}}\delta\boldsymbol{\varphi} \cdot \boldsymbol{F}\right]^{sym} : \mathbb{L} : \left[\boldsymbol{F}^t \cdot \nabla_{\boldsymbol{X}}\Delta\boldsymbol{\varphi}\right]^{sym}\mathrm{d}V \tag{2.58}$$

We obtain a geometric contribution due to the dependence of the strains on the deformations and a material contribution by virtue of the mentioned constitutive dependence of the stress tensor on the strains. We further express the directional derivative in the two-point description.

$$\Delta\delta\mathcal{W}^{int} = \int_{\mathcal{B}_0} \nabla_{\boldsymbol{X}}\delta\boldsymbol{\varphi} : \mathbb{A} : \nabla_{\boldsymbol{x}}\Delta\boldsymbol{\varphi}\,\mathrm{d}V \tag{2.59}$$

This format seems to be the most simple one. However, this format complicates the understanding of the geometrical and the material dependence of the virtual work equation because the geometrical dependence is hidden in the two-point elasticity tensor $\mathbb{A}$ (2.45), in the pair of two-point variables $\boldsymbol{F}$ and $\boldsymbol{P}$ which are associated to both configurations. Additionally, this format is more difficult from the implementation point of view because of its non-symmetric participants. Therefore, we prefer the directional derivative of the purely referential format because this format has been developed historically and is still present in many finite element codes due to its symmetry.
Concluding this part, we perform a push-forward operation and express the directional derivative of the internal virtual work in a purely spatial format.

$$\Delta\delta\mathcal{W}^{int} = \int_{\mathcal{B}_t} \left[\nabla^t_{\boldsymbol{x}}\delta\boldsymbol{\varphi} \cdot \nabla_{\boldsymbol{x}}\Delta\boldsymbol{\varphi}\right]^{sym} : \boldsymbol{\sigma}\,\mathrm{d}v + \int_{\mathcal{B}_t} \nabla^t_{\boldsymbol{x}}\delta\boldsymbol{\varphi} : \mathbb{E} : \nabla^{sym}_{\boldsymbol{x}}\Delta\boldsymbol{\varphi}\,\mathrm{d}v \tag{2.60}$$

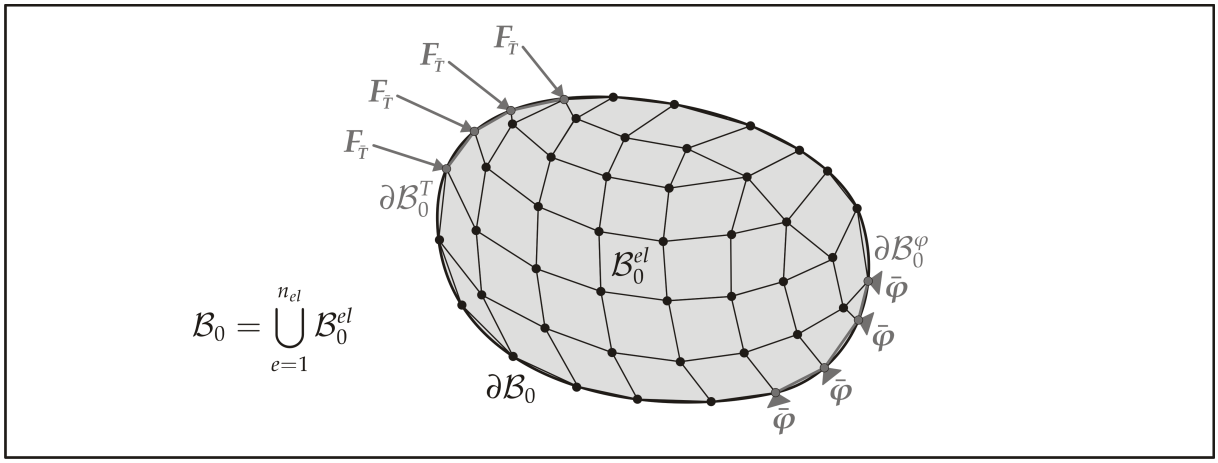

Figure 2.4.: Discretization of body $\mathcal{B}_0$ into n_{el} elements and boundaries $\partial\mathcal{B}_o$ and $\partial\mathcal{B}_t$ on which either DIRICHLET or NEUMANN boundary conditions can be prescribed in terms of nodal values.

2.6.3. Discretization

While the last subsection takes into account the linearization of the continuous equations of the non-linear boundary value problem, this part focuses on the discretization in the context of a finite element formulation. We decompose the body $\mathcal{B}_0$ in n_{el} elements $\mathcal{B}_0^{el}$, compare figure 2.4. Next, approximations for all related quantities are required. We take advantage of the isoparametric concept and use the same approximations of the space $\boldsymbol{X}$ and deformation map $\boldsymbol{\varphi}$. Moreover, we apply the BUBNOV-GALERKIN technique and use the same approximations of the deformation map $\boldsymbol{\varphi}$ and the virtual deformation map (test function) $\delta\boldsymbol{\varphi}$. By using LAGRANGIAN shape functions N_i for any of the n_{en} nodes per element $\mathcal{B}_0^{el}$ we obtain the element-wise approximation for the space, the deformation map and the virtual deformation map as follows.

$$\boldsymbol{X} = \sum_{i=1}^{n_{en}} N_i \, \boldsymbol{X}_i \qquad \boldsymbol{\varphi} = \sum_{i=1}^{n_{en}} N_i \, \boldsymbol{\varphi}_i \qquad \delta\boldsymbol{\varphi} = \sum_{i=1}^{n_{en}} N_i \, \delta\boldsymbol{\varphi}_i \tag{2.61}$$

Here, $\boldsymbol{\varphi}_i$ denotes the deformation map at the particular element node i. The gradients of the deformation map and the test function arises from the chosen approximation as follows.

$$\nabla_{\boldsymbol{X}}\boldsymbol{\varphi} = \sum_{i=1}^{n_{en}} \boldsymbol{\varphi}_i \otimes \nabla_{\boldsymbol{X}} N_i \qquad \nabla_{\boldsymbol{X}}\delta\boldsymbol{\varphi} = \sum_{i=1}^{n_{en}} \delta\boldsymbol{\varphi}_i \otimes \nabla_{\boldsymbol{X}} N_i \tag{2.62}$$

Here, the LAGRANGIAN shape functions N_i are formulated in so-called isoparametric coordinates $N_i(\boldsymbol{X}(\boldsymbol{\xi}))$ on a unit element domain $\mathcal{B}_\diamond^{el}$ to facilitate the handling of arbitrary geometries in a computational framework. Accordingly, a unique transformation $\boldsymbol{X}(\boldsymbol{\xi})$ between the element geometry given in the reference configuration $\mathcal{B}_0$ and the unit configuration $\mathcal{B}_\diamond^{el}$ configuration is required, see, e.g., ZIENKIEWICZ [217], Altenbach & Sacharov [3], BELYTSCHKO et al. [197] or WRIGGERS [210]. With these approximations at hand, we assemble all elements of the structure which is symbolized with the following assembly operator $\mathop{\mathbf{A}}_{e=1}^{n_{el}}$ and express the whole discretization of the

virtual work in the particular configuration.

$$\begin{aligned} \delta\mathcal{W} &= \mathop{\mathbf{A}}_{e=1}^{n_{el}} \delta\boldsymbol{\varphi}_i \cdot \left[\int_{\mathcal{B}_0^{el}} \nabla_{\boldsymbol{X}} N_i \cdot \boldsymbol{P}\, \mathrm{d}V - \int_{\partial\mathcal{B}_0^{el}} N_i\, \bar{\boldsymbol{T}}\, \mathrm{d}A - \int_{\mathcal{B}_0^{el}} N_i\, \boldsymbol{B_0}\, \mathrm{d}V \right] = 0 \\ \delta\mathcal{W} &= \mathop{\mathbf{A}}_{e=1}^{n_{el}} \delta\boldsymbol{\varphi}_i \cdot \left[\int_{\mathcal{B}_t^{el}} \nabla_{\boldsymbol{x}} N_i \cdot \boldsymbol{\sigma}\, \mathrm{d}v - \int_{\partial\mathcal{B}_t^{el}} N_i\, \bar{\boldsymbol{t}}\, \mathrm{d}a - \int_{\mathcal{B}_t^{el}} N_i\, \boldsymbol{b_t}\, \mathrm{d}v \right] = 0 \end{aligned} \tag{2.63}$$

This discretization leads to the following vector valued residual at all $I = 1, .., n_{np}$ global nodes.

$$\begin{aligned} \mathbf{R}_I &= \mathbf{R}_I^{int} - \mathbf{R}_I^{ext} = \mathbf{0} \\ \mathbf{R}_I^{int} &= \mathop{\mathbf{A}}_{e=1}^{n_{el}} \int_{\mathcal{B}_0^{el}} \nabla_{\boldsymbol{X}} N_i \cdot \boldsymbol{P}\, \mathrm{d}V = \mathop{\mathbf{A}}_{e=1}^{n_{el}} \int_{\mathcal{B}_t^{el}} \nabla_{\boldsymbol{x}} N_i \cdot \boldsymbol{\sigma}\, \mathrm{d}v \\ \mathbf{R}_I^{ext} &= \mathop{\mathbf{A}}_{e=1}^{n_{el}} \int_{\partial\mathcal{B}_0^{el}} N_i\, \bar{\boldsymbol{T}}\, \mathrm{d}A - \int_{\mathcal{B}_0^{el}} N_i\, \boldsymbol{B_0}\, \mathrm{d}V = \mathop{\mathbf{A}}_{e=1}^{n_{el}} \int_{\partial\mathcal{B}_t^{el}} N_i\, \bar{\boldsymbol{t}}\, \mathrm{d}a - \int_{\mathcal{B}_t^{el}} N_i\, \boldsymbol{b_t}\, \mathrm{d}v \end{aligned} \tag{2.64}$$

This latter discrete non-linear system of equations (2.64) can be understood as the discrete counterpart of the continuous virtual work problem.

2.6.4. Consistent residual linearization

The above mentioned non-linear discrete system of equations has to be solved numerically within a finite element setting. Hence, the aforementioned NEWTON-RAPHSON scheme is applied to this non-linear residual equation and a consistent linearization of this expression is required.

$$\mathbf{R}_I^{k+1} = \mathbf{R}_I^k + \Delta\mathbf{R}_I = \mathbf{0} \tag{2.65}$$

Here, $\Delta\mathbf{R}_I$ is the further introduced directional derivative with is expressed as follows.

$$\Delta\mathbf{R}_I(\boldsymbol{\varphi}_J) = \sum_{J=1}^{n_{np}} \frac{\partial\mathbf{R}_I(\boldsymbol{\varphi}_J)}{\partial\boldsymbol{\varphi}_J} \cdot \Delta\boldsymbol{\varphi}_J = \sum_{J=1}^{n_{np}} \mathbf{K}_{IJ} \cdot \Delta\boldsymbol{\varphi}_J \tag{2.66}$$

In this directional derivative, $\mathbf{K}_{IJ} = \dfrac{\partial\mathbf{R}_I(\boldsymbol{\varphi}_J)}{\partial\boldsymbol{\varphi}_J}$ is the tangent stiffness matrix which is expressed in the completely referential format as well as the two-point description and the completely spatial format.

$$\begin{aligned} \mathbf{K}_{IJ} &= \mathop{\mathbf{A}}_{e=1}^{n_{el}} \int_{\mathcal{B}_0^{el}} \nabla_{\boldsymbol{X}}^t N_i \cdot \boldsymbol{S} \cdot \nabla_{\boldsymbol{X}} N_j\, \boldsymbol{I}\, \mathrm{d}V + \int_{\mathcal{B}_0^{el}} \left[\nabla_{\boldsymbol{X}}^t N_i \cdot \boldsymbol{F}\right]^{sym} \cdot \mathbb{L} \cdot \left[\boldsymbol{F}^t \cdot \nabla_{\boldsymbol{X}} N_j\right]^{sym} \mathrm{d}V \\ \mathbf{K}_{IJ} &= \mathop{\mathbf{A}}_{e=1}^{n_{el}} \int_{\mathcal{B}_0^{el}} \nabla_{\boldsymbol{X}}^t N_i \cdot \mathbb{A} \cdot \nabla_{\boldsymbol{X}} N_j\, \mathrm{d}V \\ \mathbf{K}_{IJ} &= \mathop{\mathbf{A}}_{e=1}^{n_{el}} \int_{\mathcal{B}_t^{el}} \nabla_{\boldsymbol{x}}^t N_i \cdot \boldsymbol{\sigma} \cdot \nabla_{\boldsymbol{x}} N_j\, \boldsymbol{I}\, \mathrm{d}v + \int_{\mathcal{B}_t^{el}} \nabla_{\boldsymbol{x}}^t N_i \cdot \mathbb{E} \cdot \nabla_{\boldsymbol{x}} N_j\, \mathrm{d}v \end{aligned} \tag{2.67}$$

We recall that the small indices i and j are the particular $1, .., n_{en}$ element nodes whereas the capital indices I and J represent the total number of $1, .., n_{np}$ global nodes.

Remark 2.6.5 (Discretization and linearization) *For the continuous approximation of the deformation map in combination with elasticity the discretization of the linearized continuous equations is equal to the linearization of the discrete residual equations. Therefore, we have elaborated this solution scheme by means of the continuous equations for the sake of clarity. However, for particular non-elasticity problems as well as for structural finite elements with rotational degrees of freedom, the linearization of the continuous equations is not equal to the discrete counterpart, see, e.g.,* WRIGGERS *[210] or* BATHE *[16]. In such cases only the consistent linearization of the discrete residual system of equations provides the desired convergence behavior within the numerical solution procedure.*

3. Discontinuous solid mechanics

3.1. Motivation

This chapter introduces the governing equations as well as the discretization scheme for the mesh-independent modeling of strong discontinuities in the case of non-linear solid mechanics. It starts with an extension of the continuous kinematics to the discontinuous situation. In detail, a formulation in accordance with the works of JÄGER et al. [102, 100, 98], KUHL et al. [112], MERGHEIM [125] and MERGHEIM et al. [127, 129] based on the works of HANSBO & HANSBO [86, 85] is presented. Further, the kinematic formulation of the present approach which has recently gained more popularity, see, e.g., RABCZUK et al. [162], SONG et al. [184], AREIAS et al. [9] or MOLINO et al. [136], is compared with the more classical formulation of a discontinuous situation based on the HEAVISIDE function, see, e.g., BELYTSCHKO et al. [17], OLIVER [147], DE BORST et al. [45] in general, or especially WELLS [204], GASSER & HOLZAPFEL [71], as well as ARMERO & LINDER [11] for a large deformation setting. This is an absolutely necessary prerequisite for the understanding of the differences between the discretization schemes.
With the knowledge of the discontinuous kinematics, the governing equations are composed for a finite element formulation, and the used discretization scheme is presented in detail. This discretization scheme captures arbitrarily positioned discontinuities in finite element meshes with the requirement of additional global degrees of freedom. Accordingly, this approach is compared to the XFEM, which as mentioned in the introduction, also requires global degrees of freedom for the consideration of discontinuities, see, e.g., BELYTSCHKO & BLACK [17], DOLBOW et al. [48] based on the partition of unity method of BABUSKA & MELENK [13]. In detail, it will be shown that the present approach can be understood as a reparametrization of unknowns, see, e.g., AREIAS & BELYTSCHKO [6]. However, by applying one parametrization there are some assets and drawbacks which have to be evaluated. Moreover, we comment on the issues of higher order approximation, see, e.g., LEGAY et al. [114], STAZI et al. [187] or ENGLUND [59], blending elements, see, e.g., CHESSA et al. [34] and the discretization of structural elements like shells, see, e.g., AREIAS et al. [5, 184].
Upon completion of the comparison with the XFEM we focus on certain implementational aspects. We comment on the handling of the complex data of the geometry, see, e.g., SUKUMAR et al. [195] or BORDAS et al. [24] and mainly for three-dimensional problems, e.g., SUKUMAR [194], AREIAS & BELYTSCHKO, [4] or GASSER & HOLZAPFEL [71]. Especially, we elaborate the splitting of elements and its connected numerical integration which is required for the realization of the discontinuity, compare, e.g., MERGHEIM et al. [128] or JÄGER et al. [99]. Subsequently, we explain the visualization of a discontinuity, see, e.g., REMMERS [163] or O'BRIEN & HODGINS [144] for two-dimensional problems. Moreover, we take into account the modeling of crack tip elements to ensure the real geometric properties of a crack tip as well as partially cracked

elements, compare, e.g., RABCZUK et al. [162].
Finally, we give a numerical example to clarify the following topics. This example as a benchmark problem has to present the large deformation setting. It elaborates issues of discretization and visualization and demonstrates the problem of stress analysis at sharp crack tips in a non-linear setting. Hence, a brief comment on linear elastic fracture mechanics is required, see, e.g., GROSS & SEELIG [81] or HAHN [83] for a general overview or KUNA [113]. Moreover, we demonstrate the problem of unbounded stresses for the numerical analysis of discontinuities. This is important for the later required introduction of failure onset criteria as well as crack propagation criteria. This means that, within this chapter, we consider only stationary cracks focusing on the technical details to realize a discontinuity in the mesh without reflecting about the onset of a discontinuity.

3.2. Kinematics

The first step to incorporate a discontinuity in the deformation map is the definition of the relevant kinematical quantities. We extend the kinematics for the continuous problem and assume that the considered body $\mathcal{B}$ in the reference configuration is crossed by a discontinuity Γ, compare figure 3.1. Then, we divide the body $\mathcal{B}$ into disjoint parts $\mathcal{B}_0^-$ and $\mathcal{B}_0^+$ due to the discontinuity. Now, we define a unique spatial motion map $\boldsymbol{x} = \boldsymbol{\varphi}(\boldsymbol{X})$ which maps all particles of the related part of the body $\mathcal{B}$ from the referential into the spatial configuration.

$$\boldsymbol{\varphi}(\boldsymbol{X}) = \begin{cases} \boldsymbol{\varphi}^+(\boldsymbol{X}) & \forall\, \boldsymbol{X} \in \mathcal{B}^+ \quad \boldsymbol{\varphi}^+ : \mathcal{B}_0^+ \rightarrow \mathcal{B}_t^+ \\ \boldsymbol{\varphi}^-(\boldsymbol{X}) & \forall\, \boldsymbol{X} \in \mathcal{B}^- \quad \boldsymbol{\varphi}^- : \mathcal{B}_0^- \rightarrow \mathcal{B}_t^- \end{cases} \tag{3.1}$$

This spatial deformation map is continuous in both related parts of the body, however, it can be discontinuous along the internal discontinuity surface Γ. Accordingly, the difference of the particular deformation maps $\boldsymbol{\varphi}^-$ and $\boldsymbol{\varphi}^+$ evaluated on both sides of the discontinuity inherently provides a jump in the deformation field which represents the crack in this case of solid mechanics, see again figure 3.1.

$$[\![\boldsymbol{\varphi}]\!] = \boldsymbol{\varphi}^+|_\Gamma - \boldsymbol{\varphi}^-|_\Gamma \qquad \forall\, \boldsymbol{X} \in \Gamma \tag{3.2}$$

As a result of this definition of the spatial motion map (3.1) all related kinematic quantities as well as the introduced stress measures have to be defined on both sides $\mathcal{B}^-$ and $\mathcal{B}^+$ of the discontinuity. Hence, we obtain the deformation gradients $\boldsymbol{F}$ as the tangent maps for both parts of the body, whereby it is obvious that the deformation gradient is not defined at the discontinuity itself.

$$\boldsymbol{F} = \begin{cases} \boldsymbol{F}^+ = \nabla_{\boldsymbol{X}} \boldsymbol{\varphi}^+(\boldsymbol{X}) & \forall\, \boldsymbol{X} \in \mathcal{B}^+ \quad \boldsymbol{F}^+ : T\mathcal{B}_0^+ \rightarrow T\mathcal{B}_t^+ \\ \boldsymbol{F}^- = \nabla_{\boldsymbol{X}} \boldsymbol{\varphi}^-(\boldsymbol{X}) & \forall\, \boldsymbol{X} \in \mathcal{B}^- \quad \boldsymbol{F}^- : T\mathcal{B}_0^- \rightarrow T\mathcal{B}_t^- \end{cases} \tag{3.3}$$

Furthermore, we obtain the particular JACOBIANS as the determinants of the related deformation gradients.

$$J = \begin{cases} J^+ = \det(\boldsymbol{F}^+) & \forall\, \boldsymbol{X} \in \mathcal{B}^+ \\ J^- = \det(\boldsymbol{F}^-) & \forall\, \boldsymbol{X} \in \mathcal{B}^- \end{cases} \tag{3.4}$$

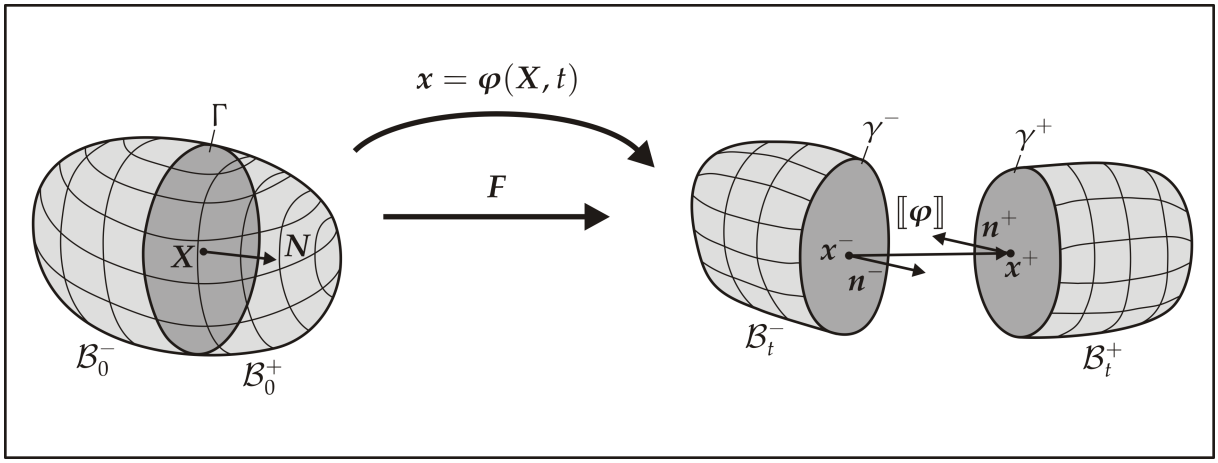

Figure 3.1.: Deformation map of a body $\mathcal{B}$ crossed by a discontinuity Γ.

Now, keeping in mind that the deformation gradient is the only independent variable for the introduced stress and strain measures, these quantities can be expressed on either side of the discontinuity. However, for the sake of simplicity, we refrain from expressing each introduced strain and stress measure of the former chapter in the same manner.

Remark 3.2.1 (Discontinuity surface tractions) *By applying the defined spatial motion map* (3.1) *on placements* $\boldsymbol{X}$ *describing the unique surface* Γ *in the reference configuration we obtain two surfaces* γ^- *and* γ^+ *in the spatial configuration, compare figure 3.1. These surfaces are described by their associated normal vectors* $\boldsymbol{n}^-$ *and* $\boldsymbol{n}^+$ *and, accordingly, a unique definition of traction vectors with their corresponding pull-back and push-forward operations on these surfaces is not possible. Hence, this issue requires a special treatment which will be given in the next chapter on the cohesive crack concept.*

Next, we consider an important aspect concerning the chosen definition of the discontinuous deformation map with its associated fragmentation in particular parts by virtue of the discontinuity. For an alternative expression of the discontinuous deformation map, we use the HEAVISIDE function.

$$\mathcal{H}(\boldsymbol{X}) = \begin{cases} 1 & \forall \boldsymbol{X} \in \mathcal{B}^+ \\ \frac{1}{2} & \forall \boldsymbol{X} \in \Gamma \\ 0 & \forall \boldsymbol{X} \in \mathcal{B}^- \end{cases} \tag{3.5}$$

Thereby, the gradient $\nabla_{\boldsymbol{X}} \mathcal{H}(\boldsymbol{X}) = \delta_\Gamma(\boldsymbol{X})\, \boldsymbol{N}$ comprises the DIRAC delta-distribution, see, e.g., MOSLER [138], SIMONE [182] or STAKGOLD [186] for a more elaborated derivation.

$$\delta_\Gamma(\boldsymbol{X}) = \begin{cases} \infty & \forall \boldsymbol{X} \in \Gamma \\ 0 & \forall \boldsymbol{X} \in \mathcal{B}^- \cup \mathcal{B}^+ \end{cases} \quad \text{with} \quad \int_{\mathcal{B}^- \cup \mathcal{B}^+} \delta_\Gamma(\boldsymbol{X})\, [\bullet](\boldsymbol{X})\, \mathrm{d}V = \int_\Gamma [\bullet](\boldsymbol{X})\, \mathrm{d}A \tag{3.6}$$

With this expression at hand, we rewrite the spatial motion map in a more compact form consisting of a continuous and a discontinuous part.

$$\begin{aligned} \boldsymbol{\varphi}(\boldsymbol{X}) &= \mathcal{H}(\boldsymbol{X})\,\boldsymbol{\varphi}^{+}(\boldsymbol{X}) + [1-\mathcal{H}(\boldsymbol{X})]\,\boldsymbol{\varphi}^{-}(\boldsymbol{X}) \\ &= \boldsymbol{\varphi}^{-}(\boldsymbol{X}) + \mathcal{H}(\boldsymbol{X})\,[\boldsymbol{\varphi}^{+}(\boldsymbol{X}) - \boldsymbol{\varphi}^{-}(\boldsymbol{X})] \end{aligned} \tag{3.7}$$

We obtain the following expression of the deformation gradient which consist of a bounded part $\boldsymbol{F}^{b}$ due to the gradients of the continuous deformation maps and an unbounded part $\boldsymbol{F}^{u}$ due to the discontinuity.

$$\begin{aligned} \boldsymbol{F} &= \delta_{\Gamma}\,\boldsymbol{\varphi}^{+} \otimes \boldsymbol{N} + \mathcal{H}\;\boldsymbol{F}^{+} - \delta_{\Gamma}\,\boldsymbol{\varphi}^{-} \otimes \boldsymbol{N} + [1-\mathcal{H}]\,\boldsymbol{F}^{-} \\ &= \underbrace{\mathcal{H}\;\boldsymbol{F}^{+} + [1-\mathcal{H}]\,\boldsymbol{F}^{-}}_{\boldsymbol{F}^{b}} + \underbrace{\delta_{\Gamma}\,[\![\boldsymbol{\varphi}]\!] \otimes \boldsymbol{N}}_{\boldsymbol{F}^{u}} \end{aligned} \tag{3.8}$$

Within this work we prefer the format given in (3.1) which is formulated among others in JÄGER et al. [98], KUHL et al. [112], MERGHEIM [125] and MERGHEIM et al. [127, 129] based on the works of HANSBO & HANSBO [86, 85]. However, the latter format is the more common one for the numerical treatment of discontinuities in solid mechanics, see, e.g., BELYTSCHKO et al. [17], OLIVER [147], DE BORST et al. [45] in general or especially WELLS [204], GASSER & HOLZAPFEL [71], as well as ARMERO & LINDER [11] for a large deformation setting. This format is essential when comparing the different available discretization schemes from the literature.

3.3. Boundary value problem

Corresponding to the former chapter, we recall the local format of the balance of linear momentum as well as the hyperelastic constitutive relation for the stresses in the particular configuration as the basic equations for the boundary value problem. Again, we use the split of the boundary $\partial\mathcal{B}$ into disjoint part $\partial\mathcal{B}_0 = \partial\mathcal{B}_0^{\varphi} \cup \partial\mathcal{B}_0^{T}$ and $\partial\mathcal{B}_t = \partial\mathcal{B}_t^{\varphi} \cup \partial\mathcal{B}_t^{t}$ with $\partial\mathcal{B}_0^{\varphi} \cap \partial\mathcal{B}_0^{T} = \varnothing$ and $\partial\mathcal{B}_t^{\varphi} \cup \partial\mathcal{B}_t^{t} = \varnothing$. Moreover, we add the boundary conditions in terms of DIRICHLET conditions taking into account fixed parts of the spatial deformation map as well as NEUMANN conditions regarding fixed tractions in the particular configuration and express the summarized strong equations for the boundary value problem as follows.

equilibrium	$\boldsymbol{0} = \mathrm{Div}\boldsymbol{P} + \boldsymbol{B}_0$	$\boldsymbol{0} = \mathrm{div}\boldsymbol{\sigma} + \boldsymbol{b}_t$	(3.9)
constitutive equation	$\boldsymbol{P} = 2\,\boldsymbol{F} \cdot \dfrac{\partial\psi}{\partial\boldsymbol{C}}$	$\boldsymbol{\sigma} = \dfrac{2}{J}\,\boldsymbol{F} \cdot \dfrac{\partial\psi}{\partial\boldsymbol{C}} \cdot \boldsymbol{F}^{t}$	(3.10)
DIRICHLET conditions	$\boldsymbol{\varphi} = \bar{\boldsymbol{\varphi}}$	$\boldsymbol{\varphi} = \bar{\boldsymbol{\varphi}}$	(3.11)
NEUMANN conditions	$\boldsymbol{T} = \boldsymbol{P} \cdot \boldsymbol{N} = \bar{\boldsymbol{T}}$	$\boldsymbol{t} = \boldsymbol{\sigma} \cdot \boldsymbol{n} = \bar{\boldsymbol{t}}$	(3.12)

Obviously, the main difference to the continuous formulation in the former chapter lies in the fact that the local balance of linear momentum has to be solved for the two

sub-domains which means the latter referential format holds for $\forall \boldsymbol{X} \in \mathcal{B}_0^+ \cup \mathcal{B}_0^-$ and $\forall \boldsymbol{x} \in \mathcal{B}_t^+ \cup \mathcal{B}_t^-$ in the spatial format, respectively.

3.3.1. Principle of virtual work

Subsequently, we consider the principle of virtual work in the same manner as introduced in detail in the former chapter. We multiply the strong form of the boundary value problem with a test function $\boldsymbol{\eta} \in H_0^1$. Then, by using integration by parts and taking into account the boundary conditions, we obtain the weak form or integral format of the boundary value problem. Again, we interpret the test function as a virtual deformation map $\boldsymbol{\eta} = \delta\boldsymbol{\varphi}$, and express the weak form in the following virtual work format.

$$\begin{aligned}
\delta\mathcal{W} &= \delta\mathcal{W}^{int} - \delta\mathcal{W}^{ext} = 0 \\
\delta\mathcal{W}^{int} &= \int_{\mathcal{B}_t^+ \cup \mathcal{B}_t^-} \nabla_{\boldsymbol{x}}^{sym} \delta\boldsymbol{\varphi} : \boldsymbol{\sigma} \, \mathrm{d}v = \int_{\mathcal{B}_0^+ \cup \mathcal{B}_0^-} \nabla_{\boldsymbol{X}} \delta\boldsymbol{\varphi} : \boldsymbol{P} \, \mathrm{d}V \\
\delta\mathcal{W}^{ext} &= \int_{\partial\mathcal{B}_t^+ \cup \partial\mathcal{B}_t^-} \delta\boldsymbol{\varphi} \cdot \bar{\boldsymbol{t}} \, \mathrm{d}a + \int_{\mathcal{B}_t^+ \cup \mathcal{B}_t^-} \delta\boldsymbol{\varphi} \cdot \boldsymbol{b}_t \, \mathrm{d}v = \int_{\partial\mathcal{B}_0^+ \cup \partial\mathcal{B}_0^-} \delta\boldsymbol{\varphi} \cdot \bar{\boldsymbol{T}} \, \mathrm{d}A + \int_{\mathcal{B}_0^+ \cup \mathcal{B}_0^-} \delta\boldsymbol{\varphi} \cdot \boldsymbol{B}_0 \, \mathrm{d}V
\end{aligned} \tag{3.13}$$

3.3.2. Discretization

First of all, we apply a decomposition of the body $\mathcal{B}_0$ in n_{el} elements $\mathcal{B}_0^{el}$ similar to the foregoing chapter. It proves convenient to distinguish between standard continuous finite elements $\mathcal{B}_0^{el,c}$ which are not affected by the discontinuity and discontinuous finite elements $\mathcal{B}_0^{el,(+,-)}$. For the former we apply the discretization introduced in the previous chapter.
Now, we come to the main section of this chapter and consider the discretization scheme for a discontinuous finite element $\mathcal{B}_0^{el,(+,-)}$. For this discontinuous element we apply an independent approximation of the deformation fields $\boldsymbol{\varphi}^+$ and $\boldsymbol{\varphi}^-$ on both sides of the discontinuity corresponding to the preferred independent format of the presented spatial motion map. Strictly speaking, both deformation maps are interpolated independently over the entire element. In detail, for each of the continuous displacement fields $\boldsymbol{\varphi}^+$ or $\boldsymbol{\varphi}^-$ the usual number of degrees of freedom is required. Although the chosen displacement field is only defined on the corresponding side of the discontinuity it is well approximated by the complete number of nodal values of the element with its usual LAGRANGIAN shape functions. Accordingly, additional degrees of freedom are required to ensure the desired independent approximation of the second deformation field on the other side of the discontinuity. We introduce the following two copies of the standard LAGRANGIAN shape functions with n_{en}^+ nodes for the part $\mathcal{B}_0^{el,+}$ and n_{en}^- nodes for $\mathcal{B}_0^{el,-}$, respectively. Each of the two sets of shape functions is set to zero on one side of the discontinuity while keeping their usual values on the other side.

$$N_i^+ = \begin{cases} N_i & \forall \boldsymbol{X} \in \mathcal{B}_0^{el,+} \\ 0 & \forall \boldsymbol{X} \in \mathcal{B}_0^{el,-} \end{cases} \qquad N_i^- = \begin{cases} 0 & \forall \boldsymbol{X} \in \mathcal{B}_0^{el,+} \\ N_i & \forall \boldsymbol{X} \in \mathcal{B}_0^{el,-} \end{cases} \tag{3.14}$$

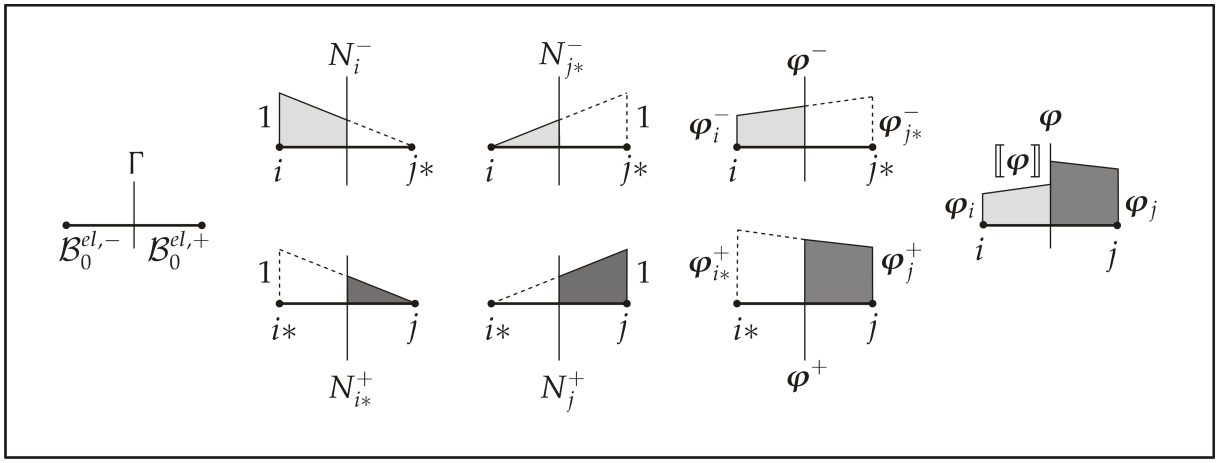

Figure 3.2.: Approximation of discontinuous deformation presented for a one-dimensional finite element.

By doing so, we double the total number of degrees of freedom for the considered element. Now, by using the isoparametric concept, regarding the same discretizations of space $\boldsymbol{X}$ and deformation field $\boldsymbol{\varphi}$ and applying the BUBNOV-GALERKIN technique, which applies an equal approximation of the deformation field $\boldsymbol{\varphi}$ and the test function $\delta\boldsymbol{\varphi}$, we obtain the following expressions for the independent approximation on both sides of the discontinuity.

$$\begin{aligned}
\boldsymbol{X}^+ &= \sum_{i=1}^{n_{en}^+} N_i^+ \, \boldsymbol{X}_i^+ & \boldsymbol{\varphi}^+ &= \sum_{i=1}^{n_{en}^+} N_i^+ \, \boldsymbol{\varphi}_i^+ & \delta\boldsymbol{\varphi}^+ &= \sum_{i=1}^{n_{en}^+} N_i^+ \, \delta\boldsymbol{\varphi}_i^+ \\
\boldsymbol{X}^- &= \sum_{i=1}^{n_{en}^+} N_i^- \, \boldsymbol{X}_i^- & \boldsymbol{\varphi}^- &= \sum_{i=1}^{n_{en}^-} N_i^+ \, \boldsymbol{\varphi}_i^- & \delta\boldsymbol{\varphi}^- &= \sum_{i=1}^{n_{en}^-} N_i^- \, \delta\boldsymbol{\varphi}_i^-
\end{aligned} \tag{3.15}$$

Here, $\boldsymbol{X}_i^{(+,-)}$ and $\boldsymbol{\varphi}_i^{(+,-)}$ are the nodal coordinates and the nodal deformation map per element. Accordingly, the gradients of the deformation map and of the test function arise naturally from the chosen approximation.

$$\begin{aligned}
\nabla_{\boldsymbol{X}}\boldsymbol{\varphi}^+ &= \sum_{i=1}^{n_{en}^+} \boldsymbol{\varphi}_i^+ \otimes \nabla_{\boldsymbol{X}} N_i^+ & \nabla_{\boldsymbol{X}}\delta\boldsymbol{\varphi}^+ &= \sum_{i=1}^{n_{en}^+} \delta\boldsymbol{\varphi}_i^+ \otimes \nabla_{\boldsymbol{X}} N_i^+ \\
\nabla_{\boldsymbol{X}}\boldsymbol{\varphi}^- &= \sum_{i=1}^{n_{en}^-} \boldsymbol{\varphi}_i^- \otimes \nabla_{\boldsymbol{X}} N_i^- & \nabla_{\boldsymbol{X}}\delta\boldsymbol{\varphi}^- &= \sum_{i=1}^{n_{en}^-} \delta\boldsymbol{\varphi}_i^- \otimes \nabla_{\boldsymbol{X}} N_i^-
\end{aligned} \tag{3.16}$$

Furthermore, the jump in the displacement field and in the test functions arises inherently as the difference of the two continuous displacement fields evaluated for the placements on the internal boundary Γ.

$$\begin{aligned}
[\![\boldsymbol{\varphi}]\!] &= \sum_{i}^{n_{en}^+} N_i^+ \,|_\Gamma \, \boldsymbol{\varphi}_i^+ - \sum_{i}^{n_{en}^-} N_i^- \,|_\Gamma \, \boldsymbol{\varphi}_i^- = \sum_{p}^{n_{en}^+ + n_{en}^-} \bar{N}_p^\Gamma \, \boldsymbol{\varphi}_p \\
[\![\delta\boldsymbol{\varphi}]\!] &= \sum_{i}^{n_{en}^+} N_i^+ \,|_\Gamma \, \delta\boldsymbol{\varphi}_i^+ - \sum_{i}^{n_{en}^-} N_i^- \,|_\Gamma \, \delta\boldsymbol{\varphi}_i^- = \sum_{p}^{n_{en}^+ + n_{en}^-} \bar{N}_p^\Gamma \, \delta\boldsymbol{\varphi}_p
\end{aligned} \tag{3.17}$$

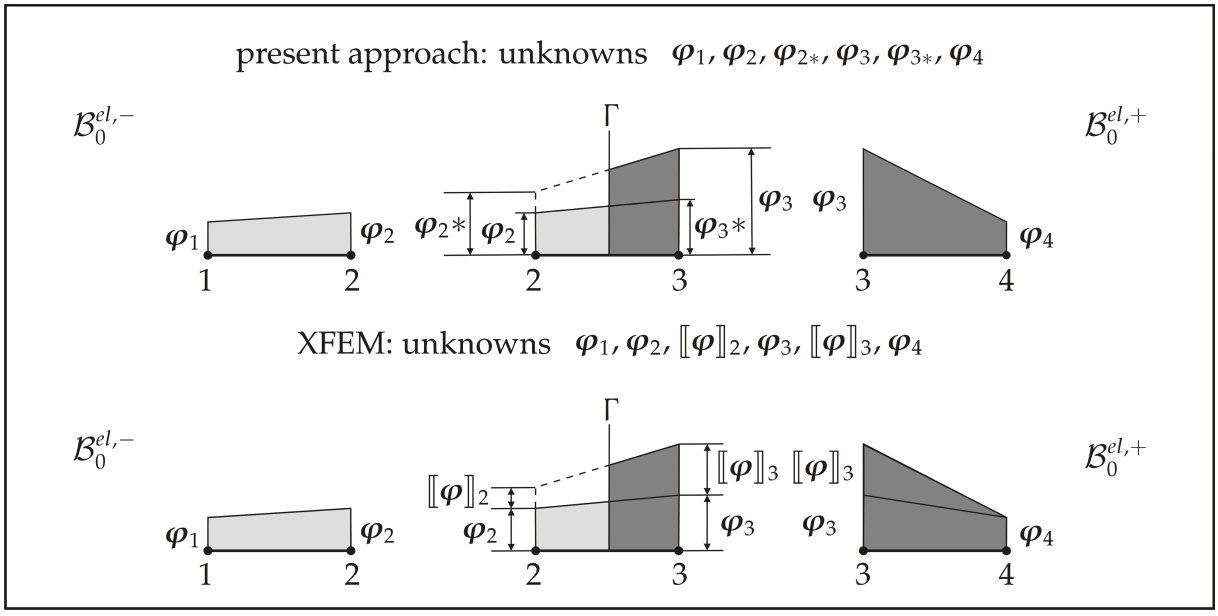

Figure 3.3.: Comparison: Discretization of present approach with XFEM discretization by means of HEAVISIDE enrichment.

Here, the newly introduced set $\bar{N}_p^\Gamma$ contains the set of shape functions evaluated on gamma with the corresponding algebraic sign. To clarify the described discretization scheme a one-dimensional discretization example is provided in figure 3.2.

Remark 3.3.1 (Comparison present approach vs. XFEM) *Let us recall the alternative formulation of a discontinuous spatial motion map* (3.7) *which is given in section 3.2. This definition of the discontinuous spatial motion map is used for* BELYTSCHKO*'s extended finite element method, see, e.g.,* BELYTSCHKO & BLACK *[17],* DOLBOW *et al. [48] based on the partition of unity method of* BABUSKA & MELENK *[13]. Within this discretization scheme, the deformation field, as mentioned before, is split into a continuous and a discontinuous part. Thereby, the discontinuous part is realized by multiplying the* LAGRANGIAN *shape functions with the mentioned* HEAVISIDE *function which keeps the attribute of a partition of unity. Broadly speaking, a partition of unity means that the sum of the element shape functions is equal to one for any considered position within the element, compare again* BABUSKA & MELENK *[13] for a detailed explanation. Accordingly, this procedure is established as* HEAVISIDE *enrichment. Enrichments with other step functions, e.g., the sign function are also possible for the XFEM discretization. Those can be advantageous in certain cases, see, e.g.,* DUMSTORFF *[54],* REMMERS *[163] for an overview or* RÉTHORÉ *[165] and* MENOUILLARD *et al. [124] for certain details. Let us clarify the differences as well as the similarities of the two approaches. Recall that the kinematics of the two approaches can be transferred into one another by expressing the deformation map, e.g., by means of the* HEAVISIDE *function. Accordingly, the discretization schemes are related and* AREIAS & BELYTSCHKO *[6] have shown that the present approach can be expressed as a linear combination of the XFEM basis functions. Therefore, it is evident that both approaches require the same number of additional global degrees of freedom to capture the discontinuity, compare again figure 3.3. The main difference is the parametrization. The present approach uses only displacement degrees of freedom which afterwards provides the displacement jump, whereas the XFEM is parametrized in continuous*

displacement degrees of freedom and so called additional or nodal jump degrees of freedom. This different interpolation may lead to certain advantages of the particular discretization schemes for selected problems. For instance, the XFEM can more easily handle partially cracked elements whereby this is a more challenging task applied to the presented discretization scheme. We will later specify this in the section about crack tip elements. With the present approach, a differing polynomial approximation of the continuous displacement field and the discontinuity is not possible. In contrast, the XFEM allows a higher order polynomial approximation for the continuous displacement field, see, e.g., LEGAY *et al. [114],* STAZI *et al. [187] or* ENGLUND *[59]. On the other hand, the present approach does not require a special treatment of neighboring elements. The XFEM discretization affects also neighboring elements, see again figure 3.3 or compare, e.g.,* CHESSA *et al. [34]. The present formulation facilitates the implementation in commercial finite element codes, see, e.g.,* JÄGER *et al. [100]. Furthermore, it can more easily treat discontinuities in shells or structural elements due to its formulation in purely deformational degrees of freedom, see, e.g.,* AREIAS *et al. [5, 184]. Additionally, it can also be an advantage for the modeling of dynamics, where the handling of mass matrices is more extensive for additional jump degrees of freedom than for purely deformational degrees of freedom, see, e.g.,* RABCZUK *et al. [162].*
Completing the comparison of the present discretization scheme with the XFEM it should be mentioned that the present approach has recently gained more popularity, see, e.g., SONG *et al. [184] or* MOLINO *et al. [136] where the approach is called method with phantom nodes and virtual node algorithm, respectively.*

Let us now focus on a concise notation for the discretized principle of virtual work. We use the abbreviation $d = (+,-)$ for the discontinuous elements to indicate the particular considered part. Additionally, we include also the continuous elements which leads to the abbreviation $N_i^{(c,d)}$ for the corresponding shape-function to the particular considered i-th element node. Accordingly, we assemble all n_{el} elements including the discontinuous part $\mathcal{B}_0^{el,d}$ and the continuous part $\mathcal{B}_0^{el,c}$ with the following assembly operator $\mathop{\mathbf{A}}_{e=1}^{n_{el}}$. We obtain the discretized principle of virtual work for the complete body $\mathcal{B}$ in the referential and the spatial format.

$$\begin{aligned}
\delta\mathcal{W} &= \mathop{\mathbf{A}}_{e=1}^{n_{el}} \delta\boldsymbol{\varphi}_i \cdot \Big[\int_{\mathcal{B}_0^{el,c}\cup\mathcal{B}_0^{el,d}} \nabla_{\boldsymbol{X}} N_i^{(c,d)} \cdot \boldsymbol{P}^{(c,d)} \,\mathrm{d}V - \int_{\partial\mathcal{B}_0^{el,c}\cup\partial\mathcal{B}_0^{el,d}} N_i^{(c,d)}\, \bar{\boldsymbol{T}}^{(c,d)} \,\mathrm{d}A - \int_{\mathcal{B}_0^{el,c}\cup\mathcal{B}_0^{el,d}} N_i^{(c,d)}\, \boldsymbol{B_0}^{(c,d)} \,\mathrm{d}V \Big] = 0 \\
\delta\mathcal{W} &= \mathop{\mathbf{A}}_{e=1}^{n_{el}} \delta\boldsymbol{\varphi}_i \cdot \Big[\int_{\mathcal{B}_t^{el,c}\cup\mathcal{B}_t^{el,d}} \nabla_{\boldsymbol{x}} N_i^{(c,d)} \cdot \boldsymbol{\sigma}^{(c,d)} \,\mathrm{d}v - \int_{\partial\mathcal{B}_t^{el,c}\cup\partial\mathcal{B}_t^{el,d}} N_i^{(c,d)}\, \bar{\boldsymbol{t}}^{(c,d)} \,\mathrm{d}a - \int_{\mathcal{B}_t^{el,c}\cup\mathcal{B}_t^{el,d}} N_i^{(c,d)}\, \boldsymbol{b_t}^{(c,d)} \,\mathrm{d}v \Big] = 0
\end{aligned} \tag{3.18}$$

Obviously, this discretization leads to the following vector valued residual.

$$\mathbf{R}_I = \mathbf{R}_I^{int} - \mathbf{R}_I^{ext} = \mathbf{0} \tag{3.19}$$

$$
\begin{aligned}
\mathbf{R}_I^{int} &= \mathop{\mathbf{A}}_{e=1}^{n_{el}} \int\limits_{\mathcal{B}_0^{el,c} \cup \mathcal{B}_0^{el,d}} \nabla_{\boldsymbol{X}} N_i^{(c,d)} \cdot \boldsymbol{P}^{(c,d)} \, \mathrm{d}V \\
&= \mathop{\mathbf{A}}_{e=1}^{n_{el}} \int\limits_{\mathcal{B}_t^{el,c} \cup \mathcal{B}_t^{el,d}} \nabla_{\boldsymbol{x}} N_i^{(c,d)} \cdot \boldsymbol{\sigma}^{(c,d)} \, \mathrm{d}v \\
\mathbf{R}_I^{ext} &= \mathop{\mathbf{A}}_{e=1}^{n_{el}} \int\limits_{\partial\mathcal{B}_0^{el,c} \cup \partial\mathcal{B}_0^{el,d}} N_i^{(c,d)} \, \bar{\boldsymbol{T}}^{(c,d)} \, \mathrm{d}A - \int\limits_{\mathcal{B}_0^{el,c} \cup \mathcal{B}_0^{el,d}} N_i^{(c,d)} \, \boldsymbol{B_0}^{(c,d)} \, \mathrm{d}V \\
&= \mathop{\mathbf{A}}_{e=1}^{n_{el}} \int\limits_{\partial\mathcal{B}_t^{el,c} \cup \partial\mathcal{B}_t^{el,d}} N_i^{(c,d)} \, \bar{\boldsymbol{t}}^{(c,d)} \, \mathrm{d}a - \int\limits_{\mathcal{B}_t^{el,c} \cup \mathcal{B}_t^{el,d}} N_i^{(c,d)} \, \boldsymbol{b_t}^{(c,d)} \, \mathrm{d}v
\end{aligned}
\tag{3.20}
$$

Next, we address the solution of this discrete non-linear system of equations.

3.3.3. Consistent residual linearization

Similar to the previous chapter, we apply the NEWTON-RAPHSON scheme with its corresponding consistent linearization.

$$
\mathbf{R}_I^{k+1} = \mathbf{R}_I^k + \Delta \boldsymbol{R}_I = \mathbf{0} \tag{3.21}
$$

Again, n_{np} denotes the total number of nodes. The following directional derivative is denoted by $\Delta \boldsymbol{R}$.

$$
\Delta \boldsymbol{R}_I(\boldsymbol{\varphi}_J) = \sum_{J=1}^{n_{np}} \frac{\partial \boldsymbol{R}_I(\boldsymbol{\varphi}_J)}{\partial \boldsymbol{\varphi}_J} \cdot \Delta \boldsymbol{\varphi}_J = \sum_{J=1}^{n_{np}} \boldsymbol{K}_{IJ} \cdot \Delta \boldsymbol{\varphi}_J \tag{3.22}
$$

We obtain the tangent stiffness matrix $\boldsymbol{K}_{IJ} = \dfrac{\partial \boldsymbol{R}_I(\boldsymbol{\varphi}_J)}{\partial \boldsymbol{\varphi}_J}$ for the complete finite element formulation, including the discontinuous as well as the continuous elements, formulated in the referential, the two-point and the spatial format.

$$
\begin{aligned}
\mathbf{K}_{IJ} &= \mathop{\mathbf{A}}_{e=1}^{n_{el}} \int\limits_{\mathcal{B}_0^{el,c} \cup \mathcal{B}_0^{el,d}} \nabla_{\boldsymbol{X}}^t N_i^{(c,d)} \cdot \boldsymbol{S}^{(c,d)} \cdot \nabla_{\boldsymbol{X}} N_j^{(c,d)} \, \boldsymbol{I} \, \mathrm{d}V \\
&\quad + \int\limits_{\mathcal{B}_0^{el,c} \cup \mathcal{B}_0^{el,d}} \left[\nabla_{\boldsymbol{X}}^t N_i^{(c,d)} \cdot \boldsymbol{F}^{(c,d)} \right]^{sym} \cdot \mathbb{L}^{(c,d)} \cdot \left[\boldsymbol{F}^{t\,(c,d)} \cdot \nabla_{\boldsymbol{X}} N_j^{(c,d)} \right]^{sym} \mathrm{d}V \\
\mathbf{K}_{IJ} &= \mathop{\mathbf{A}}_{e=1}^{n_{el}} \int\limits_{\mathcal{B}_0^{el,c} \cup \mathcal{B}_0^{el,d}} \nabla_{\boldsymbol{X}}^t N_i^{(c,d)} \cdot \mathbb{A}^{(c,d)} \cdot \nabla_{\boldsymbol{X}} N_j^{(c,d)} \, \mathrm{d}V \\
\mathbf{K}_{IJ} &= \mathop{\mathbf{A}}_{e=1}^{n_{el}} \int\limits_{\mathcal{B}_t^{el,c} \cup \mathcal{B}_t^{el,d}} \nabla_{\boldsymbol{x}}^t N_i^{(c,d)} \cdot \boldsymbol{\sigma}^{(c,d)} \cdot \nabla_{\boldsymbol{x}} N_j^{(c,d)} \, \boldsymbol{I} \, \mathrm{d}v \\
&\quad + \int\limits_{\mathcal{B}_t^{el,c} \cup \mathcal{B}_t^{el,d}} \nabla_{\boldsymbol{x}}^t N_i^{(c,d)} \cdot \mathbb{E}^{(c,d)} \cdot \nabla_{\boldsymbol{x}} N_j^{(c,d)} \, \mathrm{d}v
\end{aligned}
\tag{3.23}
$$

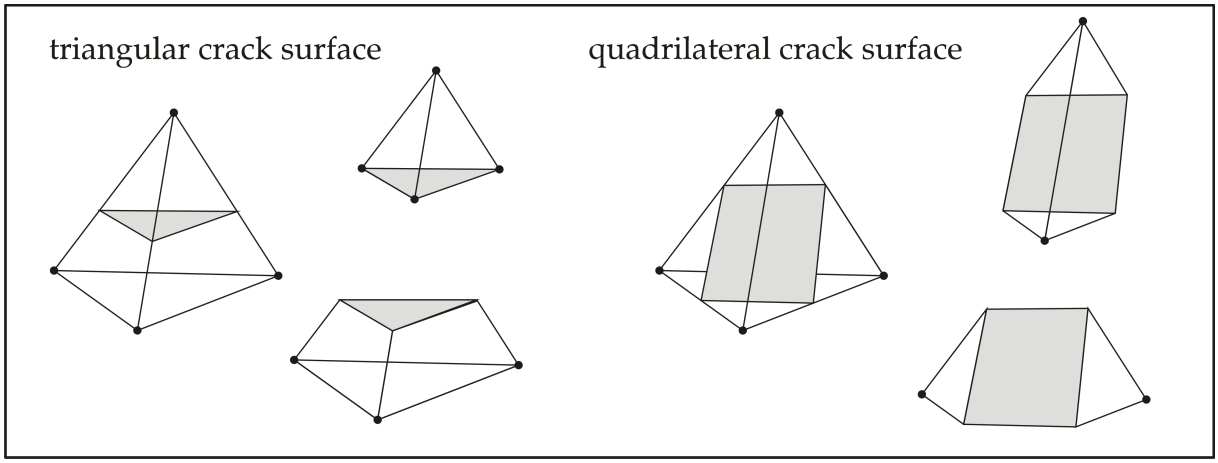

Figure 3.4.: Splitting of tetrahedral elements for triangular and quadrilateral discontinuities.

3.4. Implementation aspects

The above equations are implemented in a fully three-dimensional setting for linear tetrahedral elements. Despite their well-known accuracy deficiencies we have chosen linear tetrahedral elements due to their efficient implementation. This is related to the the crucial handling of the complex geometry data. For two-dimensional problems of this issue we refer to, e.g., SUKUMAR et al. [195] or BORDAS et al. [24] and especially for three-dimensional problems, we recommend, e.g., SUKUMAR [194], AREIAS & BELYTSCHKO [4] or GASSER & HOLZAPFEL [71]. In addition, the aspects of splitting of elements and the numerical integration, where the computational effort rises for other element types, are crucial issues which require a closer look, see, e.g., MERGHEIM et al. [128] or JÄGER et al. [99]. In the following these implementation issues, the visualization and the modeling of crack tips are discussed in detail.

3.4.1. Splitting of Elements

As a prerequisite for the numerical integration a splitting of tetrahedral elements due to the crossing discontinuity needs to be specified. Each particular element stiffness matrix $\mathbf{K}_{IJ}^{el,d}$ and each residual $\mathbf{R}_{I}^{el,d}$ has to be integrated over the particular split part $\mathcal{B}_0^{el,+}$ and $\mathcal{B}_0^{el,-}$, respectively. It is important that we do not take into account a detailed description of the discontinuity or crack front at this point. By using the mentioned linear approximation of the deformation field, the discontinuity is a planar segment through the entire finite element. Accordingly, the split of a tetrahedral element can produce two different combinations of sub-elements depending on whether the crack surface forms a triangle or quadrilateral, compare figure 3.4. The results of the splitting are either a tetrahedron and a so called six node wedge element for the triangular cut or two six node wedge elements for the scenario of the quadrilateral cut. For the numerical integration two procedures can be adopted. On the one hand, each wedge element can further be subdivided into three tetrahedral elements. This procedure is expressed for the sake of completeness and due to its generality, that means, it can be easily adapted to other classes of finite element types. On the other hand, we could

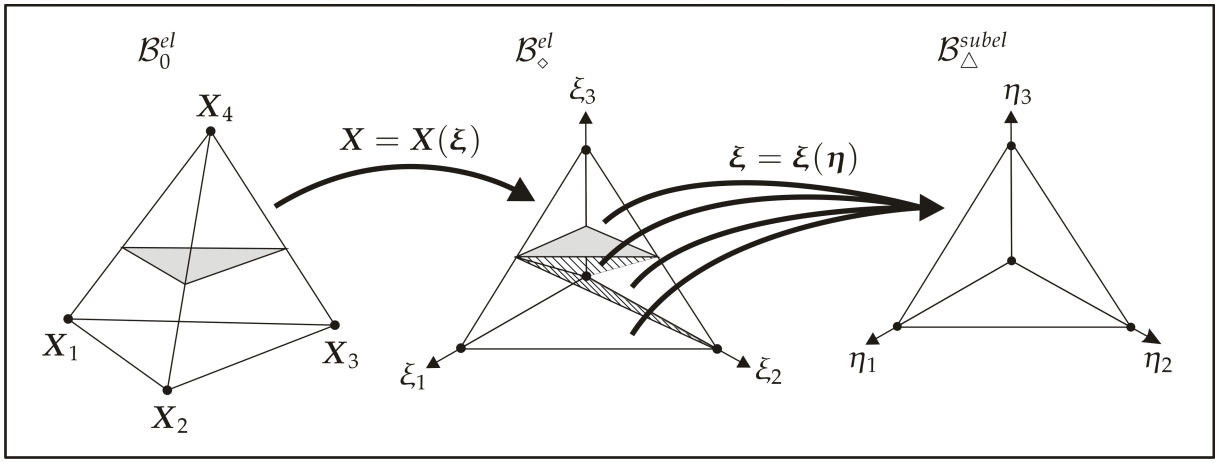

Figure 3.5.: Local coordinates in the unit configuration and local coordinates in a parent domains for a subdivided tetrahedral element.

treat the wedge element as an individual element type. This facilitates the numerical integration. For both procedures the geometry of the split elements can be simply described by the intersection points in the reference configuration. These points as well as the crack surfaces do not change during the computation. They have to be calculated only once when the discontinuity is introduced and can be stored afterwards for the ongoing computation.

3.4.2. Numerical Integration

As already mentioned, two different functions have to be evaluated on both sides of the discontinuous elements for the numerical integration of the volume integrals. For the sake of clarity, we express this integration for a general function $[\bullet]^d(\boldsymbol{X})$ which can be understood as a placeholder for the volume parts of $\mathbf{K}_{IJ}^{el,d}$ and $\mathbf{R}_I^{el,d}$. We recall the unit configuration $\mathcal{B}_\diamond^{el}$ introduced in chapter 2. Usually, for the numerical integration of a finite element, we use a unit mapping $\boldsymbol{X}(\boldsymbol{\xi})$ with $\det(J_\diamond^{el}(\boldsymbol{X}(\boldsymbol{\xi}))) = \det(\frac{\partial \boldsymbol{X}(\boldsymbol{\xi})}{\partial \boldsymbol{\xi}})$ being the JACOBIAN for the following volume transformation from the reference into the unit configuration.

$$\int_{\mathcal{B}_0^{el}} \mathrm{d}V_0^{el} = \int_{\mathcal{B}_\diamond^{el}} \det(J_\diamond^{el}(\boldsymbol{X}(\boldsymbol{\xi}))) \, \mathrm{d}V_\diamond^{el} \tag{3.24}$$

Now, we account for the intersection points which are usually given in global coordinates $\boldsymbol{X}$. We further compute the local coordinates $\boldsymbol{\xi}$ of the intersection points. This has to be done only once for any discontinuous element. With this knowledge, the discontinuous element is subdivided into four (triangular crack surface) or six (quadrilateral crack surface) sub-tetrahedra, compare figure 3.5 for the triangular crack surface. For each of these particular sub-tetrahedra $i = 1, .., 4/6$ on the particular side of the discontinuity we apply a unique mapping $\boldsymbol{\xi}(\boldsymbol{\eta}_i)$ from the unit configuration $\mathcal{B}_\diamond^{el}$ into the following particular parent domain $\mathcal{B}_\triangle^{subel,i}$, compare figure 3.5. In detail, we obtain the following transformation for the volume integrals which includes the summation

about either four or six sub-elements, with $\det(J^{el}_{\triangle,i}(\boldsymbol{\xi}(\boldsymbol{\eta}_i))) = \det(\frac{\partial \boldsymbol{\xi}(\boldsymbol{\eta}_i)}{\partial \boldsymbol{\eta}_i})$.

$$\int_{\mathcal{B}_0^{el}} \mathrm{d}V_0^{el} = \sum_{i=1}^{4/6} \int_{\mathcal{B}^{subel}_{\triangle,i}} \det(J^{el}_{\diamond}(\boldsymbol{X}(\boldsymbol{\xi}(\boldsymbol{\eta}_i)))) \det(J^{el}_{\triangle}(\boldsymbol{\xi}(\boldsymbol{\eta}_i))) \, \mathrm{d}V^{subel}_{\triangle,i} \tag{3.25}$$

The mappings are given in terms of LAGRANGIAN shape functions, $\boldsymbol{X}(\boldsymbol{\xi}) = \sum_{i=1}^{n_{en}} N_i(\boldsymbol{\xi})\, \boldsymbol{X}_i$, with $\boldsymbol{X}_i$ being the referential nodal values of the particular element geometry and $\boldsymbol{\xi}(\boldsymbol{\eta}) = \sum_{i=1}^{n_{en}} N_i(\boldsymbol{\eta})\, \boldsymbol{\xi}_i$, with $\boldsymbol{\xi}_i$ being either the local element coordinates or the local intersection points depending on the considered sub-element. Then, a numerical integration of the general function $[\bullet]^d(\boldsymbol{X})$ is performed with the following GAUSS quadrature rule.

$$\begin{aligned}
\int\limits_{\mathcal{B}_0^{el,d}} [\bullet]^d(\boldsymbol{X}) \, \mathrm{d}V_0^{el} &= \int\limits_{\mathcal{B}_0^{el,(+)}} [\bullet]^+(\boldsymbol{X}) \, \mathrm{d}V_0^{el} + \int\limits_{\mathcal{B}_0^{el,(-)}} [\bullet]^-(\boldsymbol{X}) \, \mathrm{d}V_0^{el} \\
&= \sum_{i=1}^{subel,+} \int\limits_{\mathcal{B}^{subel,+}_{\triangle,i}} [\bullet]^+(\boldsymbol{\eta}_i) \det(J^{el}_{\diamond}(\boldsymbol{\eta}_i)) \det(J^{el}_{\triangle}(\boldsymbol{\eta}_i)) \, \mathrm{d}V^{subel,+}_{\triangle,i} \\
&+ \sum_{i=1}^{subel,-} \int\limits_{\mathcal{B}^{subel,-}_{\triangle,i}} [\bullet]^-(\boldsymbol{\eta}_i) \det(J^{el}_{\diamond}(\boldsymbol{\eta}_i)) \det(J^{el}_{\triangle}(\boldsymbol{\eta}_i)) \, \mathrm{d}V^{subel,-}_{\triangle,i} \\
&= \sum_{i=1}^{subel,+} \sum_{j=1}^{n_{gp}} [\bullet]^+(\boldsymbol{\eta}_i|_j) \det(J^{el}_{\diamond}(\boldsymbol{\eta}_i|_j)) \det(J^{el}_{\triangle}(\boldsymbol{\eta}_i|_j)) \, \alpha_j \\
&+ \sum_{i=1}^{subel,-} \sum_{j=1}^{n_{gp}} [\bullet]^-(\boldsymbol{\eta}_i|_j) \det(J^{el}_{\diamond}(\boldsymbol{\eta}_i|_j)) \det(J^{el}_{\triangle}(\boldsymbol{\eta}_i|_j)) \, \alpha_j
\end{aligned} \tag{3.26}$$

Here, n_{gp} being the chosen number of quadrature points, α_j denotes the particular GAUSS point and $\boldsymbol{\eta}_i|_j$ express the coordinates of the i-th sub-element evaluated at the GAUSS point j. This procedure is of general nature and can be applied to any class of finite elements by defining its particular sub-elements, depending on the shape of the discontinuity. However, by applying linear approximations, linked with the use of tetrahedral finite elements, we obtain piecewise constant strains. The general function $[\bullet]^d(\boldsymbol{X})$ in (3.26) is a constant function. Applied to a single GAUSS point, the integration reduces to the following volume computation.

$$\begin{aligned}
\int\limits_{\mathcal{B}_0^{el,d}} [\bullet]^d \, \mathrm{d}V_0^{el} &= [\bullet]^+ \sum_{i=1}^{subel,+} \det(J^{el}_{\diamond}(\boldsymbol{\eta}_i|_{gp})) \det(J^{el}_{\triangle}(\boldsymbol{\eta}_i|_{gp})) \, \alpha_j \\
&+ [\bullet]^- \sum_{i=1}^{subel,-} \det(J^{el}_{\diamond}(\boldsymbol{\eta}_i|_{gp})) \det(J^{el}_{\triangle}(\boldsymbol{\eta}_i|_{gp})) \, \alpha_j \\
&= [\bullet]^+ \sum_{i=1}^{subel,+} V^{subel,+}_{\triangle,i} + [\bullet]^- \sum_{i=1}^{subel,-} V^{subel,-}_{\triangle,i} = [\bullet]^+ V_0^{el,+} + [\bullet]^- V_0^{el,-}
\end{aligned} \tag{3.27}$$

It is obvious that this latter formulation facilitates the numerical integration remarkably, especially from a computational point of view. We can compute the element

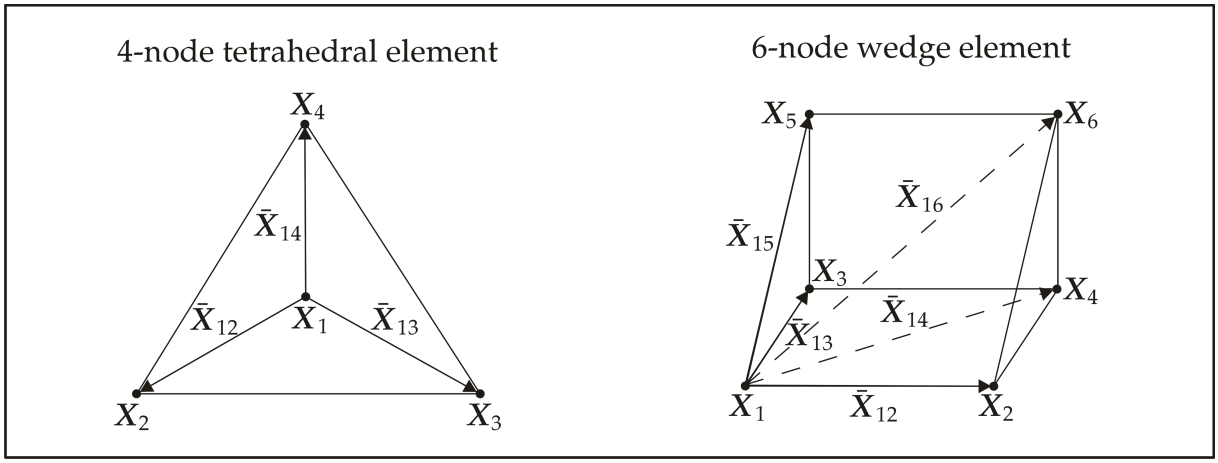

Figure 3.6.: Numbering convention of element-point vectors and element-edge vectors.

stiffness matrix and the element residual by computing the stiffness matrix and the residual under the rules of a continuous formulation and afterwards, we can weight this expression with the particular split volume. We only need to calculate the associated split volume, either from a tetrahedral element or otherwise from a six node wedge element, compare again figure 3.4. We can use the definition of the node point order from figure 3.6 and compute the associated volumes directly in terms of nodal values.

$$\begin{aligned} V^{el}_{\text{tet}} &= \frac{1}{6}\,[\bar{\boldsymbol{X}}_{12} \times \bar{\boldsymbol{X}}_{13}] \cdot \bar{\boldsymbol{X}}_{14} \\ V^{el}_{\text{wedge}} &= \frac{1}{6}\,[\bar{\boldsymbol{X}}_{13} \times \bar{\boldsymbol{X}}_{15} + \bar{\boldsymbol{X}}_{14} \times \bar{\boldsymbol{X}}_{13} + \bar{\boldsymbol{X}}_{12} \times \bar{\boldsymbol{X}}_{14}] \cdot \bar{\boldsymbol{X}}_{16} \end{aligned} \tag{3.28}$$

3.4.3. Discontinuity Visualization

This section deals with the visualization of a three-dimensional discontinuity which seems straightforward from the theoretical point of view. However, it is an absolutely necessary procedure to illustrate the crucial issue of crack path tracking which will be presented later within this work. As far as we know, this issue is only elaborated in detail for two-dimensional discontinuities, e.g., in REMMERS [163] or O'BRIEN & HODGINS [144]. We briefly summarize the procedure for the tree-dimensional case for the sake of completeness. We restrict ourselves to linear tetrahedral elements. Thus, we start with recapitulating that with the present approach a discontinuous element is realized by doubling all element degrees of freedom or broadly speaking, by doubling a continuous element, compare figure 3.7. Then, the two independent deformation maps are approximated independently with the now available eight element nodes. For the post processing of the discontinuity six or eight additional nodes dependent on the crack surface are required. In detail, we introduce a pair of nodes for any edge cut point of the discontinuity. Obviously, this pair of nodes has the same referential positions, however, by evaluating the corresponding deformation map on this nodes they provide different current positions, compare 3.7. The evaluation of the corresponding

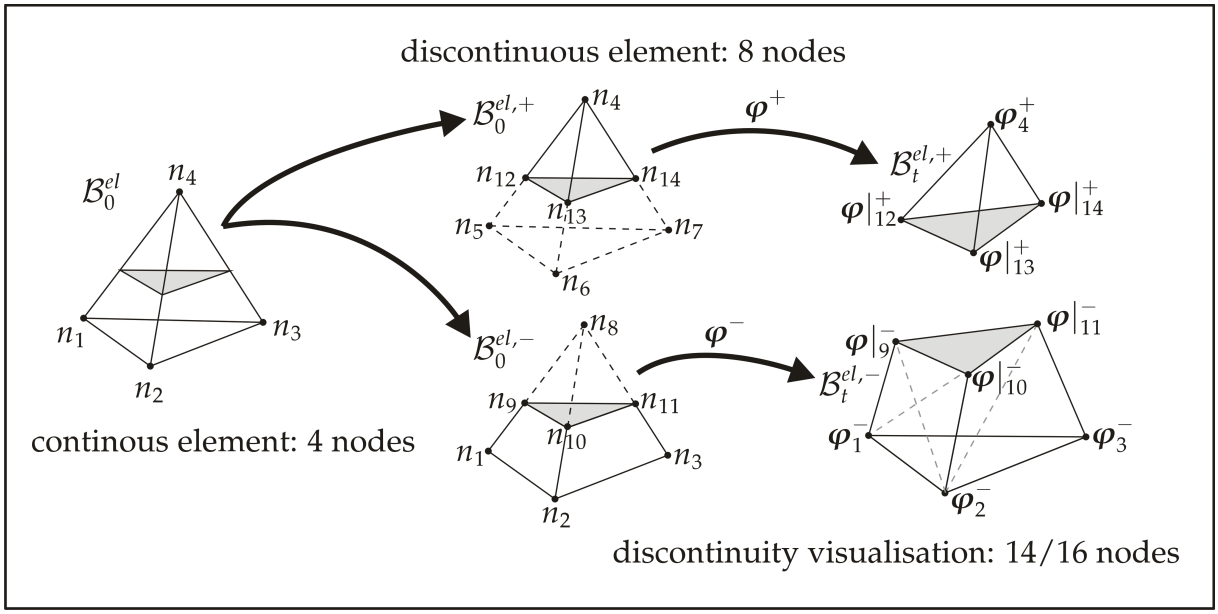

Figure 3.7.: Additionally required nodes and displacement interpolation for discontinuity visualization.

deformation map is expressed with the following notation $\varphi|_i^{(+,-)}$ for the i-th cut point. It is obvious that due to the applied GAUSS quadrature the stresses are only available at the corresponding integration point. Accordingly, we apply a standard projection of the integration point values on the nodes by virtue of the element shape functions, see, e.g., GALLAGHER [66] or ALTENBACH & SACHAROV [3] for a detailed elaboration. By doing so, we obtain the stresses for the eight nodal values of the discontinuous elements. Furthermore, an evaluation of the shape functions, in the same manner as for the displacements, provides the stress values for the additional nodes due to the visualization.

3.4.4. Crack tip elements

Next, we take into account the modeling of a crack tip(2d) or a crack front(3d). It should be mentioned that for the special case of linear elastic fracture mechanics analytical or closed-form solutions for particular crack geometries are available, see, e.g., GROSS & SEELIG [81] or HAHN [83] for a general overview. These solutions consist of singular stress distributions at sharp crack tips. As a consequence, the criticality of cracks can not be estimated by the stresses at the crack tip and therefore, for linear elastic fracture mechanics, the successful concept of stress intensity factors based on the ideas of IRVINE [97] can be applied. However, this concept is restricted to linear elasticity because it is based on the superposition of the deformation as well as the stresses in three different parts (modes). Clearly, we cannot take advantage of this concept for the modeling of discontinuities in a fully non-linear setting.
Next, we clarify the differences between the present discretization and the XFEM for crack tip elements. By its very nature, the XFEM approximation can be easily extended with general further enrichment functions , see, e.g., DOLBOW et al. [48] or ZI & BELYTSCHKO [215]. Especially, in the case of linear elastic fracture mechanics many works

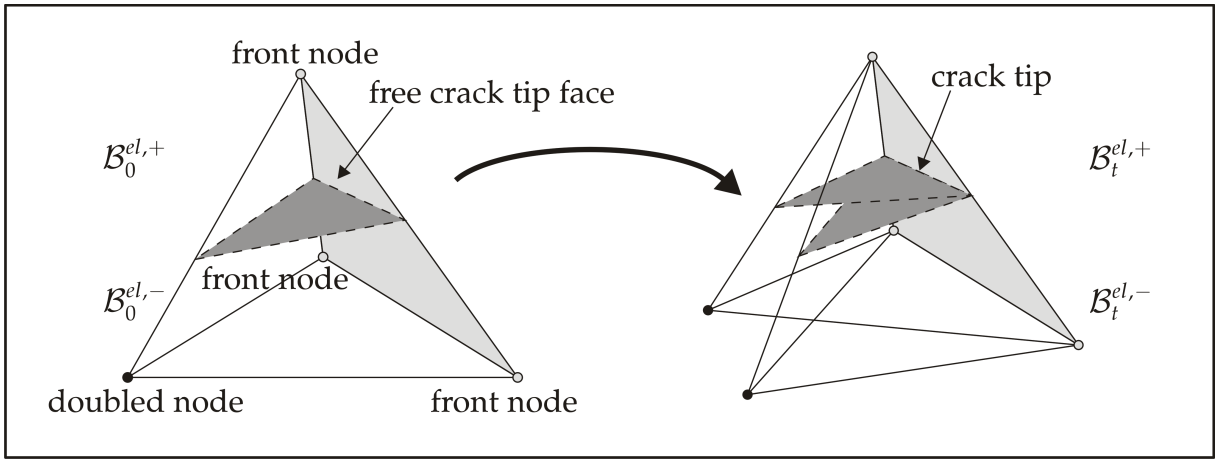

Figure 3.8.: Local element crack tip for a fully cracked element with free crack tip face, front nodes and doubled node. Left: Reference configuration. Right: Deformed configuration.

are available on crack tip elements which are able to capture the mentioned singularity, see, e.g., BUDYN et al. [28] or SUKUMAR et al. [195, 193]. These approaches embed the general deformation and stress distribution of the analytical solution in the discretization of the jump. Based on these works, the XFEM permits an straightforward modeling of elements with both geometrically correct crack tip properties and partially cracked elements. In contrast, the general modeling of a crack tip and especially partially cracked elements is considerably more cumbersome with the present approach than with the XFEM. In the following we present an easy approach for the modeling of geometrically correct crack tips for fully cracked elements. This approach is the one which is used throughout all computations within this work. Furthermore, there are recent developments by RABCZUK et al. [162] which model crack tips for partially cracked elements with the present approach. We extend this two-dimensional approach to a general three-dimensional framework.

Completely cracked elements

As mentioned before, we start with the modeling of geometrically correct crack tips for fully cracked elements where the crack surface is a planar segment through the entire finite element, see figure 3.8. To ensure a geometrically correct crack tip representation, not all nodes of the considered element are doubled. Instead, we distinguish between the nodes of the free crack tip and the nodes connected with faces of cracked neighboring elements. Accordingly, we double only the nodes of the considered part which are not part of the particular free crack tip face and obtain the resulting displacement field which ensures the geometric properties of a crack tip, compare figure 3.8.

Partially cracked elements

Now, we take into account partially cracked elements. Obviously, the essential issue of this approach is the knowledge of the position of the crack front within the element. In chapter 5, we will discuss the possibilities to compute this position within a crack

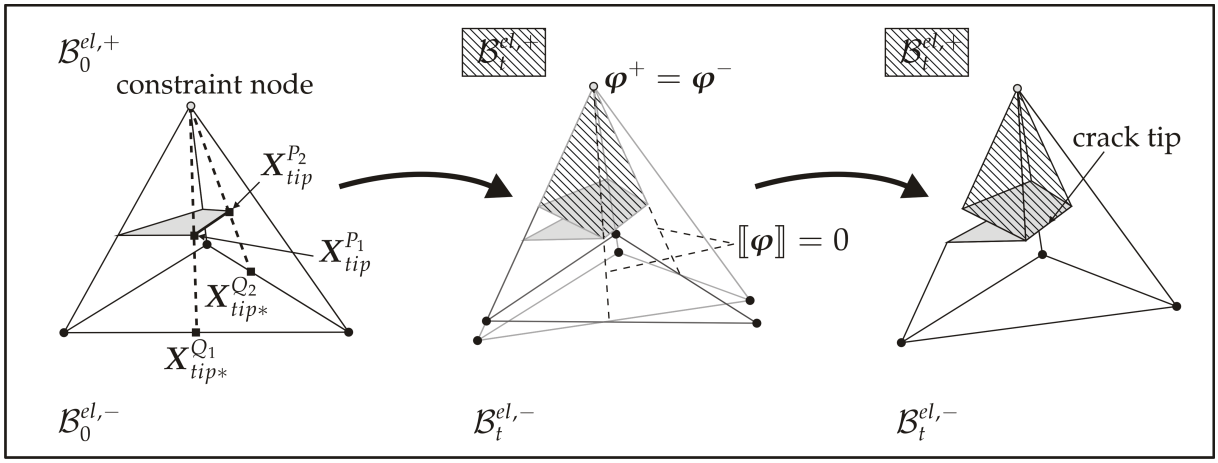

Figure 3.9.: Local element crack tip for a partially cracked element with constraint node and lines of equal deformation. Left: Reference configuration. Center/Right: Deformed configurations.

propagation computation. At this point, we assume that the crack tip is known in the form of a straight line given by the points $\boldsymbol{X}_{tip}^{P_1}$ and $\boldsymbol{X}_{tip}^{P_2}$, see figure 3.9. Thus, to ensure the properties of a crack tip it is required that the jump $[\![\boldsymbol{\varphi}]\!](\boldsymbol{X})$ is equal to zero at this straight line. First, we choose one of the element nodes which is not doubled, that means, at this node $\boldsymbol{\varphi}_i^+ = \boldsymbol{\varphi}_i^-$ holds for the chosen element node i. With this mentioned constrained node, we can express the complete constraints as follows.

$$\begin{aligned}
[\![\boldsymbol{\varphi}(\boldsymbol{X}_{tip}^{P_1})]\!] &= \sum_{i=1}^{n_{en}^+} N_i^+(\boldsymbol{X}_{tip}^{P_1})\boldsymbol{\varphi}^+ - \sum_{i=1}^{n_{en}^-} N_i^-(\boldsymbol{X}_{tip}^{P_1})\boldsymbol{\varphi}^- = 0 \\
[\![\boldsymbol{\varphi}(\boldsymbol{X}_{tip}^{P_2})]\!] &= \sum_{i=1}^{n_{en}^+} N_i^+(\boldsymbol{X}_{tip}^{P_2})\boldsymbol{\varphi}^+ - \sum_{i=1}^{n_{en}^-} N_i^-(\boldsymbol{X}_{tip}^{P_2})\boldsymbol{\varphi}^- = 0 \\
\text{with} \quad & \boldsymbol{\varphi}_i^+ = \boldsymbol{\varphi}_i^- \quad \text{for one chosen node}
\end{aligned} \tag{3.29}$$

The jump evaluated at the crack tip points has to be zero which introduces the mentioned constraints. This reduces the element degrees of freedom for a three-dimensional discontinuous tetrahedral element from 24 to $24 - 9 = 15$ or, strictly speaking, an 8 node problem becomes a 5 node problem. Furthermore, by fulfilling these constraints connected with the illustrated fragmentation of the tetrahedral element, this procedure leads to the pictured crack tip of a partially cracked element, compare again figure 3.9. To conclude, we emphasize some important aspects. The first aspect concerns the computation. For linear deformations which are given by using a 4-node tetrahedral element the chosen constraint node forms a plane together with the two crack tip points. Obviously, $[\![\boldsymbol{\varphi}]\!](\boldsymbol{X})$ is equal for all $\boldsymbol{X}$ located on this plane. Therefore, the constraints can be formulated for the points $\boldsymbol{X}_{tip*}^{Q_1}$ and $\boldsymbol{X}_{tip*}^{Q_2}$ which provides linearly dependent constraints. However, these constraints facilitate the evaluation in local element coordinates. The second aspect concerns the fulfilling of the expressed constrains. Obviously, here is a difference between two- and three-dimensional computations. This means that in two-dimensions the crack tip is only a single point, whereas we have to consider a crack front in three-dimensions. Accordingly, these constraints can be fulfilled only for $\mathcal{C}^0$-continuous crack surfaces to avoid unrealizable conflicts in the constraints. Furthermore, there is a second disadvantage in the three-dimensional for-

mulation compared with the two-dimensional one. In a two-dimensional formulation a unique crack increment formulation is possible. A crack increment has a certain length which can be uniquely determined. Unfortunately, this is not possible for the three-dimensional case. We can only formulate a crack increment in the form of a certain area increment and accordingly, the solution is over-determined.

3.5. Numerical example

Finally, we consider a numerical example. Since we have not yet addressed failure criteria and crack propagation criteria we consider only stationary cracks. We demonstrate the ability of the presented method to capture a strong discontinuity independent of the mesh. Therefore, we have chosen a simple numerical benchmark problem, compare figure 3.10. A specimen of $2[\text{mm}]$ length with a square cross section of $1[\text{mm}^2]$ is provided with an initial discontinuity of $0.5[\text{mm}^2]$. The position of the initial discontinuity can be chosen arbitrarily in the mesh, however, it is reasonable to start with a planar crack segment. To realize the initial discontinuity we discretize the specimen with continuous elements. In detail, we use eight different meshes with systematically decreasing mesh size. Thereby, we chose four uniform meshes (uf) and four discretizations with decreasing mesh size at the known crack tip (rf) for the elaboration of the stress analysis later on. We place the discontinuity into the continuous discretization, which means, we substitute the concerned continuous elements with discontinuous elements. The procedure is demonstrated by means of the discretization with 5441 elements (1458 nodes), see figure 3.10 for the particular uniform or refined continuous discretization as well as figure 3.11 for the placement of discontinuous elements in the refined mesh. For the sake of completeness, we indicate the other used continuous meshes which comprise 3631 elements (1008 nodes), 10501 elements (2662 nodes) and 26461 elements (6300 nodes), respectively. Now, with the definition of the initial discontinuity, the specimen is loaded by an imposed incremental displacement of $0.01[\text{mm}]$ until a deformation of $1[\text{mm}]$ is reached. This deformation of 50% length is especially chosen to demonstrate the large deformation setting. Here, the material parameters $\lambda = 5769.20[\text{N/mm}^2]$, $\mu = 3846.20[\text{N/mm}^2]$ or likewise $E = 10000[\text{N/mm}^2]$ and $\nu = 0.3[\text{-}]$ are selected to highlight the non-linearity of the chosen constitutive equation. We demonstrate the non-linear behavior by means of the load displacement relation $F[\text{N}]$ versus $u[\text{mm}]$, see figure 3.10. This load displacement relation shows excellently that the presented approach provides a mesh-independent solution of the displacement field, however, this mesh-independence does not hold for the stresses at the crack tip.
Subsequently, we take into account this special problem of stress analysis in detail. For elasticity problems with small strains, analytical solutions exhibit a singular stress distribution at a mathematically sharp crack tip. These analytical solutions are not directly transferable to the non-linear case and we cannot give an analytical stress distribution for the non-linear setting. However, one can argue with the path-independence of domain integrals that the non-linear solution exhibits a singular stress distribution without further knowledge of the type of the singularity. For an explanation of path-

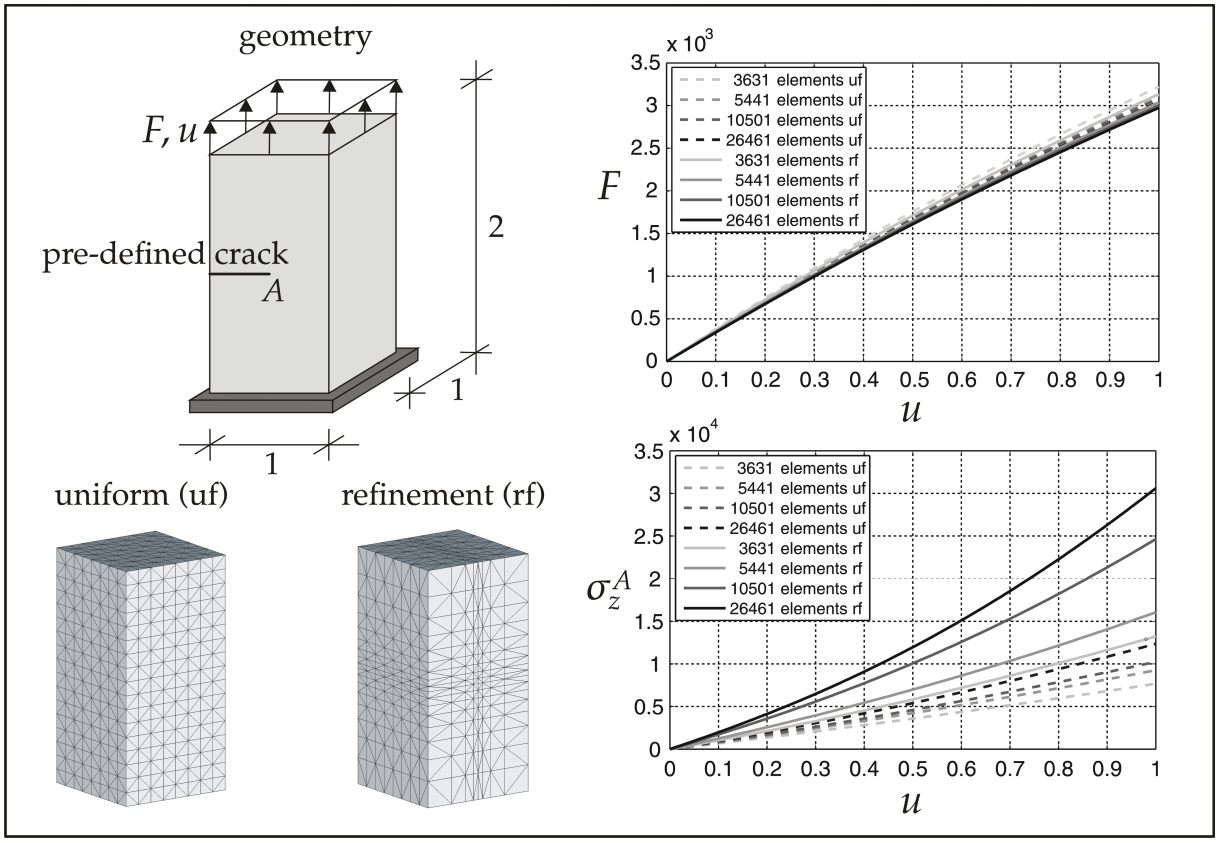

Figure 3.10.: Top left: Geometrical dimensions [mm] and loading. Top right: load displacement response F[N] versus u[mm]. Bottom left: Continuous discretization for 5441 elements. Bottom right: Stress displacement response σ_z^A[N/mm^2] versus u[mm].

independent integrals, see, e.g., MORAN & SHIH [137], GOSZ & MORAN [78] or GOSZ et al.[77]. This is important for the formulation of a stress based failure criterion and we elaborate this problem numerically. We apply a systematically decreasing mesh size at the actual crack tip and evaluate the computed stresses. Recall that the numerical solution with the finite element method connected with standard LAGRANGIAN shape functions is not able to capture a singular distribution in general. For an overview on numerical solution procedures for fracture problems, see, e.g., KUNA [113]. Consequently, without further knowledge of the assumed singularity, we expect the strains and the connected stresses to grow unboundedly with decreasing mesh size. This can be shown by the computation of the stresses σ_z^A[N/mm^2] in the loading direction at the chosen point A at the crack front. The stress displacement relation shows that the stress grows unboundedly with decreasing mesh size as expected, see 3.11. Accordingly, we cannot use the stresses at the crack tip or any criterion based on these strains or stresses to evaluate the status of a cracked specimen. Ultimatively, this is a disappointing situation since we need a failure criterion and a crack propagation criterion to simulate propagating discontinuities. This gives the motivation to introduce the cohesive crack concept in the following chapter.

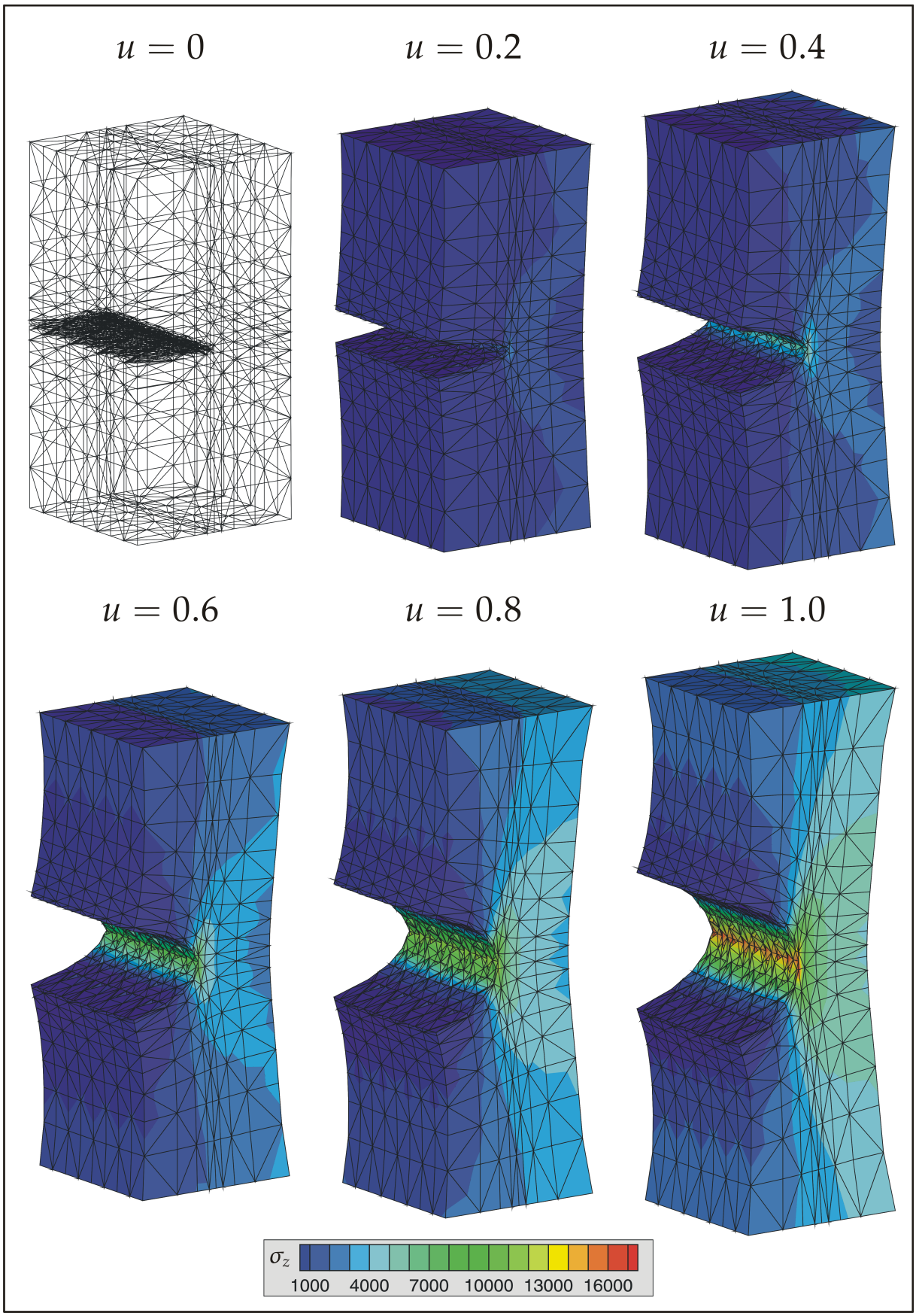

Figure 3.11.: Discretization with inserted discontinuous elements and plotted CAUCHY stresses $\sigma_z\,[\mathrm{N/mm^2}]$ in loading direction for different imposed displacements $u\,[\mathrm{mm}]$.

4. The cohesive crack concept

4.1. Motivation

In this chapter the modeling of cohesive cracks based on the discontinuous elements of the latter chapter is provided. As a prerequisite, the discontinuous kinematics is completed with regard to the special treatment of crack surface tractions. In detail, we abstain from restricting the jump in the deformation map as spatially constant, which inherently leads to parallel crack surfaces, compare, e.g., ARMERO & GARIKIPATI [10] or STEINMANN & BETSCH [191]. Instead, we adopt the procedure of WELLS [204], WELLS et al. [206], ORTIZ & PANDOLFI [155] or GASSER & HOLZAPFEL [71] and define a fictitious discontinuity surface in the spatial configuration. This procedure allows a unique crack surface traction definition with its associated pull-back and push-forward transformation. With this knowledge, we recapitulate the well-known boundary value problem of this thesis, however, enlarged with an additional equilibrium condition due to the considered crack surface tractions. This latter equilibrium condition further leads to a cohesive virtual work contribution and requires the constitutive formulation and the physical justification of the cohesive surface tractions.
However, we first extend the energy considerations of the first chapter to internal interface contributions. One the one hand, this clarifies whether a traction separation law in the desired softening format can be derived from a corresponding cohesive energy potential, see, e.g., ORTIZ & PANDOLFI [155], MERGHEIM [125], KROL [111] or STEINMANN [190]. On the other hand, this is the basis for the definition of general arguments for cohesive traction separation laws. Based on this general arguments, a linearization of the continuous virtual work contributions is applied, see, e.g., MERGHEIM [125], MERGHEIM et al. [129, 128], WELLS [204], WELLS et al. [206], or GASSER & HOLZAPFEL [71, 70]. Afterwards, a finite element formulation of the continuous equations with its corresponding discretization is performed.
With this knowledge, a detailed physical motivation of the complete cohesive crack concept based on the theoretical works of BARENBLATT [15], DUGDALE [53], or HILLERBORG [90, 91] is given. For numerical explanations of the cohesive crack concept, we refer especially to XU & NEEDLEMAN [141, 212, 213, 214] or DE BORST [42], DE BORST et al. [43, 44], WELLS & SLUYS [205], MOËS & BELYTSCHKO [133], ZI & BELYTSCHKO [215], GASSER & HOLZAPFEL [71, 70], MESCHKE & DUMSTORFF [130], RUIZ et al. [168], MARFIA & SACCO [117, 118] or UNGER et al. [199]. Following this detailed physical motivation, we clarify the difference between usual interface traction separation laws and so called initially rigid traction separation laws. For usual interface elements we refer, e.g, to SIMONE [183, 182], whereas initial rigid traction separation laws can be found in, e.g., CAMACHO & ORTIZ [30], ORTIZ & PANDOLFI [155] or MERGHEIM [125]. Subsequently, we specify different traction separation laws, based on the given general arguments. We present one energy based isotropic exponential formulation, see, e.g., MERGHEIM [125]. Then, we elaborate one direct exponential traction formulation for

the transversely isotropic case, compare, e.g., WELLS [204], WELLS & SLUYS [205], DE BORST et al. [44], REMMERS et al. [164], JÄGER et al. [102] or MERGHEIM et al. [127]. We further illustrate a novel rational direct formulation which features certain advantages for combinations with bilateral contact formulations and further exhibits more adjusting possibilities for certain brittle materials. Afterwards, we account for the explicit modeling of tractions in the tangential direction. Here, we specify a simple linear direct traction formulation. For more complicated tangential traction formulations, we refer to, e.g., REMMERS [163], XU AND NEEDLEMAN [212, 213], WELLS & SLUYS [205], DOLBOW et al. [49] or RIBEAUCOURT et al. [166]. Furthermore, we focus on traction formulations in case of overlapping between the particular crack surfaces. This, broadly speaking, bilateral contact formulation is illustrated and its consequences on the convergence behavior, resulting from the combination with initially rigid traction separation laws, are briefly discussed, see, e.g., AREIAS & RABCZUK [8]. Then, we discuss the formulation of loading and unloading processes based on damage formulations. At this point, we refer to SIMO & JU [180, 181] for the idea of damage formulations and to, e.g., AREIAS & BELYTSCHKO [4], GASSER [69, 70], GASSER & HOLZAPFEL [70], MARFIA & SACCO [118], COMI et al. [37] or ORTIZ PANDOLFI [155] for loading and unloading processes.
Next, we take into account some important implementational aspects. We comment on the numerical integration of the cohesive surface term, which includes some remarks on usual interface elements, see, e.g., SCHELLEKENS [173], SCHELLEKENS & DE BORST [174] or SIMONE [183]. Additionally, we account for the boundary conditions during the modeling of softening behavior. We discuss DIRICHLET boundary conditions for discontinuous problems, see, e.g., Moës et al. [132]. Then, we comment on numerical solution techniques regarding imposed NEUMANN boundary conditions, see, e.g., GEERS [76, 74, 75]. Moreover, we briefly introduce the principal stress based failure criterion to illustrate ongoing fracture simulations. Subsequently, we summarize the complete algorithmic treatment of the adaptive introduction of discontinuous elements, in combination with the now presented cohesive zone approach, by means of an algorithmic flowchart.
Finally, we perform two delamination tests to clarify the importance of traction separation laws and to proof the presented consistent linearization. Comparative studies of the delamination tests can be found among others in KUHL et al. [98], MERGHEIM & STEINMANN et al. [128], WELLS [204], DE BORST [43, 44], AREIAS et al. [7], MANZOLI et al. [116], or REMMERS et al. [164].

4.2. Kinematics

As mentioned in remark 3.2.1, the treatment of crack surface tractions requires a special consideration. We recall that due to the discontinuous deformation map $\boldsymbol{\varphi}$, the unique referential discontinuity surface Γ is mapped onto the particular surfaces γ^+ and γ^- in the spatial configuration, compare figure 4.1. A unique definition of crack surface tractions $\boldsymbol{t}^+$ and $\boldsymbol{t}^-$ with associated pull-back and push-forward transformations is therefore not possible. To overcome this ambiguity, the jump in the deforma-

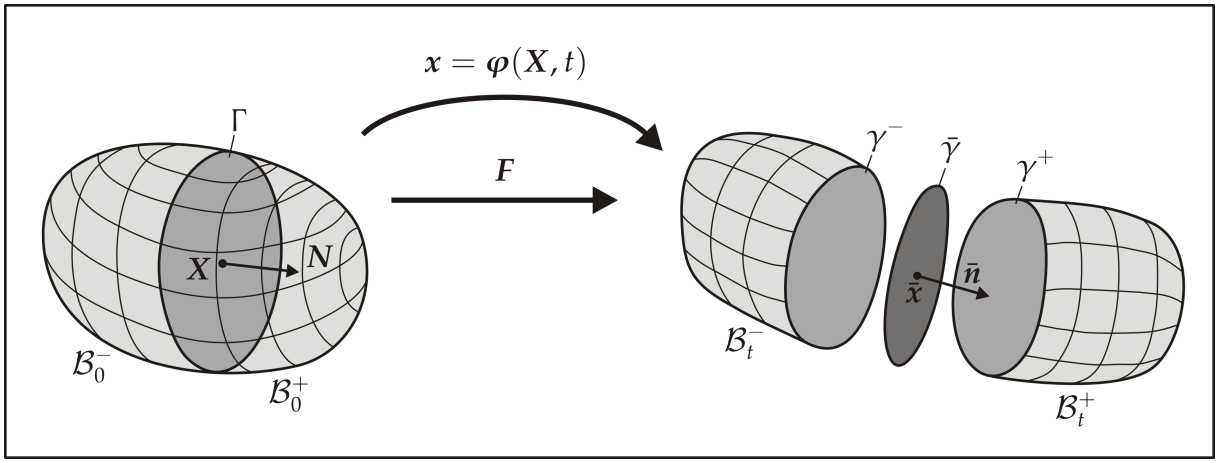

Figure 4.1.: Concept of fictitious discontinuity surface $\bar{\gamma}$ located between the surfaces γ^+ and γ^-.

tion map $[\![\boldsymbol{\varphi}]\!]$ can be restricted as spatially constant, see, e.g., ARMERO & GARIKIPATI [10] or STEINMANN & BETSCH [191]. This procedure leads to the relation $\nabla_{\boldsymbol{X}}[\![\boldsymbol{\varphi}]\!] = 0$, which inherently implies that the spatial crack surfaces γ^+ and γ^- remain parallel. However, we abstain from applying this ad hoc assumption and instead, we define a centered fictitious discontinuity surface $\bar{\gamma}$ in the spatial configuration, compare again figure 4.1. This approach is also used by WELLS [204], WELLS et al. [206], ORTIZ & PANDOLFI [155] and GASSER & HOLZAPFEL [71]. By using this concept, we define the following average deformation map $\bar{\boldsymbol{\varphi}}$ which maps placements $\boldsymbol{X}$ located on the referential discontinuity surface Γ to placements $\bar{\boldsymbol{x}}$ on the fictitious discontinuity surface.

$$\bar{\boldsymbol{\varphi}}(\boldsymbol{X}) = \frac{1}{2}\left[\,\boldsymbol{\varphi}^+|_\Gamma + \boldsymbol{\varphi}^-|_\Gamma\,\right] \qquad \bar{\boldsymbol{\varphi}} : \Gamma \rightarrow \bar{\gamma} \tag{4.1}$$

Next, we define the following average deformation gradient $\bar{\boldsymbol{F}}$ which is only defined on the fictitious discontinuity surface $\bar{\gamma}$.

$$\bar{\boldsymbol{F}} = \nabla_{\boldsymbol{X}}\bar{\boldsymbol{\varphi}} = \frac{1}{2}\left[\,\nabla_{\boldsymbol{X}}\boldsymbol{\varphi}^+ + \nabla_{\boldsymbol{X}}\boldsymbol{\varphi}^-\,\right] \qquad \bar{\boldsymbol{F}} : T\Gamma \rightarrow T\bar{\gamma} \tag{4.2}$$

Accordingly, we obtain the spatial normal vector $\bar{\boldsymbol{n}}$, describing the fictitious discontinuity surface, by applying NANSON's formula onto the referential normal vector $\boldsymbol{N}$.

$$\bar{\boldsymbol{n}}\,\mathrm{d}a = \bar{J}\,\bar{\boldsymbol{F}}^{-t}\cdot\boldsymbol{N}\,\mathrm{d}A \tag{4.3}$$

We recall that the referential normal vector $\boldsymbol{N}$ points from $\mathcal{B}_0^-$ to $\mathcal{B}_0^+$, see again figure 4.1. Furthermore, $\bar{J}$ denotes the determinant of the average deformation gradient $\bar{\boldsymbol{F}}$. With these definitions, a surface traction formulation is uniquely possible in the same manner as introduced in section 2.3. Traction equilibrium requires that $\boldsymbol{P}^+\cdot\boldsymbol{N} = \boldsymbol{P}^-\cdot\boldsymbol{N}$ is valid for the referential discontinuity surface and $\boldsymbol{\sigma}^+\cdot\bar{\boldsymbol{n}} = \boldsymbol{\sigma}^-\cdot\bar{\boldsymbol{n}}$ has to be fulfilled for the averaged spatial discontinuity surface. This traction equilibrium condition has to be included in the well known boundary value problem and additionally, a constitutive traction description is required.

4.3. Boundary value problem

We briefly recall the boundary value problem of this thesis, add the traction equilibrium condition and introduce the traction vectors $\bar{\boldsymbol{T}}^c$ and $\bar{\boldsymbol{t}}^c$ to distinguish between prescribed tractions on the outer boundaries and tractions on the discontinuity surfaces. Keeping in mind that the boundary of the body is split into disjoint parts $\partial\mathcal{B}_0 = \partial\mathcal{B}_0^\varphi \cup \partial\mathcal{B}_0^T$ and $\partial\mathcal{B}_t = \partial\mathcal{B}_t^\varphi \cup \partial\mathcal{B}_t^t$, with $\partial\mathcal{B}_0^\varphi \cap \partial\mathcal{B}_0^T = \varnothing$ and $\partial\mathcal{B}_t^\varphi \cup \partial\mathcal{B}_t^t = \varnothing$, the governing equations of the boundary value problem are summarized as follows.

equilibrium	$\boldsymbol{0} = \mathrm{Div}\boldsymbol{P} + \boldsymbol{B}_0$	$\boldsymbol{0} = \mathrm{div}\boldsymbol{\sigma} + \boldsymbol{b}_t$	(4.4)
traction equilibrium	$\boldsymbol{P}^+ \cdot \boldsymbol{N} = \boldsymbol{P}^- \cdot \boldsymbol{N} = \bar{\boldsymbol{T}}^c$	$\boldsymbol{\sigma}^+ \cdot \bar{\boldsymbol{n}} = \boldsymbol{\sigma}^- \cdot \bar{\boldsymbol{n}} = \bar{\boldsymbol{t}}^c$	(4.5)
constitutive equation	$\boldsymbol{P} = 2\,\boldsymbol{F} \cdot \dfrac{\partial\psi}{\partial\boldsymbol{C}}$	$\boldsymbol{\sigma} = \dfrac{2}{J}\,\boldsymbol{F} \cdot \dfrac{\partial\psi}{\partial\boldsymbol{C}} \cdot \boldsymbol{F}^t$	(4.6)
DIRICHLET conditions	$\boldsymbol{\varphi} = \bar{\boldsymbol{\varphi}}$	$\boldsymbol{\varphi} = \bar{\boldsymbol{\varphi}}$	(4.7)
NEUMANN conditions	$\boldsymbol{T} = \boldsymbol{P} \cdot \boldsymbol{N} = \bar{\boldsymbol{T}}$	$\boldsymbol{t} = \boldsymbol{\sigma} \cdot \boldsymbol{n} = \bar{\boldsymbol{t}}$	(4.8)

We recapitulate that the local balance of momentum has to be solved for the particular sub-domains $\mathcal{B}_0^+ \cup \mathcal{B}_0^-$ and $\mathcal{B}_t^+ \cup \mathcal{B}_t^-$, respectively. The DIRICHLET and the NEUMANN boundary conditions hold for the particular boundaries $\partial\mathcal{B}_0^\varphi \cup \partial\mathcal{B}_0^T$ and $\partial\mathcal{B}_t^\varphi \cup \partial\mathcal{B}_t^t$, whereas the additional equilibrium condition has to be fulfilled on the discontinuity surfaces Γ and $\bar{\gamma}$, respectively.

4.3.1. Principal of virtual work

For a concise notation, we focus only on the interface contribution. Under the same rules as mentioned in the foregoing chapters, we obtain the following weak form for the additional equilibrium condition in the referential and the spatial format.

$$\begin{aligned} \int_{\Gamma^+} \delta\boldsymbol{\varphi}^+ \cdot \boldsymbol{P}^+ \cdot \boldsymbol{N}\,\mathrm{d}A - \int_{\Gamma^-} \delta\boldsymbol{\varphi}^- \cdot \boldsymbol{P}^- \cdot \boldsymbol{N}\,\mathrm{d}A &= \int_{\Gamma} [\![\delta\boldsymbol{\varphi}]\!] \cdot \bar{\boldsymbol{T}}^c\,\mathrm{d}A \\ \int_{\bar{\gamma}^+} \delta\boldsymbol{\varphi}^+ \cdot \boldsymbol{\sigma}^+ \cdot \bar{\boldsymbol{n}}\,\mathrm{d}a - \int_{\bar{\gamma}^-} \delta\boldsymbol{\varphi}^- \cdot \boldsymbol{\sigma}^- \cdot \bar{\boldsymbol{n}}\,\mathrm{d}a &= \int_{\bar{\gamma}} [\![\delta\boldsymbol{\varphi}]\!] \cdot \bar{\boldsymbol{t}}^c\,\mathrm{d}a \end{aligned} \tag{4.9}$$

This latter weak form is interpreted as the interface or cohesive virtual work since the tractions $\bar{\boldsymbol{T}}^c$ and $\bar{\boldsymbol{t}}^c$ are known as cohesive tractions. This will be substantiated in more detail in section 4.4, dealing with the constitutive cohesive traction formulations.

$$\delta\mathcal{W}^{coh} = \int_{\bar{\Gamma}} [\![\delta\boldsymbol{\varphi}]\!] \cdot \bar{\boldsymbol{T}}^c\,\mathrm{d}A = \int_{\bar{\gamma}} [\![\delta\boldsymbol{\varphi}]\!] \cdot \bar{\boldsymbol{t}}^c\,\mathrm{d}a \tag{4.10}$$

Finally, we summarize the weak form for the combined bulk and interface problem with δW^{int} and δW^{ext} being the well-known bulk contributions.

$$\delta\mathcal{W} = \delta\mathcal{W}^{int} + \delta\mathcal{W}^{coh} - \delta\mathcal{W}^{ext} = 0 \tag{4.11}$$

4.3.2. Balance of mechanical energy

Next, we extend the balance of mechanical energy of subsection 2.4.4 to interface considerations, see, e.g., UTZINGER [200] or KROL [111]. Therefore, we recall the divergence term (2.34) of the balance of linear momentum, weighted with the spatial velocity.

$$\begin{aligned}\int_{\mathcal{B}_0} \boldsymbol{v} \cdot \operatorname{Div}\boldsymbol{P}\,\mathrm{d}V &= \int_{\mathcal{B}_0^+\cup\mathcal{B}_0^-} \boldsymbol{v} \cdot \operatorname{Div}\boldsymbol{P}\,\mathrm{d}V \\ &= \int_{\partial\mathcal{B}_0^+\cup\partial\mathcal{B}_0^-} \boldsymbol{T}\cdot\boldsymbol{v}\,\mathrm{d}A + \int_{\Gamma^-} \boldsymbol{T}\cdot\boldsymbol{v}\,\mathrm{d}\Gamma^+ + \int_{\Gamma^+} \boldsymbol{T}\cdot\boldsymbol{v}\,\mathrm{d}\Gamma^- - \int_{\mathcal{B}_0^+\cup\mathcal{B}_0^-} \boldsymbol{P}:\dot{\boldsymbol{F}}\,\mathrm{d}V \\ &= \int_{\partial\mathcal{B}_0^+\cup\partial\mathcal{B}_0^-} \boldsymbol{T}\cdot\boldsymbol{v}\,\mathrm{d}A - \int_{\Gamma} \bar{\boldsymbol{T}}^c\cdot[\![\boldsymbol{v}]\!]\,\mathrm{d}\Gamma - \int_{\mathcal{B}_0^+\cup\mathcal{B}_0^-} \boldsymbol{P}:\dot{\boldsymbol{F}}\,\mathrm{d}V\end{aligned} \tag{4.12}$$

Thereby, we take into account the two discontinuous parts $\mathcal{B}_0^+$ and $\mathcal{B}_0^-$ in the referential format. Additionally, we regard the split of the boundary in outer parts $\partial\mathcal{B}_0^+$ and $\partial\mathcal{B}_0^-$ and discontinuous parts Γ^+ and Γ^-. Then, by using the divergence theorem (A.9), we obtain the extended balance of mechanical energy including the interface contribution.

$$\begin{aligned}&D_t \int_{\mathcal{B}_0^+\cup\mathcal{B}_0^-} \frac{1}{2}\rho_0\,\boldsymbol{v}\cdot\boldsymbol{v}\,\mathrm{d}V + \int_{\mathcal{B}_0^+\cup\mathcal{B}_0^-} \boldsymbol{P}:\dot{\boldsymbol{F}}\,\mathrm{d}V + \int_{\Gamma} \bar{\boldsymbol{T}}^c\cdot[\![\boldsymbol{v}]\!]\,\mathrm{d}\Gamma = \int_{\partial\mathcal{B}_0^+\cup\partial\mathcal{B}_0^-} \boldsymbol{T}\cdot\boldsymbol{v}\,\mathrm{d}A + \int_{\mathcal{B}_0^+\cup\mathcal{B}_0^-} \boldsymbol{B}_0\cdot\boldsymbol{v}\,\mathrm{d}V \\ &\underbrace{D_t \int_{\mathcal{B}_t^+\cup\mathcal{B}_t^-} \frac{1}{2}\rho_t\,\boldsymbol{v}\cdot\boldsymbol{v}\,\mathrm{d}v}_{\text{kinetic energy}} + \underbrace{\int_{\mathcal{B}_t^+\cup\mathcal{B}_t^-} \boldsymbol{\sigma}:\nabla_{\boldsymbol{x}}\boldsymbol{v}\,\mathrm{d}v + \int_{\bar{\gamma}} \bar{\boldsymbol{t}}^c\cdot[\![\boldsymbol{v}]\!]\,\mathrm{d}\bar{\gamma}}_{\text{stress power}} = \underbrace{\int_{\partial\mathcal{B}_t^+\cup\partial\mathcal{B}_t^-} \boldsymbol{t}\cdot\boldsymbol{v}\;\mathrm{d}a + \int_{\mathcal{B}_t^+\cup\mathcal{B}_t^-} \boldsymbol{B}_t\cdot\boldsymbol{v}\,\mathrm{d}v}_{\text{external force power}}\end{aligned} \tag{4.13}$$

Remark 4.3.1 (Referential vs. spatial formulation) *We emphasize that the spatial balance of mechanical energy (4.13b) can only be derived via a push-forward operation of the referential one (4.13a). This is evident, since the parts of the body $\mathcal{B}_t^-$ and $\mathcal{B}_t^+$ do not form a closed volume with the mentioned fictitious discontinuity surface and we cannot apply the divergence theorem in the spatial format. However, the fictitious discontinuity surface allows the push-forward operation of the referential cohesive traction vector and enables the spatial balance of mechanical energy.*

Remark 4.3.2 (Thermodynamically conjugated variables) *In the same manner as for the continuous solid problem, the balance of mechanical energy allows for the definition of energetically conjugated variables. Obviously, the cohesive traction vectors are energetically conjugated to the material time derivative of the jump in the spatial motion map. We can thus denote the local format of the stress power in the following referential and spatial formats.*

$$W_p = \boldsymbol{P}:\dot{\boldsymbol{F}} + \bar{\boldsymbol{T}}^c\cdot[\![\dot{\boldsymbol{\varphi}}]\!] \qquad\qquad w_p = \boldsymbol{\sigma}:\nabla_{\boldsymbol{x}}\boldsymbol{v} + \bar{\boldsymbol{t}}^c\cdot[\![\dot{\boldsymbol{\varphi}}]\!] \tag{4.14}$$

Remark 4.3.3 (Variational vs. virtual work formulation) *For a variational formulation, we can model the internal bulk energy density ψ_0^b and the cohesive energy density $\bar{\psi}_0^c$ depending*

on the energetically conjugated variables, $\psi_0 = \psi_0^b(\boldsymbol{F}) + \bar{\psi}_0^c(\llbracket\boldsymbol{\varphi}\rrbracket)$. Then, we express the dissipation in the referential format of the CLAUSIUS-DUHEM *inequality.*

$$\mathcal{D}_0 = \boldsymbol{P} : \dot{\boldsymbol{F}} - \frac{\partial \psi_0^b}{\partial \boldsymbol{F}} : \dot{\boldsymbol{F}} + \bar{\boldsymbol{T}}^c \cdot \llbracket\dot{\boldsymbol{\varphi}}\rrbracket - \frac{\partial \bar{\psi}_0^c}{\partial \llbracket\boldsymbol{\varphi}\rrbracket} \cdot \llbracket\dot{\boldsymbol{\varphi}}\rrbracket \geq 0 \tag{4.15}$$

We can further divide the dissipation into a bulk part $\mathcal{D}_0^b$ for both of the discontinuous parts and an interface part $\mathcal{D}_0^c$. The bulk part $\mathcal{D}_0^b$ provides the well-known computation of the bulk stresses on both parts of the discontinuity. For a brief notation, we further regard only the following interface contribution $\mathcal{D}_0^c$.

$$\mathcal{D}_0^c = \bar{\boldsymbol{T}}^c \cdot \llbracket\dot{\boldsymbol{\varphi}}\rrbracket - \frac{\partial \bar{\psi}_0^c}{\partial \llbracket\boldsymbol{\varphi}\rrbracket} \cdot \llbracket\dot{\boldsymbol{\varphi}}\rrbracket \geq 0 \tag{4.16}$$

Now, we obtain the stresses for the elastic case as the total derivative of the referential interface potential because $\llbracket\dot{\boldsymbol{\varphi}}\rrbracket \neq \boldsymbol{0}$.

$$\bar{\boldsymbol{T}}^c = \frac{\partial \bar{\psi}_0^c}{\partial \llbracket\boldsymbol{\varphi}\rrbracket} \qquad \textit{and} \qquad \bar{\boldsymbol{t}}^c = \frac{1}{\beta}\frac{\partial \bar{\psi}_0^c}{\partial \llbracket\boldsymbol{\varphi}\rrbracket} \tag{4.17}$$

Thereby, $\bar{\boldsymbol{T}}^c = \beta\, \bar{\boldsymbol{t}}^c$ holds for the pull-back operation of the cohesive spatial traction vector, with $\beta = \frac{da}{dA}$ being the area ratio. This formulation allows a completely variational formulation of the boundary value problem. However, for many circumstances it is suitable to distinguish between opening and sliding behavior of the interface parts, we will later justify this in section 4.4 about the constitutive equations. This distinction requires a dependence of the referential energy density on the interface orientation, given by its spatial normal vector $\bar{\boldsymbol{T}}^c(\llbracket\boldsymbol{\varphi}\rrbracket, \bar{\boldsymbol{n}})$. Therefore, we recapitulate the CLAUSIUS-DUHEM *inequality, including this additional dependence on the interface normal vector.*

$$\mathcal{D}_0^c = \bar{\boldsymbol{T}}^c \cdot \llbracket\dot{\boldsymbol{\varphi}}\rrbracket - \frac{\partial \bar{\psi}_0^c}{\partial \llbracket\boldsymbol{\varphi}\rrbracket} \cdot \llbracket\dot{\boldsymbol{\varphi}}\rrbracket - \frac{\partial \bar{\psi}_0^c}{\partial \bar{\boldsymbol{n}}} \cdot \dot{\bar{\boldsymbol{n}}} \geq 0 \tag{4.18}$$

If $\dot{\bar{\boldsymbol{n}}} \neq \boldsymbol{0}$, the dissipation can only be zero if $\frac{\partial \bar{\psi}_0^c}{\partial \bar{\boldsymbol{n}}} = \boldsymbol{0}$. Clearly, this special case describes an isotropic behavior. Otherwise, the additional dependence on the normal vector leads to transverse isotropy. This means that the response of the discontinuity exhibits one preferred direction which coincides with the mentioned normal vector onto the fictitious crack surface. This is the main difference between the geometrically linear and the non-linear case, since for the geometrical linear case the derivative with respect to $\bar{\boldsymbol{n}}$ is negligible. Accordingly, traction separation formulations for the geometrically linear case can be further derived based on cohesive energy potentials. In contrast, for the geometrically non-linear case, we cannot neglect the dependence of the mentioned normal vector. This prohibits the use of a variational principle and justifies the use of the more general principle of virtual work for the elaborated boundary value problem.

Remark 4.3.4 (Crack surface strain tensor) *We mention that one can additionally consider a dependence of the cohesive interface potential on the so called surface strain or surface* CAUCHY-GREEN *tensor $\boldsymbol{C}_\Gamma = \nabla_{\boldsymbol{X}} \bar{\boldsymbol{\varphi}}^t|_\Gamma \cdot \nabla_{\boldsymbol{X}} \bar{\boldsymbol{\varphi}}_\Gamma$, see, e.g.,* ORTIZ & PANDOLFI *[155]. However, this dependence is not suitable for the description of the directional dependence of the cohesive response on the normal vector. Instead, this contribution takes into account the stretch of the fictitious discontinuity surface and the conjugated variable is an interface stress field which does not posses any normal parts.*

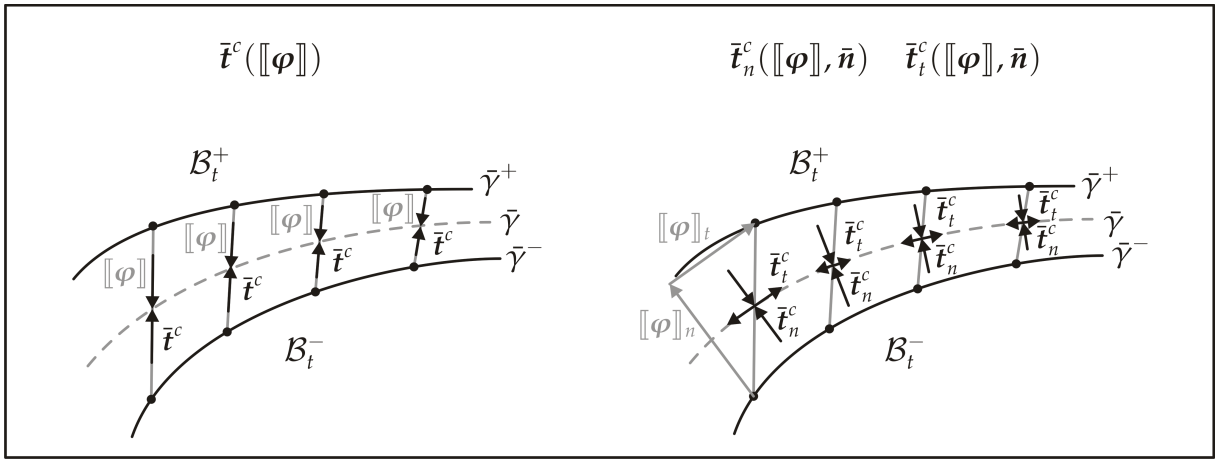

Figure 4.2.: Left: Cohesive tractions oriented in jump direction Right: Splitting of cohesive tractions in divergent and relative interface parts.

4.3.3. Linearization of continuous equations

This section focuses on the linearization of the interface contributions. As mentioned in remark 4.3.3, a decomposition of the interface contributions into opening and sliding parts is useful. In detail, the jump $\llbracket\boldsymbol{\varphi}\rrbracket$ is divided into the following divergent and relative parts to the interface, see also figure 4.2 right.

$$\begin{aligned}\llbracket\boldsymbol{\varphi}_n\rrbracket &= [\llbracket\boldsymbol{\varphi}\rrbracket\cdot\bar{\boldsymbol{n}}]\,\bar{\boldsymbol{n}}\\ \llbracket\boldsymbol{\varphi}_t\rrbracket &= \llbracket\boldsymbol{\varphi}\rrbracket-\llbracket\boldsymbol{\varphi}_n\rrbracket\end{aligned}\tag{4.19}$$

The traction vectors are also split in this different parts parts, $\bar{\boldsymbol{t}}^c=\bar{\boldsymbol{t}}^c_n+\bar{\boldsymbol{t}}^c_t$ and $\bar{\boldsymbol{T}}^c=\bar{\boldsymbol{T}}^c_n+\bar{\boldsymbol{T}}^c_t$, respectively. This enables the following format of a general constitutive relation for both fragmentations of the traction vectors.

$$\begin{aligned}\bar{\boldsymbol{t}}^c_n &= \boldsymbol{t}^c_n(\llbracket\boldsymbol{\varphi}_n\rrbracket) = \boldsymbol{t}^c_n(\llbracket\boldsymbol{\varphi}\rrbracket,\bar{\boldsymbol{n}})\\ \bar{\boldsymbol{t}}^c_t &= \boldsymbol{t}^c_t(\llbracket\boldsymbol{\varphi}_t\rrbracket) = \boldsymbol{t}^c_t(\llbracket\boldsymbol{\varphi}\rrbracket,\bar{\boldsymbol{n}})\end{aligned}\quad\text{and}\quad\begin{aligned}\bar{\boldsymbol{T}}^c_n &= \boldsymbol{T}^c_n(\llbracket\boldsymbol{\varphi}_n\rrbracket) = \boldsymbol{T}^c_n(\llbracket\boldsymbol{\varphi}\rrbracket,\bar{\boldsymbol{n}})\\ \bar{\boldsymbol{T}}^c_t &= \boldsymbol{T}^c_t(\llbracket\boldsymbol{\varphi}_t\rrbracket) = \boldsymbol{T}^c_t(\llbracket\boldsymbol{\varphi}\rrbracket,\bar{\boldsymbol{n}})\end{aligned}\tag{4.20}$$

Since both of these traction formats depend on the same arguments, a general linearization with respect to the jump in the deformation map and the average normal vector is sufficient. The further explained case of energetically conjugated variables is also included in this general format by neglecting all terms which arise due to the dependence on the average normal vector. For a comparative derivation of the linearization, we refer to, e.g., MERGHEIM [125], MERGHEIM et al. [129, 128], WELLS [204], WELLS et al. [206] or GASSER & HOLZAPFEL [71, 70]. First, the directional derivative of the jump term can be expressed as follows.

$$\llbracket\Delta\boldsymbol{\varphi}\rrbracket=\Delta\boldsymbol{\varphi}^+-\Delta\boldsymbol{\varphi}^-\tag{4.21}$$

Next, we need the following directional derivative of the average deformation gradient.

$$\Delta\bar{\boldsymbol{F}}=\frac{1}{2}\left[\Delta\bar{\boldsymbol{F}}^+ + \Delta\bar{\boldsymbol{F}}^-\right]=\frac{1}{2}\left[\nabla_{\boldsymbol{X}}\Delta\boldsymbol{\varphi}^+ + \nabla_{\boldsymbol{X}}\Delta\boldsymbol{\varphi}^-\right]\tag{4.22}$$

We recall NANSON'S formula for the discontinuity surfaces, $\boldsymbol{n}\,\mathrm{d}a = \bar{J}\,\bar{\boldsymbol{F}}^{-t}\cdot\boldsymbol{N}\,\mathrm{d}A$. Therefore, $\boldsymbol{n} \propto \bar{J}\,\bar{\boldsymbol{F}}^{-t}\cdot\boldsymbol{N}$, and we express the spatial unit vector depending on the average deformation gradient.

$$\bar{\boldsymbol{n}}(\bar{\boldsymbol{F}}) = \frac{\bar{J}\,\bar{\boldsymbol{F}}^{-t}\cdot\boldsymbol{N}}{\sqrt{\bar{J}\,\bar{\boldsymbol{F}}^{-t}\cdot\boldsymbol{N}\cdot\bar{J}\bar{\boldsymbol{F}}^{-t}\cdot\boldsymbol{N}}} = \frac{\boldsymbol{N}\cdot\bar{\boldsymbol{F}}^{-1}}{\sqrt{\boldsymbol{N}\cdot\bar{\boldsymbol{C}}^{-1}\cdot\boldsymbol{N}}} \tag{4.23}$$

Now, we express the derivative of the spatial normal vector with respect to the average deformation gradient as the following provisional result.

$$\begin{aligned}\frac{\partial\bar{\boldsymbol{n}}}{\partial\bar{\boldsymbol{F}}} &= \frac{1}{\sqrt{\boldsymbol{N}\cdot\bar{\boldsymbol{C}}^{-1}\cdot\boldsymbol{N}}}\,\frac{\partial}{\partial\bar{\boldsymbol{F}}}\left[\boldsymbol{N}\cdot\bar{\boldsymbol{F}}^{-1}\right] - \frac{\boldsymbol{N}\cdot\bar{\boldsymbol{F}}^{-1}}{2\left[\sqrt{\boldsymbol{N}\cdot\bar{\boldsymbol{C}}^{-1}\cdot\boldsymbol{N}}\right]^{3}}\otimes\frac{\partial}{\partial\bar{\boldsymbol{F}}}\left[\boldsymbol{N}\cdot\bar{\boldsymbol{C}}^{-1}\cdot\boldsymbol{N}\right] \\ &= -\boldsymbol{n}\cdot\left[\boldsymbol{I}\overline{\otimes}\bar{\boldsymbol{F}}^{-t}\right] + \boldsymbol{n}\otimes\boldsymbol{n}\otimes\boldsymbol{n}\cdot\bar{\boldsymbol{F}}^{-t} =: \overset{3}{\boldsymbol{G}}\end{aligned} \tag{4.24}$$

With this third order tensor $\overset{3}{\boldsymbol{G}}$ the directional derivative of the average spatial normal vector is summarized as follows.

$$\Delta\bar{\boldsymbol{n}} = \frac{\partial\bar{\boldsymbol{n}}}{\partial\bar{\boldsymbol{F}}} : \Delta\bar{\boldsymbol{F}} = \overset{3}{\boldsymbol{G}} : \Delta\bar{\boldsymbol{F}} \tag{4.25}$$

Next, we concentrate on the changing area of the fictitious discontinuity, depending on the deformation gradient $\mathrm{d}a(\bar{\boldsymbol{F}})$. This contribution arises, since we prefer the linearization in the spatial format. However, in the corresponding referential format, this expression can be found in the connected traction vector, recall that $\bar{\boldsymbol{T}}^{c}\,\mathrm{d}A = \bar{\boldsymbol{t}}^{c}\,\mathrm{d}a$. Then, the result for the average unit normal vector (4.23) is pasted into NANSON'S formula and we obtain the desired area element $\mathrm{d}a$ depending on the average deformation gradient.

$$\mathrm{d}a(\bar{\boldsymbol{F}}) = \bar{J}\sqrt{\boldsymbol{N}\cdot\bar{\boldsymbol{C}}^{-1}\cdot\boldsymbol{N}}\,\mathrm{d}A \tag{4.26}$$

Now, the derivative of the area element with respect to the average deformation gradient is formulated as the next provisional result.

$$\frac{\partial\mathrm{d}a}{\partial\bar{\boldsymbol{F}}} = \left[\sqrt{\boldsymbol{N}\cdot\bar{\boldsymbol{C}}^{-1}\cdot\boldsymbol{N}}\,\frac{\partial\bar{J}}{\partial\bar{\boldsymbol{F}}} + \frac{\bar{J}}{2\sqrt{\boldsymbol{N}\cdot\bar{\boldsymbol{C}}^{-1}\cdot\boldsymbol{N}}}\,\frac{\partial}{\partial\bar{\boldsymbol{F}}}\left[\boldsymbol{N}\cdot\bar{\boldsymbol{C}}^{-1}\cdot\boldsymbol{N}\right]\right]\mathrm{d}A \tag{4.27}$$

$$= \left[\boldsymbol{I}-\boldsymbol{n}\otimes\boldsymbol{n}\right]\cdot\bar{\boldsymbol{F}}^{-t}\mathrm{d}a =: \boldsymbol{H}\,\mathrm{d}a \tag{4.28}$$

With this second order tensor $\boldsymbol{H}$, we then express the directional derivative of the changing area in the fictitious discontinuity surface as follows.

$$\Delta\mathrm{d}a = \frac{\partial\mathrm{d}a}{\partial\bar{\boldsymbol{F}}} : \Delta\bar{\boldsymbol{F}} = \boldsymbol{H} : \Delta\bar{\boldsymbol{F}}\,\mathrm{d}a \tag{4.29}$$

With these particular directional derivatives, we have set the stage for a brief notation of the linearization of the complete cohesive virtual work contribution. This linearization $\Delta\delta W_{coh}$ consists of three contributions, a material one, due to the dependence of

the traction vector on the jump in the deformation map and two geometrical ones, due to the dependence of the traction vector on the average normal vector and the changing of the area of the fictitious discontinuity surface itself.

$$\Delta\delta W_{coh} = \int_{\bar{\gamma}} [\![\delta\boldsymbol{\varphi}]\!] \cdot \frac{\partial \bar{\boldsymbol{t}}_c}{\partial [\![\boldsymbol{\varphi}]\!]} \cdot [\![\Delta\boldsymbol{\varphi}]\!] \, \mathrm{d}a + \int_{\bar{\gamma}} [\![\delta\boldsymbol{\varphi}]\!] \cdot \frac{\partial \bar{\boldsymbol{t}}_c}{\partial \boldsymbol{n}} \cdot \Delta\boldsymbol{n} \, \mathrm{d}a + \int_{\bar{\gamma}} [\![\delta\boldsymbol{\varphi}]\!] \cdot \bar{\boldsymbol{t}}_c \, \Delta\mathrm{d}a \quad (4.30)$$

Since the depicted derivatives of the traction vector with respect to the jump term and the average normal vector depend on the chosen traction separation law, we define the following general tangent operators.

$$\boldsymbol{T}_\varphi = \frac{\partial \bar{\boldsymbol{t}}^c}{\partial [\![\boldsymbol{\varphi}]\!]} \qquad \text{and} \qquad \boldsymbol{T}_n = \frac{\partial \bar{\boldsymbol{t}}^c}{\partial \bar{\boldsymbol{n}}} \quad (4.31)$$

These operators will be specified later on for the particular applied constitutive equations. Now, we express the directional derivatives of the three mentioned contributions of the complete cohesive virtual work in the spatial and the referential format.

$$\begin{aligned}
&\int_{\bar{\gamma}} [\![\delta\boldsymbol{\varphi}]\!] \cdot \frac{\partial \bar{\boldsymbol{t}}^c}{\partial [\![\boldsymbol{\varphi}]\!]} \cdot [\![\Delta\boldsymbol{\varphi}]\!] \, \mathrm{d}a = \int_{\bar{\gamma}} [\![\delta\boldsymbol{\varphi}]\!] \cdot \boldsymbol{T}_\varphi \cdot [\![\Delta\boldsymbol{\varphi}]\!] \, \mathrm{d}a = \int_{\bar{\Gamma}} [\![\delta\boldsymbol{\varphi}]\!] \cdot [\beta \, \boldsymbol{T}_\varphi] \cdot [\![\Delta\boldsymbol{\varphi}]\!] \, \mathrm{d}A \\
&\int_{\bar{\gamma}} [\![\delta\boldsymbol{\varphi}]\!] \cdot \frac{\partial \bar{\boldsymbol{t}}^c}{\partial \boldsymbol{n}} \cdot \Delta\boldsymbol{n} \, \mathrm{d}a = \int_{\bar{\gamma}} [\![\delta\boldsymbol{\varphi}]\!] \cdot \boldsymbol{T}_n \cdot \overset{3}{\boldsymbol{G}} : \Delta\bar{\boldsymbol{F}} \, \mathrm{d}a = \int_{\bar{\Gamma}} [\![\delta\boldsymbol{\varphi}]\!] \cdot [\beta \, \boldsymbol{T}_n] \cdot \overset{3}{\boldsymbol{G}} : \Delta\bar{\boldsymbol{F}} \, \mathrm{d}A \\
&\int_{\bar{\gamma}} [\![\delta\boldsymbol{\varphi}]\!] \cdot \bar{\boldsymbol{t}}^c \, \Delta\mathrm{d}a = \int_{\bar{\gamma}} [\![\delta\boldsymbol{\varphi}]\!] \cdot \bar{\boldsymbol{t}}^c \; [\boldsymbol{H} : \Delta\bar{\boldsymbol{F}}] \, \mathrm{d}a = \int_{\bar{\Gamma}} [\![\delta\boldsymbol{\varphi}]\!] \cdot \bar{\boldsymbol{T}}^c \; [\boldsymbol{H} : \Delta\bar{\boldsymbol{F}}] \, \mathrm{d}A
\end{aligned} \quad (4.32)$$

We see that the second order spatial tangent operators $\boldsymbol{T}_\varphi$ and $\boldsymbol{T}_n$ change only in magnitude with the factor β during a pull-back operation. Obviously, the operators provide an infinitesimal change in the traction vectors $\bar{\boldsymbol{t}}^c$ and $\bar{\boldsymbol{T}}^c$ due to an infinitesimal change in the jump term and the average normal vector, however, the traction vectors feature the same direction. Finally, we mention that if we use the potential based formulation of the traction separation law $\bar{\boldsymbol{t}}^c([\![\boldsymbol{\varphi}]\!])$, the non-symmetric third order tensor term $\overset{3}{\boldsymbol{G}} : \Delta\bar{\boldsymbol{F}}$ and the tangent operator $\boldsymbol{T}_n$ vanish.

4.3.4. Discretization

This section provides the discretization of the cohesive virtual work contribution and therefore, completes the discretization of the complete coupled bulk and interface problem. We adopt the decomposition of the body $\mathcal{B}_0$ in n_{el} elements $\mathcal{B}_0^{el}$, including the continuous ones $\mathcal{B}_0^{el,c}$ and the discontinuous ones $\mathcal{B}_0^{el,d}$. We also apply the isoparametric concept as well as the BUBNOV-GALERKIN procedure. Then, we obtain the discretization of the jump in the spatial motion map as well as the virtual jump term inherently as the difference of the discretized continuous deformation maps $\boldsymbol{\varphi}^+$ and $\boldsymbol{\varphi}^-$ evaluated on placements $\boldsymbol{X} \in \Gamma$.

$$\begin{aligned}
[\![\boldsymbol{\varphi}]\!] &= \sum_{i}^{n_{en}^+} N_i \,|_\Gamma \; \boldsymbol{\varphi}_i^+ - \sum_{i}^{n_{en}^-} N_i \,|_\Gamma \; \boldsymbol{\varphi}_i^- &&= \sum_{p}^{n_{en}^+ + n_{en}^-} \bar{N}_p^\Gamma \, \boldsymbol{\varphi}_p \\
[\![\delta\boldsymbol{\varphi}]\!] &= \sum_{i}^{n_{en}^+} N_i \,|_\Gamma \; \delta\boldsymbol{\varphi}_i^+ - \sum_{i}^{n_{en}^-} N_i \,|_\Gamma \; \delta\boldsymbol{\varphi}_i^- &&= \sum_{p}^{n_{en}^+ + n_{en}^-} \bar{N}_p^\Gamma \, \delta\boldsymbol{\varphi}_p
\end{aligned} \quad (4.33)$$

Thereby, $\boldsymbol{\varphi}_i^+$ and $\boldsymbol{\varphi}_i^-$ depict the nodal deformations $i = 1, .., n_{en}^+$ and $i = 1, .., n_{en}^-$, respectively. The introduced set $\bar{N}_p^\Gamma$ summarizes the corresponding shape functions evaluated for placements $\boldsymbol{X} \in \Gamma$ with its corresponding sign. What remains, is the following discretization of the average deformation gradient.

$$\bar{\boldsymbol{F}} = \left[\sum_i^{n_{en}^+} \boldsymbol{\varphi}_i^+ \otimes \nabla_{\boldsymbol{X}} N_i \,|_\Gamma - \sum_i^{n_{en}^-} \boldsymbol{\varphi}_i^- \otimes \nabla_{\boldsymbol{X}} N_i \,|_\Gamma \right] = \sum_p^{n_{en}^+ + n_{en}^-} \boldsymbol{\varphi}_p \otimes \boldsymbol{L}_p^\Gamma \tag{4.34}$$

Here, $\boldsymbol{L}_p^\Gamma$ contains the respective gradients of the shape functions evaluated at placements $\boldsymbol{X} \in \Gamma$, containing the factor $\frac{1}{2}$. Then, with $\mathop{\mathbf{A}}_{e=1}^{n_{el}}$ further denoting the assembly of all n_{el} elements, including the continuous ones c for the part $\mathcal{B}_0^{el,c}$ and the discontinuous ones $d = (+,-)$ for the part $\mathcal{B}_0^{el,d}$, we obtain the following discretized cohesive virtual work contribution.

$$\delta W^{coh} = \mathop{\mathbf{A}}_{e=1}^{n_{el}} \delta\boldsymbol{\varphi}_p \cdot \left[\int_{\bar{\Gamma}^{el,d}} \bar{N}_p^\Gamma \, \bar{\boldsymbol{T}}^c \, \mathrm{d}A \right] = \mathop{\mathbf{A}}_{e=1}^{n_{el}} \delta\boldsymbol{\varphi}_p \cdot \left[\int_{\bar{\gamma}^{el,d}} \bar{N}_p^\Gamma \, \bar{\boldsymbol{t}}^c \, \mathrm{d}a \right] \tag{4.35}$$

Thereby, $\bar{\gamma}^{el,d}$ and $\bar{\Gamma}^{el,d}$ indicate that the interface term only appears for the discontinuous elements $d = (+,-)$. Subsequently, we obtain the following vector valued cohesive residual.

$$\mathbf{R}_I^{coh} = \mathop{\mathbf{A}}_{e=1}^{n_{el}} \int_{\bar{\Gamma}^{el,d}} \bar{N}_p^\Gamma \, \bar{\boldsymbol{T}}^c \, \mathrm{d}A = \mathop{\mathbf{A}}_{e=1}^{n_{el}} \int_{\bar{\gamma}^{el,d}} \bar{N}_p^\Gamma \, \bar{\boldsymbol{t}}^c \, \mathrm{d}a \tag{4.36}$$

Clearly, for the complete boundary value problem, we have to account for the whole residual, containing the internal and the external bulk contributions and the latter introduced interface residual (4.36).

$$\mathbf{R}_I = \mathbf{R}_I^{int} + \mathbf{R}_I^{coh} - \mathbf{R}_I^{ext} = \mathbf{0} \tag{4.37}$$

4.3.5. Consistent residual linearization

In the same manner as for the bulk problem, we apply again a NEWTON-RAPHSON procedure with its corresponding consistent linearization.

$$\mathbf{R}_I^{k+1} = \mathbf{R}_I^k + \Delta\boldsymbol{R}_I = \mathbf{0} \tag{4.38}$$

Again, $\Delta\boldsymbol{R}_I$ is the following directional derivative with n_{np} being the total number of nodes.

$$\Delta\boldsymbol{R}_I(\boldsymbol{\varphi}_J) = \sum_{J=1}^{n_{np}} \frac{\partial \boldsymbol{R}_I(\boldsymbol{\varphi}_J)}{\partial \boldsymbol{\varphi}_J} \cdot \Delta\boldsymbol{\varphi}_J = \sum_{J=1}^{n_{np}} \boldsymbol{K}_{IJ} \cdot \Delta\boldsymbol{\varphi}_J \tag{4.39}$$

$\boldsymbol{K}_{IJ} = \dfrac{\partial \boldsymbol{R}_I(\boldsymbol{\varphi}_J)}{\partial \boldsymbol{\varphi}_J}$ features the stiffness matrix and can be separated into a bulk and an interface part, $\boldsymbol{K}_{IJ} = \boldsymbol{K}_{IJ}^{int} + \boldsymbol{K}_{IJ}^{coh}$. Regarding only the cohesive interface contributions

to the stiffness matrix, we obtain the following result.

$$\begin{aligned} \boldsymbol{K}_{IJ}^{coh} &= \mathop{\mathbf{A}}_{e=1}^{n_{el}} \int_{\bar{\Gamma}^{el,d}} \bar{N}_p^{\Gamma} \left[\beta \, \boldsymbol{T}_{\varphi}\right] \, \bar{N}_p^{\Gamma} \, \mathrm{d}A + \int_{\bar{\Gamma}^{el,d}} \bar{N}_p^{\Gamma} \left[\beta \, \boldsymbol{T}_n\right] \cdot \overset{3}{\boldsymbol{G}} \cdot \boldsymbol{L}_p^{\Gamma} \, \mathrm{d}A + \int_{\bar{\Gamma}^{el,d}} \bar{N}_p^{\Gamma} \bar{\boldsymbol{T}}^c \left[\boldsymbol{H} \cdot \boldsymbol{L}_p^{\Gamma}\right] \mathrm{d}A \\ &= \mathop{\mathbf{A}}_{e=1}^{n_{el}} \int_{\bar{\gamma}^{el,d}} \bar{N}_p^{\Gamma} \boldsymbol{T}_{\varphi} \, \bar{N}_p^{\Gamma} \, \mathrm{d}a + \int_{\bar{\gamma}^{el,d}} \bar{N}_p^{\Gamma} \boldsymbol{T}_n \cdot \overset{3}{\boldsymbol{G}} \cdot \boldsymbol{L}_p^{\Gamma} \, \mathrm{d}a + \int_{\bar{\gamma}^{el,d}} \bar{N}_p^{\Gamma} \bar{\boldsymbol{t}}^c \left[\boldsymbol{H} \cdot \boldsymbol{L}_p^{\Gamma}\right] \, \mathrm{d}a \end{aligned} \tag{4.40}$$

4.4. Constitutive equations

With the foregoing explanations, we set the stage for the following constitutive equations, with their detailed physical motivation. The main idea for the introduction of cohesive tractions is the assumption that the material separation with its physical implications like, e.g., micro-cracking, small-scale yielding, void initiation or broadly speaking, any imaginable inelastic process, exclusively occurs in a small zone in front of the crack tip. By applying this concept, one can conclude that the material degradation, prior the material separation, takes place in this restricted cohesive zone, whereas the rest of the considered body is subjected to usual mechanic considerations, compare figure 4.3. Therefore, the key assumption of the cohesive crack concept is that the introduced crack surfaces are able to transfer the tractions within the cohesive zone of the propagating cracks, see again figure 4.3. The idea goes back to BARRENBLATT [15] who accounted for atomistic reaction forces during material separation processes and furthermore, called this special range cohesive zone. Based on this approach DUGDALE [53] developed a cohesive model to account for lamellar plastic cohesive zones in front of the crack tip, whereas especially HILLERBORG [90, 91] used the concept to account for brittle failure in concrete. Since this cohesive concept is a very elegant tool to merge all irreversible failure mechanisms into an arbitrary traction separation relation, it has been adopted for the modeling of failure by several authors. Especially, XU & NEEDLEMAN [141, 212, 213, 214] have established the concept in a numerical framework with interface elements for brittle and ductile failure, in a static and dynamical framework. Moreover, we refer the interested reader to the works of DE BORST [42], DE BORST et al. [43, 44], WELLS & SLUYS [205], MOËS & BELYTSCHKO [133], ZI & BELYTSCHKO [215], GASSER & HOLZAPFEL [71, 70], MESCHKE & DUMSTORFF [130], RUIZ et al. [168], MARFIA & SACCO [117, 118] or UNGER et al. [199].

Remark 4.4.1 (Bounded crack tip stresses) *A particularly appealing aspect of cohesive traction separation laws is that they provide bounded stresses at the considered crack tip. This means that the critical traction value is prescribed at the crack tip and therefore, the aforementioned singular stress distribution disappears. Accordingly, with the use of cohesive traction separation laws, we can account for the stresses in front of the crack tip to evaluate the status of a cracked specimen.*

Remark 4.4.2 (Initially rigid traction separation laws) *There are different numerical approaches to include a cohesive traction separation law in a finite element framework. The main difference concerns the desired adaptive introduction of discontinuities based on a chosen failure*

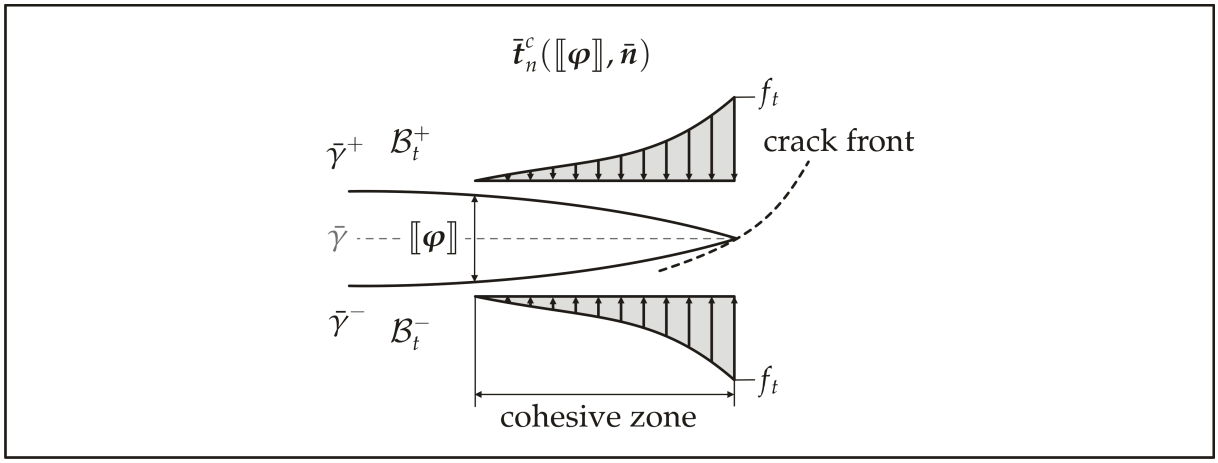

Figure 4.3.: Cohesive zone model: tractions are transferred via the fictitious discontinuity surface.

criterion. On the one hand, by knowing the crack path in advance either from experiments, or inherently from the material structure, one can apply usual cohesive interface elements along the chosen material separation. However, the connected traction separation law exhibits the characteristic that with increasing opening deformation the cohesive tractions reach a maximum, then decrease and eventually vanish with complete decohesion. Accordingly, the connected traction separation law requires an initially elastic behavior which leads to opening deformations prior to reaching the critical load, see, e.g., SIMONE *[183, 182]. On the other hand, to overcome this unphysical opening displacement, initially rigid traction separation laws have been introduced, see, e.g.,* CAMACHO & ORTIZ *[30] or* ORTIZ & PANDOLFI *[155]. These initially rigid traction separation laws ensure that the opening displacement is zero until a critical stress threshold is reached. This means that in contrast to the standard interface elements, the maximum of the cohesive tractions is achieved for a zero opening displacement and the tractions decrease with increasing opening displacement. Therefore, they are more suitable for the use within the presented discontinuous elements, see, e.g.,* MERGHEIM *[125].*

Cohesive zones for the modeling of fracture are usually formulated with at least two independent parameters, commonly the tensile strength f_t as well as the fracture energy G_f, which determines the area under the corresponding traction separation curve. The main aspect of the following part of this section is the formulation of initial traction separation laws based on these cohesive zone parameters. These traction separation laws specify brittle failure for different types of materials and provide the required general tangent operators $\boldsymbol{T}_\varphi$ and $\boldsymbol{T}_n$, compare equation (4.31). In detail, we apply two different exponential traction separation laws, where the first one is a isotropic energy based referential formulation and the second one is a direct transversely isotropic spatial formulation for the crack opening direction. Subsequently, we present a direct spatial formulation in the opening direction based on a rational function and a linear traction formulation for the sliding direction. Furthermore, we discuss the use of traction formulations to avoid a possible overlap between the particular crack surfaces and we consider loading and unloading processes.

4.4.1. Energy based exponential formulation

First, we use the following referential cohesive interface potential functional, see also MERGHEIM [125].

$$\bar{\psi}_0^c = G_f \left[1 - \exp\left(- \frac{f_t}{G_f} \, |[\![\boldsymbol{\varphi}]\!]| \right) \right] \tag{4.41}$$

As mentioned before, f_t is the maximum tensile strength and G_f represents the cohesive fracture energy. Next, we specify the referential cohesive tractions which obviously point in the direction of the jump in the deformation map.

$$\bar{\boldsymbol{T}}^c = \frac{\partial \bar{\psi}_0^c}{\partial [\![\boldsymbol{\varphi}]\!]} = f_t \, \exp\left(- \frac{f_t}{G_f} \, |[\![\boldsymbol{\varphi}]\!]| \right) \frac{[\![\boldsymbol{\varphi}]\!]}{|[\![\boldsymbol{\varphi}]\!]|} \tag{4.42}$$

Here, we use the derivative of the jump norm, compare appendix (A.12). We recall that for traction separation laws, depending exclusively on the jump in the deformation map, only the following tangent operator $\boldsymbol{T}_\varphi = \dfrac{\partial \bar{\boldsymbol{t}}^c}{\partial [\![\boldsymbol{\varphi}]\!]}$ is required.

$$\begin{aligned}
\beta \, \boldsymbol{T}_\varphi = & \quad \frac{\partial \bar{\boldsymbol{T}}^c}{\partial [\![\boldsymbol{\varphi}]\!]} = \frac{\partial^2 \bar{\psi}_0^c}{\partial [\![\boldsymbol{\varphi}]\!]^2} \\
\beta \, \boldsymbol{T}_\varphi = & \quad - \frac{f_t^2}{G_f} \, \exp\left(- \frac{f_t}{G_f} \, |[\![\boldsymbol{\varphi}]\!]| \right) \frac{[\![\boldsymbol{\varphi}]\!]}{|[\![\boldsymbol{\varphi}]\!]|} \otimes \frac{[\![\boldsymbol{\varphi}]\!]}{|[\![\boldsymbol{\varphi}]\!]|} \\
& + \frac{f_t}{|[\![\boldsymbol{\varphi}]\!]|} \, \exp\left(- \frac{f_t}{G_f} \, |[\![\boldsymbol{\varphi}]\!]| \right) \left[\boldsymbol{I} - \frac{[\![\boldsymbol{\varphi}]\!]}{|[\![\boldsymbol{\varphi}]\!]|} \otimes \frac{[\![\boldsymbol{\varphi}]\!]}{|[\![\boldsymbol{\varphi}]\!]|} \right]
\end{aligned} \tag{4.43}$$

With this tangent operator we finish the potential formulation of the traction separation based on the exponential function.

4.4.2. Direct exponential opening traction formulation

Next, we formulate a direct exponential traction separation law for the opening displacement direction, see also WELLS [204], WELLS & SLUYS [205], DE BORST et al. [44], REMMERS et al. [164] and, e.g., JÄGER et al. [102] or MERGHEIM et al. [127]. The main advantage of this formulation is the flexibility regarding the adaption of the considered softening behavior independent of the sliding behavior. This different behavior of opening and sliding direction can be verified by many experiments. This is evident, especially, if we think of the modeling of friction in the sliding direction. The traction formulation is given as follows.

$$\bar{\boldsymbol{t}}_n^c = f_t \exp\left(- \frac{f_t}{G_f} \, |[\![\boldsymbol{\varphi}_n]\!]| \right) \bar{\boldsymbol{n}} \tag{4.44}$$

We use a spatial formulation, however, a referential formulation, similar to the potential based approach, is likewise possible. Then, we specify the required two tangent

operators.

$$\begin{aligned} \boldsymbol{T}_{\varphi} &= -\frac{f_t^2}{G_f}\,\exp\left(-\frac{f_t}{G_f}\,|[\![\boldsymbol{\varphi}_n]\!]|\right)\bar{\boldsymbol{n}}\otimes\bar{\boldsymbol{n}} \\ \boldsymbol{T}_{n} &= -\frac{f_t^2}{G_f}\,\exp\left(-\frac{f_t}{G_f}\,|[\![\boldsymbol{\varphi}_n]\!]|\right)\left[\bar{\boldsymbol{n}}\otimes[\![\boldsymbol{\varphi}]\!]-\frac{G_f}{f_t}\,\boldsymbol{I}\right] \end{aligned} \tag{4.45}$$

Here, we recall that $|[\![\boldsymbol{\varphi}_n]\!]| = [\![\boldsymbol{\varphi}]\!]\cdot\bar{\boldsymbol{n}}$.

4.4.3. Direct rational opening traction formulation

It is desirable to have more options in the softening description as in the foregoing exponential format. The first option regards the initial tangent operators. We will later see that due to the bilateral contact traction formulation, to avoid an overlapping of the partial crack surfaces, we inherently observe a jump in the traction separation law itself. It is therefore suitable to introduce a transversely isotropic traction separation law $\bar{\boldsymbol{t}}^c([\![\boldsymbol{\varphi}_n]\!],\bar{\boldsymbol{n}})$, with zero initial slope with respect to $|[\![\boldsymbol{\varphi}_n]\!]|$. This initial slope can facilitate the transition from the contact range for $|[\![\boldsymbol{\varphi}_n]\!]| < 0$ to the softening part $|[\![\boldsymbol{\varphi}_n]\!]| \geq 0$ in a smooth sense, compare remark 4.4.5. Moreover, we require a numerical parameter which influences the kind of softening behavior of the traction separation law, to fit the constitutive equation to certain experiments. Therefore, we propose the following direct traction separation law formulation motivated by the LENNARD-JONES rational pair potential. We start with the basis $\bar{t}^c = f_t\left[-1\left[\frac{|[\![\boldsymbol{\varphi}_n]\!]|}{a}+1\right]^{-p}+2\left[\frac{|[\![\boldsymbol{\varphi}_n]\!]|}{a}+1\right]^{-q}\right]$, with $\bar{\boldsymbol{t}}^c = \bar{t}^c\,\bar{\boldsymbol{n}}$. If we choose $q = \frac{p}{2}$, we obviously ensure an initial zero slope with respect to $|[\![\boldsymbol{\varphi}_n]\!]|$. Furthermore, for $p > 2$ the function is uniquely integrable and $a = \frac{G_f\,[2-3p+p^2]}{f t\,[-2+3p]}$, with claiming $\int_0^\infty \bar{t}^c \mathrm{d}|[\![\boldsymbol{\varphi}_n]\!]| = G_f$. Thus, we obtain the following traction separation relation with f_t and G_f being the, broadly speaking, usual cohesive parameters and p being an additional numerical parameter to control the kind of softening behavior of the traction separation law.

$$\bar{\boldsymbol{t}}^c = f_t\left[-1\left[1+\frac{f_t\,[-2+3p]\,|[\![\boldsymbol{\varphi}_n]\!]|}{G_f\,[2-3p+p^2]}\right]^{-p}+2\left[1+\frac{f_t\,[-2+3p]\,|[\![\boldsymbol{\varphi}_n]\!]|}{G_f\,[2-3p+p^2]}\right]^{\frac{-p}{2}}\right]\bar{\boldsymbol{n}} \tag{4.46}$$

Next, we express the required tangent operators for the finite element formulation.

$$\begin{aligned} \boldsymbol{T}_{\varphi} &= f_t\,p\left[1+\frac{f_t\,[-2+3p]\,|[\![\boldsymbol{\varphi}_n]\!]|}{G_f\,[2-3p+p^2]}\right]^{-p-1}\left[\frac{f_t\,[-2+3p]}{G_f\,[2-3p+p^2]}\right]\bar{\boldsymbol{n}}\otimes\bar{\boldsymbol{n}} \\ &- f_t\,p\left[1+\frac{f_t\,[-2+3p]\,|[\![\boldsymbol{\varphi}_n]\!]|}{G_f\,[2-3p+p^2]}\right]^{\frac{-p}{2}-1}\left[\frac{f_t\,[-2+3p]}{G_f\,[2-3p+p^2]}\right]\bar{\boldsymbol{n}}\otimes\bar{\boldsymbol{n}} \end{aligned} \tag{4.47}$$

$$
\begin{aligned}
\boldsymbol{T}_n &= f_t\, p \left[1 + \frac{f_t\ [-2+3p]\ |[\![\boldsymbol{\varphi}_n]\!]|}{G_f\,[2-3p+p^2]}\right]^{-p-1} \left[\frac{f_t\,[-2+3p]}{G_f\,[2-3p+p^2]}\right] \bar{\boldsymbol{n}} \otimes [\![\boldsymbol{\varphi}]\!] \\
&- 1\, f_t \left[1 + \frac{f_t\ [-2+3p]\ |[\![\boldsymbol{\varphi}_n]\!]|}{G_f\,[2-3p+p^2]}\right]^{-p} \boldsymbol{I} \\
&- f_t\, p \left[1 + \frac{f_t\ [-2+3p]\ |[\![\boldsymbol{\varphi}_n]\!]|}{G_f\,[2-3p+p^2]}\right]^{\frac{-p}{2}-1} \left[\frac{f_t\,[-2+3p]}{G_f\,[2-3p+p^2]}\right] \bar{\boldsymbol{n}} \otimes [\![\boldsymbol{\varphi}]\!] \\
&+ 2\, f_t \left[1 + \frac{f_t\ [-2+3p]\ |[\![\boldsymbol{\varphi}_n]\!]|}{G_f\,[2-3p+p^2]}\right]^{\frac{-p}{2}} \boldsymbol{I}
\end{aligned}
\tag{4.48}
$$

We emphasize that a potential based traction formulation is likewise possible with the present format by substituting $|[\![\boldsymbol{\varphi}_n]\!]|$ with $|[\![\boldsymbol{\varphi}]\!]|$ as well as $\bar{\boldsymbol{n}}$ with $\dfrac{[\![\boldsymbol{\varphi}]\!]}{|[\![\boldsymbol{\varphi}]\!]|}$. However, as explained before, we prefer the direct formulation in the opening displacement direction.

4.4.4. Direct linear sliding traction formulation

In this subsection, we take into account the constitutive formulation of the tractions in the sliding direction. In general, one constitutive description of the tractions is sufficient to capture a possible softening behavior and to ensure bounded stresses at the crack tip. However, the preferred split in opening and sliding direction allows us the additional use of a constitutive traction formulation in tangential direction. Accordingly, dependent on the actual problem, one can decide whether a description in opening direction is sufficient or not. We will later clarify by means of representative numerical examples that for many circumstances additional sliding descriptions are not imperative. Therefore, we use a very simple constitutive relation for the sake of completeness. We apply a direct linear spatial formulation independent of the observed opening displacement. In detail, if the tangential jump arises, we will apply the following traction vector proportional to the tangential interface stiffness E_t.

$$
\bar{\boldsymbol{t}}_t^c = E_t\, [\![\boldsymbol{\varphi}_t]\!] \tag{4.49}
$$

Subsequently, we obtain the following additional tangent operators for the sliding direction.

$$
\begin{aligned}
\boldsymbol{T}_\varphi &= E_t \left[\boldsymbol{I} - \bar{\boldsymbol{n}} \otimes \bar{\boldsymbol{n}}\right] \\
\boldsymbol{T}_n &= -E_t \left[\bar{\boldsymbol{n}} \otimes [\![\boldsymbol{\varphi}]\!] + |[\![\boldsymbol{\varphi}_n]\!]|\ \boldsymbol{I}\right]
\end{aligned}
\tag{4.50}
$$

We mention that there are several different formulations for the tangential direction. We refer among others to REMMERS [163] for a linearly decreasing formulation. For an exponentially decreasing formulation we recommend the works of XU AND NEEDLEMAN [212, 213] or WELLS & SLUYS [205]. Additionally, for the coupled consideration of normal and tangential observations to account for frictional contact we refer to, e.g., DOLBOW et al. [49] or RIBEAUCOURT et al. [166].

Remark 4.4.3 (Total scalar crack opening displacement) *There are many works which use a total scalar crack opening displacement, i.e.,* $\delta = |[\![\boldsymbol{\varphi}_n]\!]| + \omega\, |[\![\boldsymbol{\varphi}_t]\!]|$. *This allows the use of only one traction separation law for the combined opening and tangential direction but requires the weighting factor* ω *between the opening and the sliding influence. For a more elaborated derivation, we refer to, e.g.,* RUIZ *et al. [168],* MESCHKE & DUMSTORFF *[130],* MOLINARI *et al. [135],* UNGER *[199].*

4.4.5. Direct linear contact traction formulation

Now, we take into account for avoiding bilateral overlapping between the separating crack surfaces. Accordingly, we have to distinguish between the range of $|[\![\boldsymbol{\varphi}_n]\!]| \geq 0$ and for the values $|[\![\boldsymbol{\varphi}_n]\!]| < 0$, to decide whether a traction separation law has to be used or a possible overlap has to be avoided. We mention that this overlapping occurs frequently during a certain crack propagation simulation, usually directly in front of the crack tip when a discontinuous element is adaptively introduced. Therefore, we apply the following direct penalty traction formulation to avoid the possible overlap.

$$\bar{\boldsymbol{t}}_t^c = \frac{E_c}{L_0^{el}}\, |[\![\boldsymbol{\varphi}_n]\!]|\, \bar{\boldsymbol{n}} \tag{4.51}$$

This linear increasing penalty traction formulation depends on the contact stiffness E_c and the finite element length L_0^{el}, with V_0^{el} being the referential finite element volume. This factor ensures that the penalty stiffness rises with decreasing mesh size which leads to avoiding overlapping with rising number of degrees of freedom. One can likewise choose the spatial finite element length l_t^{el}, however, this is unessential regarding the desired result and it requires a linearization since the spatial finite element length changes during a computation. Now, we specify the required tangent operators.

$$\begin{aligned} \boldsymbol{T}_\varphi &= \frac{E_c}{L_0^{el}}\, \bar{\boldsymbol{n}} \otimes \bar{\boldsymbol{n}} \\ \boldsymbol{T}_n &= \frac{E_c}{L_0^{el}} \left[\bar{\boldsymbol{n}} \otimes [\![\boldsymbol{\varphi}]\!] + |[\![\boldsymbol{\varphi}_n]\!]|\, \boldsymbol{I} \right] \end{aligned} \tag{4.52}$$

Remark 4.4.4 (Non-symmetric stiffness matrix) *Usually the use of direct traction formulations, depending on the jump term and the spatial normal vector, leads to a non-symmetric cohesive stiffness matrix, compare equation* (4.40). *In contrast, the energy based formulation provides a fully symmetric cohesive stiffness matrix. However, by applying a bilateral contact traction formulation, a split in normal and tangential directions is always necessary. This means that the energy based traction separation law, in combination with bilateral contact formulations, also provides a non-symmetric cohesive stiffness matrix.*

Remark 4.4.5 (Convergence behavior) *We emphasize that by using initially rigid traction formulations for opening displacements, combined with the use of contact formulations, usually a discontinuity occurs in the traction separation law itself. Obviously, this influences the numerical solution, especially, the convergence behavior for jump terms nearly equal to zero.*

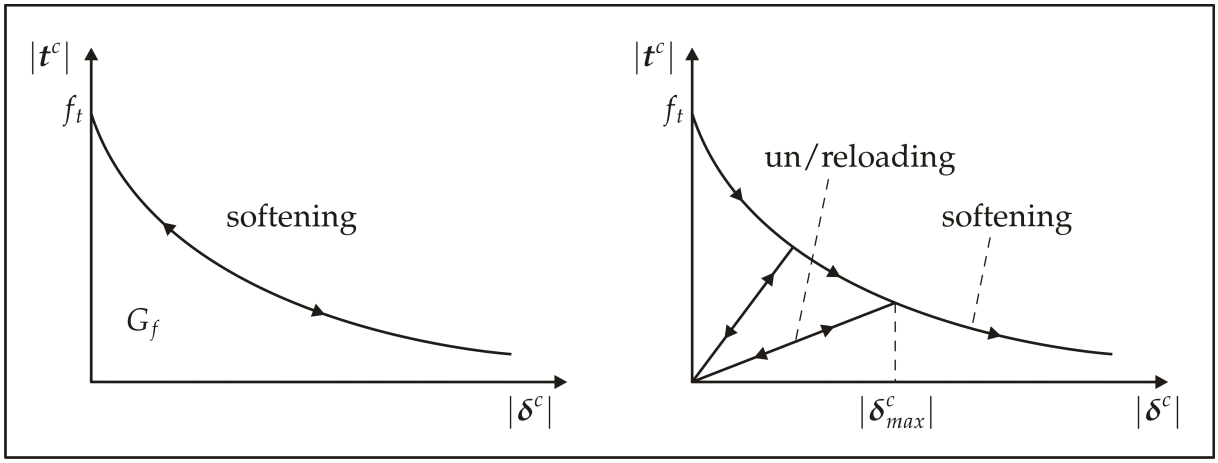

Figure 4.4.: Left: loading and unloading scheme for standard softening behavior. Right: loading and unloading to the origin for softening with provision for damage behavior.

At the worst, this leads to oscillating residuals and might prevent complete convergence. However, there are certain possibilities to ensure a stable, converging computation. As an ad hoc approach, we can apply a numerical perturbation of the opening displacement $|[\![\boldsymbol{\varphi}_n]\!]|$. Moreover, we can accept a small error zone to connect the two independent constitutive traction formulations for softening and contact behavior. This ensures the C^0-continuity of the considered traction separation law. Furthermore, this approach can be extended in a smooth sense, to ensure C^1-continuity of the traction separation relation. By using this kind of a C^1-continuous smoothing formulation the rational traction formulation, with its zero initial slope, can be very helpful. Obviously, this formulation facilitates the determination of a smooth connecting function. An elaboration of this special topic can be found in AREIAS & RABCZUK *[8].*

4.4.6. Loading and unloading processes

Generally, the main interest in fracture analysis is the determination of the failure origin and the question whether the considered crack grows or is in stable equilibrium. Therefore, in experiments and in numerical simulations one is mainly interested in this certain loading case. Fatigue fracture analysis is an exception, since one is interested in a certain number of loading and unloading cases. Accordingly, it seems at a first glance that loading and unloading processes can be neglected by focussing on one certain loading case. However, this holds only for the modeling of single opening cracks. For multiple crack propagation simulations, particular cracks can be unloaded. This means that an internal history variable is needed to specify the material degradation within the cohesive zones. Therefore, we briefly discuss the treatment of unloading and reloading processes for cohesive traction separation laws. More detailed derivations based on the idea of continuum damage formulations by SIMO & JU [180, 181], can be found among others in AREIAS & BELYTSCHKO [4], GASSER [69], GASSER & HOLZAPFEL [70], MARFIA & SACCO [118], COMI et al. [37], or ORTIZ PANDOLFI [155]. For a concise notation, we introduce a general jump measure $\boldsymbol{\delta}^c$. This measurement is equal to the opening displacement for traction separation laws with split in normal and tangential direction, $\boldsymbol{\delta}^c = [\![\boldsymbol{\varphi}_n]\!]$. Furthermore, it describes the complete jump for

the potential based traction separation formulation, $\boldsymbol{\delta}^c = [\![\boldsymbol{\varphi}]\!]$. Next, we introduce a internal history variable $|\boldsymbol{\delta}^c_{max}| = \max(|\boldsymbol{\delta}^c_{max}|, |\boldsymbol{\delta}^c|)$, which is equal to the maximum displacement jump in the history of the loading process. Then, we define the rate independent loading function $\kappa^c = |\boldsymbol{\delta}^c| - |\boldsymbol{\delta}^c_{max}|$. This loading function is equal to zero if $|\boldsymbol{\delta}^c_{max}|$ is determined by the actual jump norm $|\boldsymbol{\delta}_c|$ and $\kappa^c < 0$, otherwise. With this definitions, we define the following traction separation law allowing unloading and reloading processes to the origin.

$$\begin{aligned} \bar{\boldsymbol{t}}^c &= \text{softening} \qquad \text{if} \quad \kappa^c = 0 \\ \bar{\boldsymbol{t}}^c &= f_t \, \frac{\boldsymbol{\delta}^c}{|\boldsymbol{\delta}^c_{max}|} \qquad \text{if} \quad \kappa^c < 0 \end{aligned} \tag{4.53}$$

Here, the softening label in (4.53) stands for a particular traction separation law.

4.5. Implementation aspects

Within this section, we discuss certain implementation aspects. The first aspect regards the numerical integration. Further on, we consider the important issue of imposing boundary conditions and we briefly discuss the principal stress based failure criterion. Finally, we combine the algorithmic details of the former chapter with the currently presented ones and clarify the whole computation procedure by means of a detailed algorithmic flowchart.

4.5.1. Numerical integration

For the computation of the cohesive residual (4.36) and for the computation of the cohesive stiffness matrix (4.40) a surface integration is required. In the same manner as for the volume integration in the foregoing chapter, we express this integration for a general function $[\bullet](\boldsymbol{X})$. Since we defined the crack surface to be flat, we perform a standard two-dimensional integration. We introduce the following unit area domain $\Gamma^{el}_{\square}$, compare figure 4.5. Now, we perform a mapping $\boldsymbol{X}(\boldsymbol{\zeta})$ of the crack surface intersection points on this unit area domain, with $\det(J^{el}_{\square}(\boldsymbol{X}(\boldsymbol{\zeta}))) = \det(\frac{\partial \boldsymbol{x}(\boldsymbol{\zeta})}{\partial \boldsymbol{\zeta}})$ being the required JACOBIAN. Now, we apply the following standard numerical integration scheme, with n_{gp} being the number of GAUSS quadrature points.

$$\int_{\bar{\Gamma}^{el}} [\bullet](\boldsymbol{X}) \, \mathrm{d}\bar{\Gamma}^{el} = \int_{\Gamma^{el}_{\square}} [\bullet](\boldsymbol{X}(\boldsymbol{\zeta})) \det(J^{el}_{\square}(\boldsymbol{X}(\boldsymbol{\zeta}))) \, \mathrm{d}\bar{\Gamma}^{el}_{\square} = \sum_{i=1}^{n_{gp}} [\bullet](\boldsymbol{\zeta}_i) \det(J^{el}_{\square}(\boldsymbol{\zeta}_i)) \, \alpha_i \tag{4.54}$$

In general, we use three integration points for the triangular crack surface and four integration points for the quadrilateral crack plane.

Remark 4.5.1 (Integration accuracy) *The particular traction separation law for the softening behavior is an exponential or rational function, respectively. Therefore, the use of more quadrature points as well as a systematical accuracy elaboration could be reasonable. Within this work, we have not focused on this issue of integration accuracy. However, this numerical*

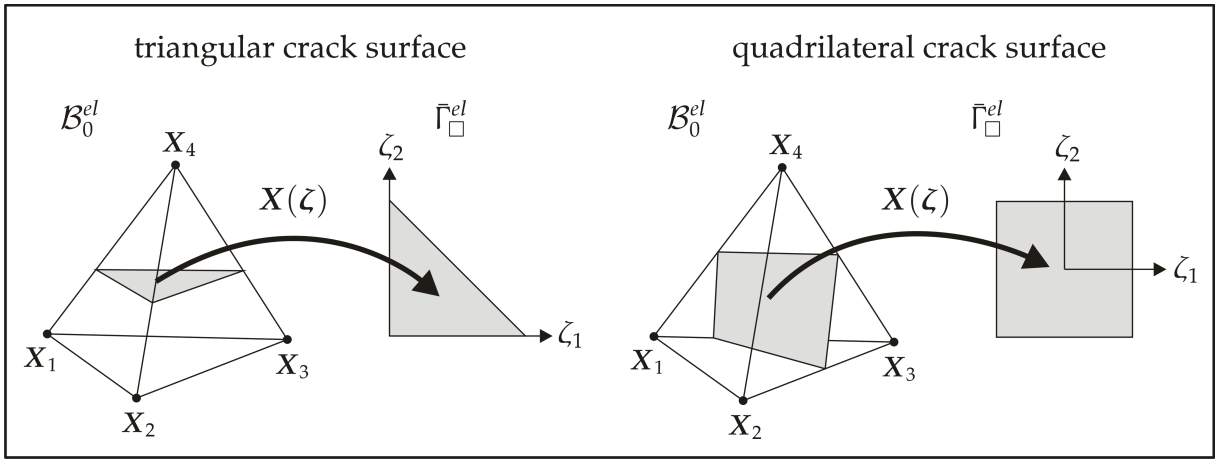

Figure 4.5.: Local crack surface coordinates in unit configuration for subdivided tetrahedral elements.

integration is comparable to the integration of standard interface elements and we refer to, e.g. SCHELLEKENS *[173],* SCHELLEKENS & DE BORST *[174]. Furthermore, for a comparison of interface elements with the strong discontinuity approach, we refer to* SIMONE *[183].*

4.5.2. Boundary conditions

Since we consider softening structural responses within the numerical simulations, special solution methods are required to avoid possible snapping behavior. Within this work, we apply only incrementally imposed DIRICHLET boundary conditions of suitable size, to capture the desired softening responses. For the accuracy of DIRICHLET boundary conditions within fracture simulations and their influence on the convergence behavior, we refer to MOËS et al. [132]. Moreover, for an overview of numerical solution techniques regarding imposing NEUMANN boundary conditions and the treatment of snapping behavior in structural responses, we propose the works of REMMERS [163] and GEERS [76, 74].

4.5.3. Failure criterion

We recall that the introduction of cohesive tractions leads to bounded stresses at the crack tip, compare remark 4.4.1. Therefore, we can use a failure criterion based on the stresses in front of the crack tip. We use a principal stress based RANKINE criterion to determine the critical stress state. We compute the eigenvalues of the CAUCHY stress tensor $\boldsymbol{\sigma} = \sum_{i=1}^{3} \lambda_i^{\sigma} \, \boldsymbol{n}_i^{\sigma} \otimes \boldsymbol{n}_i^{\sigma}$. Then, if the largest positive eigenvalue $\lambda_i^{\sigma_{max}} > 0$ exceeds the tensile strength, a discontinuity is adaptively introduced in the finite element. This issue is mentioned here for the sake of comprehensibility. A more detailed elaboration also considering the crack propagation direction will be given in the next chapter about crack tracking algorithms. Accordingly, for the numerical examples within this chapter, we restrict ourselves to situations with predetermined crack propagation direction.

4.5.4. Algorithmic flowchart

Now, we focus on a complete algorithmic overview for the adaptively introduced discontinuous finite elements, with its corresponding management of the complex geometry data, the failure criterion and the use of cohesive traction separation laws. For the sake of clarity, this complete operation is illustrated by means of a flowchart, compare figure 4.6. For a better understanding of the flowchart, we recall that the body $\mathcal{B}$ is decomposed in n_{el} finite elements, containing n_{el}^c continuous ones and n_{el}^d discontinuous ones. Moreover, we recapitulate that the stiffness matrices for the discontinuous elements are separated into the internal $\mathbf{K}_{IJ}^{int,d}$ and the cohesive part $\mathbf{K}_{IJ}^{coh,d}$, compare equations (3.23) and (4.40). Additionally, the calculation of the stresses contains the mentioned projection on the element nodes. The part of the crack path tracking is highlighted in gray since we will restrict the algorithmic description in the next chapter on this highlighted part. Next, we take into account the current set of crack tip elements. To avoid a crack extension search over the entire number of elements, potentially new crack tip elements are stored in a list of active crack tip elements. This set of active crack tip elements is then updated continuously, by checking the direct neighbors of the active crack tip elements. Furthermore, this set of crack tip elements is initially predefined. Then if the actual failure criterion is violated for one of this current crack tip elements, we apply the geometry handling. This requires the introduction of additional nodes, the update of the crack tip elements and the handling of crack tip front nodes, to ensure the geometric property of a crack tip. Finally, the crack geometry has to be extended, which requires the computation of the crack surface intersection points with its corresponding unit mappings and JACOBIANS.

4.6. Numerical Examples

In contrast to the latter chapter, where only stationary cracks are considered, we now consider the simulation of propagating cracks. We perform two delamination peel tests, with predefined crack path, to illustrate the discussed traction separation relations.

4.6.1. Symmetric bilateral peel test

The first example is the classical symmetric bilateral peel test which has been studied extensively in the related literature, for two as well as for three-dimensional crack propagation, see, e.g., KUHL et al. [98], MERGHEIM & STEINMANN et al. [128], WELLS [204], DE BORST [43, 44], AREIAS et al. [7], MANZOLI et al. [116], or REMMERS et al. [164]. A cantilever beam with a length of $10[\mathrm{mm}]$ and a cross section of $1[\mathrm{mm}^2]$ is fixed on one side, whereas a displacement is imposed on the upper and lower edge of the other side, compare figure 4.7. The displacement is imposed in 200 incremental load steps of $0.04[\mathrm{mm}]$, until a deformation of $8[\mathrm{mm}]$ is reached. The specimen is discretized with 2250(816 nodes), 3750(1116 nodes) and 6250(1836 nodes) structured finite elements, compare figure 4.7 for the discretization with 6250 elements. The material parameters are chosen as $\lambda = 2777.80[\mathrm{N/mm}^2]$ and $\mu = 4166.70[\mathrm{N/mm}^2]$, which

loadstep

solution of elastic bulk and cohesive interface problem
global NEWTON iteration

loop over n_{el}^{c} continuous elements $\mathcal{B}^{el,c}$

computation of element residuals $\mathbf{R}_I^{el,c}$
and incremental stiffness matrices $\mathbf{K}_{IJ}^{el,c}$

loop over n_{el}^{d} discontinuous elements $\mathcal{B}^{el,d}$

computation of element residuals $\mathbf{R}_I^{el,d}$
and incremental stiffness matrices $\mathbf{K}_{IJ}^{el,d}$

assembly $\overset{n_{el}}{\underset{e=1}{\mathbf{A}}}$ of global residuum and incremental stiffness matrix $\mathbf{R}_I$, $\mathbf{K}_{IJ}$

until equilibrium is reached

calculation of nodal deformation map $\boldsymbol{\varphi}_J$

calculation of CAUCHY stress $\boldsymbol{\sigma}$

crack path tracking
fix crack propagation direction

loop over crack tip elements

controll failure criterion
if $\max(\lambda_i^{\sigma}) - f_t > 0$

geometry handling
introduce new additional degrees of freedom
update list of crack tip elements
update list of crack tip front nodes
update crack geometry

controll geometry
if at least one crack tip element failed

start new global NEWTON iteration

else

geometry is stable, new loadstep can be applied

Figure 4.6.: Algorithmic flowchart of finite element based failure algorithm.

is equal to $E = 10000[\mathrm{N/mm^2}]$ and $\nu = 0.2[\text{-}]$. The material parameters for the cohesive zone model are $f_t = 200[\mathrm{N/mm^2}]$, $G_f = 100[\mathrm{N/mm}]$, $p = 4$ for the rational

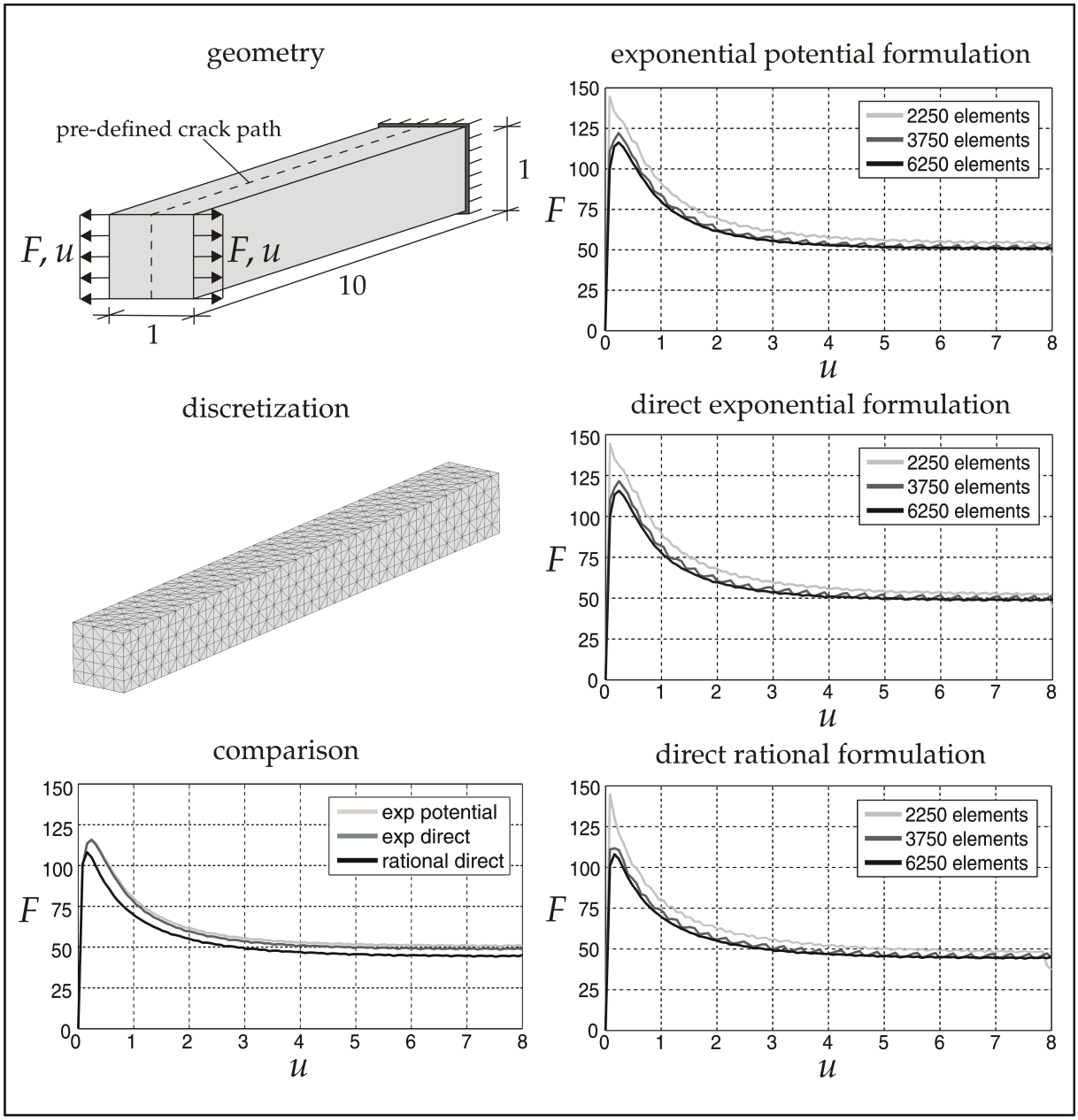

Figure 4.7.: Top left: Geometric dimensions [mm] and loading. Center left: Discretization with 6250 structured finite elements. Others: Load displacement response F[N] versus u[mm] for the different traction separation formulations.

cohesive traction separation law and $E_c = 1000000[\mathrm{N/mm^2}]$. The sliding parameter is $E_t = 0[\mathrm{N/mm^2}]$ because obviously, the jump inherently points in the opening direction, which supersedes the use of tangential tractions. We emphasize that the material parameters are chosen to compare the results to the related literature and not to a certain material or experiment. The crack is initialized in the middle of the beam, as depicted in the geometry description and the smooth peeling of the two layers during the ongoing crack propagation is clearly illustrated in figure 4.8. The deformation is symmetric as expected, due to the symmetry of the problem and accordingly, the normal vector of the fictitious discontinuity surface does not change during ongoing crack propagation.

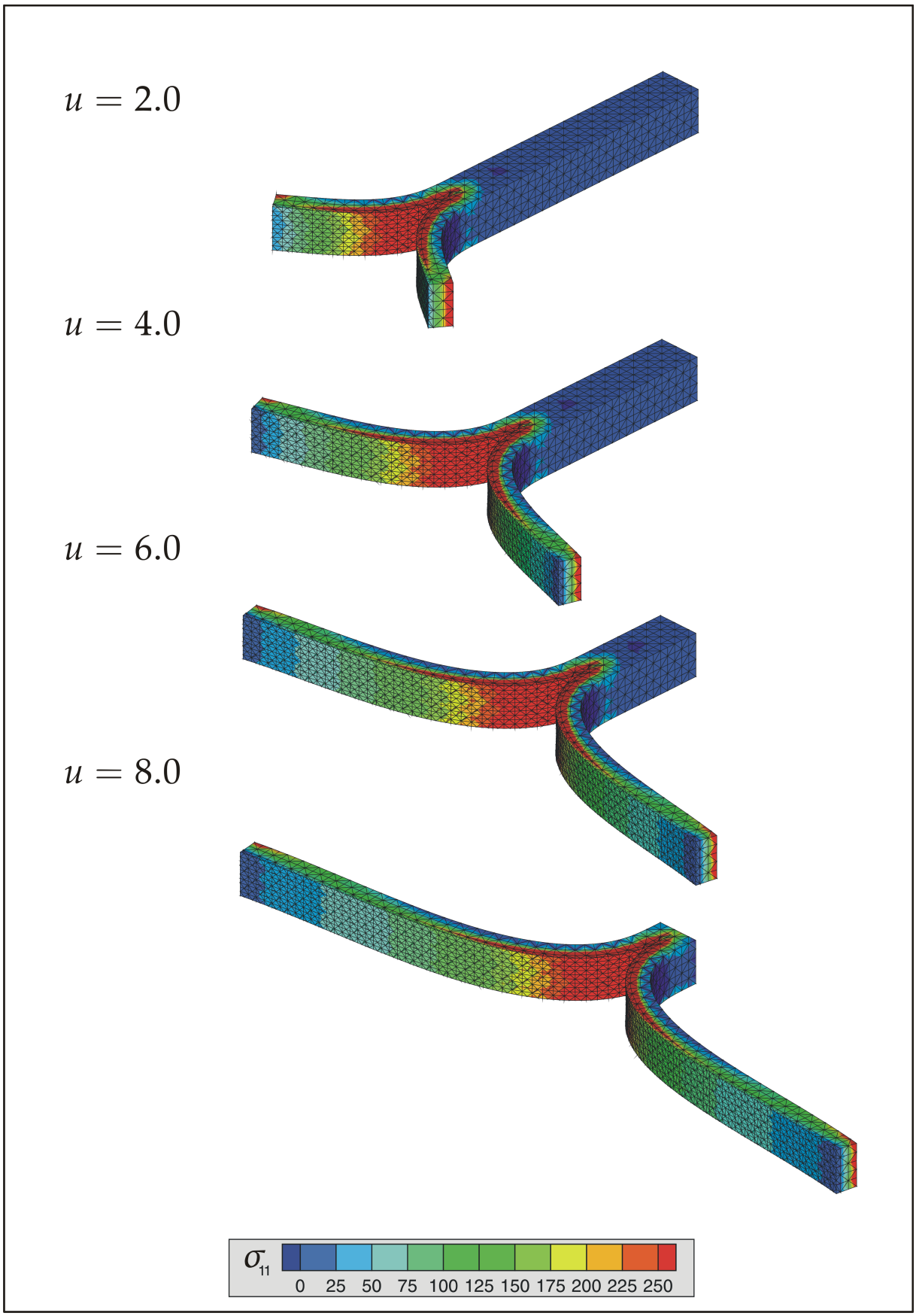

Figure 4.8.: Contour plot series of principal stress $\sigma_{11}\,[\mathrm{N/mm^2}]$ for the symmetric bi-lateral peel test discretized with 6250 structured finite elements and the direct exponential traction separation law formulation.

Thus, the dependence of the different traction separation laws on the fictitious normal vector is negligible, which leads to equivalent load displacement responses for the energy based and the direct exponential traction formulation, compare figure 4.7. It is noticeable that the load displacement response for the discretization with 2250 elements is overestimated and also the post peak behavior shows mentionable differences. The main reasons is the used failure criterion, the elements in front of the crack tip are too large to capture the occurring large stress gradients correctly. Broadly speaking, the smeared stresses in the large elements are smaller which leads to occurring later failure. Accordingly, the comparison of the three different traction separation relations is illustrated for the discretization with 6250 elements.

4.6.2. Non-symmetric unilateral peel test

Next, we analyze the non-symmetric bilateral peel test. We peel off the top layer of the specimen while the bottom layer is fixed, compare figure 4.9. For comparative analysis of this benchmark we refer among others to KUHL et al. [98], MERGHEIM & STEINMANN et al. [128], JÄGER et al. [102], WELLS [204] or REMMERS et al. [164]. Apart from the boundary conditions, the illustrated displacement is imposed in 120 incremental load steps of $0.08[\mathrm{mm}]$ until a deformation of $9.6[\mathrm{mm}]$ is reached, the three analyzed discretizations are similar to the previous example. The material parameters are almost the same, only the fracture energy differs, $G_f = 50[\mathrm{N/mm}]$, and the stiffness for the sliding direction is chosen as $E_t = 100[\mathrm{N/mm^2}]$ for the direct traction formulations. In contrast to the symmetric peel test, this example is chosen because the fictitious discontinuity surface undergoes significant rotations. Hence, this example is used to elaborate the correctness of the consistent linearization of the cohesive residual. We mention, without further illustration that the computations exhibit the desired quadratic convergence in the sense of the used NEWTON-RAPHSON procedure. Moreover, figure 4.10 illustrates the contour plots of the stresses at selected stages of the simulation. Similar to the previous example, the crack opens progressively and a smooth peeling can be observed. Figure 4.9 elaborates the structural responses for the different traction separation relations. Again the discretization with 2250 elements is to coarse to capture the failure process appropriately, whereas the finer meshes render likewise identical results. However, also the structural responses of the finer meshes exhibit a non-vanishing zig-zag characteristic behavior. This is substantiated by the chosen failure criterion. This means that the predefined crack path is, in contrast to the former symmetric example, not concordant to the preferred crack path, determined by the failure criterion. This preferred crack path tends to the top of the specimen. However, this not important since this example fulfills the required benchmark purposes. More important is the difference between the illustrated traction separation relations. As one can observe, the direct exponential formulation exhibits the maximum peak load, whereas the rational formulation shows the lowest one due to the chosen numerical parameter. The peak load of the potential based approach, which regards for tractions in jump direction, is situated between the aforementioned results. Additionally, the potential based approach exhibits only softening behavior whereas the other two approaches features a further rising in the structural response.

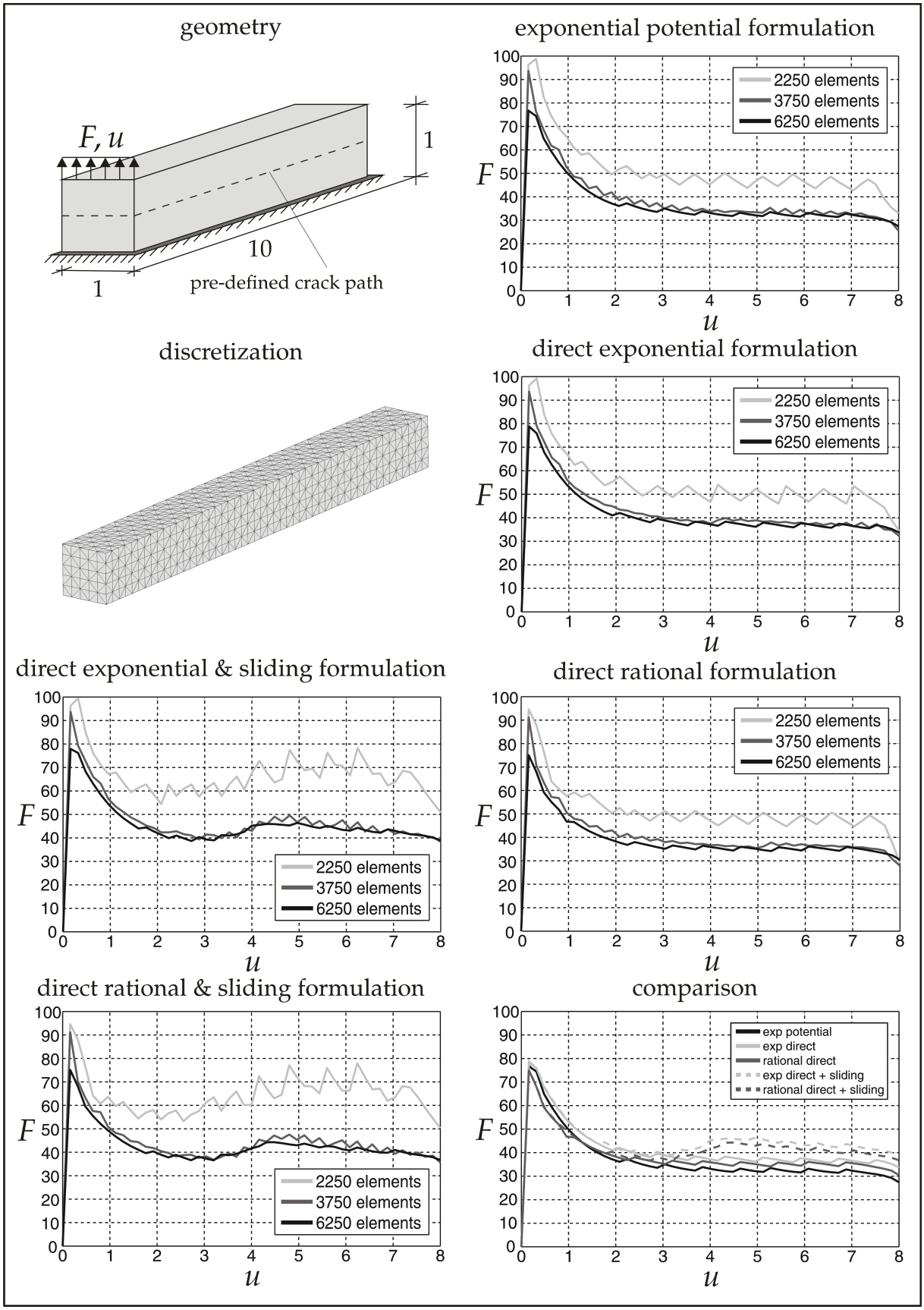

Figure 4.9.: Top left: Geometric dimensions [mm] and loading. Center left: Discretization with 6250 structured finite elements. Others: Load displacement response F[N] versus u[mm] for the different traction separation formulations.

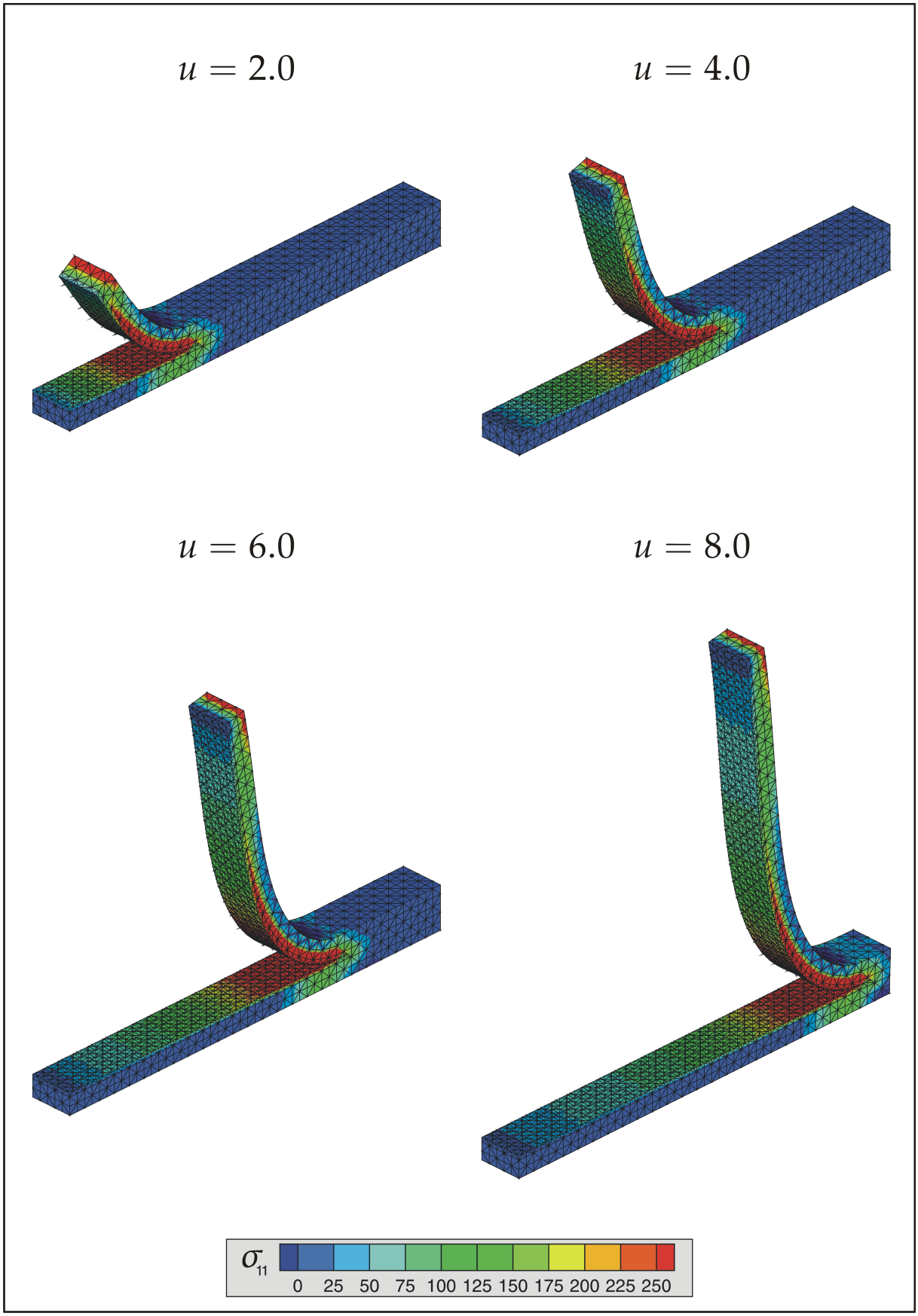

Figure 4.10.: Contour plot series of principal stress $\sigma_{11}\,[\mathrm{N/mm^2}]$ for the non-symmetric bi-lateral peel test discretized with 6250 structured finite elements and the direct exponential traction separation law formulation.

This is substantiated by the additional use of the tangential interface stiffness E_t, which provides a traction contribution in loading direction independent of the cohesive parameters G_f and f_t. This is the main difference to the potential based approach and the mentioned approaches from the related literature, where a total crack opening measure depending on the opening and the relative displacement is introduced. Finally, we mention that we have presented the cohesive crack concept, which allows the mesh-independent computation of propagating cracks by means of the presented discretization scheme.

5. Crack path tracking strategies

5.1. Motivation

The description and the computation of the current crack surface, based on the actual status of the considered body, is the key issue of the following chapter. We emphasize that in a two-dimensional finite element setting the geometrical description of the crack surface is only a line. Accordingly, tracking the crack path is a unique procedure and its algorithmic realization is more or less straightforward. Once a finite element is identified to fail, usually based on the presented principal stress based failure criterion, the crack extends from a neighboring crack point on the particular element edge in the desired direction. While this procedure always renders a unique and smooth $\mathcal{C}^0$-continuous failure representation in two-dimensional analysis, it usually yields a non-smooth failure representation in a fully three-dimensional setting.
Recent attempts in the literature have addressed the issue of crack propagation in three-dimensions. For mesh-adaptation or computations with mesh refinement we refer to, e.g., ASKES & SLUYS [12], SCHÖLLMANN et al. [176], or BUCHOLZ et al. [27]. Three-dimensional computations with interface elements are given, e.g., by RUIZ et al. [168] or ORTIZ [155], whereas simulations containing embedded discontinuities can be found in, e.g., OLIVER et al. [154, 153, 152], SANCHO et al. [171], or MOSLER & MESCHKE [140]. Moreover, for applications with the extended finite element method we refer to AREIAS & BELYTSCHKO [4], BORDAS & MORAN [25], GASSER & HOLZAPFEL, [71, 70, 72, 73], GRAVOUIL et al. [80], MOËS et al. [134] or SUKUMAR et al. [194, 193]. Furthermore, boundary element applications can be found in KOLK & KUHN [109, 110], for completely meshfree methods we refer to RABCZUK et al. [161, 159, 160] and a first three-dimensional attempt with the presented discretization scheme is given by MERGHEIM et al. [128].
In the following, based on our works, JÄGER et al. [102, 100], we present five of the most common approaches to track crack surfaces within a three-dimensional finite element setting. We compare the particular approaches by means of common quality measures such as robustness, stability, efficiency, computational cost and crack surface continuity. Prior to discussing these approaches we elaborate the principal stress criterion for brittle materials more detailed than in the previous chapter. Thereby, we also introduce the computation of average stress and strain measures, see, e.g., WELLS & SLUYS [205], WELLS et. al. [207] or MERGHEIM et al. [127] for two-dimensional problems, GASSER & HOLZAPFEL [71] or MERGHEIM [125] for three-dimensional problems and for average strain measures, e.g., GRASSL & JIRASEK, [79] or JIRASEK [104]. Then we discuss the so called fixed tracking algorithm for which, similar to computations based on classical interface elements, the crack path has to be known a priori. A slightly more complicated approach is the local tracking algorithm, which can be interpreted as the three-dimensional generalization of cracking in two-dimensional failure analysis. Here, based on the idea of AREIAS & BELYTSCHKO [4], the current crack

plane, depending on the failure criterion, is adjusted with the help of the neighboring crack points. However, in case of too many neighboring points the computation of the adjusted crack plane can be over-determined. Afterwards, we present a non-local tracking strategy which is able to remedy this over-determination. By averaging the crack plane normal over a certain neighborhood, GASSER & HOLZAPFEL [72] ensure that the generated failure surface is smooth in average, see also GASSER [69] and FEIST & HOFSTETTER [63]. However, as for all non-local averaging techniques, this concept is not really tailored to the modular element-wise nature of finite element analysis. Although theoretically elegant, it is rather cumbersome to include it into existing finite element codes. Subsequently, we present an extremely elegant and yet very powerful strategy that circumvents nearly all of the deficiencies above. This so called global tracking scheme was introduced recently by OLIVER et al. [153, 152] and SAMANIEGO [169]. Furthermore, this concept is currently also used, as far as we know, by CHAVES [57], DUMSTORFF & MESCHKE [55], CERVERA & CHIUMENTI [32], FEIST & HOFFSTETTER [62, 61]. It provides a finite element specific solution to the problem of kinematical crack characterization as it introduces an additional field of scalar valued or level set unknowns that in particular define one or multiple crack surfaces. Arbitrarily shaped crack surfaces can thus be described in a completely smooth and stable manner, however, at the cost of solving an additional partial differential equation. Since it is neglected in most of the related literature, we further discuss the initial boundary conditions for the additional field as the key feature for this global tracking approach, see, e.g., JÄGER et al. [99, 101]. Then we illustrate the level set approach for the sake of completeness. This approach describes the crack surfaces and the current crack front with two independent scalar valued level set functions based on the level set theory for moving interfaces, see, e.g., SETHIAN [178]. Thereby, the description of the complete crack is reduced to a certain region around the current crack front and the evolution of the crack surface requires the knowledge of the current crack front velocity. Applications and formulations for fracture simulations combined with the level set approach can be found, e.g., in BELYTSCHKO et al. [19], CHESSA & BELYTSCHKO [33], STOLARSKA et al [192], BORDAS & MORAN [25], MOËS et al. [134], GRAVOUIL et al. [80] or SUKUMAR et al. [193].
Finally, we clarify the assets and drawbacks of the presented approaches by means of an illustrative benchmark. We discuss a rectangular block under two different loading scenarios to provide a straight planar crack segment and a curved crack situation.

5.2. Crack Propagation

We recall that throughout a discontinuity computation we usually impose the initial position of the crack by specifying a certain number of initial crack tip elements and the accurate position within these elements. From there on, the actual set of crack tip elements is computed and updated dynamically by checking the direct neighbors of the considered crack tip element as mentioned in chapter 4. Accordingly, the next critical task is the determination of the direction in which the discontinuity is extending. Therefore, we firstly take into account for the principal stress based failure criterion.

Afterwards, we consider a first elementary geometrical description of the total crack surface based on the result of the principal stress based failure criterion and a single point to characterize the connection to the next finite element. Furthermore, we explain the arising non-uniqueness of this kind of crack surface description in a three dimensional framework and its inherent emerging problems for the crack path tracking connected to the applied discontinuous discretization scheme.

5.2.1. Failure criterion

The main idea of the RANKINE criterion is the assumption that the considered material is characterized by two mechanical properties, the tensile strength f_t and the compression strength f_c. Then, material failure occurs if the maximum principal stress exceeds one of these mechanical properties. Accordingly, the failure criterion requires the computation of the principal stresses by solving the following eigenvalue problem for the CAUCHY stress tensor $\boldsymbol{\sigma} \cdot \boldsymbol{n}_i^\sigma = \lambda_i^\sigma \boldsymbol{n}_i^\sigma$ which results in the decomposition of the stress tensor in its eigenvectors and corresponding eigenvalues.

$$\boldsymbol{\sigma} = \sum_{i=1}^{3} \lambda_i^\sigma \, \boldsymbol{n}_i^\sigma \otimes \boldsymbol{n}_i^\sigma \qquad \text{failure if:} \quad \begin{cases} \lambda_i^{\sigma_{max}} > \quad f_t \\ \lambda_i^{\sigma_{max}} < -f_c \end{cases} \tag{5.1}$$

The corresponding failure surface in the space of principal stresses is equal to the surface area of a cube, see among others GROSS & SEELIG [81]. Since compression failure is usually accompanied with shattering or bursting of the material, we restrict our further considerations to tensile dominated failure. Thus, we allow for failure only if the largest positive eigenvalue $\lambda_i^{\sigma_{max}} > 0$ exceeds the maximum tensile strength f_t. Furthermore, the eigenvector $\boldsymbol{n}^{\sigma_{max}}$ related to the maximum eigenvalue $\lambda_i^{\sigma_{max}}$ determines the spatial crack propagation direction $\boldsymbol{n}^{crk} = \boldsymbol{n}^{\sigma_{max}}$. Finally, the referential crack propagation direction is given by applying NANSON's formula $\boldsymbol{N}^{crk} = \frac{1}{J} \boldsymbol{F}^t \cdot \boldsymbol{n}^{crk}$.

Remark 5.2.1 (Adaptive discontinuity introduction) *We emphasize that during the adaptive introduction of the discontinuity the current element is a continuous element in front of the actual crack tip. Thus, J and $\boldsymbol{F}$ are the deformation gradient and the* JACOBIAN *introduced in chapter 2. Furthermore, the referential crack normal $\boldsymbol{N}^{crk}$ is then constant and facilitates the unique fragmentation of the now discontinuous element. The spatial normal of the fictitious crack surface during ongoing crack propagation is then provided by applying* NANSON*'s formula onto the referential crack normal $\boldsymbol{N}^{crk}$ for the particular loading state. This means that we use the average deformation gradient $\bar{\boldsymbol{F}}$ of the fictitious spatial crack surface $\bar{\gamma}$ for the now discontinuous element.*

5.2.2. Crack surface description

Once the direction of crack propagation is known from the evaluation of the failure criterion, an appropriate geometrical representation of the crack surface in three dimensions is needed. We further remind that we apply a linear approximation of the deformation field and accordingly, the crack surface is represented by piecewise planar triangles and quadrilaterals in the reference configuration. Thus, in a three-dimensional

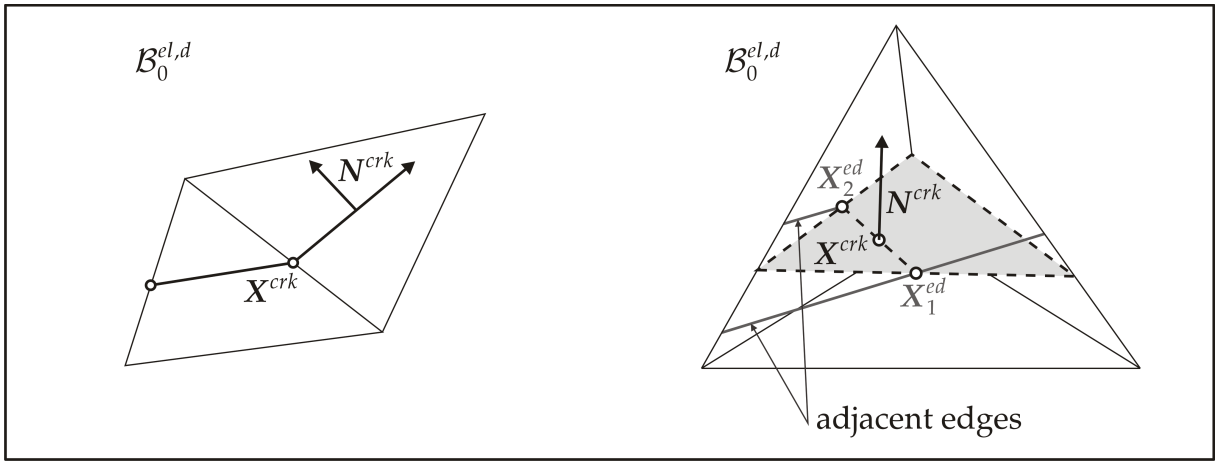

Figure 5.1.: Unique discontinuity connecting point $\boldsymbol{X}^{crk}$ for the two-dimensional case and averaged connecting point $\boldsymbol{X}^{crk}$ depending on the adjacent cracked element edges $\boldsymbol{X}^{ed}$ for the three-dimensional case.

finite element setting, the orientation of an element discontinuity is defined by the mentioned reference normal vector $\boldsymbol{N}^{crk}$ and a single point $\boldsymbol{X}^{crk}$ to characterize the connection to the next element discontinuity. In contrast to two-dimensional problems, where this point $\boldsymbol{X}^{crk}$ is always uniquely defined by the previous cracked finite element, this is not the case for three-dimensional problems, see figure 5.1. Therefore, we firstly adopt the procedure of GASSER & HOLZAPFEL [71] and define the point $\boldsymbol{X}^{crk}$ as the average of the pictured crack points $\boldsymbol{X}_i^{ed}$, i.e., the midpoints of all adjacent cracked element edges $i = 1, .., n_{ed}$.

$$\boldsymbol{X}^{crk} = \frac{1}{n_{ed}} \sum_{i=1}^{n_{ed}} \boldsymbol{X}_i^{ed} \tag{5.2}$$

Accordingly, we define a first possible crack propagation transfer within the discrete finite element setting in three dimensions. However, a major problem occurs since this introduced crack surface description leads to possible non-smooth failure surfaces which requires the development of crack tracking algorithms.

5.3. Crack tracking

For practically relevant applications non-smooth failure surfaces are undesirable because of potential crack bifurcations for large crack deviation angle and possible ambiguities for the introduction of the additional degrees of freedom, we will specify this issue in remark 5.3.1. Therefore, we essentially need to identify powerful tracking algorithms to obtain almost smooth or at best fully smooth representations of the crack surface. In the following we systematically review the most common tracking strategies for three-dimensional crack propagation. We perform a systematic comparison in terms of standard algorithmic quality measures such as mesh-independency, efficiency, robustness, stability and computational cost. Moreover, we discuss more specific issues such as crack path continuity and integrability in commercial finite element codes.

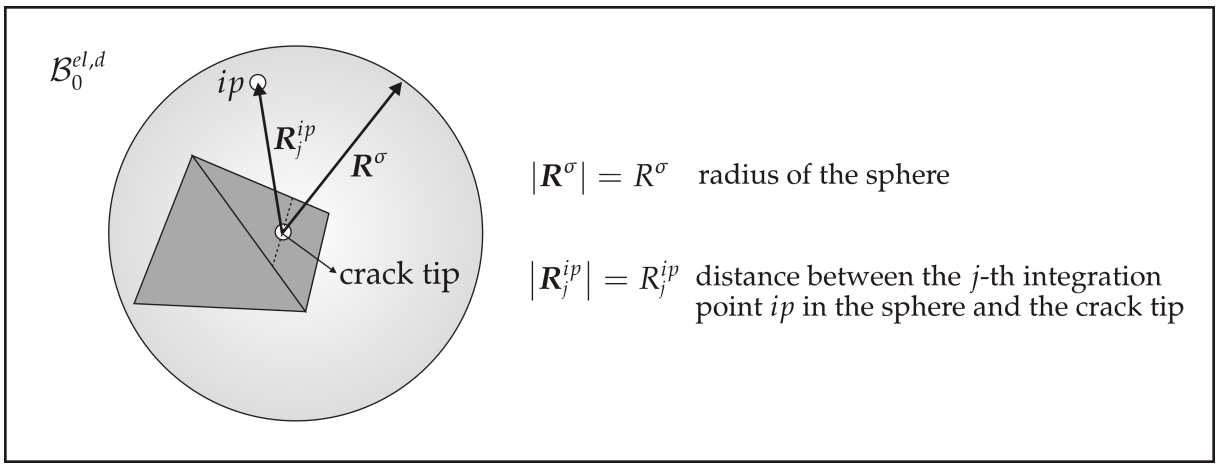

Figure 5.2.: Stress averaging sphere around the crack tip element introducing the set $\mathcal{I}$ of all integration points ip within the sphere.

5.3.1. Fixed tracking

The easiest way to achieve fully smooth or at least $\mathcal{C}^0$-continuous crack surfaces is the use of a predefined crack plane. The delamination examples of the former chapter have shown that this kind of crack path tracking can successfully be used when the failure surface is a priori known. Typical examples of predefined failure surfaces are welded interfaces between substructures of the same material or joining zones between substantially different materials. Additionally, more complicated crack surfaces can be likewise imposed if the path is known either from the specimen geometry or from experiments. However, the aim is to perform fracture simulations which provide the crack propagation direction depending on the current state of the considered specimen. Hence, we usually abstain from using the fixed tracking algorithm to capture the crack path.

5.3.2. Average and weighted stress computation

A first attempt to avoid the occurring spurious crack path oscillations of the crack plane normals, which leads to the non-smooth description of the complete crack surface, is the use of non-local average strains or non-local average stress measures. Therefore, according to the literature, we assume a non-local zone around the current crack tip which is responsible for the crack propagation direction, see, e.g., WELLS & SLUYS [205], WELLS et. al. [207], MERGHEIM et al. [127], MERGHEIM [125] or GASSER & HOLZAPFEL [71]. We define a sphere with radius R^σ around the actual crack tip of the considered finite element, see figure 5.2. Typically R^σ is chosen to be two to four times the characteristic finite element length $L_0^{el} = \sqrt[3]{V_0^{el}}$, introduced in the former chapter. We further denote the distance between j-th integration point ip within the sphere and the current discontinuity tip with R_j^{ip}, compare again figure 5.2. Then, we define V^{ip} the referential element volume related to the j-th integration point ip and introduce

the set $\mathcal{I}$ of all integration points n_{ip} within the non-local averaging sphere.

$$\mathcal{I} = \left\{ j \in \{1, .., n_{ip}\} \,|\, R_j^{ip} < R^{\sigma} \right\} \tag{5.3}$$

This set $\mathcal{I}$ is divided into two disjoint subsets $\mathcal{I} = \mathcal{I}^{\sigma} \cup \mathcal{I}^{n}$, where $\mathcal{I}^{\sigma}$ contains the integration points of the un-cracked elements and $\mathcal{I}^{n}$ the integration points of the cracked elements in $\mathcal{I}$. Furthermore, we define the total number of connected integration points with $n_{\sigma} = \text{card}\,(\mathcal{I}^{\sigma})$ and $n_n = \text{card}\,(\mathcal{I}^{n})$. We then compute the non-local stress tensor $\widetilde{\boldsymbol{\sigma}}$ as the following expression.

$$\widetilde{\boldsymbol{\sigma}} = \frac{1}{\sum\limits_{k \in \mathcal{I}^{\sigma}} V_k^{ip}} \sum_{j \in \mathcal{I}^{\sigma}} V_j^{ip}\, \boldsymbol{\sigma}_j \tag{5.4}$$

Here, the used index j indicates that the stress tensor corresponding to the j-th un-cracked finite element is multiplied by its connected volume V_j^{ip}. For the sake of completeness, we mention that most of the related works further multiply the non-local stress with a certain weight function, depending on the distance to the current crack tip, see, e.g., REMMERS [163] or WELLS & SLUYS [205]. However, we follow GASSER & HOLZAPFEL [72] and use only a volume averaging procedure. We emphasize that the use of this non-local stresses can obviously exhibit undesired results close to the boundary of the considered geometry. Additionally, a non-local formulation is also possible for strain measures, see, e.g., FEIST & HOFSTETTER [62] and in conjunction with non-local damage, e.g., GRASSL & JIRASEK [79] or JIRASEK [104]. Next, we compute the eigenvector decomposition of the average CAUCHY stress tensor in the same manner as for the usual principal stress based failure criterion.

$$\widetilde{\boldsymbol{\sigma}} = \sum_{i=1}^{3} \lambda_i^{\widetilde{\sigma}}\, \boldsymbol{n}^{\widetilde{\sigma}} \otimes \boldsymbol{n}^{\widetilde{\sigma}} \qquad \text{failure if:} \quad \begin{cases} \lambda_i^{\widetilde{\sigma}_{max}} > \quad f_t \\ \lambda_i^{\widetilde{\sigma}_{max}} < -f_c \end{cases} \tag{5.5}$$

Accordingly, the non-local eigenvector $\widetilde{\boldsymbol{n}}^{\widetilde{\sigma}_{max}}$ related to the maximal eigenvalue $\lambda^{\widetilde{\sigma}_{max}}$ determines the crack propagation direction. Moreover, following practice in the related literature, we restrict the crack deviation angle θ^{crk} between the current crack tip element and the average normal vector of the sphere, compare, e.g., GASSER & HOLZAPFEL [72]. However, this is only an ad hoc attempt to avoid unphysical crack bifurcations and spurious turning of cracks due to the non-smooth description of the complete crack surface. This crack deviation restriction requires the computation of the following average normal vector $\widetilde{\boldsymbol{n}}^{n}$ of all integration points n_n of the cracked elements within the set $\mathcal{I}^{n}$.

$$\widetilde{\boldsymbol{n}}^{n} = \frac{1}{n_n} \sum_{i \in \mathcal{I}^{n}} \boldsymbol{n}_i^{crk} \tag{5.6}$$

Technically speaking, we determine the spatial crack propagation direction of the considered j-th crack tip element according to the following crack deviation angle condition.

$$\boldsymbol{n}_j^{crk} = \begin{cases} \widetilde{\boldsymbol{n}}_j^{\widetilde{\sigma}_{max}} & \text{if} \quad \theta^{crk} < \theta^{crit} \\ \widetilde{\boldsymbol{n}}_j^{n} & \text{if} \quad \theta^{crk} \geq \theta^{crit} \end{cases} \qquad \text{with} \quad \cos(\theta^{crk}) = \widetilde{\boldsymbol{n}}^{n} \cdot \widetilde{\boldsymbol{n}}_j^{\widetilde{\sigma}_{max}} \tag{5.7}$$

The critical crack deviation angle θ^{crit} is usually chosen to $\theta^{crit} = \pi/6$ or $\theta^{crit} = \pi/4$, for the exclusive use of the average stress criterion.

Validation and implementation comments

Remark 5.3.1 (Continuity) *The average stress computation, is only an ad hoc attempt to avoid spurious crack path oscillations in the field of crack plane normal vectors. Indeed, it provides a smoothing of the total crack surface depending on the chosen radius of the sphere R^σ. This smoothing, in combination with the crack deviation criterion, is helpful to avoid big or remarkable jumps between particular element discontinuity patches. But obviously, it can not ensure a continuous or at least almost continuous description of the total crack surface. This is an important problem, especially, using the present discontinuous discretization scheme. The main problem occurs, if a discontinuity patch of a certain element strikes the vicinity of an element node and the element patch of the neighboring element also strikes the vicinity of the element node, however, from the opposite side because of a possible jump between these element patches. In this case, the mentioned jump at the element edges impedes the unique introduction of the additional node with its classification of its orientation to the $\mathcal{B}_0^+$ or $\mathcal{B}_0^-$ side of the discontinuity. This is an essential drawback of the present approach compared with the mentioned extended finite element method. For the latter approach this situation is handled by enhancing only the nodes which are not stricken from the discontinuity patch, recall that the standard extended formulation is based on enhanced jump degrees of freedom and compare, e.g.,* SUKUMAR & PRÉVOST *[195] for the so called area criterion. Clearly, this non-enrichment of the considered node facilitates also the situation that one of the element discontinuity patches is situated within the defined vicinity of the considered node, whereas the opposite neighbor is located outside of the defined node vicinity. In fact, this is an important difference to the present approach since if we try to capture a discontinuity at an element edge, or an element face, this requires the unique classification of the considered element node. Accordingly, with the present approach and without using more additional degrees of freedom than emerging with the doubling of the considered finite element, we can only capture a discontinuity patch on an element edge or an element surfaces with a complete $\mathcal{C}^0$-continuous crack surface description. As a consequence, the exclusive use of the average stress criterion is useful for computations which provide planar or almost planar crack surfaces. In such cases the latter prescribed situation can be avoided. For more complicated crack plane geometries, the exclusive use of the average stress criterion is not suitable. However, it can be useful to apply the average stress criterion in combination with the following crack tracking algorithms.*

Remark 5.3.2 (Computational cost) *The computational cost of this average stress computation requires only the mentioned list of the element face neighbors. Then a loop over all n_{tip} crack tip elements is needed, with a following loop over the particular element face neighbors to compute all integration point variables within the set $\mathcal{I}^\sigma$ and $\mathcal{I}^n$, respectively.*

5.3.3. Local tracking

Now, we consider the so called local tracking algorithm. This method was initially proposed by AREIAS & BELYTSCHKO [4] and is based on a modification of the discontinuity direction depending on the cracked neighboring elements. Therefore, let us

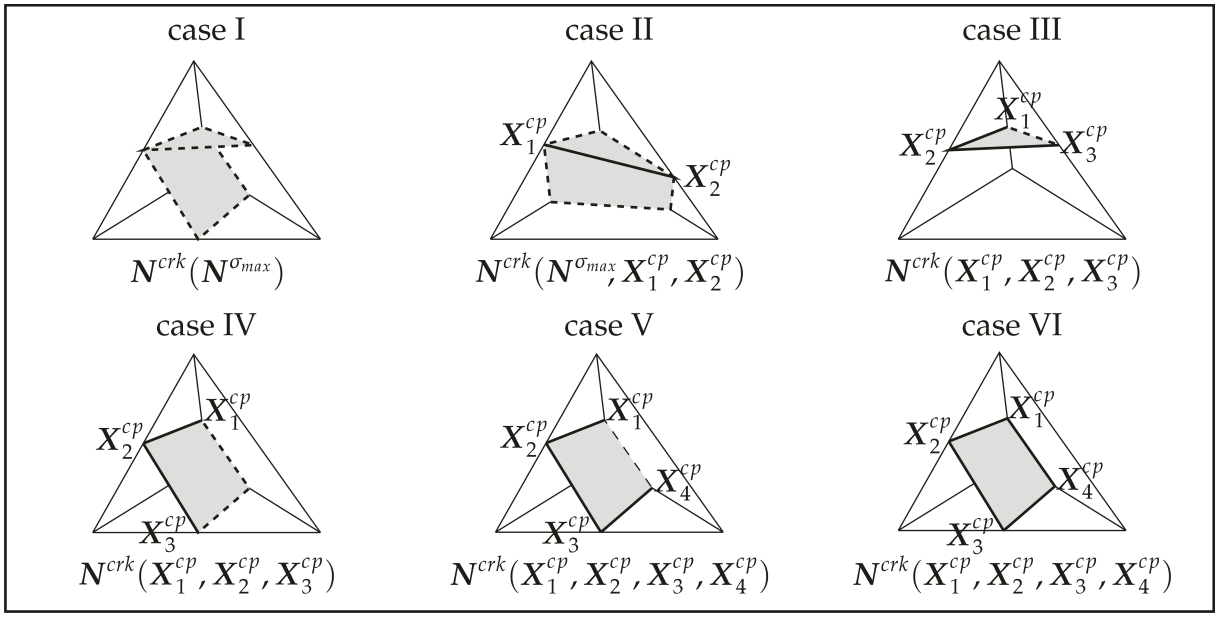

Figure 5.3.: Local tracking: Illustration of different crack scenarios I-VI, corresponding crack neighbor points X_i^{cp} and dependencies of crack plane normal vector N^{crk}.

case	crack	normal	normal to discontinuity surface
I	initiation	$N^{crk}(N^{\sigma_{max}})$	$N^{crk} = N^{\sigma_{max}}$
II	propagation	$N^{crk}(N^{\sigma_{max}}, X_i^{cp})$	$N^{crk} = \left[I - \frac{\left[X_1^{cp} - X_2^{cp}\right] \otimes \left[X_1^{cp} - X_2^{cp}\right]}{\left\lvert X_1^{cp} - X_2^{cp} \right\rvert^2} \right] \cdot N^{\sigma_{max}}$
III-VI	propagation	$N^{crk}(X_i^{cp})$	$N^{crk} = [\, X_1^{cp} - X_2^{cp} \,] \times [\, X_3^{cp} - X_2^{cp} \,]$

Table 5.1.: Local tracking algorithm - summary of crack scenarios I-VI with particular definition of referential crack plane normal N^{crk}.

assume that the current crack surface is represented by n_{cp} crack points cp. These are the element-wise intersection points X_i^{cp} of the element discontinuities and the element edges, compare figure 5.3. As such, they represent the corners of the element-wise planar triangular or quadrilateral discontinuity plane. The number of crack neighbor points can vary between zero and four, i.e., $i \in \{0, 2, 3, 4\}$ and introduces six possible fundamentally different crack scenarios as illustrated in figure 5.3. Case I only occurs during crack initiation, i.e., $i = 0$. At initiation, the referential crack plane normal N^{crk} is chosen to be identical to the referential direction of maximum tensile stress $N^{\sigma_{max}}$. Thereby, it should again be mentioned that this latter referential direction of maximum tensile strength can be either taken as a pull-back result from the usual principal stress criterion, $n^{\sigma_{max}}$, or likewise from the average principal stress criterion, $\widetilde{n}^{\widetilde{\sigma}_{max}}$. Next, we consider case II which corresponds to one single cracked neighbor element, i.e., $i = 2$. In this case, the new crack plane normal N^{crk} depends on both, the initial crack geometry X_i^{cp} and the direction of maximum tensile stress $N^{\sigma_{max}}$. Cases III-VI are entirely determined by the three or four given neighboring crack points X_i^{cp}, i.e., $i = 3, 4$. The

crack plane normal $\boldsymbol{N}^{crk}$ then depends exclusively on the previous crack geometry and is completely independent from the chosen maximum principal stress direction $\boldsymbol{N}^{\sigma_{max}}$. The element-wise definition of the new normal to the discontinuity $\boldsymbol{N}^{crk}$ for all six cases is summarized in table 5.1. From the given definitions, it is obvious that $\boldsymbol{N}^{crk}$ is not necessarily a unit vector and accordingly, a standardization is needed. We emphasize that during an usual crack propagation simulation cases II and III occur most frequently.

Validation and implementation comments

Remark 5.3.3 (Continuity) *The major drawback of the local tracking scheme is that it is severely restrictive by construction since the new crack plane normal $\boldsymbol{N}^{crk}$ might eventually be fully determined by the previous crack geometry. This might lead to non-uniqueness because it requires that all four cut points $\boldsymbol{X}_i^{cp}$ are located on a plane which is uniquely determined by three of these cut points. Provided that this restriction is not violated, however, the algorithm generates perfectly C^0-continuous discontinuity surfaces at extremely low computational cost. Typical examples in which the local tracking scheme has been applied successful are planar or slightly kinked discontinuity surfaces because otherwise the mentioned restriction occurs.*

Remark 5.3.4 (Computational cost) *For the discussion of the implementational effort, we recall again the dynamic list of crack tip elements contains n_{tip} entries. Moreover, each tetrahedral element has four neighboring elements which are identified and stored in the mentioned neighbor list at the initialization of the mesh. The computational effort of this algorithm is thus, remarkably small. In fact, it is restricted to looping over the four neighboring elements of all elements in the cracked element list.*

5.3.4. Non-local tracking

An alternative strategy that successfully circumvents the limitations of the local tracking scheme has been introduced by GASSER & HOLZAPFEL [72], see also GASSER [69] and FEIST & HOFSTETTER [63]. It essentially consists of two steps. The predictor step is applied to compute the normal vector $\boldsymbol{N}^{\sigma_{max}}$ and the point $\boldsymbol{X}^{crk}$. Clearly, the crack propagation direction can be computed either from the chosen common $\boldsymbol{N}^{\sigma_{max}}$ or from the average failure criterion $\widetilde{\boldsymbol{N}}^{\sigma_{max}}$. Indeed, for many situations, the newly calculated element crack surface does not match the previously existing discontinuity. In many cases it is yet geometrically impossible to close a crack surface if the element has been approached by cracks from different sides. Therefore, a corrector step is introduced to close the existing crack surface as continuously as possible. During the corrector step, the current crack plane normal $\boldsymbol{N}^{\sigma_{max}}$ of the chosen failure criterion is changed with accounting for additional information of the neighboring elements. In general the complete existing crack surface is represented by a total number of n_{crk} crack surface points. These are all of the n_{cp} element-wise intersection points $\boldsymbol{X}_i^{cp}$ of the particular element discontinuities and the element edges. As such, they represent the element-wise corners of the involved triangular or quadrilateral discontinuity planes. We further define that their position vectors $\boldsymbol{X}_i^{cp}$ for $i = 1..n_{crk}$ are given relative to a global CARTESIAN coordinate system $\{X, Y, Z\}$ with the orthonormal base vectors $\boldsymbol{E}_1^c, \boldsymbol{E}_2^c, \boldsymbol{E}_3^c$,

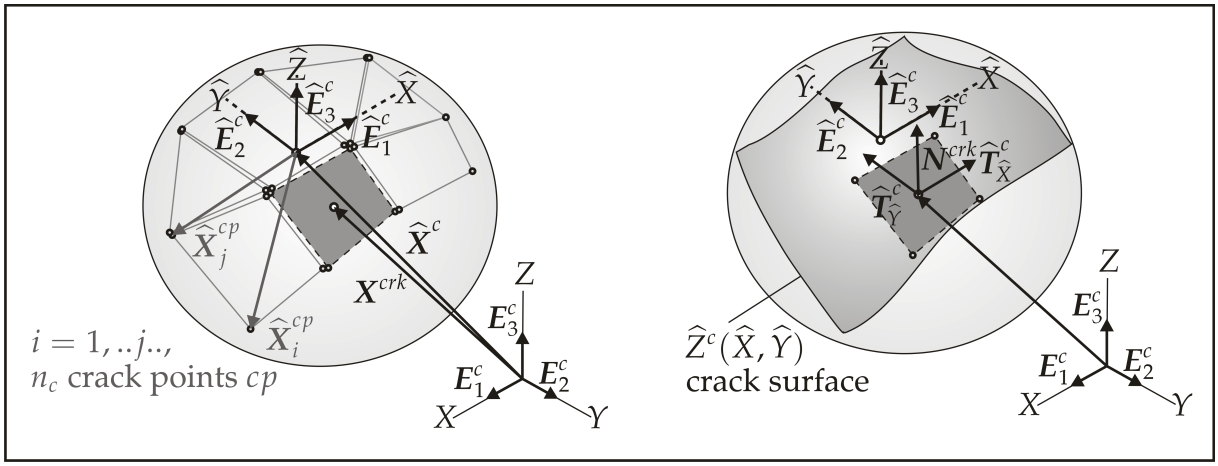

Figure 5.4.: Non-local tracking: Normal averaging sphere around the center point $\widehat{\boldsymbol{X}}^c$ introducing the set $\mathcal{I}^c$ of n_c crack points cp within the sphere. Element-wise crack surface defined through local tangential vectors $\widehat{\boldsymbol{T}}^c_{\widehat{X}}$ and $\widehat{\boldsymbol{T}}^c_{\widehat{Y}}$.

see figure 5.4. Thereby, the superscript c has been added to avoid a mix-up with the GREEN-LAGRANGE strain tensor. We then, again, introduce a sphere with the radius R^c around the single point $\boldsymbol{X}^{crk}$ of the currently analyzed element. Its radius R^c can just be chosen equivalent to the sphere's radius R^σ from the computation of the average stress tensor but this is not imperative. For the sake of clarity let us introduce the following set $\mathcal{I}^c$ of all intersection points $\boldsymbol{X}^{cp}_i$ within this latter sphere.

$$\mathcal{I}^c = \left\{ i \in \left\{1, .., n^{crk}\right\} \,|\, R^{cp}_i < R^c \right\} \qquad \text{with} \qquad n_c = \text{card}\left(\mathcal{I}^c\right) \tag{5.8}$$

Here, $R^{cp}_i = \left| \boldsymbol{X}^{cp}_i - \boldsymbol{X}^{crk} \right|$ obviously denotes the distance of the $i-$th crack intersection point from the current element center $\boldsymbol{X}^{crk}$. The set of points $\mathcal{I}^c$ is essential for the following smoothing strategy. It forms a point cloud with the center point $\widehat{\boldsymbol{X}}^c$.

$$\widehat{\boldsymbol{X}}^c = \frac{1}{n_c} \sum_{i \in \mathcal{I}^c} \boldsymbol{X}^{cp}_i \tag{5.9}$$

The orientation of this point cloud is given through a second local CARTESIAN coordinate system $\{\widehat{X}, \widehat{Y}, \widehat{Z}\}$ which is characterized by a second set of orthonormal bases vectors $\widehat{\boldsymbol{E}}^c_1, \widehat{\boldsymbol{E}}^c_2, \widehat{\boldsymbol{E}}^c_3$. These orthonormal base vectors are the principal axes of the point cloud $\mathcal{I}^c$ which are characterized in terms of the covariance tensor $\boldsymbol{\Sigma}^c$.

$$\boldsymbol{\Sigma}^c = \sum_{i \in \mathcal{I}^c} \left[\boldsymbol{X}^{cp}_i - \widehat{\boldsymbol{X}}^c \right] \otimes \left[\boldsymbol{X}^{cp}_i - \widehat{\boldsymbol{X}}^c \right] \tag{5.10}$$

The second set of base vectors $\widehat{\boldsymbol{E}}^c_1, \widehat{\boldsymbol{E}}^c_2, \widehat{\boldsymbol{E}}^c_3$ then follows straightforwardly from the corresponding eigenvalue decomposition.

$$\boldsymbol{\Sigma}^c = \sum_{i=1}^{3} \lambda^{\Sigma^c}_i \, \widehat{\boldsymbol{E}}^c_i \otimes \widehat{\boldsymbol{E}}^c_i \tag{5.11}$$

Next, we compute the corner points $\widehat{\boldsymbol{X}}^{cp}_i = \boldsymbol{X}^{cp}_i - \widehat{\boldsymbol{X}}^c$ related to the center point $\widehat{\boldsymbol{X}}^c$ and transform the components of the respective corner points $\left[\widehat{\boldsymbol{X}}^{cp}_i\right]$ from the global

coordinate system $\{X, Y, Z\}$ into the local coordinate system $\{\widehat{X}, \widehat{Y}, \widehat{Z}\}$ with the help of the following orthogonal transformation tensor $\boldsymbol{Q}^c$.

$$\boldsymbol{Q}^c = \sum_{i=1}^{3} \widehat{\boldsymbol{E}}_i^c \otimes \boldsymbol{E}_i^c \tag{5.12}$$

The main idea of the corrector step is now to assume that the crack surface can be represented by either a linear or a quadratic function in the local coordinate system.

$$\widehat{Z}^c = \begin{cases} a_0 + a_1\,\widehat{X} + a_2\,\widehat{Y} & \text{linear} \\ a_0 + a_1\,\widehat{X} + a_2\,\widehat{Y} + a_3\,\widehat{X}^2 + a_4\,\widehat{Y}^2 + a_5\,\widehat{X}\widehat{Y} & \text{quadratic} \end{cases} \tag{5.13}$$

The $j = 0, .., 5$ coefficients a_j in the local coordinate system follow then from solving the corresponding least square's problem. Thereby, $\widehat{Z}_i$ are the particular component of the local corner point $\widehat{\boldsymbol{X}}_i^{cp}$ in the $\widehat{\boldsymbol{E}}_3^c$ direction, whereas $\widehat{X}_i$ and $\widehat{Y}_i$ are the respective components in $\widehat{\boldsymbol{E}}_1^c$ and $\widehat{\boldsymbol{E}}_2^c$ direction.

$$\Phi^c(a_j) = \sum_{i \in \mathcal{I}^c} \left[\widehat{Z}_i - \widehat{Z}^c(a_j; \widehat{X}_i, \widehat{Y}_i) \right]^2 \rightarrow \min \tag{5.14}$$

Its solution introduces the following symmetric system of linear equations for both cases, the linear and the quadratic approach.

$$\sum_{i \in \mathcal{I}^c} \begin{bmatrix} 1 & \widehat{X}_i & \widehat{Y}_i & \widehat{X}_i^2 & \widehat{Y}_i^2 & \widehat{X}_i\widehat{Y}_i \\ & \widehat{X}_i^2 & \widehat{X}_i\widehat{Y}_i & \widehat{X}_i^3 & \widehat{X}_i\widehat{Y}_i^2 & \widehat{X}_i^2\widehat{Y}_i \\ & & \widehat{Y}_i^2 & \widehat{X}_i^2\widehat{Y}_i & \widehat{Y}_i^3 & \widehat{X}_i\widehat{Y}_i^2 \\ & & & \widehat{X}_i^4 & \widehat{X}_i^2\widehat{Y}_i^2 & \widehat{X}_i^3\widehat{Y}_i \\ & & & & \widehat{Y}_i^4 & \widehat{X}_i\widehat{Y}_i^3 \\ & & & & & \widehat{X}_i^2\widehat{Y}_i^2 \end{bmatrix} \begin{bmatrix} a_0 \\ a_1 \\ a_2 \\ a_3 \\ a_4 \\ a_5 \end{bmatrix} = \sum_{i \in \mathcal{I}^c} \begin{bmatrix} \widehat{Z}_i \\ \widehat{X}_i\widehat{Z}_i \\ \widehat{Y}_i\widehat{Z}_i \\ \widehat{X}_i^2\widehat{Z}_i \\ \widehat{Y}_i^2\widehat{Z}_i \\ \widehat{X}_i\widehat{Y}_i\widehat{Z}_i \end{bmatrix} \tag{5.15}$$

By construction, this element crack surface fits the existing corner points $\widehat{\boldsymbol{X}}_i^{cp}$ of the triangular and quadrilateral crack planes in a least-square sense. The coefficients a_j uniquely determine a smooth parametric representation of the crack surface and therefore, we obtain the following two tangent vectors at an arbitrary point on the crack surface since the axis $\widehat{Z}$ is always perpendicular to that surface.

$$\widehat{\boldsymbol{T}}_{\widehat{X}}^c = \widehat{\boldsymbol{E}}_1^c + \frac{\partial \widehat{Z}}{\partial \widehat{X}}\,\widehat{\boldsymbol{E}}_3^c \qquad \text{and} \qquad \widehat{\boldsymbol{T}}_{\widehat{Y}}^c = \widehat{\boldsymbol{E}}_2^c + \frac{\partial \widehat{Z}}{\partial \widehat{Y}}\,\widehat{\boldsymbol{E}}_3^c \tag{5.16}$$

With these tangent vectors $\widehat{\boldsymbol{T}}_{\widehat{X}}^c$ and $\widehat{\boldsymbol{T}}_{\widehat{Y}}^c$, we compute the local representation of the desired crack plane normal $\boldsymbol{N}^{crk}$ as the following vector product.

$$\boldsymbol{N}^{crk} = \widehat{\boldsymbol{T}}_{\widehat{X}}^c \times \widehat{\boldsymbol{T}}_{\widehat{Y}}^c \tag{5.17}$$

Then, we transform the components of the desired crack plane normal vector $\left[\boldsymbol{N}^{crk}\right]$ from the local coordinate system $\{\widehat{X}, \widehat{Y}, \widehat{Z}\}$ into the desired global coordinate system $\{X, Y, Z\}$ with the help of the mentioned orthogonal transformation tensor $\boldsymbol{Q}^c$. Note that in case of a linear surface description the resulting normal vector $\boldsymbol{N}^{crk}$ is patch-wise constant. In case of a quadratic surface description this vector would be evaluated at the local element connection point $\widehat{\boldsymbol{X}}^{crk}$.

Validation and implementation comments

Remark 5.3.5 (Continuity) *Please note that although the failure surface is fitted in a least squares sense for each element, the overall surface representation might eventually be non-continuous, i.e., by construction, the discontinuity surface $\boldsymbol{N}^{crk}$ is only $\mathcal{C}^{-1}$-continuous. The smoothing radius R^c takes the interpretation of a weighting parameter between the maximum principal stress direction $\boldsymbol{N}^{\sigma_{max}}$ on the one hand and the existing crack kinematics $\boldsymbol{X}_i^{cp}$ on the other hand.*

Remark 5.3.6 (Computational Cost) *Concerning the computational cost, we recall that all n_{tip} crack tip elements are stored in a dynamic crack tip list. For each crack tip element, we need to evaluate the point set $\mathcal{I}^c$ within the corresponding sphere of radius R^c. Technically, this set can be calculated and stored once when the mesh is initialized. Then, at each step, a 3×3 (respective 6×6) system needs to be solved for each of the n_{tip} elements. The computational effort is thus larger than for the previous local tracking algorithm but yet significantly smaller than for the global tracking algorithm to be discussed in the next section. However, from our personal experience, the non-local tracking algorithm is rather cumbersome and the complexity of its implementation is relatively high.*

Remark 5.3.7 (Crack deviation angle) *Additionally, for computational reasons, it proves reasonable to ensure that the crack plane normals $\boldsymbol{N}^{crk}$ between neighboring elements do not exceed a critical crack deviation angle in the same manner as for the average stress computation. This restriction is obviously of purely algorithmic nature but it can be used successfully to avoid spurious zig-zag type crack surfaces.*

Remark 5.3.8 (Non-local Averaging) *As for every non-local averaging scheme, the quality of the averaging procedure strongly relies on the number of crack points n^c within the averaging set $\mathcal{I}^c$. Clearly, a minimum amount of points is essential for the solution of the least squares problem which in turn crucially influences the quality of the crack tracking algorithm itself. Especially at the onset of cracking, when the number of averaging points is rather limited, it seems reasonable to turn off the averaging mechanism and only switch it on when a sufficiently large number of data points n^c is available.*

5.3.5. Global tracking

To ensure a unique $\mathcal{C}^0$-continuous representation of the discontinuity in crack propagation problems, OLIVER et al. [152, 153] have proposed a robust and yet very elegant strategy that can be incorporated into commercial finite element codes in a remarkably efficient fashion. Their initial idea has been adopted successfully to simulate discrete fracture, as far as we now, by CHAVEZ [57], DUMSTORFF & MESCHKE [55], CERVERA & CHIUMENTI [32] and FEIST & HOFFSTETTER [62, 61]. The key feature of OLIVER'S global tracking algorithm is to provide iso-surfaces $\mathcal{I}^\phi$ which in the discrete setting take the interpretation of element-wise planar iso-patches. These patches can be described by a function $\phi(\boldsymbol{X})$ whose level contours (or level sets), i.e., the collection of all patches of $\phi(\boldsymbol{X}) = \phi_{\mathcal{I}^\phi} = \text{const}$, define the corresponding iso-surface $\mathcal{I}^\phi = \{\boldsymbol{X} \in \mathcal{B}_0 \,|\, \phi(\boldsymbol{X}) = \phi_{\mathcal{I}^\phi}\}$. A particular iso-surface of constant value, e.g., the surface of level zero $\phi(\boldsymbol{X}) = 0$, is then the kinematic representation of the discrete failure

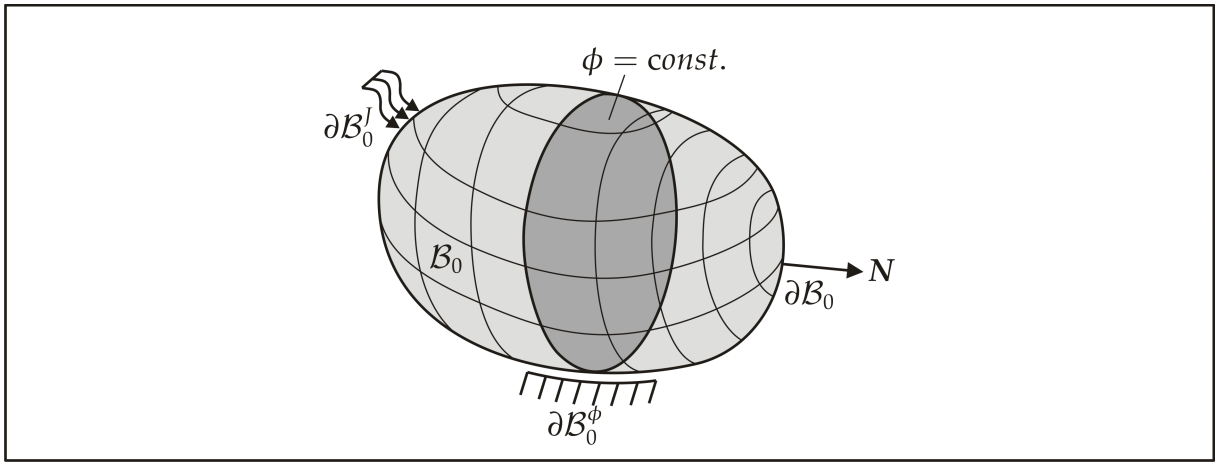

Figure 5.5.: Global tracking: Boundary value problem of body $\mathcal{B}_0$ with external boundary $\partial\mathcal{B}_0$ on which either DIRICHLET boundary conditions $\phi = \bar{\phi}$ or NEUMANN boundary conditions $\boldsymbol{J} \cdot \boldsymbol{N} = \bar{J}$ can be prescribed.

surface, see, e.g., figure 5.5. Conceptually speaking, the ultimate goal of the algorithm is to find the scalar field $\phi(\boldsymbol{X})$ whose level surfaces are envelopes of the patches defined by the following vectors $\boldsymbol{T}_2^{crk}$ and $\boldsymbol{T}_3^{crk}$, tangential to the propagating discontinuity plane. Thus, we use the remaining eigenvectors of the chosen principal stress based crack propagation criterion as the crack tangent vectors. In detail, we have ordered the eigenvalues of either the usual or the average principle stress based criterion as $\lambda^{\sigma_{max}} > \lambda^{\sigma_2} > \lambda^{\sigma_3}$. The two remaining spatial eigenvectors, $\boldsymbol{t}_2^{crk} = \boldsymbol{n}_2^{\sigma}$ and $\boldsymbol{t}_3^{crk} = \boldsymbol{n}_3^{\sigma}$, related to the mentioned second and third eigenvector span the crack plane in the spatial configuration. Accordingly, we use their following referential counterparts as the required material tangent vectors.

$$\boldsymbol{T}_2^{crk} = \frac{\boldsymbol{F}^{-1} \cdot \boldsymbol{t}_2^{crk}}{\left|\boldsymbol{F}^{-1} \cdot \boldsymbol{t}_2^{crk}\right|} \qquad \text{and} \qquad \boldsymbol{T}_3^{crk} = \frac{\boldsymbol{F}^{-1} \cdot \boldsymbol{t}_3^{crk}}{\left|\boldsymbol{F}^{-1} \cdot \boldsymbol{t}_3^{crk}\right|} \tag{5.18}$$

Clearly, just like in the previous non-local tracking strategy of section 5.3.4, these tangents to the discontinuity surface, here represented in the global coordinate system, obviously obey the orthogonality condition $\boldsymbol{T}_2^{crk} \cdot \boldsymbol{N}^{crk} = 0$ and $\boldsymbol{T}_3^{crk} \cdot \boldsymbol{N}^{crk} = 0$, or rather $\boldsymbol{N}^{crk} = \boldsymbol{T}_2^{crk} \times \boldsymbol{T}_3^{crk}$. More importantly, by construction, these patches are always orthogonal to the gradient of the iso-surface $\phi(\boldsymbol{X})$, thus $\boldsymbol{T}_2^{crk} \cdot \nabla_{\boldsymbol{X}}\phi = 0$ and $\boldsymbol{T}_3^{crk} \cdot \nabla_{\boldsymbol{X}}\phi = 0$. The multiplication of these conditions with $\boldsymbol{T}_2^{crk}$ and $\boldsymbol{T}_2^{crk}$, respectively, motivates the introduction of a the following referential flux vector.

$$\boldsymbol{J} = [\, \boldsymbol{T}_2^{crk} \otimes \boldsymbol{T}_2^{crk} + \boldsymbol{T}_3^{crk} \otimes \boldsymbol{T}_3^{crk} \,] \cdot \nabla_{\boldsymbol{X}}\phi \tag{5.19}$$

A reinterpretation of the above considerations in terms of the classical field equations defines an equilibrium condition as the vanishing divergence of this referential flux vector $\boldsymbol{J}$.

$$\mathrm{Div}\boldsymbol{J} = 0 \qquad \forall\, \boldsymbol{X} \in \mathcal{B}_0 \tag{5.20}$$

Moreover, it motivates a constitutive equation with the flux being a linear function of the gradient of $\nabla_{\boldsymbol{X}}\phi$.

$$\boldsymbol{J} = \boldsymbol{D} \cdot \nabla_{\boldsymbol{X}}\phi \qquad \forall\, \boldsymbol{X} \in \mathcal{B}_0 \tag{5.21}$$

The particular format for the mentioned anisotropic constitutive tensor $\boldsymbol{D}$

$$\boldsymbol{D} = \boldsymbol{T}_2^{crk} \otimes \boldsymbol{T}_2^{crk} + \boldsymbol{T}_3^{crk} \otimes \boldsymbol{T}_3^{crk} \tag{5.22}$$

ensures that the flux is restricted to the $\{\boldsymbol{T}_2^{crk}, \boldsymbol{T}_3^{crk}\}$-plane, i.e. it is always a weighted linear combination of the tangent vectors $\boldsymbol{T}_2^{crk}$ and $\boldsymbol{T}_3^{crk}$. Accordingly, the problem of finding iso-surfaces $\mathcal{I}^{\phi}$ is obviously a classical boundary value problem in terms of the field $\phi(\boldsymbol{X})$ characterized through an anisotropic LAPLACE type equation. Thus, the referential boundary $\partial\mathcal{B}_0$ can be subdivided into the disjoint parts $\partial\mathcal{B}_0 = \partial\mathcal{B}_0^{\phi} \cup \partial\mathcal{B}_0^{J}$ with $\partial\mathcal{B}_0^{\phi} \cap \partial\mathcal{B}_0^{J} = \varnothing$ on which either DIRICHLET boundary conditions $\phi = \bar{\phi}$ or NEUMANN boundary conditions $\boldsymbol{J} \cdot \boldsymbol{N} = \bar{J}$ can be prescribed, see again figure 5.5. We typically assume a flux-free boundary and apply homogeneous NEUMANN boundary conditions $\boldsymbol{J} \cdot \boldsymbol{N} = \bar{J} = 0$. Moreover, the DIRICHLET boundary conditions for the global tracking problem are of great importance for the desired failure simulation and therefore, we will discuss this issue more detailed later on in this chapter.

Remark 5.3.9 (Referential flux formulation) *We have defined a referential flux vector $\boldsymbol{J}$ which constitutively depends on the pull-back of the spatial principal stress directions. Clearly, it is also possible to define a spatial flux vector which directly depends on the principal stress directions of the respective* CAUCHY *stress tensor. Then, we can perform a pull-back of the spatial flux vector and we have likewise to solve a crack tracking problem. For the latter recomputed experiments of brittle failure in concrete this makes no difference due to the emerging small deformations setting. However, for future work, it may be of interest to evaluate the differences for a large deformation example like the later presented computations of faulting rocks.*

Discretization

First of all, the detailed elaborated elastic bulk problem and cohesive interface problem are inherently strongly coupled. Both however, are only weakly coupled to the mentioned crack tracking problem. In detail, we apply the elaborated, simultaneously solving of the elastic bulk and the cohesive interface problem and then we solve the following crack tracking problem in a post processing step. Therefore, as a prerequisite for a finite element formulation we perform a multiplication with an admissible test function $\delta\phi \in H_0^1$. Then, by integrating over the domain $\mathcal{B}_0$ and including the NEUMANN boundary conditions $\boldsymbol{J} \cdot \boldsymbol{N} = \bar{J}$, the equilibrium equation (5.20) is cast into the following referential weak form.

$$\delta\mathcal{W}_0^{\phi} = \int_{\mathcal{B}_0} \nabla_{\boldsymbol{X}}\delta\phi \cdot \boldsymbol{D} \cdot \nabla_{\boldsymbol{X}}\phi \,\mathrm{d}V - \int_{\partial\mathcal{B}_0^{J}} \delta\phi\, \bar{J} \,\mathrm{d}A = 0 \tag{5.23}$$

Similar to the deformation problem, we then apply the following standard linear interpolation of the iso-surfaces ϕ, the test function $\delta\phi$ and their gradients.

$$\begin{aligned} \phi &= \sum_{i=1}^{n_{en}} N_i\,\phi_i & \qquad \delta\phi &= \sum_{i=1}^{n_{en}} N_i\,\delta\phi_i \\ \nabla_{\boldsymbol{X}}\phi &= \sum_{i=1}^{n_{en}} \nabla_{\boldsymbol{X}} N_i\,\phi_i & \qquad \nabla_{\boldsymbol{X}}\delta\phi &= \sum_{i=1}^{n_{en}} \nabla_{\boldsymbol{X}} N_i\,\delta\phi_i \end{aligned} \tag{5.24}$$

With these approximations at hand, we assemble all elements of the structure as symbolized by the assembly operator $\overset{n_{el}}{\underset{e=1}{\mathbf{A}}}$. Subsequently, we express the whole referential discretization of the elaborated global tracking problem in the following virtual work format.

$$\delta\mathcal{W}_0^{\phi} = \overset{n_{el}}{\underset{e=1}{\mathbf{A}}} \delta\phi_i \Big[\int_{\mathcal{B}_0} \nabla_{\boldsymbol{X}} N_i \cdot \boldsymbol{D} \cdot \nabla_{\boldsymbol{X}} N_j\,\phi_j \,\mathrm{d}V - \int_{\partial\mathcal{B}_0^l} N_i\,\bar{J}\,\mathrm{d}A \Big] = 0 \tag{5.25}$$

Obviously, this latter format provides the following linear system of equation $\sum_{J=1}^{n_{np}} \mathsf{K}_{IJ}\,\phi_J = \mathsf{F}_I$ to solve for the crack tracking problem.

$$\begin{aligned} \mathsf{R}_I^{int} &= \mathsf{R}_I^{ext} \\ \mathsf{R}_I^{int} &= \overset{n_{el}}{\underset{e=1}{\mathbf{A}}} \int_{\mathcal{B}_0} \nabla_{\boldsymbol{X}} N_I \cdot \boldsymbol{D} \cdot \nabla_{\boldsymbol{X}} N_J\ \phi_J \,\mathrm{d}V = \sum_{J=1}^{n_{np}} \mathsf{K}_{IJ}\,\phi_J \\ \mathsf{R}_I^{ext} &= \overset{n_{el}}{\underset{e=1}{\mathbf{A}}} \int_{\partial\mathcal{B}_0^l} N_I\,\bar{J}\,\mathrm{d}A = \mathsf{F}_I \end{aligned} \tag{5.26}$$

Here, n_{np} are the total number of element nodes. Furthermore, the linear interpolation of $\phi(\boldsymbol{X})$ implies that the discrete iso-surfaces $\mathcal{I}^{\phi}$ take an element-wise planar representation, just like the failure surfaces in the local and non-local tracking schemes of sections 5.3.3 and 5.3.4. Clearly, once the mentioned discrete global linear system of equations is solved for the unknown field ϕ, the desired normal to the discontinuity surface $\boldsymbol{N}^{crk}$ follows from a straightforward post-processing procedure on the element level.

Boundary conditions

Next, we focus on the important issue of imposing boundary conditions for the additional field of unknowns ϕ. To guarantee the invertibility of the required system matrix the level of the iso-surfaces ϕ has to be prescribed at least at two initial points. However, fixing more than two points is likewise possible and accordingly, the physical interpretation, the understanding and the appropriate choice of DIRICHLET boundary conditions are the most essential ingredients of the global crack tracking scheme to ensure physically meaningful solutions. Therefore, we try to give the following overview of possible boundary conditions based on JÄGER et al. [101]. Prior to the overview, we emphasize that the set of boundary nodes for the linear crack tracking problem

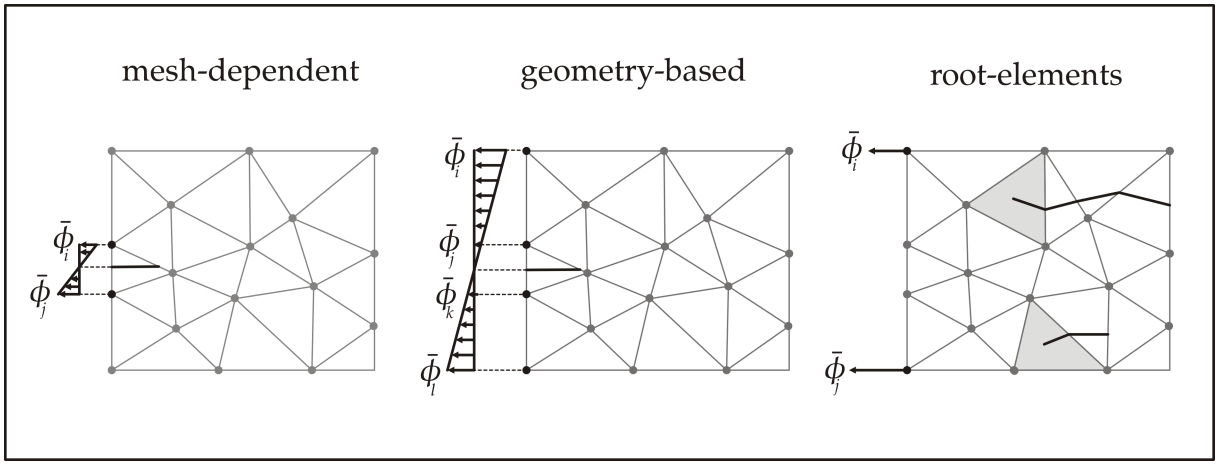

Figure 5.6.: Different types of crack onset boundary conditions for global tracking algorithms, clarified by means of the particular imposed values $\phi = \bar{\phi}$ and the respective crack onset.

increases during ongoing crack propagation to ensure the kinematical continuity of the crack tracking problem. This implies that we have to update the set of boundary conditions continuously during ongoing crack propagation. To this end, we add the actual ϕ values of the considered cracked elements at iteration step n to the set of fixed boundary conditions $\bar{\phi}_\phi$ at iteration step $n+1$ and solve the mentioned linear system of equations for the free ϕ_f values, symbolized in the following static condensation scheme with index f.

$$\begin{bmatrix} \mathsf{K}_{\phi\phi} & \mathsf{K}_{\phi f} \\ \mathsf{K}_{f\phi} & \mathsf{K}_{ff} \end{bmatrix} \begin{bmatrix} \bar{\phi}_\phi^n \\ \phi_f^{n+1} \end{bmatrix} = \begin{bmatrix} \mathsf{R}_\phi^{n+1} \\ \mathsf{R}_f^{n+1} \end{bmatrix} \tag{5.27}$$

This static condensation scheme once more clarifies that we further have to define initial boundary conditions to determine the crack onset during a fracture simulation. As advertised, we categorize the choice of possible initial boundary conditions in the sequel.

Mesh-dependent initial boundary conditions

The simplest way to define initial boundary conditions is to fix the ϕ values for the nodal values of a crack tip or the notch. In the case of tetrahedral elements, we thus have fixed at least three element nodes which are in fact enough to ensure that the linear system of equations for the global tracking field is solvable. Note that only the slope of the chosen start values, or the gradient of the respective field of start values, is important. If, e.g., the crack should start in the middle of the element, the chosen start values will be set to $\bar{\phi}_\phi^{initial} = \pm\alpha$, where α can be chosen arbitrarily. Theoretically, the crack surface value $\phi = \text{const.}$ that characterizes the crack surface can also be chosen arbitrarily, although we typically suggest $\phi = \text{const.} = 0$. Mesh-dependent boundary conditions are extremely useful in case of a single crack and with relatively simple meshes, as we will illustrate later in the chapter about the representative numerical examples. The fundamental drawback of mesh-dependent boundary conditions is that

they have to be adapted for each discretization to ensure crack onsets at the same geometric positions.

Geometry-based initial boundary conditions

To avoid the modifications of the boundary conditions for each mesh, we recommend a definition of the boundary conditions based on the geometry. This then allows to predetermine and fix the start values for the entire geometry. This procedure ensures that both, the onset of crack and the boundary conditions are the same for all different meshes. The first situation is extremely helpful for more demanding geometries. The latter issue is crucial to ensure symmetric initial boundary conditions in the case of more than one single crack, which we will also document later within this work with a representative numerical example. Moreover, similar to the previous class of boundary conditions, we can choose the crack surface value arbitrarily as $\phi = \text{const}$.

Root-element onset boundary conditions

Finally, a promising technique is the determination of crack onsets during crack propagation, see, e.g., OLIVER [152] or FEIST & HOFSTETTER [61]. This strategy allows the description of multiple crack propagation without having to pre-define particular initial boundary conditions for each crack surface. At detection of failure, we first check the minimal and maximal computed values of the crack tracking field for the considered element. Next, we check if a root element exists within this range. If so, we take the stored $\phi = \text{const}$. value for this root element. Otherwise we introduce a new root element and assign the $\phi = \text{const}$. value to the particular element center point. This procedure uniquely ensures C^0-continuity, for all possible crack surfaces and is more general than the one reported by ourselves, JÄGER et al. [99], where root elements are predefined. Although this approach seems to be the most general one, an essential drawback remains: By using finite elements as the root of crack propagation, it is obvious that the number of cracks will inherently depend on the number of elements. This disadvantage, however, can only be avoided by describing the complete crack surface independent of the finite element mesh.

Validation and implementation comments

Remark 5.3.10 (Continuity) *Since the global tracking algorithm introduces the discrete crack in terms of the scalar iso-surface value ϕ on the global level, its failure surface representation is inherently C^0-continuous, however, at the price of having to solve an additional global system of equations. This global continuous kinematic description has some advantages over the traditional approaches because it inherently avoids an ill-posedness of the stiffness matrix in a relatively simple manner. In detail, the ill-posedness of the stiffness matrix usually occurs if the crack surface strikes the vicinity of a element node and the resulting crack surface becomes very small. In the present approach based on a C^0-continuous scalar valued tracking function, however, we are able to control the minimum edge-length of the support of a node, i.e., all element edges connected to the considered node, by simply modifying the ϕ value of the concerned node.*

In particular the ϕ value is modified if the minimal edge length is less than 0.5% *which turned out to provide reasonable results.*

Remark 5.3.11 (Computational Cost) *The global tracking algorithm essentially relies on the assembly and solution of an additional global system of equations with one degree of freedom per node. In addition, a neighbor list needs to be initialized ab initio to evaluate average crack tip element values. The total computational cost of this algorithm is therefore the highest of all implemented algorithms discussed yet within this chapter. However, it should be emphasized that the global crack tracking algorithm is also the most flexible and most stable of all presented algorithms. Note that due to its modular nature, its implementation in commercial finite element codes is rather straightforward.*

Remark 5.3.12 (Invertibility of the anisotropy tensor) *Next, we take into account the invertibilty of the anisotropy tensor $\boldsymbol{D}$. For solving the discrete system of equations* (5.27)*, the global system matrix $\boldsymbol{K}$ needs to be inverted. Since the anisotropy tensor $\boldsymbol{D}$ introduced in equation 5.22 is rank deficient, we apply slight perturbations ε as $\boldsymbol{D} = \boldsymbol{T}_2^{crk} \otimes \boldsymbol{T}_2^{crk} + \boldsymbol{T}_3^{crk} \otimes \boldsymbol{T}_3^{crk} + \varepsilon \boldsymbol{I}$ to ensure that the overall system is solvable. For the sake of completeness we mention that we usually choose $\varepsilon = 10^{-4}$.*

Remark 5.3.13 (Integration into commercial finite element codes) *Although this algorithm has been termed global tracking algorithm it involves only local modifications on the element level. It is extremely attractive from a practical point of view since the scalar-valued global degrees of freedom ϕ can be treated as the temperature in* FOURIER*'s heat conduction or as the concentration in* FICK*'ian diffusion in any standard commercial finite element program. Moreover, the algorithm is in principle able to handle multiple cracking. Due to its computational simplicity, it is extremely robust, stable and highly efficient.*

5.3.6. Level set method

This method is presented for the sake of completeness since it has been applied successfully for the tracking of crack paths in linear elastic fracture mechanics in a two and a fully three-dimensional setting, compare, e.g., BELYTSCHKO et al. [19], CHESSA & BELYTSCHKO [33], STOLARSKA et al [192], BORDAS & MORAN [25], MOËS et al. [134], GRAVOUIL et al. [80] or SUKUMAR et al. [193]. This means that the further elaboration of the level set approach is only of theoretical nature. The level set method is usually used for the description of moving interfaces, a historic review and complete description can be found, e.g., SETHIAN [178]. The main idea of this concept in the framework of fracture simulations is the time-dependent EULERIAN description of the moving and evolving crack placements $\boldsymbol{X}^{\Gamma}(t) \in \mathcal{B}_0$ within the fixed reference configuration by two level set functions. The orientation of the crack surface is like as in the former global tracking algorithm given by a referential scalar valued function $\phi(\boldsymbol{X}^{\Gamma}(t), t)$ whose level contours $\mathcal{I}^{\phi} = \{\boldsymbol{X}^{\Gamma} \in \mathcal{B}_0 | \, \phi(\boldsymbol{X}^{\Gamma}(t), t) = \text{const.} \equiv 0\}$ represent the crack surface. Thereby, the zero iso-surface is chosen to be the kinematical representation of the crack surface. Additionally, the crack front is given by a further zero level contour of the so called crack front level set function $\chi(\boldsymbol{X}^{\Gamma}(t), t)$ with $\mathcal{I}^{\chi} = \{\boldsymbol{X}^{\Gamma} \in \mathcal{B}_0 | \, \chi(\boldsymbol{X}^{\Gamma}(t), t) = \text{const.} \equiv 0\}$. Hence, the complete description of the

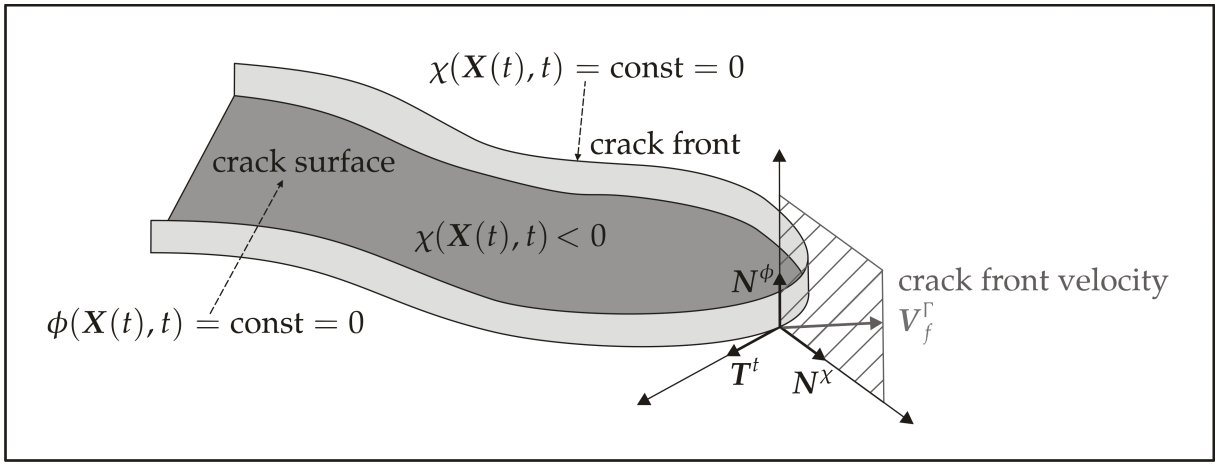

Figure 5.7.: Crack path description with level set functions and illustration of the inherent accompanying coordinate system with crack front velocity.

moving and evolving crack surface within the considered referential body $\mathcal{B}_0$ is given by the following expressions, compare also figure 5.7.

$$\begin{array}{llll} \boldsymbol{X}_s^{\Gamma} \in \mathcal{I}^{\phi} & \text{crack surface} & \phi(\boldsymbol{X}^{\Gamma}(t),t) \equiv 0 & \chi(\boldsymbol{X}^{\Gamma}(t),t) < 0 \\ \boldsymbol{X}_f^{\Gamma} \in \mathcal{I}^{\phi} \cap \mathcal{I}^{\chi} & \text{crack front} & \phi(\boldsymbol{X}^{\Gamma}(t),t) \equiv 0 & \chi(\boldsymbol{X}^{\Gamma}(t),t) \equiv 0 \end{array} \tag{5.28}$$

We emphasize that the crack front $\boldsymbol{X}_f^{\Gamma} \in \boldsymbol{X}^{\Gamma}$ is given by the intersection of the zero iso-surfaces of the two level set functions ϕ and χ, whereas the existing crack surface $\boldsymbol{X}_s^{\Gamma} \in \boldsymbol{X}^{\Gamma}$ is given for the zero iso-surface of the crack surface level set ϕ and negative crack front level set values χ. Clearly, the crack surface level set ϕ is usually not required for $\chi > 0$. However, for necessary crack extensions or crack front updates within a numerical fracture simulation the level set ϕ has to be defined in a certain region in front of the crack front, that means, for $\chi > 0$. This latter region in front of the crack front is called level set sub-domain $\mathcal{I}^{upd}$. It is further important that the two level set functions have to be orthogonal functions, i.e., $\nabla_{\boldsymbol{X}^{\Gamma}}\phi \cdot \nabla_{\boldsymbol{X}^{\Gamma}}\chi = 0$. Therefore, by ensuring that the level sets are orthogonal functions, the current crack front is always uniquely defined because it is impossible that the two level set functions provide the same tangent plane. Clearly, the following definition of an accompanying coordinate system of placements $\boldsymbol{X}^{\Gamma}$ of the complete current crack is useful, especially for placements of the current crack front $\boldsymbol{X}_f^{\Gamma}$.

$$\begin{array}{lll} \boldsymbol{N}^{\phi} = \dfrac{\nabla_{\boldsymbol{X}^{\Gamma}}\phi}{|\nabla_{\boldsymbol{X}^{\Gamma}}\phi|} & & \text{unit crack surface normal vector} \\ \boldsymbol{N}^{\chi} = \dfrac{\nabla_{\boldsymbol{X}^{\Gamma}}\chi}{|\nabla_{\boldsymbol{X}^{\Gamma}}\chi|} & & \text{unit crack front normal vector} \\ \boldsymbol{T}^{t} = \boldsymbol{N}_{\phi} \times \boldsymbol{N}_{\chi} & & \text{unit crack front tangent vector} \end{array} \tag{5.29}$$

Now, the key ingredient of the level set approach is the following definition of the crack front velocity $\boldsymbol{V}_f^\Gamma$ in the $\{\boldsymbol{N}_\phi, \boldsymbol{N}_\chi\}$-plane, see again figure 5.7.

$$\boldsymbol{V}_f^\Gamma = V^\phi \, \boldsymbol{N}^\phi + V^\chi \, \boldsymbol{N}^\chi \tag{5.30}$$

If it is possible to compute such a crack front velocity $\boldsymbol{V}_f^\Gamma$ by means of a possible fracture criterion, the evolution equation for the moving crack front can be formulated.

Remark 5.3.14 (Crack front velocity) *We mention that in* STOLARSKA *et al. [192],* MOËS *et al. [134] and* GRAVOUIL *et al. [80], a* PARIS *law is applied, whereby the rate of crack growth is connected to the load cycles and the load cycles itself were interpreted as a time like variable. For these linear elastic fracture approaches, the amount of the crack front velocity can be determined by the* PARIS *law, whereas the direction of the crack front velocity is given by a usual linear elastic crack propagation criterion, i.e., based on the computation of stress intensity factors via path-independent integrals, see, e.g.,* GOSZ *et al. [77, 78],* HUBER *et al. [95], or* SUKUMAR *et al. [194]. Up to now, we have not concentrated on finding a criterion which provides the crack front velocity in a complete non-linear framework. However, if this will eventually be possible in the future, this approach provides a great development potential, especially considering the inclusion of the partially cracked elements where knowledge about the crack front is required, compare section 3.4.4. Due to its potential and for the sake of completeness this approach is included in the comparison of crack path tracking approaches. For the following description of this approach we assume therefore that the current crack front velocity is known.*

Assuming that the crack front velocity is given, the evolution equation for the level set function is given by so called HAMILTON-JACOBI equations, compare, e.g., SETHIAN [178] or BURCHARD et al. [29]. Since $[\bullet](\boldsymbol{X}^\Gamma(t), t) = \text{const.} \equiv 0$ is required for a general level set function, the material time derivative needs to vanish, $D_t[\bullet] = \partial_t[\bullet](\boldsymbol{X}, t) = 0$, which provides the following general equations for the complete crack placements $\boldsymbol{X}^\Gamma$.

$$\begin{aligned} \frac{\partial \phi}{\partial t} + \nabla_{\boldsymbol{X}^\Gamma} \phi \cdot \frac{\partial \boldsymbol{X}^\Gamma}{\partial t} &= 0 \quad \forall \, \boldsymbol{X}^\Gamma \in \mathcal{B}_0 \\ \frac{\partial \chi}{\partial t} + \nabla_{\boldsymbol{X}^\Gamma} \chi \cdot \frac{\partial \boldsymbol{X}^\Gamma}{\partial t} &= 0 \quad \forall \, \boldsymbol{X}^\Gamma \in \mathcal{B}_0 \end{aligned} \tag{5.31}$$

In the latter equation (5.31), $D_t \, \boldsymbol{X}^\Gamma$ describes the material time derivative of the crack placements in the reference configuration and can be likewise expressed in the accompanying coordinate system. However, its is obvious that usually only the crack front velocity $D_t \, \boldsymbol{X}_f^\Gamma$ can be determined by crack propagation criteria. Accordingly, the evolution equations for the complete crack placements $\boldsymbol{X}^\Gamma$ are reduced to the evolution equation for the current crack front placements $\boldsymbol{X}_f^\Gamma$. Thus, regarding the accompanying coordinate system, compare again figure 5.7, the material time derivative of the crack front placement is given as $D_t \, \boldsymbol{X}_f^\Gamma = \dfrac{\partial \boldsymbol{X}_f^\Gamma}{\partial t} = V^\phi \, \boldsymbol{N}^\phi + V^\chi \, \boldsymbol{N}^\chi + V^t \, \boldsymbol{T}^t$. Exploiting the orthogonality of the accompanying base vectors, $\nabla_{\boldsymbol{X}_f^\Gamma} \phi \cdot D_t \, \boldsymbol{X}_f^\Gamma = \left| \nabla_{\boldsymbol{X}_f^\Gamma} \phi \right| V^\phi$ and $\nabla_{\boldsymbol{X}_f^\Gamma} \chi \cdot$

$D_t \boldsymbol{X}_f^\Gamma = \left|\nabla_{\boldsymbol{X}_f^\Gamma}\chi\right| V^\chi$ leads to a simplified projected formulation of the HAMILTON-JACOBI equations for the crack front placements.

$$\begin{aligned} \frac{\partial \phi}{\partial t} + \left|\nabla_{\boldsymbol{X}_f^\Gamma}\phi\right| V^\phi &= 0 \quad \forall \boldsymbol{X}_f^\Gamma \in \mathcal{B}_0 \\ \frac{\partial \chi}{\partial t} + \left|\nabla_{\boldsymbol{X}_f^\Gamma}\chi\right| V^\chi &= 0 \quad \forall \boldsymbol{X}_f^\Gamma \in \mathcal{B}_0 \end{aligned} \tag{5.32}$$

Clearly, by knowing the crack front velocity, the level set approach requires generally the solution of the latter HAMILTON-JACOBI equations of the crack front. Accordingly, a numerical solution procedure with finite elements and explicit time integration is usually applied which can be subdivided in the following four essential steps.

1. **Level set initialization and re-initialization**
   At first, a crack surface must be initialized for a fracture simulation. This is comparable to the formulation of boundary conditions for the global tracking field, see, section 5.3.5. However, in contrast to the global tracking problem, where the gradient of the additional field can be chosen arbitrarily, it is more suitable to ensure that the amount of the particular gradients of the level set functions becomes one, $\left|\nabla_{\boldsymbol{X}_f^\Gamma}\phi\right| = 1$ and $\left|\nabla_{\boldsymbol{X}_f^\Gamma}\chi\right| = 1$, respectively. If this can be ensured, compare remark 5.3.15 for the possibilities, the considered level set function is called a signed distance function. The signed distance function then provides the current distance of the actual crack front to a certain point in the fixed reference configuration. Accordingly, this initialization has to be performed for the initial level set values and additionally, has to be repeated prior to each update step which is called re-initialization.

2. **Orthogonal crack extension**
   The level set functions are approximated with the usual finite element shape functions, compare remark 5.3.16. Since this level set values are only available in the level set sub-domain of the former time or iteration step, the next step within the level set approach is the temporary orthogonal extension of the current crack in the level set sub-domain of the actual time or iteration step. In detail, the level set values of the current crack tip elements are interpolated. Subsequently, the temporary level set values ϕ^{tmp} and χ^{tmp} of the remaining elements within $\mathcal{I}^{upd}$ are computed with claiming $\nabla_{\boldsymbol{X}^\Gamma}[\bullet]^{tmp} \cdot \nabla_{\boldsymbol{X}_f^\Gamma}\phi = 0$ and $\nabla_{\boldsymbol{X}^\Gamma}[\bullet]^{tmp} \cdot \nabla_{\boldsymbol{X}_f^\Gamma}\chi = 0$, for each of the considered temporary level set functions ϕ^{tmp} and χ^{tmp}. This is a virtual crack extension along orthogonal lines of the current crack front, obviously, it always ensures $\nabla_{\boldsymbol{X}^\Gamma}\phi^{tmp} \cdot \nabla_{\boldsymbol{X}^\Gamma}\chi^{tmp} = 0$. A possible numerical procedure for the realization of this requirement is given in remark 5.3.17.

3. **Velocity formulation, orthogonal extension and modification**
   As mentioned, the velocity is assumed to be known at the current crack front placements. However, for the update of the temporary level set values ϕ^{tmp} and χ^{tmp} the velocity is needed in the whole level set sub-domain $\mathcal{I}^{upd}$. Therefore, it is suitable to formulate the velocity itself with higher dimensional functions.

This means that the vector components V^{ϕ} and V^{χ} are assumed to be given by two scalar valued velocity fields, approximated in the same manner as level set functions for the crack itself. Now, we can apply the same procedure as for the temporary crack level set values. In detail, the velocity fields of the current crack tip elements are interpolated and afterwards orthogonally extended to the remaining nodes within $\mathcal{I}^{upd}$. Thereby, we claim $\nabla_{\boldsymbol{X}^{\Gamma}}[\bullet] \cdot \nabla_{\boldsymbol{X}^{\Gamma}} \phi^{tmp} = 0$ and $\nabla_{\boldsymbol{X}^{\Gamma}}[\bullet] \cdot \nabla_{\boldsymbol{X}^{\Gamma}} \chi^{tmp} = 0$, respectively, for each of the extended velocities $V^{\phi,tmp}$ and $V^{\chi,tmp}$. Accordingly, the velocity fields are extended along orthogonal lines from the current interface. Therefore, the numerical solution procedure is comparable to the former orthogonal extension of the crack level set values which is explained in remark 5.3.17. We mention that this orthogonal velocity update matches the given velocity of the crack front and it would move the temporary crack level set functions while preserving the signed distance property, compare, e.g., SETHIAN [178] or ADELSTEINER & SETHIAN [1] for more details. However, within a fracture simulation, we have to ensure that the existing crack surface level set values, the ϕ values for $\chi < 0$, are frozen during the level set update. This means that we can take $V^{\chi,upd} = V^{\chi,tmp}$ as the update velocity since it evolves the crack, however, we have to modify the temporary crack surface velocity $V^{\phi,tmp}$. In detail, we can compute the value of the crack level set where the crack front is assumed to be at the end of the current time step, $\chi^{mod} = V^{\chi}\,\Delta t$, compare remark 5.3.16 for the time step computation. Now, with the use of the HEAVISIDE function, we adopt the velocity modification of GRAVOUIL et al. [80] and compute the updated crack surface velocity as $V^{\phi,upd} = \mathcal{H}(\chi)\, V^{\phi,tmp} \frac{\chi}{\chi^{mod}}$. This modification ensures that the crack surface velocity $V^{\phi,upd}$ becomes zero for $\chi < 0$, that means, for the existing crack surface. Furthermore, it linearly increases the crack surface velocity field $V^{\phi,upd}$ between the current crack front and the $\chi^{mod} = V^{\chi}\Delta t$ value, where the front is expected to be at the end of the level set update. Clearly, V^{χ} must be greater than zero because otherwise, the crack cannot grow and the updated crack surface velocity will impose a discontinuity in the update crack level sets.

4. **Level set update** The first update of the level set function regards the crack surface level set function ϕ^{upd} because this function governs the change in the crack orientation. All prerequisites are performed, that means, the temporary crack level set values ϕ^{tmp} and the updated velocity $V^{\phi,upd}$ are available at each finite element node within the level set sub-domain $\mathcal{I}^{upd}$. Thus, the main equation (5.32a) can be solved which provides the updated values ϕ^{upd}. Next, the crack front level set is updated. Accordingly, equation (5.32b) is solved to steady state based on the temporary values χ^{tmp} and the updated velocity $V^{\chi,upd}$. The result are updated crack front values χ^{tmp} which describe a crack extension in the interface direction. Therefore, after the crack surface level set is updated, a reinitialization of both level set functions as well as an orthogonalization of the χ^{upd} values with respect to the further computed ϕ^{upd} values is performed. This ensures that $\nabla_{\boldsymbol{X}^{\Gamma}} \phi^{upd} \cdot \nabla_{\boldsymbol{X}^{\Gamma}} \chi^{upd} = 0$ is never violated.

Remark 5.3.15 (Signed distance functions) *Level set functions are called signed distance functions if their gradients with respect to the associated space variable provides one,* $\left|\nabla_{\boldsymbol{X}^\Gamma}[\bullet]\right| = 1$. *There are different possibilities to accomplish this requirement. A simple ad hoc approach would require the computation of the distance in the particular gradient direction between the current zero level set value and each finite element node within the set* $\mathcal{I}^{upd}$. *This is also referred to as the closest point description and often used in a two-dimensional level set framework, see, e.g.,* VENTURA *et al. [201, 202] for a vector level set description. Another possibility is solving the eikonal equation ,*$\left|\nabla_{\boldsymbol{X}^\Gamma}[\bullet]\right| = 1$, *with the so called fast marching method, see, e.g.,* SUKUMAR *[193] or* SETHIAN *[179, 178]. Finally, also the solution of an additional partial differential equation* $D_t[\bullet] = sign[\bullet]\left[1 - \nabla_{\boldsymbol{X}^\Gamma}[\bullet] = 0\right]$, *for each of the level set functions, ensures the property of a signed distance function because steady state is reached for the time variable if* $\left|\nabla_{\boldsymbol{X}^\Gamma}[\bullet]\right| = 1$ *holds. Thereby,* $sign[\bullet]$ *denotes the signum function and the time within this equation is always a supporting pseudo time which is not connected to the mechanical problem. A more detailed elaboration can be found likewise in* PENG *[157],* CECIL & MARTHALER *[31],* GRAVOUIL *[80] or* SETHIAN *[178].*

Remark 5.3.16 (Time and space discretization) *For the solution of the mentioned* HAMILTON-JACOBI *equations a numerical solution with finite elements is usually applied in the related literature. In this manner, the unknown level set values are discretized with the usual finite element shape functions within the level set sub-domain* $\mathcal{I}^{upd}$, *i.e.,* $[\bullet]^{el}(\boldsymbol{X}, t) = \sum_i^{n_{en}} N_i(\boldsymbol{X})\,[\bullet]_i(t)$. *Furthermore, in* MOËS *et al. [134] and* GRAVOUIL *et al. [80] an explicit time integration procedure is recommended. In this case, a critical time step* Δt *has to be determined to ensure the* COURANT-FRIEDRICHS-LEWY *(CFL) condition. In detail, the critical time step for the crack level sets is determined as* $\Delta t = \min\{L^{el}_{0,j}/\left|V^\Gamma_f\right|\}$. *Here,* $L^{el}_{0,j}$ *being the referential finite element length of the smallest finite element within the level set update domain, to ensure that the crack moves at least through this considered element. It is noticeable that within fully dynamic fracture simulation and level sets, the time of the crack level set equations corresponds to the physical time of the problem, whereas for the sake of quasi-static fracture simulations, with the help of the* PARIS *law, the time becomes a pseudo time since the rate of crack growth is computed depending on a quasi-static problem.*

Remark 5.3.17 (Level set orthogonalization) *For the orthogonal extension of the crack level sets and the velocity fields and additionally, to ensure the orthogonality between the crack level set functions after the update process, an orthogonalization is required. In* GRAVOUIL *et. [80],* DUFLOT *[51],* PENG *et al. [157] and* BURCHARD *et al. [29], an orthogonalization process based on a further additional* HAMILTON-JACOBI *equation is recommended. This approach can be used for any of the required orthogonalizations. In general, we assume that the gradient of the desired scalar valued function* $\nabla_{\boldsymbol{X}^\Gamma}[\bullet]$ *should be orthogonal to the gradient of a further scalar valued function, e.g.,* α. *Thus,* $D_t[\bullet] + sign(\alpha)\,\dfrac{\nabla_{\boldsymbol{X}^\Gamma}\alpha}{\left|\nabla_{\boldsymbol{X}^\Gamma}\alpha\right|} \cdot \nabla_{\boldsymbol{X}^\Gamma}[\bullet] = 0$, *ensures the orthogonality because if this equation is brought to steady state,* $\nabla_{\boldsymbol{X}^\Gamma}\alpha \cdot \nabla_{\boldsymbol{X}^\Gamma}[\bullet] = 0$. *Thereby, the sign function ensures that the* $[\bullet]$ *values are only changed with keeping the desired zero level set value constant. Obviously, as for the initialization and re-initialization, the time for this auxiliary equation is always a pseudo time like variable.*

Validation and implementation

Remark 5.3.18 (Continuity) *Due to the failure surface representation with scalar valued level set functions and its suitable approximations with the usual $\mathcal{C}^0$-continuous finite element shape functions, the failure surface approximation is $\mathcal{C}^0$-continuous.*

Remark 5.3.19 (Computational cost) *Since the presentation of the level set method is of rather theoretical nature, we can only comment on the expected computational effort. In the author's view, the computation of the finite element nodes within the chosen level set sub-domain $\mathcal{I}^{upd}$ is comparable to the computation of the integration points within the averaging sphere for the non-local crack path tracking, compare remark 5.3.6. Furthermore, the initialization and re-initialization and the presented orthogonalization processes require the solution of the presented* HAMILTON-JACOBI *equations. This seems to be a lot of effort, however, the chosen solution procedure for the implementation can be used for all* HAMILTON-JACOBI *equations by substituting the particular* HAMILTONIAN*, compare, e.g.,* SETHIAN *[178]. Thus, the computational effort ultimatively depends on the size of the level set domain $\mathcal{I}^{upd}$ but it is less than the one for the global tracking algorithm. In contrast, the implementational effort is comparable to the one of the non-local tracking scheme. This means that the implementation of the four steps until the level set update is reached is more complex than the modular global tracking. However, by applying this approach the position of the crack front is additionally provided.*

5.3.7. Discussion and comparison

With neglecting the average stress criterion as a crack path tracking algorithm, five conceptually different strategies for the algorithmic treatment of three-dimensional failure phenomena have been discussed. All five schemes are essentially based on a purely deformation based HANSBO-type finite element interpolation of the discrete failure surface. Although they apply a discretization that is slightly different from the one applied in classical extended finite element schemes, the five different crack tracking strategies underlying the four algorithms could equally well be combined with the extended finite element method as such. Table 5.2 summarizes the outcome of the comparative analysis in terms of computational cost, generality and crack surface continuity.

tracking	**crack plane normal**		**crack surface**		**continuity**	
fixed	prescribed	-	a priori known	-	$\mathcal{C}^{-1}/\mathcal{C}^0$	+
local	neighbor dependent	+	planar/slightly kinked	-	$\mathcal{C}^0$	+
non-local	non-locally averaged	-	slightly curved	+	$\mathcal{C}^{-1}$	–
global	unknown dof $\in \mathcal{B}_0$	-	arbitrarily shaped	+	$\mathcal{C}^0$	+
level sets	unknown dof $\in \mathcal{I}^{upd}$	○	arbitrarily shaped	+	$\mathcal{C}^0$	+

Table 5.2.: Comparison of fixed, local, non-local, global crack tracking scheme and level sets in terms of computational cost, generality and crack surface continuity.

First of all, we would like to state that four of the five strategies have been applied successfully to produce mesh-independent results, i.e., provided the underlying discretization is sufficiently fine, the algorithmic response does not become more brittle

with increased mesh refinement. As expected, the fixed crack tracking turned out to be the computationally cheapest and most robust technique to capture discrete failure. It is able to capture $\mathcal{C}^0$-continuous planar and curved crack paths provided that the failure surface is known a priori. For problem classes with predefined weak material interfaces, joints or welding zones, the fixed tracking strategy should, of course, be the method of choice. For problem classes in which the propagating discontinuity surface is not known a priori but rather a part of the solution itself either the local, the non-local, level sets, or the global crack tracking strategy can be applied. Ideally, the failure surface should then be a function of the stress state, e.g., the crack plane normal could be chosen as the eigenvector related to the largest eigenvalue of either the local or the non-local CAUCHY stress. For two-dimensional crack propagation phenomena, a purely stress driven crack propagation criterion seems to be the natural choice since it renders a unique smooth crack surface. In that sense, the local crack tracking algorithm can be interpreted as the three-dimensional counterpart of most existing two-dimensional crack propagation schemes. The crack is treated locally as an extension of the existing crack surface on the element level. Starting from the crack intersection points of the neighboring element, the crack propagates smoothly based on the principal stress direction with slight adjustments based on the neighboring crack points. It is quite obvious that this local crack tracking strategy always produces $\mathcal{C}^0$-continuous failure surfaces at extremely low computational cost. Unfortunately, however, these surfaces might eventually be over-constrained in the case of too many pre-existing neighbor crack points. Accordingly, the failure surface typically hardly deviates from a planar or slightly kinked crack path and the structural stiffness would be severely overestimated. In summary, if the failure surface is expected to be rather planar or only slightly kinked, we would advise to use the stable, cheap and robust local crack tracking scheme.

In all other cases, a non-local or global tracking scheme should be applied. To be able to predict failure surfaces of arbitrary shape, the discrete failure surface introduced on the element level essentially needs to incorporate information of the surrounding elements. Within a finite element setting, there are two fundamentally different ways to carry information of a certain neighborhood to the element or rather the integration point level. The first method smoothes the failure surface in a least squares sense based on the non-locally averaged information within a certain neighborhood. This method is local in the sense that it does not introduce additional global degrees of freedom. Accordingly, however, the generated failure surfaces might show slight jumps at the inter-element boundaries. The non-local crack tracking scheme might be computationally cheaper than the global one since it does not rely on the solution of an additional system of equations. Nevertheless, its underlying algorithmic changes are quite cumbersome and integration into commercial finite element codes would require sophisticated modifications on the integration point level, on the element level and on the system level. An alternative strategy that is somewhat more tailored to the notion of finite elements is the global crack tracking scheme. At the expense of introducing an additional scalar-valued field of unknowns and having to invert the related system matrix, the global tracking scheme is the only one that really combines advantages of all the previous schemes. It is robust and stable, it is able to reliably capture smooth,

curved, arbitrarily shaped C^0-continuous failure surfaces and it is straightforwardly integrable into commercial finite element codes. The level set method is at first glance comparable with the global tracking due to the equal description of the crack surface with a scalar valued function. However, within the level set method the crack surface is only computed within a domain around the current crack front. In contrast to the global tracking algorithm the level set method provides the position about the current crack front, however, this approach requires the current crack front velocity. Finally, we are convinced that the description of the crack surface with scalar valued level set functions is the method of choice within finite element fracture simulations. Thereby, the global crack tracking strategy is the most general of all analyzed schemes in the notation of finite elements. However, both latter approaches, the global tracking as well as the level set approach are applicable in all cases where the failure surface is not known a priori and not necessarily expected to be planar.

5.4. Numerical Examples

A comprehensive series of numerical benchmark tests for all four schemes has been performed but only two illustrative benchmarks will be presented within this chapter. In detail, a rectangular block is subjected to different load cases to provide a planar and a curved crack path situation based on our works, compare JÄGER et al. [102, 100].

5.4.1. Rectangular block under tension - straight crack

The pictured rectangular block has a square cross section of $1[\text{mm}^2]$ and a height of height $2[\text{mm}]$, compare figure 5.8. The block is fixed on the bottom and loaded by 60 incremental displacement steps of $0.01[\text{mm}]$ until a deformation of $0.6[\text{mm}]$ is reached. Failure is initialized on one side of the specimen. The material parameters for the bulk are $\lambda = 576.90[\text{N/mm}^2]$ and $\mu = 384.60[\text{N/mm}^2]$ which is equal to $E = 1000[\text{N/mm}^2]$ and $\nu = 0.3[\text{-}]$. We use the exponential softening relation and the interface parameters are $G_f = 100[\text{N/mm}]$ and $f_t = 200[\text{N/mm}^2]$ as well as $E_t = 0[\text{N/mm}^2]$ and $E_c = 200000[\text{N/mm}^2]$ for the tangential direction and the contact stiffness, respectively. In order to compare the described tracking algorithms the computations are carried out with two structured meshes consisting of 4410 (1024 nodes) and 10501 (2662 nodes) elements. For the crack path tracking algorithms we apply the average stress computations for all presented algorithms, with $R^\sigma = 2\,L_0^{el}$ for the averaging sphere. The radius of the sphere for the non-local tracking algorithm is chosen as $R^c = 2\,L_0^{el}$. Furthermore, we have chosen mesh-dependent boundary conditions for the global tracking problem. In detail, we have fixed the upper and lower values of the crack onset element to $\bar{\phi} = \pm 1$. Subsequently, we discuss the computational results. As soon as the critical stress state is reached, the crack propagates through the specimen perpendicular to the loading direction as expected. The complete separation of the two emerging blocks is slowed down by the applied cohesive tractions. This means that an initially elastic behavior can be observed before the critical load is reached. Afterwards, the load decreases exponentially with increasing crack opening, compare the load displacement response and the series of deformation snapshots in figure 5.8.

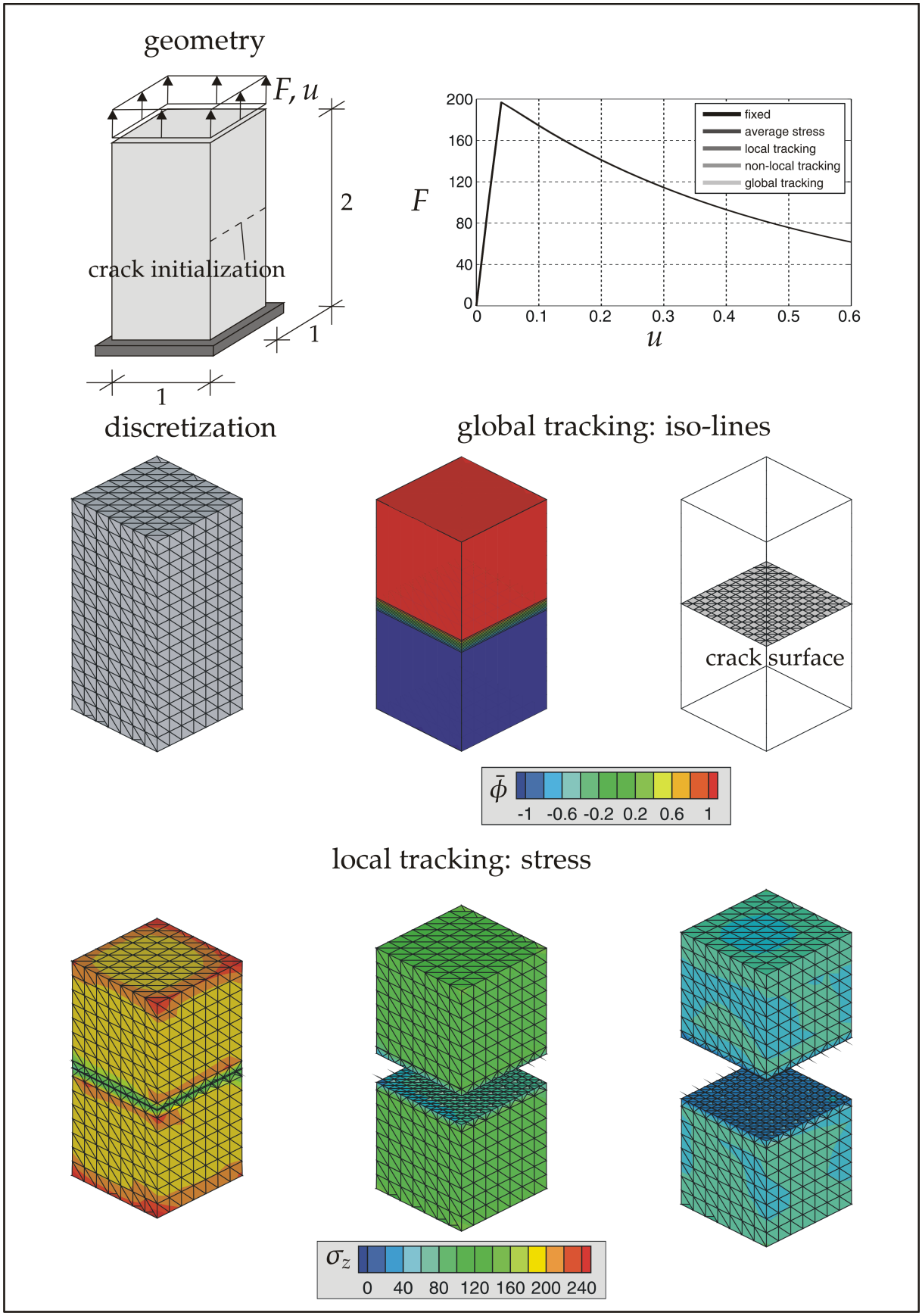

Figure 5.8.: Top: geometry $[\text{mm}]$, loading and load displacement response $F[\text{N}]$ versus $u[\text{mm}]$. Center: Discretization with 4410 elements and iso-lines with zero iso-surface illustration for global tracking algorithm. Bottom: Deformed configuration with plotted stress $\sigma_z[\text{N}/\text{mm}^2]$ in loading direction for imposed displacements $u = 0.05[\text{mm}]$, $u = 0.3[\text{mm}]$ and $u = 0.6[\text{mm}]$.

The results are in good agreement with MERGHEIM [125] and MERGHEIM et al. [128], where this example is computed with the fixed tracking algorithm. Obviously, the solutions are mesh-independent, the curves of the different computations feature nearly the same values regarding the chosen visualization accuracy for the load displacement response. Furthermore, the structural response is independent of the applied tracking algorithm for this simple straight crack example. Nevertheless, this equivalence holds only for the load displacement response relation and not for the smoothness of the crack surface. Here, the fixed tracking, the local tracking and the global tracking provide a totally smooth crack surface, whereas the crack surface computed only with average stresses exhibits jumps at the element boundaries which become smaller when applying the non-local tracking algorithm. Thereby, for the non-local tracking algorithm only a linear approximation of the crack surface is applied. Figure 5.8 also illustrates the iso-lines on the outer boundary and the computed iso-surface of the global tracking algorithm. Finally, this example has shown that a straight crack can be computed without a tracking algorithm by the computation with the average stress criterion. However, this holds only for structured meshes where the explained problems with the jumps at the inter-element boundaries can be inherently avoided by carefully mesh construction. The next example will highlight that this is only possible for special cases. Furthermore, this example has shown that all of the presented tracking algorithms are able to capture this simplest case of a straight crack.

5.4.2. Rectangular block under tension - curved crack

Next, we discuss the computation of a curved crack through the rectangular block. The complete setup, that means, the geometry, the material parameters, the tracking parameters and the discretization are equal to the former example with a straight crack. Only the loading conditions differ, the incremental displacement of $0.01\,[\mathrm{mm}]$ is only applied on the edge of the crack initialization side to construct a curved crack situation, see figure 5.9. It is noticeable that for the computation of this example with the non-local tracking strategy an initial crack surface is needed, compare remark 5.3.8. Accordingly, we have fixed the crack plane normal for the first row of initially cracked elements. This is further done for all applied methods for the sake of comparison. Subsequently, we discuss the results for the different tracking algorithms. We emphasize that a computation using only average stresses is no longer possible since the jumps at the inter-element boundaries lead to the mentioned problems during the classification of the additional nodes, compare remark 5.3.1. Furthermore, the limit of the local crack criterion is met after the crack has propagated two thirds of the specimen, i.e., the intersection points of the adjacent elements no longer lie within one plane. Thus, the example is completely computed for the fixed tracking, the non-local tracking and the global tracking algorithm, compare figure 5.10. Thereby, for the fixed tracking algorithm we use an imposed parabolic crack path to re-produce the results of the other two approaches. For the non-local tracking strategy, we further observe jumps at the inter-element edges, however, less small due to the applied smoothing. This allows us the computation for the presented discretization, however, we cannot exclude that the same restriction as for the average stresses will occur for other meshes with mesh

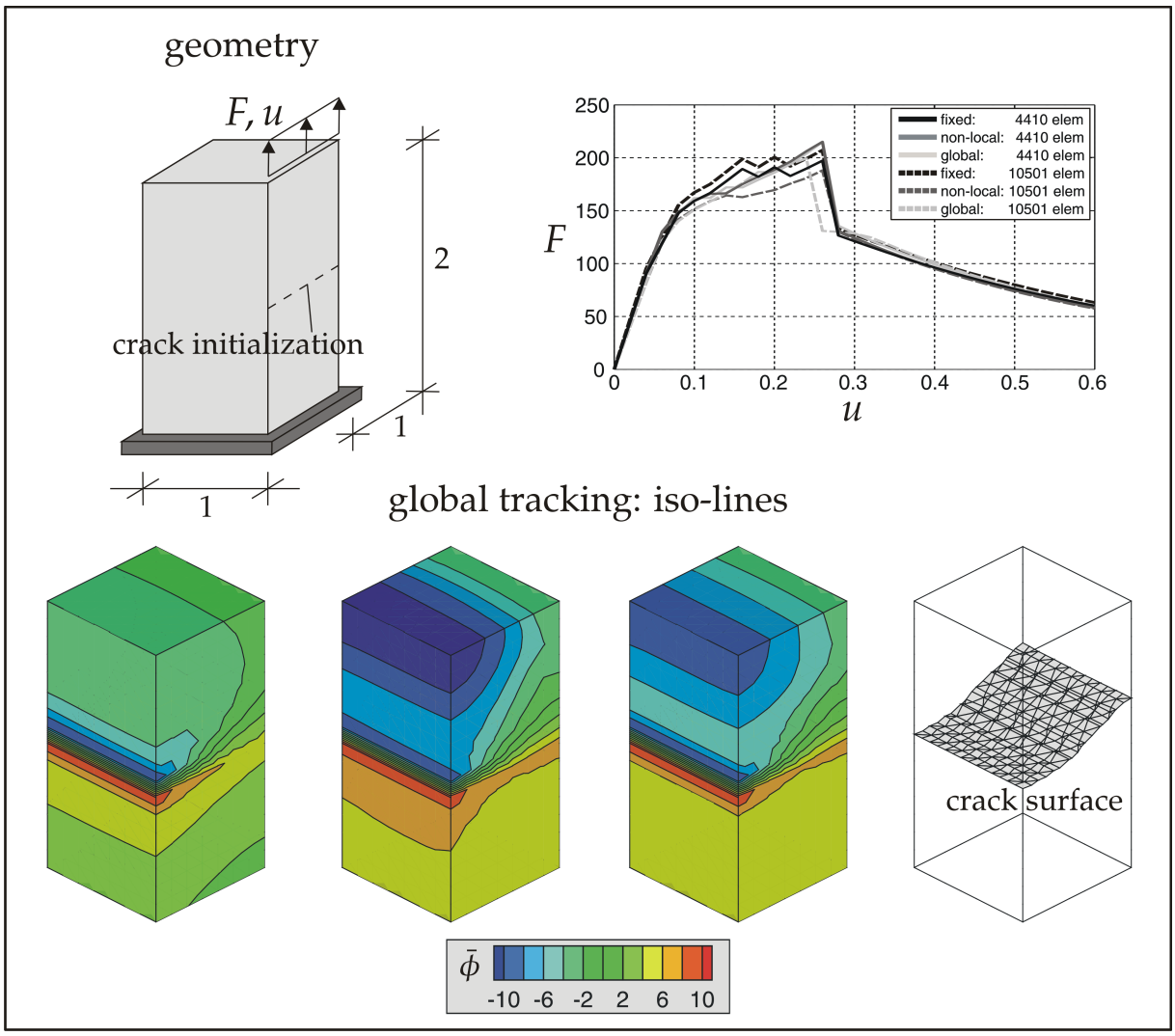

Figure 5.9.: Top: geometry [mm], loading and load displacement response F[N] versus u[mm]. Center: Plot series of iso-lines for global tracking algorithm for imposed displacements $u = 0.1$[mm], $u = 0.2$[mm], $u = 0.6$[mm] and zero iso-surface illustration.

refinement. For the global tracking algorithm we have again used mesh-dependent initial conditions, the values for the crack surface function are set to $\bar{\phi} = \pm 10$ for the crack onset element. The crack path is inherently $\mathcal{C}^0$-continuous and is illustrated by means of the iso-lines at the outer boundary and the referential iso-surface, compare figure 5.9. The load displacement curves for the three applied algorithms are depicted in figure 5.9. It is important to note that this example is only a benchmark construction for a curved crack situation. Clearly, this example has again no physical background. Therefore, also the load displacement response is rather of theoretical nature. In detail, we observe a loading drop until the maximum displacement is reached. This occurs when the block reaches equilibrium after it completely breaks into two parts. The load displacement response is comparable for the different tracking approaches, that means, the results are identical for the presented strategies. Accordingly, this benchmark has suitably illustrated the ability to capture a curved crack for the different crack path tracking algorithms.

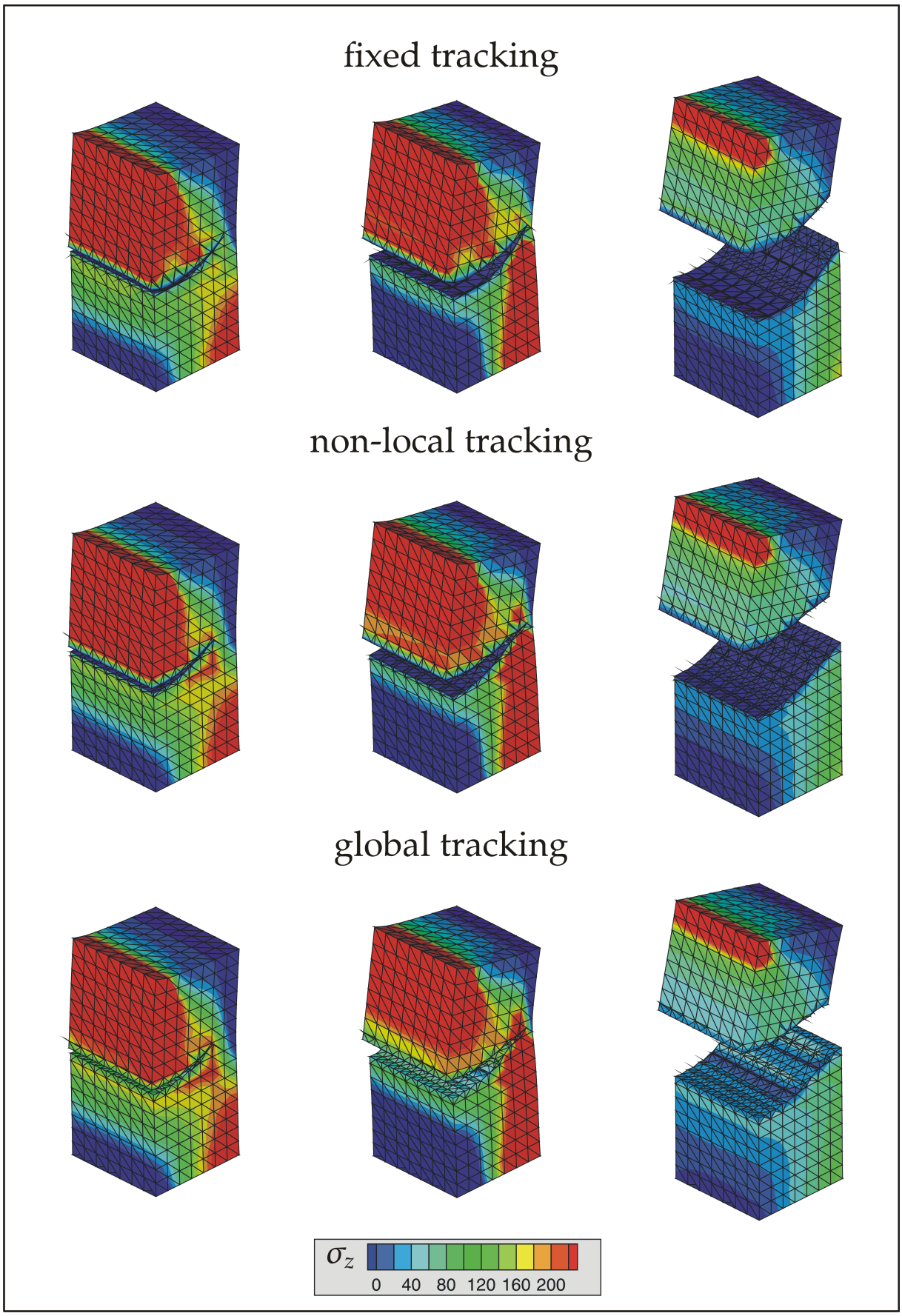

Figure 5.10.: Contour plot series for stress $\sigma_z\,[\mathrm{N/mm^2}]$ in loading direction for imposed displacements $u = 0.1\,[\mathrm{mm}]$, $u = 0.2\,[\mathrm{mm}]$, $u = 0.6\,[\mathrm{mm}]$ and the different crack path tracking algorithms.

6. Representative numerical examples

6.1. Motivation

Brittle or quasi-brittle fracture is characterized by an abrupt collapse of the considered material or structure. This characteristic behavior takes place when a material reaches the limit of its strength and no plastic deformation can be observed prior to failure. This kind of failure ranges from materials like shattered glasses or ceramics over concrete to faults formed in the crust of the earth. It has recently drawn increasing attention in the context of safety and reliability of concrete buildings, bridges, storage containers, and other engineering structures subjected to high impact loading or explosion.
Many experimental results as well as comparative computations are available for brittle fracture in concrete, see, e.g., GÁLVEZ et al. [68, 67] et al., GEERS et al. [76] or SANCHO et al. [170, 172, 171]. Therefore, we firstly verify our finite element tool to capture the failure behavior in this engineering material. This part is mainly based on JÄGER et al. [101]. We emphasize that this concrete examples could actually be computed with a geometrically linear small strain formulation. However, these examples are tailored to address the following aims: (i) to validate the proposed finite element tool in terms of well-documented experimental benchmark problems, (ii) to compare the algorithmic performance in relation to existing algorithms in the literature, and (iii) to illustrate the choice of boundary conditions for the additional field of the chosen global tracking problem.
Afterwards we focus on the modeling of brittle fracture in folding rocks, which obviously requires the chosen geometric non-linear formulation. Since we found no previous numerical studies of this issue, we have designed our own benchmark problem for the modeling of brittle failure in folding rocks, compare JÄGER et al. [99]. Thereby, we account for multiple crack surfaces and accordingly, we again discuss the required boundary conditions for the crack tracking field with multiple fracture simulations.

6.2. Brittle concrete fracture

The numerical treatment of tensile dominated brittle fracture of concrete has been under extensive research interest in the past decade, see, e.g., GEERS et al. [76], RUIZ et al. [168], OLIVER et al. [152], GASSER [69], FEIST & HOFSTETTER [63, 62] or SANCHO et al. [170, 172, 171]. Here, tensile dominated failure refers to degradation phenomena in which the tensile failure patterns can be regarded as dominant over shear failure which, in turn, is common in metallic materials. As a first approximation to this so called mixed mode failure, fracture parameters for the opening case (mode I) can be used if the shear to tension ratio is moderately small. As soon as the shear stress becomes dominant, shear friction and aggregate interlocking can no longer be neglected. Tensile failure of concrete involves progressive microscopic cracking, debonding and

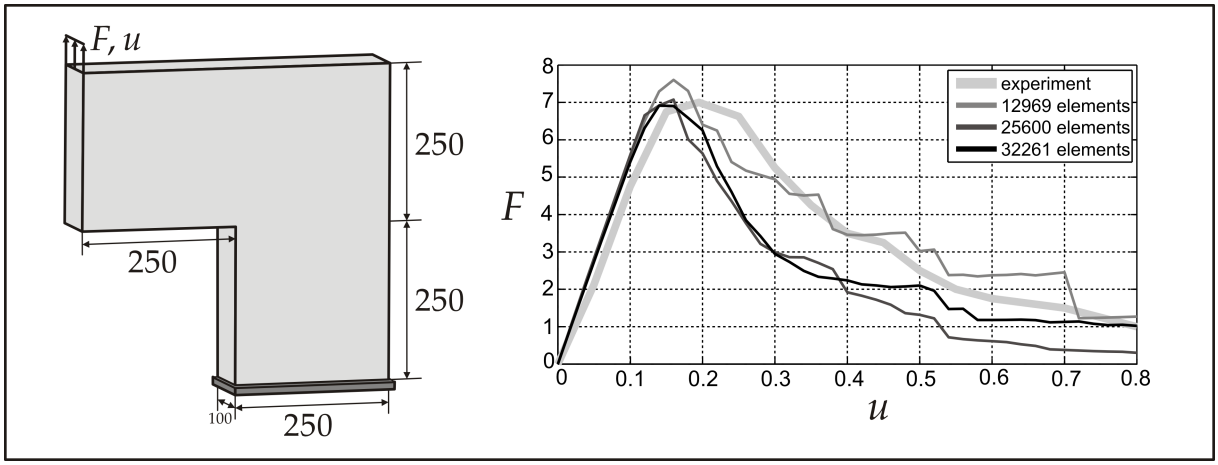

Figure 6.1.: Left: Geometrical dimensions [mm] and applied loading. Right: Load displacement response F[kN] versus u[mm].

other complex irreversible processes of internal damage. The associated softening can coalesce into a discontinuity that separates the material. To verify that the presented discrete crack concept combined with an appropriate cohesive zone model can reflect these phenomena, we perform the following computations based on the well-documented experimental data.

6.2.1. L-shaped Panel

The first example is an L-shaped concrete panel. The geometry and the loading conditions can be found in figure 6.1 on the left. This geometry was elaborated experimentally by WINKLER et al. [208, 209]. Comparative discrete failure simulations of this benchmark problem can be found, e.g., in DUMSTORFF & MESCHKE [55], or DUMSTORFF [54], however, their analysis is restricted to a two-dimensional setting. Furthermore, a computation based on a damage formulation can be found in, e.g., HUND [96]. The domain is discretized with three different meshes. One structured mesh with 12969 (2886 nodes) tetrahedral elements and two unstructured meshes with 25600 (6237 nodes) and 32261 (6472 nodes) tetrahedral elements, respectively. The chosen bulk material parameters are $E = 25850[\mathrm{N/mm^2}]$ and $\nu = 0.18[\text{-}]$. We use the direct exponential traction separation formulation with $G_f = 0.065[\mathrm{N/mm}]$ and $f_t = 2.7[\mathrm{N/mm^2}]$. The contact stiffness is chosen as $E_c = 200000[\mathrm{N/mm^2}]$. The load is applied incrementally through displacement control, i.e., the upper left row of nodes is displaced by $u = 0.02[\mathrm{mm}]$ in 40 load steps each. The corresponding load displacement curves and the reference solution of the experimental investigation are displayed in figure 6.1 right. For the boundary conditions of the global tracking problem we choose the mesh dependent case. That implies that we define the onset of crack propagation in the top element of the bottom margin for the discretization with 32261 elements. We choose the boundary conditions to $\bar{\phi} = \pm 100$, compare figure 6.2 on the right hand side of the top. Clearly, we have to modify the boundary conditions for the other two meshes, to ensure the same initial crack onset conditions for each of the three cases. In detail, we fix the value of 100 on the upper side of the element and com-

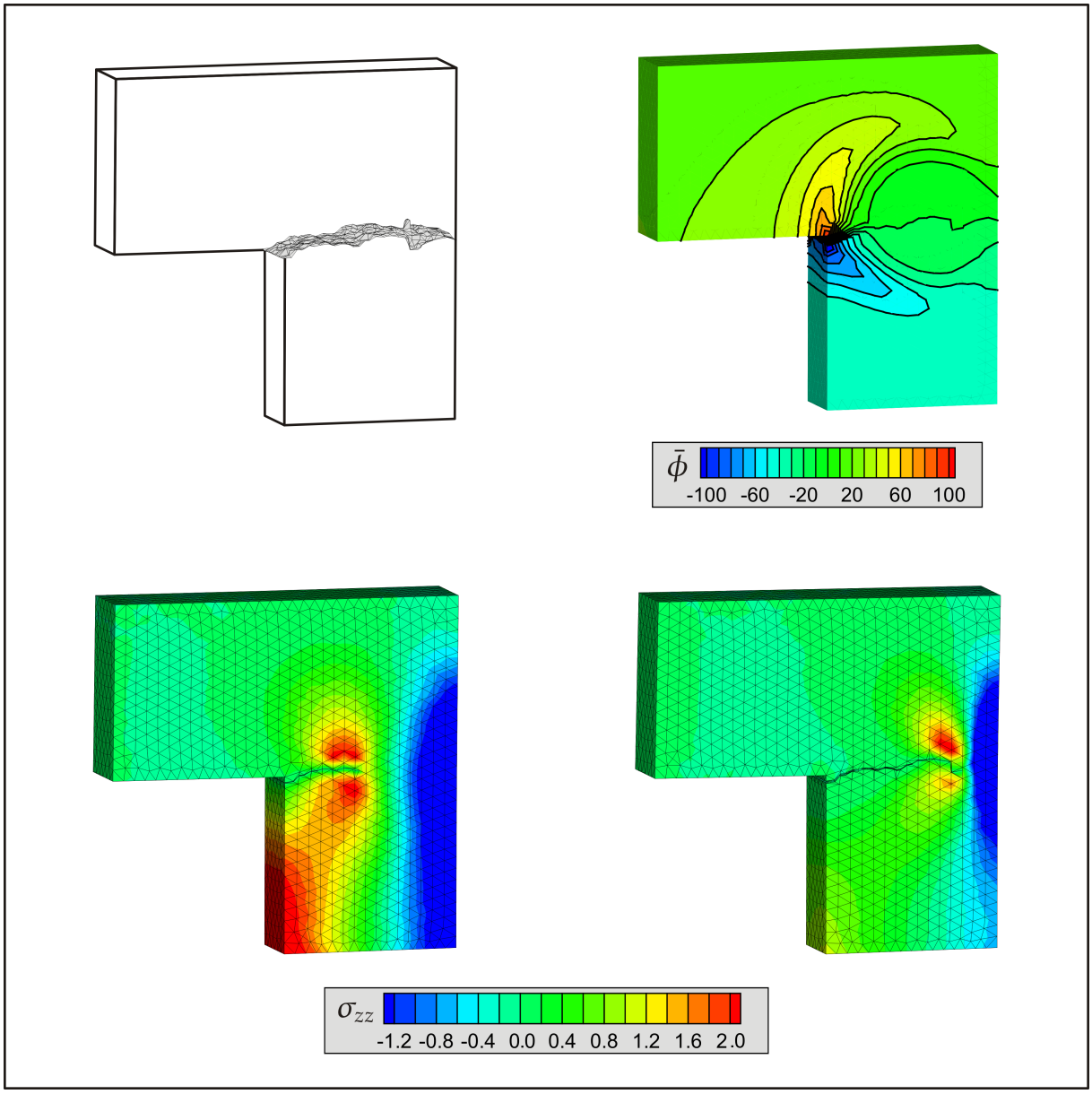

Figure 6.2.: Top: Potential crack surface and iso-surfaces for an imposed displacement of $u = 0.8[\text{mm}]$. Bottom: Contour plot of stress distribution $\sigma_{zz}\,[\text{N}/\text{mm}^2]$ in loading direction for imposed displacements $u = 0.2[\text{mm}]$ and $u = 0.4[\text{mm}]$.

pute the lower value with regard to the known crack starting position. The solution is truly mesh independent and in remarkably good agreement with the experimental reference curve, compare figure 6.1. Figure 6.2 on the right hand side shows the stress distribution plotted on the deformed configuration. The displayed analysis is based on the discretization with 32261 linear tetrahedral elements and shows the results of load steps 10 and 20, i.e., at an applied deformation of $u = 0.2[\text{mm}]$ and $u = 0.4[\text{mm}]$, respectively. By means of the iso-lines on the outer boundary of the L-shaped panel, figure 6.2 also shows how the crack propagates smoothly to the right edge of the specimen as the load is increased. Additionally, figure 6.2 displays the crack surface, or rather the zero iso-surface, for an imposed displacement of $u = 0.08[\text{mm}]$.

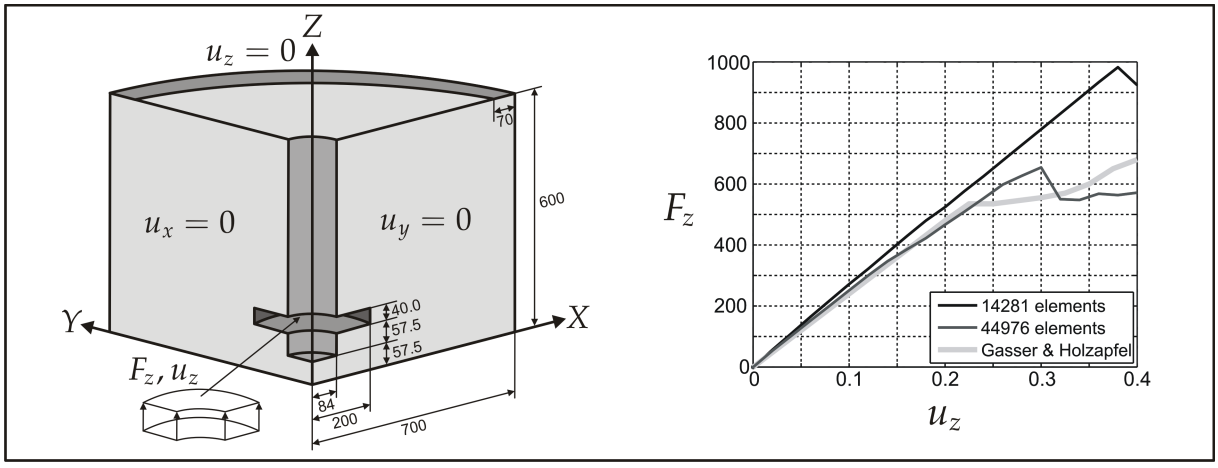

Figure 6.3.: Left: Geometrical dimensions [mm] and applied loading. Right: Load displacement response F_z[kN] versus u_z[mm].

In summary, this example of the cracked L-shaped panel shows that the numerical method is able to capture brittle fracture of a single crack surface in a realistic way. The computational simulation matches the experimental findings. The results of the finer meshes are truly mesh independent. For examples with simple geometries, such as the L-shape, the first type of boundary conditions for the additional field proves to be straightforward and extremely useful.

6.2.2. Anchor pull-out test

The second example treats the pull-out of a steel anchor embedded in a cylindrical concrete block. The geometrical dimensions of the problem with its loading and boundary conditions are displayed in figure 6.3, for one quarter of the block. The geometry as well as the following material parameters, $E = 30000[\mathrm{N/mm^2}]$, $\nu = 0.2[\text{-}]$, $f_t = 3[\mathrm{N/mm^2}]$ and $G_f = 0.106[\mathrm{N/mm}]$ are chosen similar to those in GASSER & HOLZAPFEL [71], AREIAS & BELYTSCHKO [4], RABCZUK et al. [161] or FEIST & HOFSTETTER [62]. Further numerical investigations of anchor bolts as well as comparisons with experiments can be found in, e.g. ELFGREN et al. [58], BOCCA [22] or VERVUURT et al. [203]. Within this computation, the steel anchor is not explicitly modeled. Instead an incremental vertical displacement of $u_z = 0.01[\mathrm{mm}]$ is imposed in 60 load steps, until the final displacement of $u_z = 0.6[\mathrm{mm}]$ is reached. Note that for a regular mesh, the considered problem is axis-symmetric and can as well treated with a computation especially for axis-symmetric conditions, compare, e.g., DE BORST [41] or ELFGREN et al. [58]. Since the focus of this chapter is the investigation of our three-dimensional algorithm, we explore the pull-out test in a fully three-dimensional setting. Because of the rather complicated geometry, we apply the second category of defined boundary conditions. Accordingly, we pre-define the initial boundary conditions for the entire area which is in contact with the surface of the steel disc. In detail, we set the nodal values of the upper edge of this part to $\bar{\phi} = 20$ whereas the nodal values of the bottom are set to $\bar{\phi} = -30$. Additionally, we compute all nodal values of the intermediate nodes keeping in mind the favored crack onset. Hence, we can ensure that the crack onset and

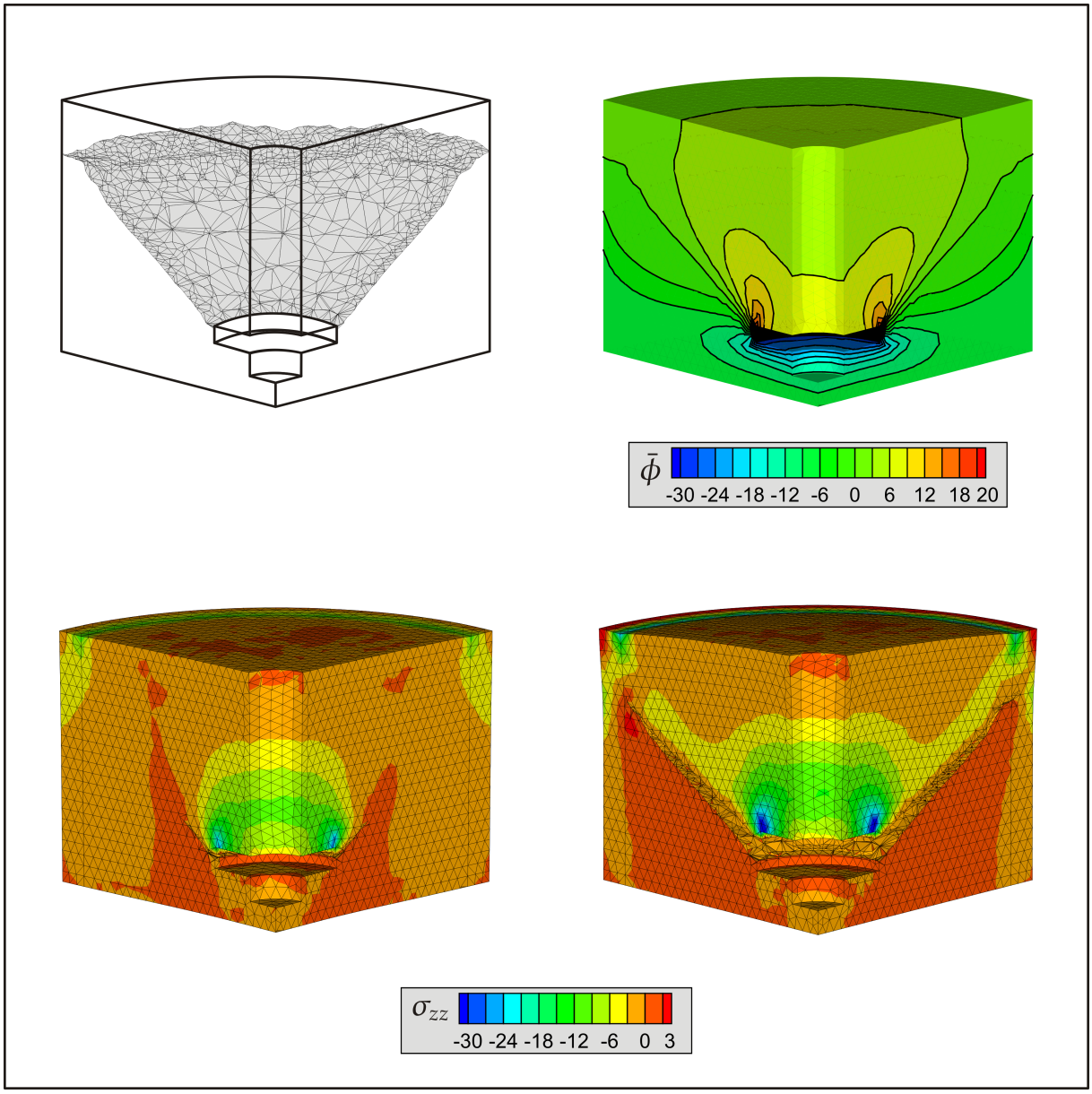

Figure 6.4.: Top: Potential crack surface and iso-surfaces for an imposed displacement of $u = 0.6[\text{mm}]$. Bottom: Contour plot of stress distribution $\sigma_{zz}\,[\text{N}/\text{mm}^2]$ in loading direction for imposed displacements $u = 0.25[\text{mm}]$ and $u = 0.6[\text{mm}]$.

the boundary conditions are equal for various different meshes. To explore the mesh independency of our algorithm, we use two unstructured meshes containing of 14281 (3175 nodes) and 44976(9486 nodes) elements, respectively. The corresponding load displacement curves are shown in figure 6.3, where the two computations are compared with the results from the literature, see GASSER & HOLZAPFEL [71]. Note that the load displacement curves are only displayed until a displacement of $u = 0.4[\text{mm}]$, for the sake of comparison. The reaction force is linear until the maxim load is reached. Afterwards, we observe a short decrease of the load for both meshes until a re-increase can be noticed for the finer mesh. This occurs since the crack starts from the onset at the steel disc and propagates further to the inside edge of the counterpressure ring,

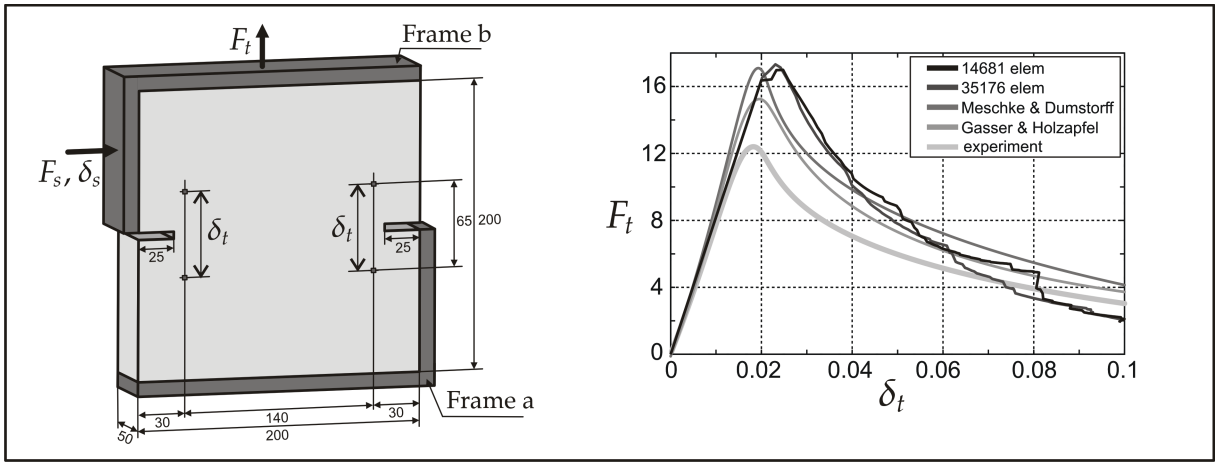

Figure 6.5.: Left: Geometrical dimensions [mm] and applied loading. Right: Load displacement response F_t[kN] versus δ_t[mm].

compare figure 6.4, where the iso-lines and the detailed zero iso-surface are depicted. Then, because of the tensile failure criterion, the maximal reaction force is observed prior the crack runs below the counterpressure ring. This means that mentioned re-increase occurs due to the fact that the failure behavior switches from tensile/shear to compression/shear behavior which cannot yet be captured with the presented numerical framework. It is obvious that the first mesh is too coarse to capture the failure behavior precisely: The peak load is over-estimated and accordingly, the re-increasing of the load occurs later. The reaction force of the finer mesh, however, shows the same linear slope as in the comparison literature and the load exhibits the characteristic re-increase reported in GASSER & HOLZAPFEL [71]. Finally, figure 6.4 also shows the stress distribution plotted on the deformed configuration. The displayed analysis is based on the discretization with 44976 linear tetrahedral elements and shows the results of load steps 25 and 60, i.e., at an applied deformation of $u = 0.25$[mm] and $u = 0.6$[mm], respectively.
In summary this example of the pull-out test documents that the proposed algorithmic tool set is able to capture brittle failure in more complex geometries. The results of the simulation agree nicely with the results documented in the literature. For complex geometries such as the pull-out test, however, the second type of boundary conditions seems to be the appropriate choice to capture the documented failure behavior appropriately.

6.2.3. Nooru-Mohamed test

The third example is a tension-shear test which has been performed experimentally by NOORU-MOHAMED [143]. From the documented experiments we choose the specimen with size 200x200x50[mm] and loading protocol 4b as illustrated in figure 6.5. In this test, a double notched specimen is first loaded by a shear force $F_s = 10$[kN] on the upper left frame b, whereas frame a is fixed in loading direction. The applied shear force leads to a relative shear displacement δ_s. Afterwards, the specimen is loaded by an imposed tensile displacement u_t on the upper left frame while keeping the shear

force constant at $F_s = 10[\text{kN}]$. The imposed tensile displacement induces a tensile load F_t whereas, for the results, this tensile load is plotted versus the depicted relative displacement δ_t, see again figure 6.5. It is obvious that keeping the shear load constant leads to a further increase in shear displacement during tensile loading. Due to this loading protocol, the principal stresses rotate during loading and result in two curvilinear cracks starting from the opposite notches. This example is thus an excellent test platform for our algorithm to simulate more than one crack. For the presented simulations we use two unstructured meshes consisting of 14681 (3101 nodes) and 35176 (7007 nodes) elements, respectively. The material parameters are chosen as $E = 30.000[\text{N/mm}^2]$, $\nu = 0.2[\text{-}]$, $f_t = 3[\text{N/mm}^2]$ and $G_f = 0.11[\text{N/mm}]$, similar to those in NOORU-MOHAMED [143] and MESCHKE & DUMSTORFF [130]. Again, we use the direct exponential traction formulation in opening direction and the contact stiffness is chosen to $E_c = 200000[\text{N/mm}^2]$. Further comparative discrete failure simulations of this benchmark problem can be found, e.g., in MANZOLI et al. [116], OLIVER et al. [152], GASSER & HOLZAPFEL [72] or FEIST & HOFSTETTER [61]. We emphasize that to ensure the mentioned loading protocol we couple the degrees of freedom in the shear direction to apply the constant shear force. Then we use 320 displacement controlled load steps of $u_t = 0.001[\text{mm}]$.

This example is well suited to demonstrate the importance of boundary conditions for the crack tracking problem in the context of defining symmetric initial conditions. Obviously, if we want to achieve a symmetric solution for the crack tracking problem and for the mechanical problem, we have to begin with a symmetric setup. Accordingly, the mesh dependent boundary conditions previously used in the literature are not useful. We thus choose to apply the initial boundary conditions on the geometry. In detail, we pre-define the particular areas of the notches starting with $\bar{\phi} = -50$ on the outside and ending with $\bar{\phi} = 5$ on the inner side of the particular area introducing symmetric initial boundary conditions as displayed in figure 6.6 on the right hand side of the top. The onset of crack propagation occurs on the notches as imposed. Thereby, the cracks will propagate under 45° as long as the shear load is applied. Afterwards, with increasing tensile loading, the cracks rotate, compare again figure 6.6, in which both the iso-lines and the zero-iso-surface are displayed. The crack path is in remarkably good qualitative agreement with the crack pattern of the experiments, see NOORU-MOHAMED [143]. The reaction force is mesh independent but the peak load is slightly overestimated compared to the experiment. However, this is also the case for the comparison numerical analyses of MESCHKE & DUMSTORFF in two dimensions and GASSER & HOLZAPFEL in three dimensions, whereas the latter simulation is in closest agreement with the experiments. The over-estimation of the peak can be explained by the following considerations: First, the fracture energy $G_f = 0.11[\text{N/m}]$ is not experimentally determined in the original work of NOORU-MOHAMED [143]. Its value is only estimated for the numerical simulations in the corresponding literature. We therefore assume that the fracture energy could be overestimated itself. Second, the used exponential cohesive model could have over-estimated the peak load because only tractions normal to the interface are considered. This is a first approach reasonable for tensile-dominated failure. For the present mixed-mode example, which is dominated by shear failure, especially at the onset of cracking, we should also account for

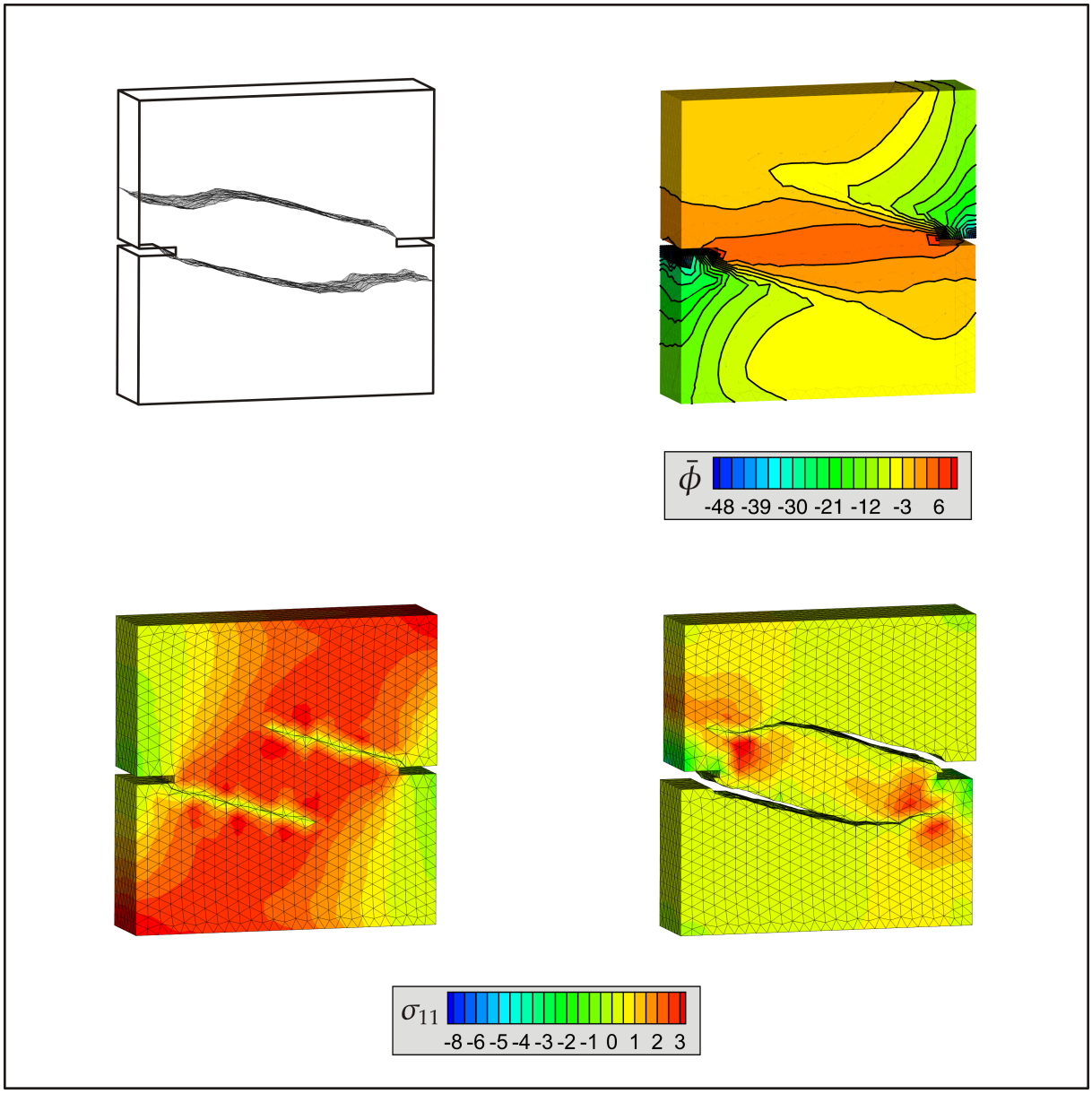

Figure 6.6.: Top: Potential crack surface and iso-surfaces for an imposed displacement of $u_t = 0.28[\text{mm}]$ ($\delta_t = 0.0922[\text{mm}]$). Bottom: Contour plot of stress distribution $\sigma_{11}[\text{N/mm}^2]$ for imposed displacements $u_t = 0.025[\text{mm}]$ ($\delta_t = 0.0247[\text{mm}]$) and $u_t = 0.28[\text{mm}]$ ($\delta_t = 0.0922[\text{mm}]$).

tangential tractions. Third, we have used relatively uniform meshes without mesh refinement at the notches. Finally, figure 6.6 shows the principal stress distribution of the deformed configuration. The displayed analysis is based on the discretization with 35176 elements and shows the results of imposed displacements of $u_t = 0.025[\text{mm}]$ ($\delta_t = 0.0247[\text{mm}]$) and $u_t = 0.28[\text{mm}]$ ($\delta_t = 0.0922[\text{mm}]$), whereby the displacement is scaled with factor 25.

In summary, the simulation of the NOORU-MOHAMED test demonstrates the potential of the proposed tool set to model multiple curved cracks. The results of the computational simulation agree qualitatively and quantitatively with experimental findings as well as with computational results achieved with alternative simulation tools.

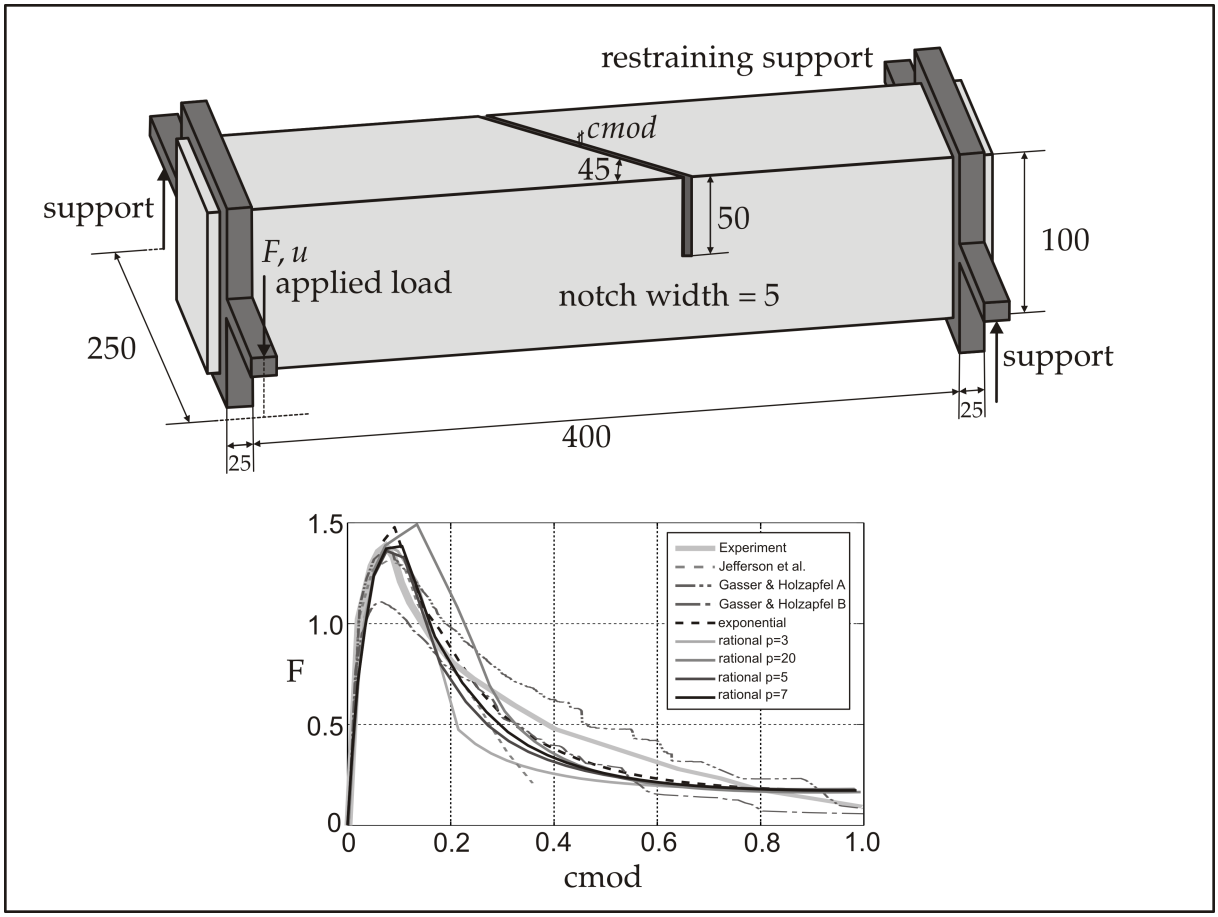

Figure 6.7.: Left: Geometrical dimensions [mm] and applied loading. Right: Load displacement response F[kN] versus opening displacement $cmod$[mm].

6.2.4. Brokenshire test

The next examples is a torsion fracture test, taken from the experimental work of BROKENSHIRE [26]. We chose the notched prismatic specimen with geometric dimensions 450x100x100[mm] under torsion loading, compare figure 6.7. This example is especially chosen since it exhibits a crack surface which cannot be simplified for a modeling into two dimensions. In addition, this example is used to demonstrate the functionality of the rational traction separation relation to accurately capture softening behavior in brittle materials. We emphasize that we have performed a lot of computations with different discretizations until we end up with a mesh which is suitable to capture the emerging crack surface and, additionally, is comparative to the experimental pattern and provide a mesh independent response. The final mesh consists of 26868 tetrahedral elements containing of (5964 nodes). Thereby, we have applied a mesh resolution in the middle of the specimen to capture the emerging crack surface more accurately. The material parameters are chosen as $E = 34.900[\mathrm{N/mm^2}]$, $\nu = 0.2[\text{-}]$, $f_t = 2.3[\mathrm{N/mm^2}]$ and $G_f = 0.08[\mathrm{N/mm}]$, similar to those in the comparative analysis of GASSER & HOLZAPFEL [72], JEFFERSON et al. [103] or GÜRSES [82]. The contact stiffness is chosen to $E_c = 203.000[\mathrm{N/mm^2}]$. We perform one computation with the exponential traction separation law and four computations $m = \{3, 20, 7, 5\}$ with the

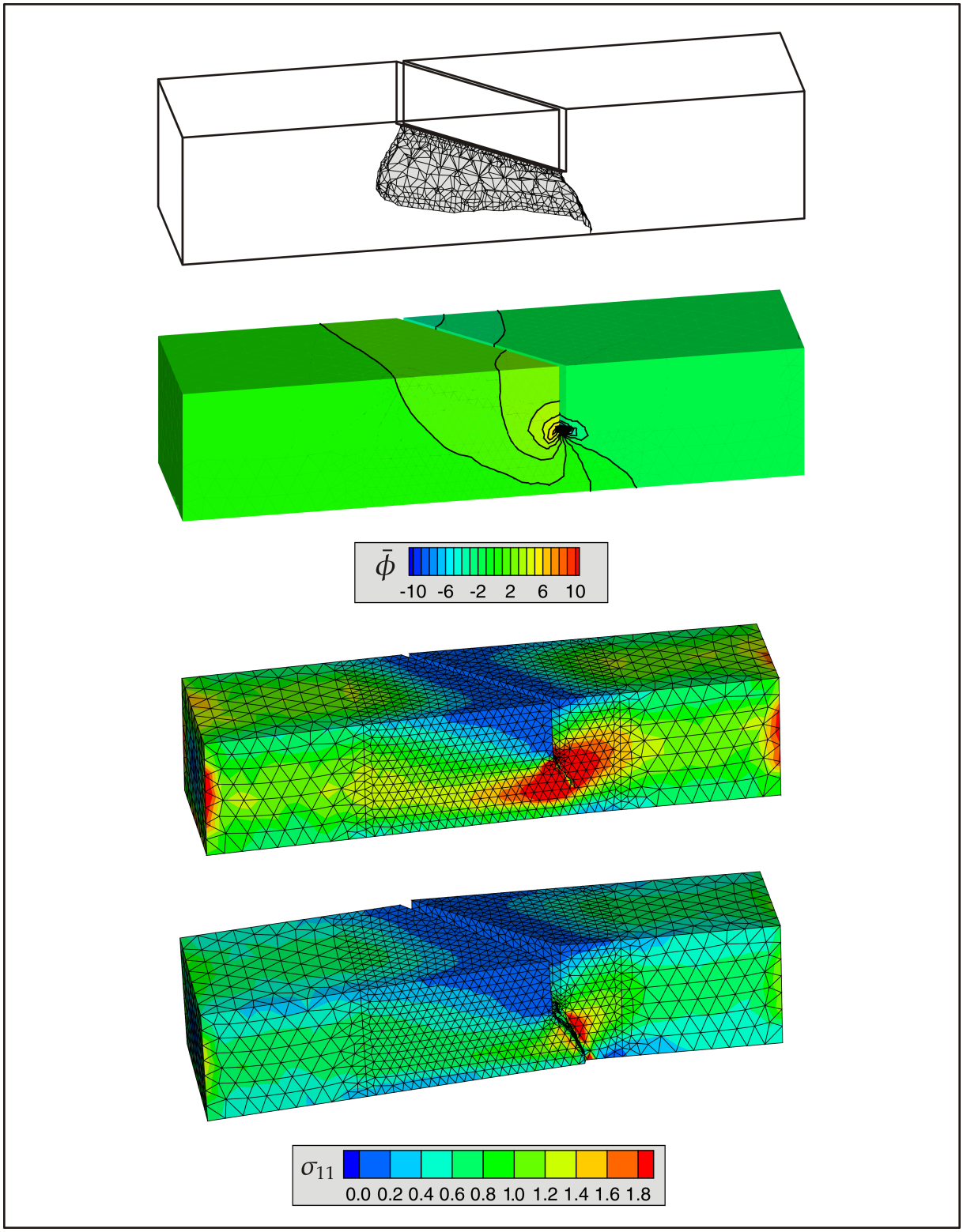

Figure 6.8.: Top: Potential crack surface and iso-surfaces for an imposed displacement $u = 0.25[\text{mm}]$ ($cmod = 0.0211[\text{mm}]$). Bottom: Contour plot of stress distribution $\sigma_{11}[\text{N/mm}^2]$ for imposed displacements $u = 0.25[\text{mm}]$ ($cmod = 0.0211[\text{mm}]$) and $u = 0.5[\text{mm}]$ ($cmod = 0.0682[\text{mm}]$).

direct rational formulation, see figure 6.7. The boundary conditions for the additional field are applied directly on the notch to $\bar{\phi} = \pm 10$, see figure 6.8. This means that we

chose mesh dependent boundary conditions. For the applied DIRICHLET boundary conditions, we assume the steel loading construction to be rigid. By further assuming an imposed angle of rotation with respect to the center of rotation, we can compute the corresponding imposed displacements for the boundary of the left end-place of the specimen. Then, with ensuring the determinateness of the structure through restricting the imposed displacements to the end-planes of the specimen, we can straightforwardly compute the corresponding load F. The load F is then depicted with respect to the crack mouth opening displacement *cmod*, i.e. the relative displacements normal to the notch. Figure 6.7 further shows this load-*cmod* relation compared with the comparative computations and the experimental data. The reaction force computed with the exponential traction separation relation is in relatively good agreement with the experimental data with a kind of accuracy similar to the foregoing concrete examples. In detail, the peak-load is slightly overestimated and the corresponding softening behavior differs until an opening displacement $cmod = 0.22$ is reached. In contrast the rational traction separation allows for capturing the softening behavior more detailed with only a few iterations for the numerical parameter m. Finally, figure 6.8 shows the corresponding failure surface and two snapshots of the principal stress distribution of the deformed configuration. One can see that the failure surface is in excellent agreement with the experimental failure pattern.
In summary, the simulation of the BROKENSHIRE test demonstrates nicely the capacity of the presented algorithm to capture complicated curved crack surfaces with appropriate engineering accuracy. Furthermore, the ability of the rational traction separation to capture softening behavior in a detailed fashion is illustrated.

6.2.5. Validation

We have illustrated the computational capacity of the presented modular algorithmic tool for modeling brittle fracture in concrete. The results are in relatively good agreement with either the experimental data or the results form the related literature, especially with the use of the rational traction separation formulation. In summary, the examples have demonstrated that our novel finite element tool is able to characterize the formation of arbitrarily shaped failure surfaces in engineering applications. Based on the validation of chapter 5 we have decided to focus on the global tracking problem for the computation of the failure surfaces. Since this approach is relatively novel, it still faces a number of difficulties which we have also tried to address by means of the presented examples. Similar to most multifield problems which are not directly linked to first principles, the formulation of boundary conditions for the additional field requires a closer look. Therefore, according to our classification of boundary conditions in subsection 5.3.5, the examples clarify the advantage of using either mesh dependent or geometry based boundary conditions in case of one or two arising crack surfaces. The remaining case of multiple crack propagation will be discussed in the following section.

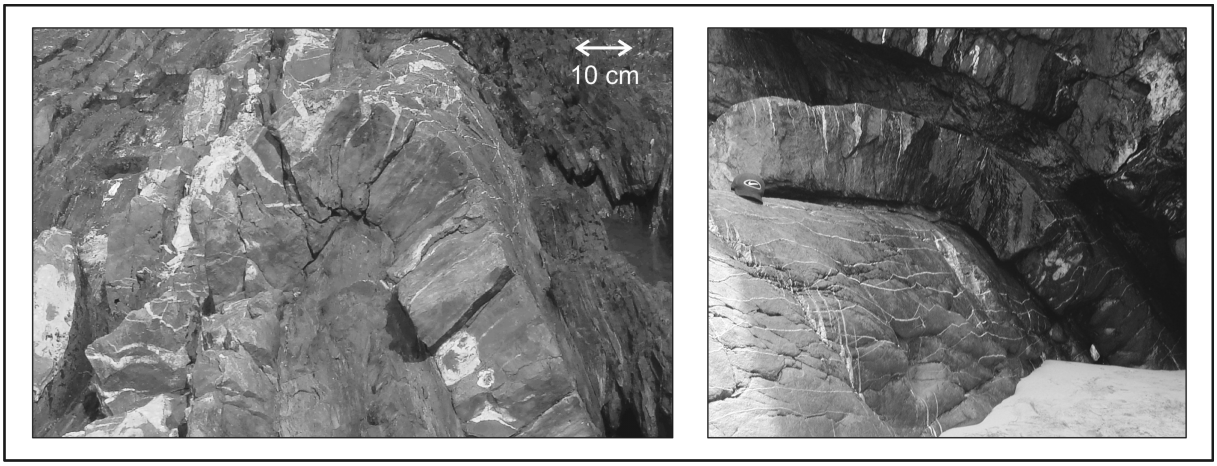

Figure 6.9.: Folded sandstone layers embedded in shale, south-west Portugal. Wedge-shaped dilational fractures filled with quartz are visible at the outer part of the fold hinge. Pictures by S.M. SCHMALHOLZ taken from JÄGER et al. [99].

6.3. Brittle fracture during folding of rocks

Folds are very common structures in nature and occur on many scales, from millimeter to hundreds of kilometers, see, e.g., BIOT [21], TURCOTTE & SCHUBERT [198] or SCHMALHOLZ et al. [175]. The folds discussed in this section are the result of folding, or buckling, which is a mechanical instability that arises during the layer-parallel compression of mechanically strong layers or plates, see, e.g., BIOT [21]. Rock units can also be bent without buckling which is sometimes termed forced folding, see, e.g. COSGROVE & AMEEN [38]. However, this mechanism is not discussed within this study. Especially folded rocks of the upper crust, such as sandstones and limestones, often exhibit fractures and fracture sets with specific orientations relative to the fold geometry, see figure 6.9. The temporal and spatial relationship between folding and fracturing is of great importance for geologists because studying the fold-fracture relationships improves the understanding of their formation mechanism and allows predicting fracture orientations and fracture densities in natural folded rocks, compare, e.g., CLOOS [36], HANCOCK [84] or BERGBAUER & POLLARD [20]. These predictions are particularly important for industrial applications such as groundwater and hydrocarbon flow because fractures control the permeability of rock units, see, e.g., MCQUILLAN [119] or BERGBAUER & POLLARD [20]. Usually, there are several fracture sets with different orientations around folded upper crustal rocks and it is often difficult to determine which fracture sets are related to the folding and which are not. Therefore, a main question for field geologists studying fold-fracture relationships is to determine if the fractures in the folded rocks have formed before, during or after folding. Fractures that formed before folding are not related to the characteristic stress field caused by folding but may have introduced some anisotropy in the folded rocks, see, e.g., MCQUILLAN [119] or BERGBAUER & POLLARD [20]. Fractures that formed after folding during for example the uplift and exhumation of the folded rocks may have orientations completely unrelated to the stress field during folding. However, fractures that formed during folding are expected to show orientations that are related to the stress field caused by

folding. The fracture orientations that form during folding can be predicted for simple folding scenarios, see, e.g., PRICE & COSGROVE [158]. For example, the two most common dilational fracture sets related to folding are expected to be both perpendicular to the bedding but either parallel or orthogonal to the fold axes, see, e.g., PRICE & COSGROVE [158] or compare figure 6.9. This means that there are two fundamental types of fractures: dilational fractures (also termed extension fractures or joints) and shear fractures (also termed faults). Both fracture types can be generated during folding.
Within this section, the development of fractures during folding of an elastic plate is numerically simulated in three dimensions. As mentioned before, no previous numerical studies exist for this problem. Accordingly, a relatively simple model setup is chosen here based on the following simplifications: (i) the folded plate is free and not embedded in a mechanically weaker medium, (ii) the rheology is purely elastic, (iii) the plate is initially homogeneous and isotropic and no initial fractures exist, and (iv) only dilational fractures are considered using the elaborated Rankine criterion for brittle materials.
Although the fold-fracture relationship is important for geologists, there are no numerical models that satisfactorily simulate simultaneous fractures during folding of elastic rocks. One reason presumably is that while folding of an elastic plate is relatively easy to model numerically, fracturing is not.
The main aims of this study are therefore: i) to use the presented finite element tool to simulate the simultaneous processes of fracturing and folding in a self consistent way, (ii) to quantify the temporal evolution of dilational fractures during folding, (iii) to quantify the spatial orientation of fractures during folding, (iv) to quantify the impact of layer-parallel shearing, or rather wrenching, on the temporal and spatial formation of fractures, (v) to quantify the impact of fractures on the fold amplification, and (vi) to present a first numerical study for folding controlled fracturing which can be elaborated for more sophisticated practical geological applications in the future.

6.3.1. Model for simultaneous fracturing and folding

All numerical simulations in this manuscript are based on the unified benchmark problem of a single plate with dimensions $L = 10[\mathrm{m}]$, $B = 5[\mathrm{m}]$ and $H = 1[\mathrm{m}]$. To trigger a geometric instability, we initialize the plate with a sinusoidal deformation $u_z^{\mathrm{init}} = u^{\mathrm{init}} \sin(\pi X/L)$ where $u^{\mathrm{init}} = 0.1[\mathrm{m}]$ as illustrated in figure 6.10. We discretize the folding plate with 39360 elements introducing a total number of 23814 degrees of freedom.
In geodynamic modeling, the folding plate is typically embedded in a weaker medium. For simplicity, however, we assume that the plate is free to move in the thickness direction. This is a valid end-member case if the folding rock layer is mechanically significantly stronger than the embedding rocks. On the lower left and right edge, however, the plate is supported vertically. We thus apply homogeneous Dirichlet boundary conditions $u_z = 0$ in thickness direction as indicated in figure 6.10. Plate folding is initiated through displacement driven in-plane compression and superposed shear on the entire left and right side of the plate. To elaborate the impact of layer-parallel shearing on the temporal and spatial formation of fractures, we define seven individual load

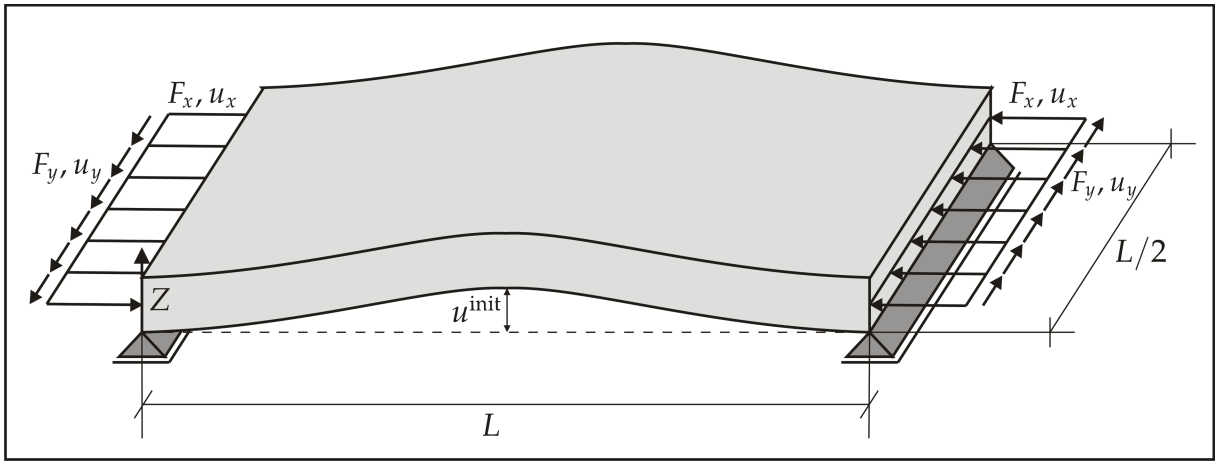

Figure 6.10.: Benchmark problem of single-layered folding plate - Geometry and spatial dimensions.

cases. Each load case is characterized through the same amount of in-plane compression $u_x = \pm 0.01[\text{m}]$ while the in-plane shear u_y is varied systematically. Table 6.1 summarizes load cases I to VII classified in terms of the shear-to-compression ratio $u_y : u_x$.

load case		I	II	III	IV	V	VI	VII
in-plane compression	u_x	0.01	0.01	0.01	0.01	0.01	0.01	0.01
in-plane shear	u_y	0	0.0025	0.005	0.01	0.02	0.03	0.04
shear : compression ratio	$u_y : u_x$	0	1/4	1/2	1	2	3	4

Table 6.1.: Definition of load cases I to VII in terms of the shear-to-compression ratio $u_y : u_x$.

Since we allow multiple cracking, we choose root elements for the failure surface initialization, compare section 5.3.5. However, to avoid a dependence of the number of emerging cracks on the discretization, i.e., on the number of finite elements, we introduce root elements at predefined locations. These root elements are activated as soon as the Rankine criterion is violated locally. We introduce potential crack root elements on the top of the plate ($Z = H$) in the middle element ($Y = L/4$) of every other row ($X =$const). By doing so, we allow multiple crack propagation on the one hand and ensure continuity of the potential crack paths on the other hand. For the sake of completeness, we choose to apply Dirichlet initial boundary conditions of $\bar{\phi} = \pm 100$ at the upper left and upper right edge to be able to solve the crack tracking problem, compare also figure 6.12 on the left. Initially, the plate rheology is purely elastic, it is homogeneous and no initial fracture exists. For the elastic material parameters of the plate, we choose $\lambda = 2 \cdot 10^{10}[\text{Pa}]$ and $\mu = 2 \cdot 10^{10}[\text{Pa}]$, corresponding to Young's modulus $E = 5 \cdot 10^{10}[\text{Pa}]$ and Poisson's ratio to $\nu = 0.25$. These are suitable parameters to describe sandstone or limestone, see, e.g. [198]. For the rupture stress we assume a value of $f_t = 0.25 \cdot 10^{10}[\text{Pa}]$. The interface contact stiffness is chosen to $E_c = 5 \cdot 10^{10}[\text{Pa}]$. This particular choice of the interface stiffness had been found reasonable during various

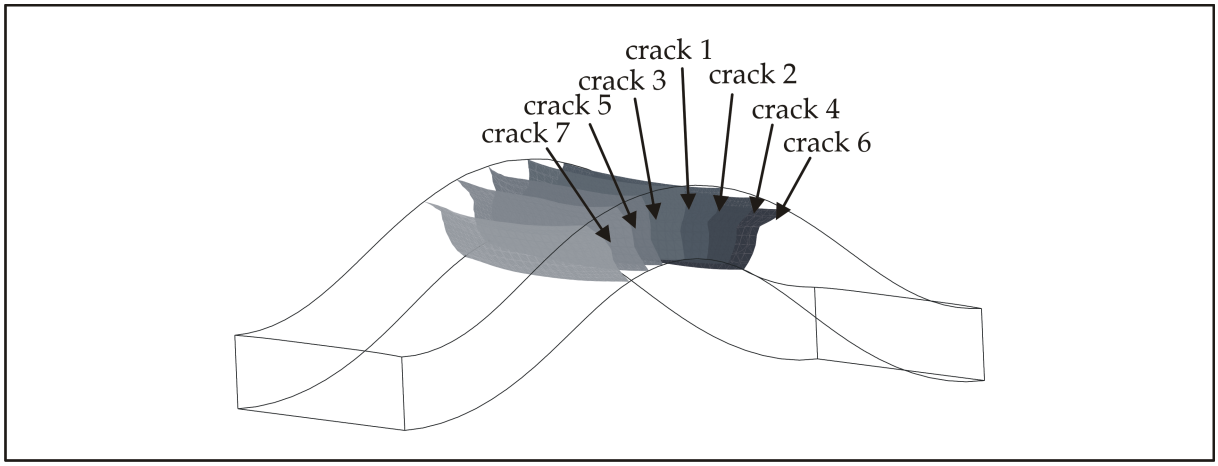

Figure 6.11.: Chronological order of the emerging cracks displayed for their potential crack surfaces.

different case studies of this folding problem.

Remark 6.3.1 (Fracture energy and cohesive resistance) *Since we have no experimental observations on the fracture energy of rocks, we refrain from using a cohesive traction separation law. At a first glance this is unusual since this obviously provides unbounded crack tip stresses with mesh refinement. However for this example this is a suitable assumption for a first feasibility study due to the following facts: i) The root elements are bulk elements without any notch or predefined crack. Accordingly the stresses which leads to the root element activation are bounded bulk stresses. ii) We will see later that the different emerging cracks will stop until the upper part of the plate exhibits compression stresses. Usually, with mesh resolution at the corresponding crack tip, we ever observe a small tensile dominated stress zone which further influences the considered crack to propagate. That means, if we chose the element size small enough to account for the real transition between tensile and compression, we obviously have to account the cohesive tractions. Otherwise the crack is unable to stop because of the occurring crack tip singularity. However, our finite element tool is restricted to the number of degrees of freedom describing the presented mesh of the plate. Therefore we can refrain from using a cohesive traction separation law since as a first basic computation which further accelerates the complete simulation remarkably.*

6.3.2. Temporal evolution of dilatational fractures during folding

To elaborate aim (ii), we observe the temporal sequence of emerging cracks during a computation cycle. We identify a total of seven emerging cracks for load cases I to V, and nine cracks for load cases VI and VII. The chronological order of emerging cracks is illustrated in figure 6.11. The analyzed crack initiation sequence corresponds to an imposed maximum in-plane compression displacement of $u_x = \pm 0.7[\mathrm{m}]$ on each side. Surprisingly, the temporal order of emerging cracks is identical in all seven load cases. Table 6.2 summarizes the amount of compression u_x at crack initiation for each of the seven cracks based on the numbers introduced in figure 6.11. Obviously, the compression deformation intervals u_x between the emerging cracks decrease with increasing shear deformation u_y. As the shear-to-compression ratio increases, we observe a

load case	I	II	III	IV	V	VI	VII
shear : compression ratio	0	1/4	1/2	1	2	3	4
u_x @ crack 1	0.28	0.28	0.28	0.27	0.25	0.23	0.22
u_x @ crack 2	0.29	0.29	0.29	0.28	0.26	0.24	0.22
u_x @ crack 3	0.30	0.30	0.29	0.29	0.27	0.24	0.22
u_x @ crack 4	0.33	0.33	0.33	0.33	0.29	0.26	0.22
u_x @ crack 5	0.35	0.35	0.34	0.33	0.30	0.26	0.23
u_x @ crack 6	0.53	0.53	0.54	0.49	0.38	0.29	0.26
u_x @ crack 7	0.59	0.58	0.57	0.51	0.38	0.29	0.26

Table 6.2.: Imposed compression displacement $u_x[\mathrm{m}]$ at crack initiation for all seven cracks 1 to 7 and all load cases I to VII.

smooth transition from plain tensile failure in load case I to a shear dominated failure in load case VII. For the plain compression case I, we observe the first crack initiation in the tensile zone right in the middle of the upper plate surface, see crack number 1 in figure 6.11. After this crack initiation, the stress state is partially relaxed and the maximum tensile stress gradually moves from the center to the left and to the right. Next, a set of cracks, numbered 2 and 3 in figure 6.11, is initiated left and right to the first crack. Theoretically, these two cracks should emerge simultaneously because of the symmetric geometry of the problem setup. Due to our particular structured triangular discretization, however, the mesh is biased such that crack 2 on the right is initiated slightly before crack 3 on the left. Crack sets 4 and 5 and then sets 6 and 7 evolve in a similar way. If now, shear is applied in addition to compression, the load increment between the onsets of cracking decreases remarkably. In the extreme case VII with a shear-to-compression ratio of $u_y : u_x = 4$, all seven cracks emerge almost simultaneously. This example nicely illustrates the remarkable influence of the shear-to-compression ratio, or rather of the stress state in the plate, on the dominant failure mechanism and thus on the chronological evolution of failure surfaces. In addition to

load case	I	II	III	IV	V	VI	VII
shear-to-compression ratio	0	1/4	1/2	1	2	3	4
X^{orig} @ crack 1	5.00	5.00	4.99	5.00	5.00	4.99	5.01
X^{orig} @ crack 2	5.52	5.51	5.51	5.51	5.50	5.48	5.49
X^{orig} @ crack 3	4.49	4.49	4.49	4.49	4.49	4.50	4.53
X^{orig} @ crack 4	6.04	6.04	6.03	6.03	6.00	6.00	5.98
X^{orig} @ crack 5	3.96	3.96	3.97	3.98	3.99	4.00	4.06
X^{orig} @ crack 6	6.58	6.58	6.58	6.56	6.51	6.49	6.45
X^{orig} @ crack 7	3.41	3.41	3.41	3.42	3.47	3.51	3.58
$X^{\mathrm{orig}}_{\mathrm{max}} - X^{\mathrm{orig}}_{\mathrm{min}}$	3.17	3.17	3.17	3.14	3.04	2.98	2.88

Table 6.3.: Crack origin positions $X^{\mathrm{orig}}[\mathrm{m}]$ at crack initialization for all seven cracks 1 to 7 and all load cases I to VII.

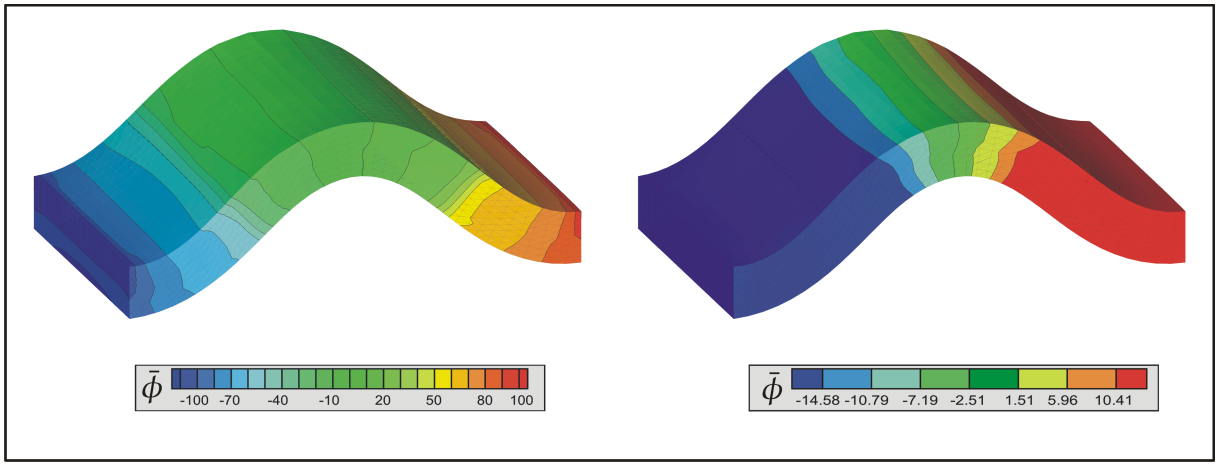

Figure 6.12.: Crack tracking problem: Iso-surfaces representing potential crack directions. Left: Load case I for entire range of $\bar{\phi}$ values with Dirichlet boundary conditions $\bar{\phi} = \pm 100$ on left and right boundary. Right: Representation of root ϕ iso-surfaces corresponding to cracks 1 to 7.

the temporal sequence of emerging cracks, it is interesting to analyze the spatial origin x^{orig} of the emerging cracks. Recall that we prescribe the potential location of the crack root, however, we do not know where exactly the crack will emerge. The final location of all crack origins is a quantitative measure for the plate failure in the form of damage. Table 6.3 displays the widths of the damaged zone $X^{\text{orig}}_{\text{max}} - X^{\text{orig}}_{\text{min}}$ for all seven load cases, which, for our particular problem, is equal to the distance between the origin of crack 6 and 7. Here, we have defined the X-width of the projection of the cracked area onto the original X, Y-plane in the reference configuration as a qualitative measure for the damaged area. For load case I it takes a maximum width of $3.17[\text{m}]$ decreasing to a damage zone width of $2.88[\text{m}]$ for load case VII.

6.3.3. Spatial orientation of fractures during folding

Next we address point (iii), i.e., the spatial orientation of the failure surfaces during folding. At first we can use the potential crack iso-surfaces visible at the outer boundary as illustrated in figure 6.12 for load case I. The cracks clearly trace the direction perpendicular to the principal Cauchy stress as determined through the Rankine criterion. For the displayed plain compression case, discrete failure surfaces are introduced element-wise in the direction orthogonal to the maximum principle stress direction, i.e., perpendicular to the compression axis.

6.3.4. Impact of layer-parallel shearing on formation of fractures

In addition to the qualitative iso-surfaces of the previous subsection, we quantify fracture in terms of the crack deviation angle for the emerging cracks. This angle is measured in reference to our fixed coordinate system and thereby address question iv), i.e., the impact of layer-parallel shearing on the temporal and spatial formation of fracture. In detail, we use the two endpoints of each emerging crack to compute its actual length and its orientation with respect to the fixed Y-axis, see figure 6.13. The measured an-

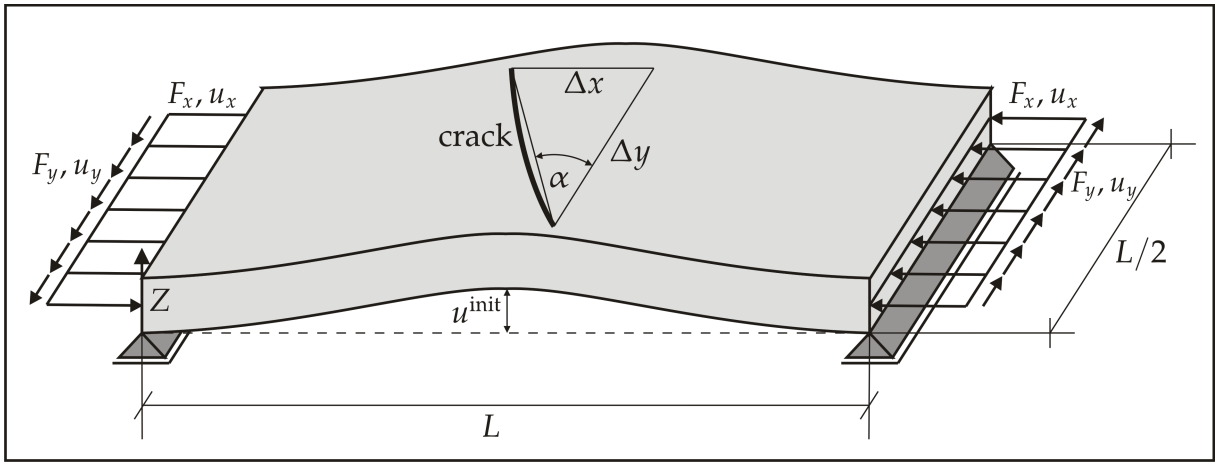

Figure 6.13.: Measurement of the crack deviation angle α.

load case	I	II	III	VI	V	VI	VII
shear : compression ratio	0	1/4	1/2	1	2	3	4
α @ crack 1	0.0	1.6	3.4	5.2	8.5	11.6	51.7
α @ crack 2	0.0	1.7	3.2	4.0	8.0	11.5	51.4
α @ crack 3	0.0	0.4	2.2	4.1	8.0	11.4	50.8
α @ crack 4	0.0	1.6	2.4	5.2	8.8	16.5	63.9
α @ crack 5	0.0	1.5	2.1	4.1	8.9	13.8	50.4
α @ crack 6	0.0	2.7	4.5	8.8	16.3	26.1	54.2
α @ crack 7	0.0	3.6	5.5	8.6	12.4	20.8	49.6
average α	0.0	1.9	3.3	5.7	10.1	15.9	53.1

Table 6.4.: Crack deviation angle $\alpha\,[^\circ]$ for for all seven cracks 1 to 7 and all load cases I to VII.

gles are summarized in table 6.4. For load case I, i.e., the case of pure compression, the crack deviation angle with respect to the Y-axis is zero. The principal stress is parallel to the X-axis and the crack is oriented perpendicular to the loading axis. As the shear-to-compression ratio is increased from $u_y : u_x = 0$ to 4, the average crack deviation angle α increases gradually. To clarify the influence of imposed shear displacement on the spatial formation of fracture, we display this relation for each of the cracks I to VII and for the average crack deviation angle α in figure 6.14. Remarkably, the average crack deviation angle increases linearly from $\alpha = 0.0^o$ for load case I of plain compression to $\alpha = 15.9^o$ for load case VI at a shear-to-compression ratio of $u_y : u_x = 3$. For higher shear-to-compression ratios, however, the crack deviation angle increases non-linearly. At a shear-to-compression ratio of $u_y : u_x = 4$, the average crack deviation angle is measured to $\alpha = 53.1^o$. At crack initiation, tensile stresses dominate the failure mode for the first six load cases. For load case I, failure occurs under pure tension while for load cases II to VI, shear stresses are superposed in addition. For load case VII, however, shear stresses clearly dominate the failure mechanism. It is interesting that the relation between the crack deviation angle and the shear-to-compression ratio is linear, as long as the dominant deformation mode during crack formation is folding

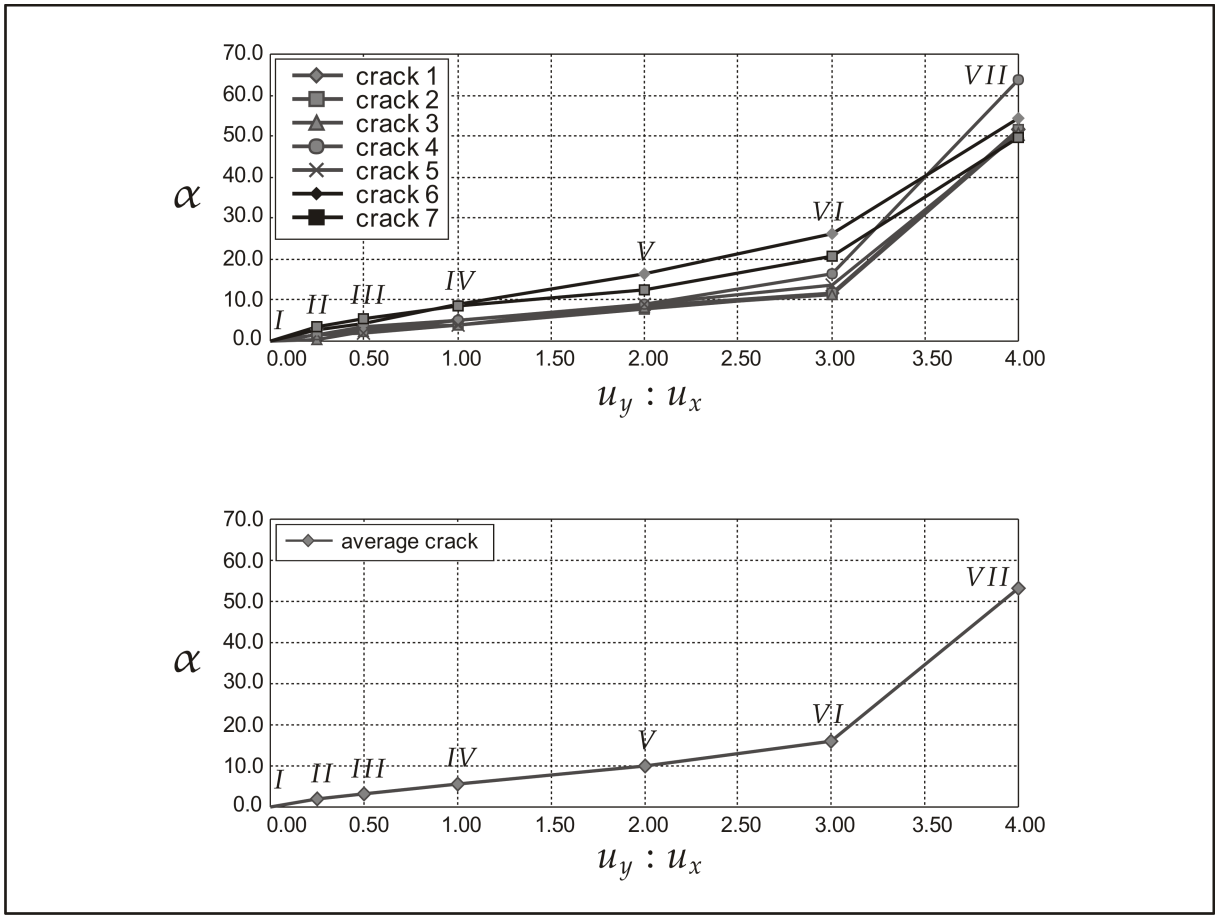

Figure 6.14.: Crack deviation angle $\alpha\,[^\circ]$ vs shear-to-compression ratio. Top: For all seven cracks 1 to 7 for all load cases I to VII. Bottom: Average crack deviation angle for all load cases I to VII.

due to the compression.

6.3.5. Impact of fractures on fold amplification

According to our list of aims, we finally address item (v) and quantify the impact of fractures on fold amplification. To illustrate the evolution and development of folding, figure 6.15 displays a typical time sequence of folding for load case I of pure compression. For this load scenario, all cracks form perpendicular to the loading direction. Clearly, the Cauchy stress and the amplification, i.e., the maximum out-of-plane deformation, increase upon increased compression. In addition, figure 6.16 shows a snapshot for load cases II to VII for the stage at which all seven cracks have developed, compare table 6.2. On the one hand figure 6.16 nicely illustrates the crack deviation angles for the different load cases. On the other hand it clearly displays that the amplification decreases with increasing shear-to-compression ratio. The depicted folding patterns provide a clear explanation of the decrease in amplification. For plain compression in load case I, the plate buckles in one direction and one single fold forms as triggered by the initial sinusoidal deformation. For increased shear-to-compression ratios, however, the fold tends to rotate away from the compression axis. For the final load cases VII at a shear-to-compression ratio of $u_y : u_x = 4$, the formation of two smaller folds

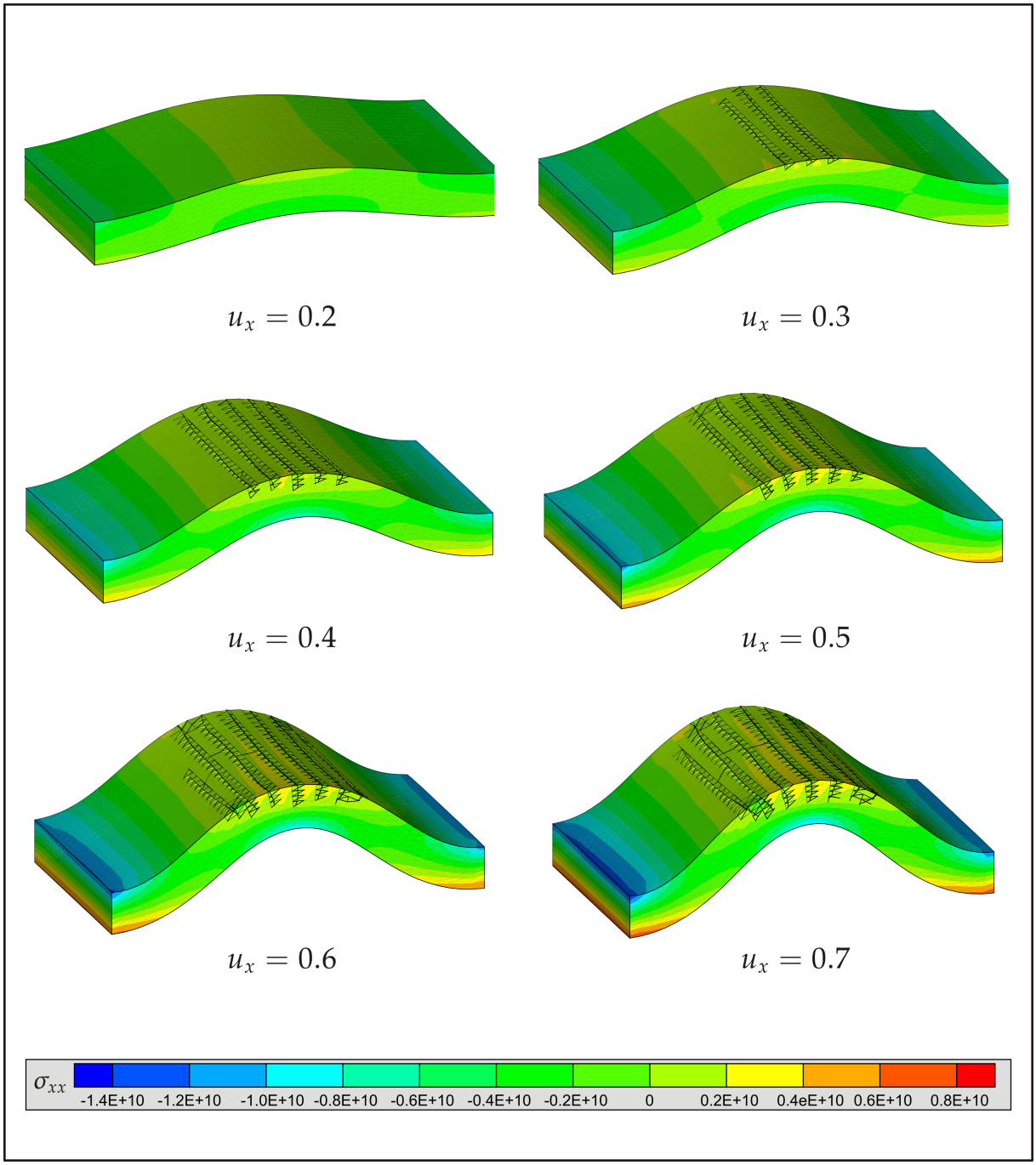

Figure 6.15.: Normal component of Cauchy stress σ_{xx}[Pa] in direction of compression displayed for load case I at different load stages u_x[m].

can be observed. These, of course, are smaller in amplification than the single fold in the previous load cases. The multifold buckling of load case VII is an extremely complex failure phenomenon the simulation of which is computationally challenging. For this load case, maximum tensile stresses are not only restricted to the top of the plate and potential crack root elements should also be introduced on the plate bottom. It is thus not surprising that for load case VII, the algorithm fails to capture a further load increase.

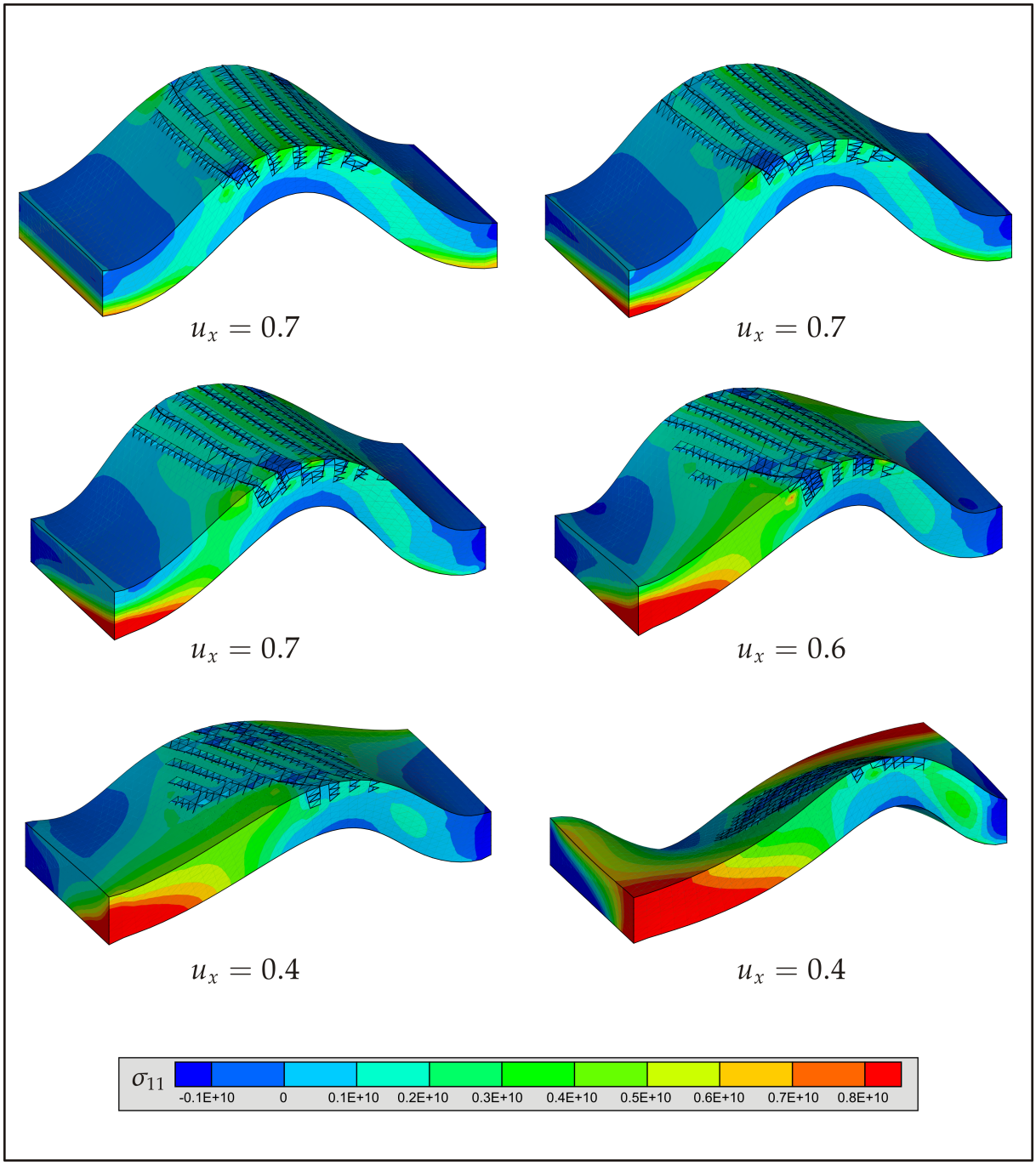

Figure 6.16.: Cauchy stress σ_{11}[Pa] displayed for load cases II to VII at final load stage u_x[m] with seven cracks.

To further quantify the amplification, we analyze the amplification compression relation for all seven load cases I to VII. To this end, we plot the maximum out of plane displacement u_z[m] at the top center point of the plate versus the prescribed compressive displacement u_x[m] in figure 6.17, top. For all seven load cases, the amplification u_z increases linearly with increasing prescribed compression u_x until a critical compression of $u_x = 0.1$[m]. Above this critical compression, the amplification-compression behavior becomes non-linear and differs significantly for the different load cases. For the

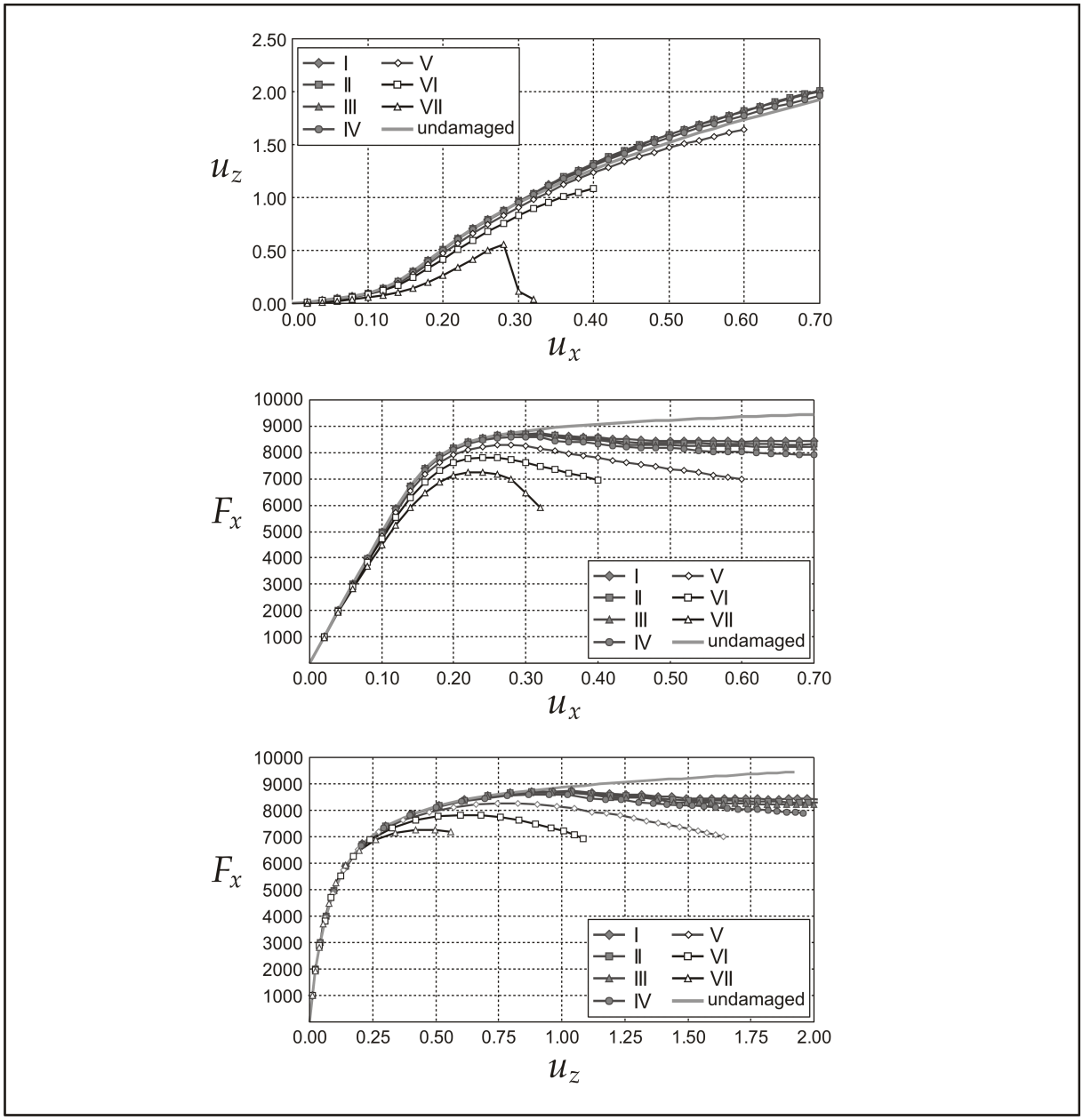

Figure 6.17.: Top: Amplification compression relation u_z[m] vs u_x[m]. Bottom left: Compressive force displacement relation F_x[MN] vs u_x[m]. Bottom right: Compressive force amplification relation Force F_x[MN] vs u_z[m].

sake of comparison, we compute a purely elastic plate without allowing for fracture to quantify the overall influence of failure. Intuitively, one would expect this undamaged plate to display the smallest amplification. Surprisingly, load cases V and VII, however, show a smaller amplification than the elastic reference case. For the load cases V-VII with a shear-to-compression ratio larger than one, we observe a rotation of the plate's cross section. This rotation is associated with an increase of bending resistance in the out-of-plane direction, despite emerging fracture. In addition, load case VII is associated with the transition to a multiple buckling mode which is initiated at an imposed compression of 0.27m. This folding mode transition associated with the corresponding

computational difficulties is the reason why we have limited our analysis to a maximum shear-to-compression ratio of $u_y : u_x = 4$.
Figure 6.17, gives further insight into the different folding modes associated with the seven load cases. We illustrate the compressive force $F_x[\mathrm{MN}]$ versus the compressive displacement $u_x[\mathrm{m}]$ in figure 6.17, center, and the compressive force $F_x[\mathrm{MN}]$ versus the amplification $u_z[\mathrm{m}]$ in figure 6.17, bottom, respectively. As expected, the undamaged elastic plate of the reference solution shows the highest load carry capacity and its load-displacement relation is monotonically increasing. All plates with emerging fracture show a decreasing load after the limit load is reached. This limit load, however, crucially depends on the shear-to-compression ratio. In accordance with figure 6.16, load cases I, II and III with a shear-to-compression ratio below one display an almost identical compression dominated single fold buckling. Accordingly, their force-compression and force-amplification curves are nearly identical. With an increasing shear-to-compression ratio, the overall response becomes more brittle. Remarkably, the limit load under load case VII with a shear-to-compression ratio of $u_y : u_x = 4$ is about 20% smaller than the limit load for the plain compression case with $u_y : u_x = 0$. Subjected to load case VII, the plate shows a pronounced drop in load-carrying capacity after the limit load is reached. This drastic loss of load-carrying capacity associated with the complex multifold failure mechanism could possibly explain the failure of the suggested computational algorithm at even larger shear-compression ratios.

6.3.6. Validation

For the first time, we have presented a computational analysis for the simulation of folding-induced fracturing of geological rock layers in a self consistent way. To elaborate the features of the suggested algorithm, we have defined a unique three -dimensional model problem of plate folding (or plate buckling). With this model setup, we analyze brittle tensile failure governed by the traditional principle stress based Rankine criterion. In contrast to classical model problems for quasi-brittle materials such as concrete or rock, loading is not applied in the form of tension or bending. Here, we apply a pure displacement driven layer-parallel compression and superpose a gradually varying amount of in-plane shear to systematically study the influence of the stress state on the failure mode. For our particular model problem, brittle failure in the tensile regime of the plate is a mere result of folding or rather buckling, a geometric instability that requires a kinematically exact characterization of large deformations.
The two most common fracture sets related to folding are both perpendicular to the bedding but either parallel or orthogonal to the fold axes, see, e.g., PRICE & COSGROVE [158]. Since both of these fractures open orthogonally to the least principle stress direction, they cannot form simultaneously. In this study only fractures with an orientation sub-parallel to the fold axes emerge. Branching and intersecting cracks are not considered within the present framework. For the present finite element based fracture algorithm, the failure mode is primarily controlled by the principle stress based Rankine failure criterion, the choice of boundary conditions and the magnitude of the failure stress.
In the present study, the elastic plate is free to buckle and not embedded in a mechan-

ically weaker medium. An embedding medium changes the stress magnitude and distribution within the folding layer and may therefore influence the mode of fracturing. However, most probably, the first order results provided by this study will not change dramatically due to an embedding medium.
A component of layer-parallel shearing, or wrenching, results in a systematic variation of the fracture orientation. The results show that above a certain shear-to-compression ratio, shear fractures originate first and not dilational fractures. This shear dominant regime is governed by multiple folding and high crack deviation angles. Below the critical shear-to-compression ratio, however, the crack deviation angle varies linearly with the shear-to-compression ratio. Within this linear regime, the crack deviation angle, i.e., the deviation in orientation of dilational fractures from the fold axis, may be used in the field to estimate the action and magnitude of wrenching during folding. The fracturing during folding changes the effective mechanical properties of the plate, in particular the plate becomes weaker at the outer hinge area and the flexural rigidity becomes smaller at the fold hinge. This weakening would cause an increased amplification for layer-parallel shortening under a constant compression force.
Within this thesis, we suggest a non-linear coupled finite element based algorithm to simulate brittle fracture in folding rocks. An alternative method to study simultaneous folding and fracturing is the discrete element method, see, e.g., HARDY & FINCH [88]. Here the folding rock is assumed to consist of multiple particles ab initio. To simulate discrete element based folding and fracturing with an acceptable numerical resolution, however, requires a significantly higher computational effort than using finite elements. Another drawback of discrete element methods is that most established failure criteria based on laboratory rock deformation experiments such as the Rankine criterion are expressed in terms of stress tensor components. These are difficult to define within the discrete element method. Accordingly, the suggested finite element algorithm is believed to provide a stable, robust, efficient and powerful analysis tool to study the complex failure phenomena in brittle fracture and folding. The proposed framework can be used to generate individual tables of crack deviation angles versus shear-to-compression ratios for various types of rocks. These tables can potentially be applied in the field to improve the understanding of the evolution and structural development of complex failure patterns in natural rocks. Since these fractures severely influence the permeability of geological structures, this understanding is of crucial importance for industrial applications such as groundwater and hydrocarbon flow.

7. Discussion

7.1. Summary

Within this thesis we present a novel approach towards the modeling of strong discontinuities in a three dimensional finite element framework for large deformations. This novel finite element framework is modularly constructed containing three essential parts: (i) the bulk problem, ii) the cohesive interface problem and iii) the crack tracking problem.
Within this modular design, **chapter 2** (*Continuous solid mechanics)* treats the behavior of the bulk problem (i). It includes the overall description of the continuous kinematics, the required balance equations, the constitutive setting and the finite element formulation with its corresponding discretization and required solution strategy for the emerging highly non-linear equations.
Subsequently, we discuss the modeling of strong discontinuities within finite element discretization schemes in **chapter 3** (*Discontinuous solid mechanics)*. Starting with an extension of the continuous kinematics to the discontinuous situation, we discuss the phantom-node discretization scheme based on the works of HANSBO & HANSBO. Thereby, in addition to a comparison with the extended finite element method (XFEM), importance is attached to the technical details for the adaptive introduction of the required discontinuous elements: The splitting of finite elements, the numerical integration, the visualization and the formulation of geometrical correct crack tip elements.
In **chapter 4** (*The cohesive crack concept)*, we consider the treatment of cohesive process zones and the associated treatment of cohesive tractions. By applying this approach we are able to merge all irreversible, crack propagation accompanying, failure mechanisms into an arbitrary traction separation relation. Additionally, this concept ensures bounded crack tip stresses and allows the use of stress-based failure criteria for the determination of crack growth. In summary, the use of the discontinuous elements in conjunction with cohesive traction separation allows the mesh-independent computation of crack propagation along pre-defined crack paths. Therefore, this combination is defined as the interface problem (ii) and represents the next building block in the modular design of this thesis.
The description and the computation of the evolving crack surface, based on the actual status of a considered specimen is the key issue of **chapter 5** (*Crack path tracking strategies)*. In contrast to the two-dimensional case, where tracking the path in a C^0-continuous way is straightforward, three-dimensional crack path tracking requires additional strategies. We discuss the currently available approaches regarding this issue and further compare the approaches by means of usual quality measures. In the modular design of this thesis these algorithms represent the last main part which is classified as the crack tracking problem (iii).
Finally **chapter 6** (*Representative numerical examples)* verifies the finite element tool by comparisons of the computational results which experiments and benchmarks

of engineering fracture problems in concrete. Afterwards the finite element tool is applied to model folding induced fracture of geological structures.

7.2. Future work

Due to its modular nature, recall that the finite element tool is subdivided in the bulk problem (i), the interface problem (ii) and the crack tracking problem (iii) the proposed tool shows a great development potential:

- **In-elastic bulk materials.** Other kinds of materials can be treated by simply modifying the constitutive equations for the bulk problem (i). Especially accounting of inelastic bulk behavior in the pre-failure regime by means of the presented discretization scheme will be of great interest regarding ductile materials. Studies on strong discontinuities with plasticity can be found, e.g. in OLIVER et al. [149]. Here the strong discontinuity is introduced as the collapse of a weak-discontinuity governed by a bifurcation analysis of the underlying plasticity model. Recently there are further contributions on the modeling of large deformation plasticity with discrete failure models, see, e.g., MEDIAVILLA [121, 120, 122] for two-dimensional simulations or KHOEI [108] for the three-dimensional case.

- **Dynamic crack propagation.** Time dependent problems can be treated through a straight forward extension of the bulk problem. In particular, high impact failure and explosion of engineering structures can be simulated by adding transient terms, see, e.g., RUIZ et al. [168] for a time-dependent simulation of the brazilian test on concrete cylinders. Additionally, the transient terms enhance the possibilities for the choice of different time dependent bulk materials, see, e.g., SONG et al. [184] for a two-dimensional elasto-viscoplastic analyses of the KALTHOFF-WINKLER experiment. Adding time-dependence requires relatively small implementation modifications, depending on the chosen time-integration scheme. To save computational time, recent attempts on modeling the extended finite element method (XFEM) with explicit-time integration schemes can be found, e.g., in CHESSA [33], MENOUILLARD et al. [124]. We emphasize that the presented discretization scheme based on the purely deformation degrees of freedom seems to be more suited for explicit time integration, see, e.g. RABCZUK et al. [161].

- **Post-peak behavior.** Whereas the bulk problem treats the material behavior in the pre-failure regime, the corresponding post-peak behavior is represented through the interface problem (ii). Accordingly, dependent on the chosen type of material a suited cohesive traction separation relation can be developed to account for the softening response. Since this suggested framework relies on only very few material parameters and the examples have demonstrated that their fit is straightforward, cohesive laws seem to be ideally suited to incorporate a particular post peak-behavior in a phenomenological sense.

- **Material forces.** Concerning the crack tracking problem (iii) the consideration of the behavior of other kind of material requires corresponding crack propagation

criteria. A very promising and general technique is the computation of material or configurational forces, see, e.g., DENZER [46], DENZER et al. [47] or STEINMANN [189], [189]. However, the accurate computation of material forces within propagating fracture simulations requires an adequate re-solution of the finite element mesh at the crack tip or crack front, see, e.g., HEINTZ [89], FAGERSTRÖM [60] or CONSTANZO [39]. Furthermore, the crack propagation direction has to be determined based on the material force vectors. This is elegantly realized with r-apdative crack propagation algorithms since these approaches feature nodes directly at the crack tip or crack front. Accordingly, the crack propagation direction is given directly by a material force vector at this considered node, see, e.g., MIEHE & GÜRSES [131] or GÜRSES [82]. However, for inelastic materials this generates the same technical problems for the internal variables like usual remeshing approaches. Applying this concept of material forces within a crack propagation simulation by means of the presented phantom node approach requires the determination of the crack propagation direction by means of the nodal material forces of the considered discontinuous element. Clearly, the connection of the material force method with one of the available crack path tracking algorithms is the first required future task, whereas the other part concerns the accuracy of the nodal material forces within the presented discontinuous element. We are currently exploring the potential of the proposed algorithm of generalizations along these lines.

- **Stress and strain accuracy.** To increase the accuracy of the stress or strain computations on the considered crack tip or front (iii), hierarchical homogenization techniques are a proper choice, see, e.g., MERGHEIM [126], HUND [96], or WYART et al. [211]. Applying these techniques, a certain sub-structure is taken from the considered specimen. This sub-structure is refined on a scale of $1:1$ and then individually computed by means of boundary conditions depending on the computation of the complete specimen.

- **Multi-scale computations.** A further possible future task is to incorporate the underlying microstructure of the material. For micro-structures with dimensions much smaller than the considered global structure first order homogenization schemes can be applied. For microstructures for which scale separation is not valid a length scale information is needed and second order homogenization techniques can be applied. These homogenization techniques are suitable to demonstrate the influence of the underlying microstructure on the crack propagation problem, see, e.g., MEIER [123]. This can be used either for the modeling of the bulk material (i) or for the determination of the cohesive fracture parameters (ii), see, e.g., HIRSCHBERGER [92]. However, the computational effort increases considerably which may suggest the use of parallel computing. In summary, applying these techniques is desirable but up to now not straightforward for three-dimensional crack propagation analysis in engineering structures.

- **Crack branching and intersection.** A desirable extension of the present work is the treatment of branching or intersecting cracks during multiple crack propa-

gation simulation. Within two-dimensional computations of the extended finite element method this is elaborated by, e.g., DAUX et al. [40], ZI et al. [216] or BUDYN et al. [28]. For tree-dimensional applications within the present discretization scheme, the modeling of crack branching is possible, however, requires even more additional degrees of freedom than a single discontinuity. Broadly speaking, for a single crack surface, branching into two surfaces, the element degrees of freedom have at least to be tripled.

- **Discontinuities in biomechanics.** Regarding other engineering applications one main field of interest is the modeling of failure in biological materials. Within this field the presented approach can be used, e.g., to model the consequences of cutting processes during surgeries. Alternatively the propagation of arterial dissections can be treated, see, e.g., GASSER [73] or the modeling of biofilm growth can be considered, see, e.g., DUDDU [50].

- **Discontinuities in geophysics.** An interesting field which requires the modeling of discontinuities within a large deformation setting and many of the aforementioned technical future extensions is the modeling of fracture processes in geophysics. Based on our feasibility study on folding rocks we further summarize certain model-specific options. The folding model requires the embedment into a weaker incompressible medium. The stress accuracy at the crack tip has to be increased for what the hierarchical homogenization seems to a suitable procedure. In addition the mechanics of the crack onset have to be studied intensively to avoid spacing, i.e., the arising number of cracks with mesh-resolution. Here the use of strain softening constitutive equations in the pre-failure regime with a corresponding bifurcation analysis seems to be a promising approach. A coupled normal and tangential interface law could be another possible extension that would be relevant in many geophysic problems. In addition it would be interesting to account for the influence of fracture zones on the permeability of rocks. Recent attempts for capturing fracture mechanics with hydromechanics can be found, e.g., in JOX & MESCHKE[107]. Finally, it would be desirable to account for the influence of the temperature on fractures to accurately describe rock formation processes. For recent works in thermoelastic fracture mechanics we refer, e.g., to DUFLOT [52].

In summary the field of three-dimensional modeling of discrete failure is relatively new and wide open to many exiting applications. In this thesis, we have classified and compared existing schemes and designed a new modular three-component algorithm. We have demonstrated its potential to model brittle failure in cohesive frictional materials and we have illustrated new promising future applications.

A. Notation

Throughout this thesis all scalar quantities are denoted by standard (non-bold) symbols, e.g., α. All vector and tensor components are denoted with $[\bullet]_{i,..,l}$ and their related base vectors are orthonormal unit vectors $\boldsymbol{e}_{i,..,l}$. Thereby, vectors and tensors of second order are labeled with bold symbols. It should be emphasized that there is no difference in the notation of these quantities. Consequently, it follows from the context if we consider a vector or a tensor of second order. However, for the sake of clarity of this notation overview, we have chosen $\boldsymbol{a}$ and $\boldsymbol{b}$ as a placeholder for vectors and $\boldsymbol{A}$ and $\boldsymbol{B}$ as a placeholder for tensors of second order. Tensors of third order are denoted with bold symbols and an overset three, e.g., $\overset{3}{\boldsymbol{A}}$, and tensors of fourth order are labeled with a special font-type, e.g., $\mathbb{A}$.
In the following the notation is illustrated and the frequently used calculation rules are briefly summarized. Subsequently, the used notation for tensor analysis is presented with some particular derivatives which are frequently used, especially for linearization.

- **Tensor notation**

$$\begin{aligned} a &= [a] \\ \boldsymbol{a} &= [\boldsymbol{a}]_i \ \boldsymbol{e}_i \\ \boldsymbol{A} &= [\boldsymbol{A}]_{ij} \ \boldsymbol{e}_i \otimes \boldsymbol{e}_j \\ \overset{3}{\boldsymbol{A}} &= [\boldsymbol{A}]_{ijk} \ \boldsymbol{e}_i \otimes \boldsymbol{e}_j \otimes \boldsymbol{e}_k \\ \mathbb{A} &= [\mathbb{A}]_{ijkl} \ \boldsymbol{e}_i \otimes \boldsymbol{e}_j \otimes \boldsymbol{e}_k \otimes \boldsymbol{e}_l \end{aligned} \tag{A.1}$$

- **Kronecker symbol**

$$\delta_{ij} = \begin{cases} 1 & \text{for} \quad i = j \\ 0 & \text{for} \quad i \neq j \end{cases} \tag{A.2}$$

- **Permutation symbol**

$$\epsilon_{ijk} = \begin{cases} +1 & \text{for} \ \{ijk\} \ \text{even permutation of} \ \{1,2,3\} \\ -1 & \text{for} \ \{ijk\} \ \text{odd permutation of} \ \{1,2,3\} \\ 0 & \text{for} \quad \text{else} \end{cases} \tag{A.3}$$

- **Tensor contractions**

single contractions

$$\begin{aligned} a &= \boldsymbol{a}\cdot\boldsymbol{b} &&= [\boldsymbol{a}]_i\,[\boldsymbol{b}]_j \\ \boldsymbol{a} &= \boldsymbol{A}\cdot\boldsymbol{b} &&= [\boldsymbol{A}]_{ij}\,[\boldsymbol{b}]_j\;\boldsymbol{e}_i \\ \boldsymbol{A} &= \boldsymbol{A}\cdot\boldsymbol{B} &&= [\boldsymbol{A}]_{ik}\,[\boldsymbol{b}]_{kj}\;\boldsymbol{e}_i\otimes\boldsymbol{e}_j \end{aligned}$$

double contractions

$$\begin{aligned} a &= \boldsymbol{A}:\boldsymbol{B} &&= [\boldsymbol{A}]_{ij}\,[\boldsymbol{B}]_{ij} \\ \boldsymbol{a} &= \overset{3}{\boldsymbol{A}}:\boldsymbol{B} &&= [\overset{3}{\boldsymbol{A}}]_{ijk}\,[\boldsymbol{B}]_{jk}\,\boldsymbol{e}_i \\ \boldsymbol{A} &= \mathbb{A}:\boldsymbol{B} &&= [\mathbb{A}]_{ijkl}\,[\boldsymbol{B}]_{kl}\;\boldsymbol{e}_i\otimes\boldsymbol{e}_j \end{aligned} \tag{A.4}$$

- **Dyadic products**

standard

$$\begin{aligned} \boldsymbol{a}\otimes\boldsymbol{b} &= [\boldsymbol{a}]_i\;[\boldsymbol{b}]_j\,\boldsymbol{e}_i\otimes\boldsymbol{e}_j \\ \boldsymbol{A}\otimes\boldsymbol{B} &= [\boldsymbol{A}]_{ij}\;[\boldsymbol{B}]_{kl}\,\boldsymbol{e}_i\otimes\boldsymbol{e}_j\otimes\boldsymbol{e}_k\otimes\boldsymbol{e}_l \end{aligned}$$

non-standard

$$\begin{aligned} \boldsymbol{A}\,\overline{\otimes}\,\boldsymbol{B} &= [\boldsymbol{A}]_{ik}\;[\boldsymbol{B}]_{jl}\,\boldsymbol{e}_i\otimes\boldsymbol{e}_j\otimes\boldsymbol{e}_k\otimes\boldsymbol{e}_l \\ \boldsymbol{A}\,\underline{\otimes}\,\boldsymbol{B} &= [\boldsymbol{A}]_{il}\;[\boldsymbol{B}]_{jk}\,\boldsymbol{e}_i\otimes\boldsymbol{e}_j\otimes\boldsymbol{e}_k\otimes\boldsymbol{e}_l \end{aligned} \tag{A.5}$$

- **Special tensors**

second order unit tensor

$$\boldsymbol{I} = \delta_{ij}\,\boldsymbol{e}_i\otimes\boldsymbol{e}_j$$

fourth order unit tensor

$$\mathbb{I} = \delta_{ik}\,\delta_{jl}\,\boldsymbol{e}_i\otimes\boldsymbol{e}_j\otimes\boldsymbol{e}_k\otimes\boldsymbol{e}_l \tag{A.6}$$

transpose tensor

$$\boldsymbol{A}^t = [A]_{ji}\;\boldsymbol{e}_i\otimes\boldsymbol{e}_j = [A]_{ij}\;\boldsymbol{e}_j\otimes\boldsymbol{e}_i$$

inverse tensor

$$\boldsymbol{A}\cdot\boldsymbol{A}^{-1} = \boldsymbol{A}^{-1}\cdot\boldsymbol{A} = \boldsymbol{I}$$

symmetric tensor

$$\boldsymbol{A}^{sym} = \frac{1}{2}\left[\boldsymbol{A}+\boldsymbol{A}^t\right]$$

skew-symmetric tensor

$$\boldsymbol{A}^{skw} = \frac{1}{2}\left[\boldsymbol{A}-\boldsymbol{A}^t\right]$$

jump term

$$[\![\boldsymbol{a}]\!] = \boldsymbol{a}^+ - \boldsymbol{a}^-$$

third order permutation tensor

$$\overset{3}{\boldsymbol{e}} = \epsilon_{ijk}\,\boldsymbol{e}_i\otimes\boldsymbol{e}_j\otimes\boldsymbol{e}_k$$

- **Invariants of second order tensors**

$$\begin{aligned} \mathrm{I}_A &= \boldsymbol{A}:\boldsymbol{I} = \mathrm{tr}(\boldsymbol{A}) \\ \mathrm{II}_A &= \frac{1}{2}\left[[\boldsymbol{A}:\boldsymbol{I}]^2 - \boldsymbol{A}^2:\boldsymbol{I}\right] = \frac{1}{2}\left[\mathrm{tr}^2(\boldsymbol{A}) - \mathrm{tr}(\boldsymbol{A}^2)\right] \\ \mathrm{III}_A &= \det(\boldsymbol{A}) \end{aligned} \tag{A.7}$$

- **Tensor analysis**

gradient

$$\nabla_{\boldsymbol{x}} a(\boldsymbol{x}) = \frac{\partial a(\boldsymbol{x})}{\partial \boldsymbol{x}} = [a(\boldsymbol{x})]_{,i}\, \boldsymbol{e}_i$$
$$\nabla_{\boldsymbol{x}} \boldsymbol{a}(\boldsymbol{x}) = \frac{\partial \boldsymbol{a}(\boldsymbol{x})}{\partial \boldsymbol{x}} = [\boldsymbol{a}(\boldsymbol{x})]_{i,j}\, \boldsymbol{e}_i \otimes \boldsymbol{e}_j$$

divergence

$$\operatorname{div}\boldsymbol{a}(\boldsymbol{x}) = \nabla_{\boldsymbol{x}} \boldsymbol{a}(\boldsymbol{x}) : \boldsymbol{I} = [\boldsymbol{a}(\boldsymbol{x})]_{i,i}$$
$$\operatorname{div}\boldsymbol{A}(\boldsymbol{x}) = \nabla_{\boldsymbol{x}} \boldsymbol{A}(\boldsymbol{x}) : \boldsymbol{I} = [\boldsymbol{A}(\boldsymbol{x})]_{ij,j}\, \boldsymbol{e}_i$$

(A.8)

transformation formulas

$$\begin{aligned} \operatorname{div}[a\ \boldsymbol{A}] &= a \operatorname{div}\boldsymbol{A} + \boldsymbol{A} \cdot \nabla_{\boldsymbol{x}} a \\ \operatorname{div}[\boldsymbol{a} \cdot \boldsymbol{A}] &= \boldsymbol{a} \operatorname{div}\boldsymbol{A} + \boldsymbol{A} : \nabla_{\boldsymbol{x}} \boldsymbol{a} \end{aligned} \tag{A.9}$$

integral theorems

$$\begin{aligned} \int_{\partial\mathcal{B}} a\, \boldsymbol{n}\, \mathrm{d}a &= \int_{\mathcal{B}} \nabla_{\boldsymbol{x}} a\, \mathrm{d}V \\ \int_{\partial\mathcal{B}} \boldsymbol{a} \cdot \boldsymbol{n}\, \mathrm{d}a &= \int_{\mathcal{B}} \operatorname{div}\boldsymbol{a}\, \mathrm{d}V \\ \int_{\partial\mathcal{B}} \boldsymbol{A} \cdot \boldsymbol{n}\, \mathrm{d}a &= \int_{\mathcal{B}} \operatorname{div}\boldsymbol{A}\, \mathrm{d}V \\ \int_{\partial\mathcal{B}} \boldsymbol{a} \times \boldsymbol{A} \cdot \boldsymbol{n}\, \mathrm{d}a &= \int_{\mathcal{B}} [\boldsymbol{a} \times \operatorname{div}\boldsymbol{A} + \nabla_{\boldsymbol{x}} \boldsymbol{a} \times \boldsymbol{A}]\, \mathrm{d}V \end{aligned} \tag{A.10}$$

derivatives of second order tensors

$$\begin{aligned} \frac{\partial \boldsymbol{A}}{\boldsymbol{A}} &= \boldsymbol{I} \mathbin{\overline{\otimes}} \boldsymbol{I} \\ \frac{\partial \boldsymbol{A}^t}{\boldsymbol{A}} &= \boldsymbol{I} \mathbin{\underline{\otimes}} \boldsymbol{I} \\ \frac{\partial \boldsymbol{A}^{-1}}{\boldsymbol{A}} &= -\boldsymbol{A}^{-1} \mathbin{\overline{\otimes}} \boldsymbol{A}^{-t} \\ \frac{\partial \boldsymbol{A}^{-t}}{\boldsymbol{A}} &= -\boldsymbol{A}^{-t} \mathbin{\underline{\otimes}} \boldsymbol{A}^{-1} \end{aligned}$$

derivatives of invariants

$$\begin{aligned} \frac{\partial \mathrm{I}_A}{\partial \boldsymbol{A}} &= \boldsymbol{I} \\ \frac{\partial \mathrm{II}_A}{\partial \boldsymbol{A}} &= \operatorname{tr}(\boldsymbol{A})\boldsymbol{I} - \boldsymbol{A}^t \\ \frac{\partial \mathrm{III}_A}{\partial \boldsymbol{A}} &= \det(\boldsymbol{A})\, \boldsymbol{A}^{-1} \end{aligned}$$

(A.11)

further derivatives

$$\begin{aligned} \frac{\partial |\boldsymbol{a}|}{\partial \boldsymbol{a}} &= \frac{\boldsymbol{a}}{|\boldsymbol{a}|} \\ \frac{\partial}{\partial \boldsymbol{a}} \left[\frac{1}{|\boldsymbol{a}|}\right] &= -\frac{\boldsymbol{a}}{|\boldsymbol{a}|^3} \end{aligned} \tag{A.12}$$

Bibliography

[1] D. Adelsteinsson and J.A. Sethian. The fast construction of extension velocities in level set methods. *Journal of Computational Physics*, 148(1):2–22, 1999. 3

[2] J. Altenbach and H. Altenbach. *Einführung in die Kontinuumsmechanik*. B.G. Teubner, Stuttgart, 1 edition, 1994. 2.1, 2.4.1, 2.5, 2.5

[3] J. Altenbach and A.S. Sacharov. *Die Methode der finiten Elemente in der Festkörpermechanik*. Carl Hanser Verlag, München, 1 edition, 1982. 2.1, 2.6.3, 3.4.3

[4] P.M.A. Areias and T. Belytschko. Analysis of three-dimensional crack initiation and propagation using the extended finite element method. *Int. J. Numer. Methods Engng.*, 63(5):760–788, 2005. 1.2, 3.1, 3.4, 4.1, 4.4.6, 5.1, 5.3.3, 6.2.2

[5] P.M.A Areias and T. Belytschko. Non-linear analysis of shells with arbitrary evolving cracks using XFEM. *Int. J. Numer. Methods Engng.*, 62(3):384–415, 2005. 3.1, 3.3.1

[6] P.M.A. Areias and T. Belytschko. A comment on the article 'A finite element method for simulation of strong and weak discontinuities in solid mechanics' By A. Hansbo and P. Hansbo [Comput. methods Appl. Mech. Engrg. 193 (2004) 3523-3540]. *Comput. Methods Appl. Mech. Engrg.*, 195(9-12):1275–1276, 2006. 1.2, 3.1, 3.3.1

[7] P.M.A. Areias, J.M.A.C. de Sa, C.A.C. Antonio, J.A.S.A.Q. Carneiro, and V.M.P. Teixeira. Strong displacement discontinuities and Lagrange multipliers in the analysis of finite displacement fracture problems. *Comput. Mech.*, 35(1):54–71, 2004. 4.1, 4.6.1

[8] P.M.A. Areias and T. Rabczuk. Quasi-static crack propagation in plane and plate structures using set-valued traction-separation laws . *Int. J. Numer. Methods Engng.*, 74(3):475–505 , 2008. 1.2, 4.1, 4.4.5

[9] P.M.A. Areias, J.H. Song, and T. Belytschko. Analysis of fracture in thin shells by overlapping paired elements. *Comput. Methods Appl. Mech. Engrg.*, 195(41-43):5343–5360, 2006. 3.1

[10] F. Armero and K. Garikipati. An analysis of strong discontinuities in multiplicative finite strain plasticity and their relation with the numerical simulation of strain localization in solids. *Int. J. Solids Struct.*, 33(20-22):2863–2885, 1996. 1.2, 4.1, 4.2

[11] F. Armero and C. Linder. New finite elements with embedded strong discontinuities in the finite deformation range. *Comput. Methods Appl. Mech. Engrg.*, 197(33-40):3138–3170, 2008. 1.2, 3.1, 3.2

[12] H. Askes, L.J. Sluys, and B.B.C. de Jong. Remeshing techniques for r-adaptive and combined h/r-adaptive analysis with application to 2D/3D crack propagation. *Struct. Eng. Mech.*, 12(5):475–490, 2001. 1.2, 5.1

[13] I. Babuska and J.M. Melenk. The partition of unity method. *Int. J. Numer. Methods Engng.*, 40(4):727–758, 1997. 1.2, 3.1, 3.3.1

[14] A. Bakker. *The Three-Dimensional J-Integral*. PhD thesis, Delft University of Technology, 1984. 1.2

[15] G.I. Barenblatt. The mathematical-theory of equilibrium cracks in brittle-fracture. *Advances in Appl. Mech.*, 7:55–129, 1962. 1.2, 4.1, 4.4

[16] K.J. Bathe. *Finite-Elemente-Methoden*. Springer Verlag, Berlin, 1 edition, 1995. 2.1, 2.6.5

[17] T. Belytschko and T. Black. Elastic crack growth in finite elements with minimal remeshing. *Int. J. Numer. Methods Engng.*, 45(5):601–620, 1999. 1.2, 3.1, 3.2, 3.3.1

[18] T. Belytschko, N. Moës, S. Usui, and C. Parimi. Arbitrary discontinuities in finite elements. *Int. J. Numer. Methods Engng.*, 50(4):993–1013, 2001. 1.2

[19] T. Belytschko, C. Parimi, N. Moës, N. Sukumar, and S. Usui. Structured extended finite element methods for solids defined by implicit surfaces. *Int. J. Numer. Methods Engng.*, 56(4):609–635, 2003. 1.2, 5.1, 5.3.6

[20] S. Bergbauer and D. Pollard. A new conceptual fold-fracture model including prefolding joints, based on Emigrant gap anticline wyoming. *Geological Society of America bulletin*, 116(3-4):294–307, 2004. 6.3

[21] M.A. Biot. Theroy of folding of stratified viscoelastic media and its implications in tectonics and orogenesis. *Geological Society of America bulletin*, 72(11):1595–1602, 2004. 6.3

[22] P. Bocca. The Application of pull-out tests to high strenght concrete estimation. *Materials and Structures*, 17(3):1359–5997, 1984. 6.2.2

[23] G. Bolzon. Formulation of a triangular finite element with an embedded interface via isoparametric mapping. *Comput. Mech.*, 27(6):463–473 , 2001. 1.2

[24] S. Bordas, C. Dugnant, and A. Guidoum and. H. Nguyen-Dang. An extended finite element library. *Int. J. Numer. Methods Engng.*, 71(6):703–732, 2007. 3.1, 3.4

[25] S. Bordas and B. Moran. Enriched finite elements and level sets for damage tolerance assessment of complex structures. *Engng. Fract. Mech.*, 73(9):1176–1201, 2006. 1.2, 5.1, 5.3.6

[26] D.R. Brokenshire. *A Study of Torsion Fracture Tests*. PhD thesis, University of Wales, Cardiff, 1995. 6.2.4

[27] F.G. Buchholz, V. Just, and H.A. Richard. Computational simulation and experimental findings of three-dimensional fatigue crack growth in a single-edge notched specimen under torsion loading. *Fatigue and Fracture of Engeneering Materials and Structures*, 28(1-2):127–134, 2005. 5.1

[28] E. Budyn, G. Zi, N. Moës, and T. Belytschko. A method for multiple crack growth in brittle materials without remeshing. *Int. J. Numer. Methods Engng.*, 61(10):1741–1770, 2004. 3.4.4, 7.2

[29] P. Burchard, L.T. Cheng, B. Merriman, and S. Osher. Motion of curves in three spatial dimensions using a level set approach. *Journal of Computational Physics*, 170(2):720–741, 2001. 1.2, 5.3.6, 5.3.17

[30] G.T. Camacho and M. Ortiz. Computational modelling of impact damage in brittle materials. *Int. J. Solids Struct.*, 33(20-22):2899–2938, 1996. 4.1, 4.4.2

[31] T. Cecil and D.E. Marthaler. A variational approach to path planning in three dimensions using level set methods. *Journal of Computational Physics*, 211(1):179–197, 2006. 1.2, 5.3.15

[32] M. Cervera and M. Chiumenti. Mesh objective tensile cracking via a local continuum damage model and a crack tracking technique. *Comput. Methods Appl. Mech. Engrg.*, 196(1-3):304–320, 2006. 1.2, 5.1, 5.3.5

[33] J. Chessa and T. Belytschko. Arbitrary discontinuities in space-time finite elements by level sets and X-FEM. *Int. J. Numer. Methods Engng.*, 61(15):2595–2614, 2004. 1.2, 5.1, 5.3.6, 7.2

[34] J. Chessa, H.W. Wang, and T. Belytschko. On the construction of blending elements for local partition of unity enriched finite elements. *Int. J. Numer. Methods Engng.*, 57:1015–1038, 2003. 3.1, 3.3.1

[35] R. Citarella and M. Perrella. Multiple surface crack propagation: numerical simulations and experimental tests. *Fatigue and Fracture of Engeneering Materials and Structures*, 28(1-2):135–148, 2005. 1.2

[36] H. Cloos. Gang und Gewehrk einer Falte. *Zeitschrift der deutschen Gesellschaft für Geowissenschaften*, 100(4):290–303, 1948. 6.3

[37] C. Comi, S. Mariani, and U. Perego. An extended FE strategy for transition from continuum damage to mode I cohesive crack propagation . *International Journal for Numerical and Analytical Methods in Geomechanics*, 31(2):213–238, 2007. 4.1, 4.4.6

[38] J.W. Cosgrove and M.S. Ameen. Forced folds and fractures. *Geological Society - Special publication - Elseviewer*, 169, 2001. 6.3

[39] F. Costanzo. An analysis of 3D crack propagation using cohesive zone models and the theory of configurational forces. *Mathematics and Mechanics of Solids*, 6(2):149–173, 2001. 1.2, 7.2

[40] C. Daux, N. Moës, J. Dolbow, N. Sukumar, and T. Belytschko. Arbitrary branched and intersecting cracks with the extended finite element method. *Int. J. Numer. Methods Engng.*, 48(12):1741–1760, 2000. 7.2

[41] R. de Borst. *Non-linear Analysis of Frictional Materials*. PhD thesis, Delft University of Technology, 1986. 1.2, 6.2.2

[42] R. de Borst. Numerical aspects of cohesive-zone models. *Engng. Fract. Mech.*, 70(14):1743–1757, 2003. 1.2, 4.1, 4.4

[43] R. de Borst, M.A. Gutierrez, G.N. Wells, J.J.C. Remmers, and H. Askes. Cohesive-zone models, higher-order continuum theories and reliability methods for computational failure analysis. *Int. J. Numer. Methods Engng.*, 60(1):289–315, 2004. 1.2, 4.1, 4.4, 4.6.1

[44] R. de Borst, J.J.C. Remmers, and A. Needleman. Mesh-independent discrete numerical representations of cohesive-zone models. *Engng. Fract. Mech.*, 73(2):160–177, 2006. 1.2, 4.1, 4.4, 4.4.2, 4.6.1

[45] R. de Borst, J.J.C. Remmers, A. Needleman, and M.A. Abellan. Discrete vs smeared crack models for concrete fracture: bridging the gap. *International Journal for Numerical and Analytical Methods in Geomechanics*, 28(7-8):583–607, 2004. 1.2, 3.1, 3.2

[46] R. Denzer. *Computational Configurational Mechanics*. PhD thesis, Kaiserslautern University of Technology, 2006. 1.2, 7.2

[47] R. Denzer, F.J. Barth, and P. Steinmann. Studies in elastic fracture mechanics based on the material force method. *Int. J. Numer. Methods Engng.*, 58(12):1817–1835, 2003. 1.2, 7.2

[48] J. Dolbow, N. Moës, and T. Belytschko. Discontinuous enrichment in finite elements with a partition of unity method. *Finite Elements in Analysis and Design*, 36(3-4):235–260, 2000. 1.2, 3.1, 3.3.1, 3.4.4

[49] J. Dolbow, N. Moës, and T. Belytschko. An extended finite element method for modeling crack growth with frictional contact. *Comput. Methods Appl. Mech. Engrg.*, 190(51-52):6825–6846, 2001. 4.1, 4.4.4

[50] R. Duddu, S. Bordas, D. Chopp, and B. Moran. A combined extended finite element and level set method for biofilm growth. *Int. J. Numer. Methods Engng.*, 74(5):848–870, 2008. 1.2, 7.2

[51] M. Duflot. A study of the representation of cracks with level sets. *Int. J. Numer. Methods Engng.*, 70(11):1261–1302, 2007. 1.2, 5.3.17

[52] M. Duflot. The extended finite element method in thermoelastic fracture mechanics. *Int. J. Numer. Methods Engng.*, 74(5):827–847 , 2008. 7.2

[53] D.S. Dugdale. Yielding of steel sheets containing slits. *J. Mech. Phys. Solids*, 8(2):100–104, 1960. 1.2, 4.1, 4.4

[54] P. Dumstorff. *Modellierung und numerische Simulation von Rissfortschritt in spröden und quasi-spröden Materialien auf der Basis der Extended Finite Element Method*. PhD thesis, Ruhr-Universität Bochum, 2006. 3.3.1, 6.2.1

[55] P. Dumstorff and G. Meschke. Crack propagation criteria in the framework of X-FEM-based structural analyses. *International Journal for Numerical and Analytical Methods in Geomechanics*, 31(2):239–259, 2007. 1.2, 5.1, 5.3.5, 6.2.1

[56] E.N. Dvorkin, A.M. Cuitino, and G. Gioia. Finite-elements with displacement interpolated embedded localization lines insensitive to mesh size and distortions. *Int. J. Numer. Methods Engng.*, 30(3):541–564, 1990. 1.2

[57] W. Eduardo and V. Chaves. Tracking 3D crack path. *International Conference on Mathematical and Statistical Modeling in Honor of Enrique Castillo*, 2006. 1.2, 5.1, 5.3.5

[58] L. Elfgren, R. Eligehausen, and J.G. Rots. Anchor bolts in concrete structures: summary of round robin tests and analysis arranged by RILEM TC 90-FMA 'Fracture Mechanics of Concrete - Applications'. *Materials and Structures*, 34(242):451–457, 2001. 6.2.2

[59] J. Englund. A higher order scheme for two-dimensional quasi-static crack growth simulations. *Comput. Methods Appl. Mech. Engrg.*, 196(21-24):2527–2538, 2007. 3.1, 3.3.1

[60] Martin Fagerström. *Modelling of large deformation crack propagation based on the extended finite element method*. PhD thesis, Chalmers University of Technology, 2007. 1.2, 7.2

[61] C. Feist and G. Hofstetter. An embedded strong discontinuity model for cracking of plain concrete. *Comput. Methods Appl. Mech. Engrg.*, 195(52):7115–7138, 2007. 1.2, 5.1, 5.3.5, 5.3.5, 6.2.3

[62] C. Feist and G. Hofstetter. Three-dimensional fracture simulations based on the SDA. *International Journal for Numerical and Analytical Methods in Geomechanics*, 31(2):189–212, 2007. 1.2, 5.1, 5.3.2, 5.3.5, 6.2, 6.2.2

[63] C. Feist and G. Hofstetter. Validation of 3D crack propagation in plain concrete. Part I: Experimental investigation - the PCT3D test. *Computers and Concrete*, 4(1):49–66, 2007. 5.1, 5.3.4, 6.2

[64] A. Frangi. Fracture propagation in 3D by the symmetric Galerkin boundary element method. *International Journal of Fracture*, 116(4):313–330, 2002. 1.2

[65] N.E. Frost and D.S. Dugdale. The propagation of fatigue crack in sheet specimens. *Journal of the Mechanics and Physics of Solids*, 6(2):91–110, 1958. 1.2

[66] R.H. Gallagher. *Finite-Element-Analysis*. Springer Verlag, Berlin, 1 edition, 1976. 3.4.3

[67] J.C. Galvez, D.A. Cendon, and J. Planas. Influence of shear parameters on mixed-mode fracture of concrete. *International Journal of Fracture*, 118(2):163–189, 2002. 6.1

[68] J.C. Galvez, M. Elices, G.V. Guinea, and J. Planas. Mixed mode fracture of concrete under proportional and nonproportional loading. *International Journal of Fracture*, 94(3):267–284, 1998. 6.1

[69] T.C. Gasser. Validation of 3D crack propagation in plain concrete. Part II: Computational modeling and predictions of the PCT3D test. *Computers and Concrete*, 4(1):67–82, 2007. 1.2, 4.1, 4.4.6, 5.1, 5.3.4, 6.2

[70] T.C. Gasser and G.A. Holzapfel. Geometrically non-linear and consistently linearized embedded strong discontinuity models for 3D problems with an application to the dissection analysis of soft biological tissues. *Comput. Methods Appl. Mech. Engrg.*, 192(47-48):5059–5098, 2003. 1.2, 4.1, 4.3.3, 4.4, 4.4.6, 5.1

[71] T.C. Gasser and G.A. Holzapfel. Modeling 3D crack propagation in unreinforced concrete using PUFEM. *Comput. Methods Appl. Mech. Engrg.*, 194(25-26):2859–2896, 2005. 1.2, 3.1, 3.2, 3.4, 4.1, 4.2, 4.3.3, 4.4, 5.1, 5.2.2, 5.3.2, 6.2.2, 6.2.2

[72] T.C. Gasser and G.A. Holzapfel. 3D Crack propagation in unreinforced concrete: A two-step algorithm for tracking 3D crack paths. *Comput. Methods Appl. Mech. Engrg.*, 195(37-40):5198–5219, 2006. 1.2, 5.1, 5.3.2, 5.3.2, 5.3.4, 6.2.3, 6.2.4

[73] T.C. Gasser and G.A. Holzapfel. Modeling the propagation of arterial dissection. *Euro. J. Mech. A/Solids*, 25(4):617–633, 2006. 1.2, 5.1, 7.2

[74] M.G.D. Geers. Enhanced solution control for physically and geometrically non-linear problems. Part I - The subplane control approach. *Int. J. Numer. Methods Engng.*, 46(2):177–204 , 1999. 4.1, 4.5.2

[75] M.G.D. Geers. Enhanced solution control for physically and geometrically non-linear problems. Part II - Comparative performance analysis. *Int. J. Numer. Methods Engng.*, 46(2):205–230, 1999. 4.1

[76] M.G.D. Geers, R. de Borst, and R.H.J. Peerlings. Damage and crack modeling in single-edge and double edge notched concrete beams. *Engng. Fract. Mech.*, 65(2-3):247–261, 2000. 4.1, 4.5.2, 6.1, 6.2

[77] M. Gosz, J. Dolbow, and B. Moran. Domain integral formulation for stress intensity factor computation along curved three-dimensional interface cracks. *Int. J. Solids Struct.*, 35(15):1763–1783, 1998. 1.2, 3.5, 5.3.14

[78] M. Gosz and B. Moran. An interaction energy integral method for computation of mixed-mode stress intensity factors along non-planar crack fronts in three dimensions. *Engng. Fract. Mech.*, 69(3):299–319, 2002. 1.2, 3.5, 5.3.14

[79] P. Grassl and M. Jirasek. Plastic model with non-local damage applied to concrete. *International Journal for Numerical and Analytical Methods in Geomechanics*, 30(1):71–90, 2006. 1.2, 5.1, 5.3.2

[80] A. Gravouil, N. Moës, and T. Belytschko. Non-planar 3D crack growth by the extended finite element and level sets - Part II: Level set update. *Int. J. Numer. Methods Engng.*, 53(11):2569–2586, 2002. 1.2, 5.1, 5.3.6, 5.3.14, 3, 5.3.15, 5.3.16, 5.3.17

[81] D. Gross and Th. Seelig. *Bruchmechanik*. Springer Verlag, Berlin, 3 edition, 2001. 1.2, 3.1, 3.4.4, 5.2.1

[82] E. Gürses. *Aspects of Energy minimization in Solid Mechanic: Evolution of Inelastic Microstructures and Crack Propagation*. PhD thesis, Universität Stuttgart, 2007. 1.2, 6.2.4, 7.2

[83] H.G. Hahn. *Bruchmechanik*. Teubner Verlag, Stuttgart, 1 edition, 1976. 1.2, 3.1, 3.4.4

[84] P. Hancock. Brittle microtectonics: Principles and practise. *Journal of Structural Geology*, 7(3-4):437–457, 1985. 6.3

[85] A. Hansbo and P. Hansbo. An unfitted finite element method, based on Nitsche's method, for elliptic interface problems. *Comput. Methods Appl. Mech. Engrg.*, 191(47-48):5537–5552, 2002. 1.2, 3.1, 3.2

[86] A. Hansbo and P. Hansbo. A finite element method for the simulation of strong and weak discontinuities in solid mechanics. *Comput. Methods Appl. Mech. Engrg.*, 193(33-35):3523–2540, 2004. 1.2, 3.1, 3.2

[87] A. Hansbo, P. Hansbo, and M.G. Larson. A finite element method on composite grids based on Nitsche's method. *ESAIM- mathematical modelling and numerical analysis modelisation mathematique et analyse numerique*, 37(3):495–514, 2003. 1.2

[88] S. Hardy and E. Finch. Discrete element modeling of detached folding. *Basin Research*, 17(4):507–520, 2005. 6.3.6

[89] P.C.J. Heintz. *Finite Element Procedures for the Numerical Simulation of Crack Propagation and Bilateral Contact*. PhD thesis, Chalmers University of Technology, 2006. 1.2, 7.2

[90] A. Hillerborg. Analysis of crack formation and crack growth by means of fracture mechanics and finite elements. *Cement Concrete Research*, 6:773–782, 1976. 1.2, 4.1, 4.4

[91] A. Hillerborg. Application of the fictitious crack model to different types of materials. *International Journal of Fracture*, 51(2):95–102, 1991. 4.1, 4.4

[92] C.B. Hirschberger. *A treatise on Micromorphic Continua. Theory, Homogenization, Computation*. PhD thesis, Kaiserslautern University of Technology, 2008. 7.2

[93] G. A. Holzapfel. *Nonlinear Solid Mechanics*. John Wiley & Sons, LTD, 1 edition, 2001. 2.1, 2.2, 2.5, 2.6.2

[94] R. Huang, N. Sukumar, and J.H. Prevost. Modeling quasi-static crack growth with the extended finite element method Part II: Numerical applications. *Int. J. Solids Struct.*, 40(26):7539–7552, 2003. 1.2

[95] O. Huber, J. Nickel, and G. Kuhn. On the decomposition of the J-integral for 3D crack problems. *International Journal of Fracture*, 64:339–348, 1993. 1.2, 5.3.14

[96] A.S. Hund. *Hierarchische Mehrskalenmmodellierung des Versagens von Werkstoffen mit Mikrostruktur*. PhD thesis, Universität Stuttgart, 2007. 6.2.1, 7.2

[97] G.R. Irvine. "Fracture". *Handbuch der Physik, Springer, Berlin*, 6:551–590, 1958. 3.4.4

[98] P. Jäger, J. Mergheim, E. Kuhl, and P. Steinmann. Modelling and Computation of 3D Discontinuities in Solids. PAMM, Proceedings of the GAMM Annual Meeting Berlin, WILEY-VCH Verlag, 2006. 3.1, 3.2, 4.1, 4.6.1, 4.6.2

[99] P. Jäger, S.M. Schmalholz, D.W. Schmid, and E. Kuhl. Brittle fracture during folding of rocks: A finite element study. *Philosophical Magazine*, 88(28-29):3245–3263, 2008. 3.1, 3.4, 5.1, 5.3.5, 6.1, 6.9

[100] P. Jäger, P. Steinmann, and Kuhl E. Modeling three-dimensional crack propagation - A comparison of crack path tracking strategies. *Int. J. Numer. Methods Engng.*, 76(9):1328–1352, 2008. 3.1, 3.3.1, 5.1, 5.4

[101] P. Jäger, P. Steinmann, and E. Kuhl. Global crack path tracking in three-dimensional brittle fracture . *ASME J. Appl. Mech.*, submitted for publication, 2008. 5.1, 5.3.5, 6.1

[102] P. Jäger, P. Steinmann, and E. Kuhl. On local tracking algorithms for the simulation of three-dimensional discontinutities. *Comput. Mech.*, 42(3):395–406, 2008. 3.1, 4.1, 4.4.2, 4.6.2, 5.1, 5.4

[103] A.D. Jefferson, B.I.G. Barr, T. Bennet, and S.C. Hee. Three dimensional finite element simulation of fracture tests using the Craft concrete model. *Computers and Concrete*, 3(1):261–284, 2004. 6.2.4

[104] M. Jirasek, S. Rolshoven, and P. Grassl. Size effect on fracture energy induced by nonlocality. *International Journal for Numerical and Analytical Methods in Geomechanics*, 28(7-8):653–670, 2004. 1.2, 5.1, 5.3.2

[105] M. Jirasek and T. Zimmermann. Embedded crack model: I. basic formulation. *Int. J. Numer. Methods Engng.*, 50(6):1269–1290, 2001. 1.2

[106] M. Jirasek and T. Zimmermann. Embedded crack model: II. Combination with smear cracks. *Int. J. Numer. Methods Engng.*, 50(6):1291–1305, 2001. 1.2

[107] S. Jox, P. Dumstorff, and G. Meschke. Aspects of crack propagation and hydro-mechanical coupling using X-FEM. Proceedings: III European Conference on Computational Mechanics Solids, Structures and Coupled Problems in Engineering C.A. Mota Soares et.el. (Eds.), 5-8 June, 2006. 7.2

[108] A.R. Khoei, S.O.R. Biabanaki, and M. Anahid. Extended finite element method for three-dimensional large plasticity deformations on arbitrary interfaces. *Comput. Methods Appl. Mech. Engrg.*, 197(9-12):1100–1114, 2008 . 7.2

[109] K. Kolk and G. Kuhn. A predictor-corrector scheme for the optimization of 3D crack front shapes. *Fatigue and Fracture of Engeneering Materials and Structures*, 28(1-2):117–126, 2005. 1.2, 5.1

[110] K. Kolk and G. Kuhn. The advanced simulation of fatigue crack growth in complex 3D structures. *Arch. Appl. Mech.*, 76(11-12):699–709, 2006. 1.2, 5.1

[111] O. Krol. *Thermo-mechanical modelling of solids and interfaces - theory, numerics and applications -*. PhD thesis, Kaiserslautern University of Technology, 2007. 4.1, 4.3.2

[112] E. Kuhl, P. Jäger, J. Mergheim, and P. Steinmann. On the application of Hansbo's method for interface problems. Proceedings of the IUTAM Symposium on Discretization Methods for Evolving Discontinuities, Combescure A, de Borst R, Belytschko T (Eds), Springer Verlag, 2006. 3.1, 3.2

[113] M. Kuna. *Numerische Beanspruchung von Rissen*. Vieweg + Teubner, Wiesbaden, 1 edition, 2008. 1.2, 3.1, 3.5

[114] A. Legay, H.W. Wang, and T. Belytschko. Strong and weak arbitrary discontinuities in spectral finite elements. *Int. J. Numer. Methods Engng.*, 64(8):991–1008, 2005. 3.1, 3.3.1

[115] T. Liebe. *Theory and numerics of higher gradient inelastic material behavior*. PhD thesis, Kaiserslautern University of Technology, 2003. 1.2

[116] O.L. Manzoli and P.B. Shing. A general technique to embed non-uniform discontinuities into standard solid finite elements. *Comput. Struct.*, 84(10-11):742–757, 2006. 4.1, 4.6.1, 6.2.3

[117] S. Marfia and E. Sacco. A fracture evolution procedure for cohesive materials. *International Journal of Fracture*, 110(3):241–261 , 2001. 4.1, 4.4

[118] S. Marfia and E. Sacco. Numerical techniques for the analysis of crack propagation in cohesive materials. *Int. J. Numer. Methods Engng.*, 57(11):1577–1602 , 2003. 4.1, 4.4, 4.4.6

[119] H. McQuillan. Small-scale fracture density in asmari foundation of southwest iran and its relation to bed thickness and structural setting. *The American Association of Petroleum Geologists Bulletin AAPPG*, 57(12):2367–2385, 1973. 6.3

[120] J. Mediavilla, R.H.J. Peelings, and M.G.D. Geers. Discrete crack modelling of ductile fracture driven by non-local softening plasticity. *Int. J. Numer. Methods Engng.*, 66(4):661–688, 2006. 7.2

[121] J. Mediavilla, R.H.J. Peerlings, and M.G.D. Geers. An integrated continuous-discontinuous approach towards damage engineering in sheet metal forming processes. *Engng. Fract. Mech.*, 73(7):895–916, 2006. 7.2

[122] J. Mediavilla, R.H.J. Peerlings, and M.G.D. Gem. A robust and consistent remeshing-transfer operator for ductile fracture simulations. *Comput. Struct.*, 84(8-9):604–623, 2006. 7.2

[123] H.A. Meier, P. Steinmann, and E. Kuhl. Towards multiscale computation of confined granular media - Contact forces, stresses and tangent operators -. *Technische Mechanik*, 4:165–175, 2008. 7.2

[124] T. Menouillard, J. Réthore, N. Moës, A. Combescure, and H. Bung. Mass lumping strategies for X-FEM explicit dynamics: Application to crack propagation . *Int. J. Numer. Methods Engng.*, 74(3):447–474 , 2008. 3.3.1, 7.2

[125] J. Mergheim. *Computational Modeling of Strong and Weak Discontinuities*. PhD thesis, Kaiserslautern University of Technology, 2006. 1.2, 3.1, 3.2, 4.1, 4.3.3, 4.4.2, 4.4.1, 5.1, 5.3.2, 5.4.1

[126] J. Mergheim. A variational multiscale method to model crack propagation at finite strains. *Int. J. Numer. Methods Engng.*, submitted for publication, 2008. 7.2

[127] J. Mergheim, E. Kuhl, and P. Steinmann. A finite element method for the computational modelling of cohesive cracks. *Int. J. Numer. Methods Engng.*, 63(2):276–289, 2005. 1.2, 3.1, 3.2, 4.1, 4.4.2, 5.1, 5.3.2

[128] J. Mergheim, E. Kuhl, and P. Steinmann. Towards the algorithmic treatment of 3D strong discontinuities. *Commun. Numer. Methods Engng.*, 23(2):97–108, 2007. 3.1, 3.4, 4.1, 4.3.3, 4.6.1, 4.6.2, 5.1, 5.4.1

[129] J. Mergheim and P. Steinmann. A geometrically nonlinear FE approach for the simulation of strong and weak discontinuities. *Comput. Methods Appl. Mech. Engrg.*, 195(37-40):5037–5052, 2006. 1.2, 3.1, 3.2, 4.1, 4.3.3

[130] G. Meschke and P. Dumstorff. Energy-based modeling of cohesive and cohesionless cracks via X-FEM. *Comput. Methods Appl. Mech. Engrg.*, 196(21-24):2388–2357, 2007. 4.1, 4.4, 4.4.3, 6.2.3

[131] C. Miehe and E. Gürses. A robust algorithm for configurational-force-driven brittle crack propagation with r-adaptive mesh alignment. *Int. J. Numer. Methods Engng.*, 72(2):127–155, 2007. 1.2, 7.2

[132] N. Moës, E. Bechét, and M. Tourbier. Imposing dirichlet boundary conditions in the extended finite element method. *Int. J. Numer. Methods Engng.*, 67(12):1641–1669 , 2006 . 4.1, 4.5.2

[133] N. Moës and T. Belytschko. Extended finite element method for cohesive crack growth. *Engng. Fract. Mech.*, 69(7):813–833, 2002. 4.1, 4.4

[134] N. Moës, A. Gravouil, and T. Belytschko. Non-planar 3D crack growth by the extended finite element and level sets-Part I: Mechanical model. *Int. J. Numer. Methods Engng.*, 53(11):2549–2568, 2002. 1.2, 5.1, 5.3.6, 5.3.14, 5.3.16

[135] J.F. Molinari, G. Gazonas, R. Raghupathy, A. Rusinek, and F. Zhou. The cohesive element approach to dynamic fragmentation: The question of energy convergence. *Int. J. Numer. Methods Engng.*, 69(3):484–503 , 2007 . 4.4.3

[136] N. Molino, Z.S. Bao, and R. Fedkiw. A virtual node algorithm for changing mesh topology during simulation. *ACM transactions on graphics*, 23(3):385–392, 2004. 3.1, 3.3.1

[137] B. Moran and C.F. Shih. A general treatment of crack tip contour integrals. *International Journal of Fracture*, 35(4):295–310, 1987. 3.5

[138] J. Mosler. *Finite Elemente mit sprungstetigen Abbildungen des Verschiebungsfeldes für numerische Analysen lokalisierter Versagenszustände in Tragwerken*. PhD thesis, Ruhr-Universität Bochum, 2002. 1.2, 3.2

[139] J. Mosler. A novel algorithmic framework for the numerical implementation of locally embedded strong discontinuities. *Comput. Methods Appl. Mech. Engrg.*, 194(45-47):4731–4757, 2005. 1.2

[140] J. Mosler. Modeling strong discontinuities at finite strains - A novel numerical implementation. *Comput. Methods Appl. Mech. Engrg.*, 195(33-36):4396–4419, 2006. 5.1

[141] A. Needleman. An analysis of decohesion along an imperfect interface. *International Journal of Fracture*, 42(1):21–40, 1990. 1.2, 4.1, 4.4

[142] J. Nitsche. Über ein Variationsprinzip zur Lösung von Dirichlet-Problemen bei Verwendung von Teilräumen, die keinen Randbedingungen unterworfen sind. *Abh. Math. Sem. Univ. Hamburg*, 36(1):9–15, 971. 1.2

[143] M.B. Nooru-Mohamed. *Mixed-Mode fracture of Concrete an experimental approach*. PhD thesis, Delft University of Technology, 1992. 6.2.3, 6.2.3

[144] J.F. O'Brien and J.K. Hodgins. Graphical modeling and animation of brittle fracture. SIGGRAPH 99 Conference Proceedings : 26th International Conference on Computer Graphics and Interactive Techniques Los Angeles, 1999. 3.1, 3.4.3

[145] R.W. Ogden. *Non-Linear Elastic Deformations*. Dover Publications, New York, 1 edition, 1984. 2.1, 2.5, 2.6.2

[146] J. Oliver. A consistent characteristic length for smeared cracking models. *Int. J. Numer. Methods Engng.*, 28(2):461–474, 1989. 1.2

[147] J. Oliver. Modelling strong discontinuities in solid mechanics via strain softening constitutive equations .1. Fundamentals. *Int. J. Numer. Methods Engng.*, 39(21):3575–3600, 1996. 1.2, 3.1, 3.2

[148] J. Oliver. Modelling strong discontinuities in solid mechanics via strain softening constitutive equations .2. Numerical simulation. *Int. J. Numer. Methods Engng.*, 39(21):3601–3623, 1996. 1.2

[149] J. Oliver, M. Cervera, and O. Manzoli. Strong discontinuities and continuum plasticity models: the strong discontinuity approach. *Int. J. Plasticity*, 15(3):319–351, 1999. 1.2, 7.2

[150] J. Oliver, A.E. Huespe, M.D.G. Pulido, and E. Samaniego. On the strong discontinuity approach in finite deformation settings. *Int. J. Numer. Methods Engng.*, 56(7):1051–1082, 2003. 1.2

[151] J. Oliver, A.E. Huespe, and E. Samaniego. A study on finite elements for capturing strong discontinuities. *Int. J. Numer. Methods Engng.*, 56(14):2135–2161, 2003. 1.2

[152] J. Oliver, A.E. Huespe, E. Samaniego, and E.W.V. Chaves. Continuum approach to the numerical simulation of material failure in concrete. *International Journal for Numerical and Analytical Methods in Geomechanics*, 28(7):609–632, 2004. 1.2, 5.1, 5.3.5, 5.3.5, 6.2, 6.2.3

[153] J. Oliver, E. Huespe, E. Samaniego, and E. Chaves. On strategies for tracking strong discontinuities in computational failure mechanics. *Proceedings of the Fifth World Congress on Computational Mechanics (WCCM V), Vienna*, 2002. 1.2, 5.1, 5.3.5

[154] J. Oliver and A.E. Huespe und P.J. Sanchez. A comparative study on finite elements for capturing strong discontinuities: E-FEM vs X-FEM. *Comput. Methods Appl. Mech. Engrg.*, 37-40(195):4732–4752, 2006. 5.1

[155] M. Ortiz and A. Pandolfi. Finite-deformation irreversible cohesive elements for three-dimensional crack-propagation analysis. *Int. J. Numer. Methods Engng.*, 44(9):1267–1282, 1999. 1.2, 4.1, 4.2, 4.3.4, 4.4.2, 4.4.6, 5.1

[156] B. Patzak and M. Jirasek. Process zone resolution by extended finite elements. *Engng. Fract. Mech.*, 70(7-8):957–977, 2003. 1.2

[157] D. Peng, B. Merriman, S. Osher, H. Zhao, and M. Kang. A PDE-based fast local level set method. *Journal of Computational Physics*, 155(2):410–438, 1999. 5.3.15, 5.3.17

[158] N. J. Price and J.W. Cosgrove. *Analysis of Geological Structures*. Cambridge university press, 1 edition, 1990. 6.3, 6.3.6

[159] T. Rabczuk and T. Belytschko. A three-dimensional large deformation meshfree method for arbitrary evolving cracks. *Comput. Methods Appl. Mech. Engrg.*, 196(29-30):2777–2799, 2007. 1.2, 5.1

[160] T. Rabczuk, S. Bordas, and G. Zi. On three-dimensional modelling of crack growth using partition of unity methods. *Comput. Struct.*, in press, 2008. 5.1

[161] T. Rabczuk, S. Bordas, and G.S. Zi. A three-dimensional meshfree method for continuous multiple-crack initiation, propagation and junction in statics and dynamics. *Comput. Mech.*, 40(3):473–495, 2007. 1.2, 5.1, 6.2.2, 7.2

[162] T. Rabczuk, G. Zi, A. Gerstenberger, and W.A. Wall. A new crack tip element for the phantom-node method with arbitrary cohesive cracks. *Int. J. Numer. Methods Engng.*, 75(5):577–599 , 2008. 3.1, 3.3.1, 3.4.4

[163] J. Remmers. *Discontinuities in Materials and Structures - A Unifying Computational Approach*. PhD thesis, Delft University of Technology, 2006. 1.2, 3.1, 3.3.1, 3.4.3, 4.1, 4.4.4, 4.5.2, 5.3.2

[164] J.J.C. Remmers, R. de Borst, and A. Needleman. A cohesive segments method for the simulation of crack growth. *Comput. Mech.*, 31(1-2):69–77, 2003. 4.1, 4.4.2, 4.6.1, 4.6.2

[165] J. Rethore, A. Gravouil, and A. Combescure . An energy-conserving scheme for dynamic crack growth with the extended finite element method. *Int. J. Numer. Methods Engng.*, 63(5):631–659, 2005. 3.3.1

[166] R. Ribeaucort, M.C. Baletto-Dubourg, and A. Gravouil. A new fatigue frictional contact crack propagation model with the coupled X-FEM/LATIN method. *Comput. Methods Appl. Mech. Engrg.*, 196(33-34):3230–3247, 2007. 4.1, 4.4.4

[167] H.A. Richard, M. Fulland, F.G. Buchholz, and M. Schollmann. 3D fracture criteria for structures with cracks. *Steel research international*, 74(8):491–497, 2003. 1.2

[168] G. Ruiz, M. Ortiz, and A. Pandolfi. Three-dimensional finite-element simulation of the dynamic Brazilian tests on concrete cylinders. *Int. J. Numer. Methods Engng.*, 48(7):963–994, 2000. 1.2, 4.1, 4.4, 4.4.3, 5.1, 6.2, 7.2

[169] E. A. Samaniego. *Contributions to the continuum modelling of strong discontinuities in two-dimensional solids*. PhD thesis, Technical University of Catalonia (UOC), Barcelona, 2003. 1.2, 5.1

[170] J.M. Sancho, J. Planas, D.A. Cendon, E. Reyes, and J.C. Galvez. An embedded crack model for finite element analysis of concrete fracture. *Engng. Fract. Mech.*, 74(1-2):75–86, 2007. 6.1, 6.2

[171] J.M. Sancho, J. Planas, A.M. Fathy, J.C. Galvez, and D.A. Cendon. Three-dimensional simulation of concrete fracture using embedded crack elements without enforcing crack path continuity. *International Journal for Numerical and Analytical Methods in Geomechanics*, 31(2):173–187, 2007. 5.1, 6.1, 6.2

[172] J.M. Sancho, J. Planas, J.C. Galvez, E. Reyes, and D.A. Cendon. An embedded cohesive crack model for finite element analysis of mixed mode fracture of concrete. *Fatigue and Fracture of Engeneering Materials and Structures*, 29(12):1056–1065, 2006. 6.1, 6.2

[173] J.C.J. Schellekens. *Computational Strategies for Composite Structures*. PhD thesis, Delft University of Technology, 1992. 4.1, 4.5.1

[174] J.C.J. Schellekens and R. de Borst. On the numerical integration of interface elements. *Int. J. Numer. Methods Engng.*, 36(1):43–66, 1993. 1.2, 4.1, 4.5.1

[175] S.M. Schmalholz, Y.Y. Podladchikov, and J.P. Burg. Control of folding by gravity and matrix thickness: Implications for large scale folding. *Journal of Geophysical Research*, 107(B1):ETG 1–1, 2002. 6.3

[176] M. Schollmann, M. Fulland, and H.A. Richard. Development of a new software for adaptive crack growth simulations in 3D structures. *Engng. Fract. Mech.*, 70(2):249–268, 2003. 5.1

[177] J. Schröder and J. Löblein. A geometric nonlinear triangular finite element with an embedded discontinuity for the simulation of quasi-brittle fracture. *Comput. Mech.*, 36(2):139–157, 2005. 1.2

[178] J. A. Sethian. *Level Set Methods and Fast Marching Methods*. Cambridge university press, 2 edition, 1999. 1.2, 5.1, 5.3.6, 5.3.6, 3, 5.3.15, 5.3.19

[179] J.A. Sethian. Fast marching methods. *SIAM REVIEW*, 41(2):199–235, 1999. 5.3.15

[180] J.C. Simo and J.W. Ju. Strain-based and stress-based continuum damage models. 1. formulation. *Int. J. Solids Struct.*, 23(7):821–840, 1987. 1.2, 4.1, 4.4.6

[181] J.C. Simo and J.W. Ju. Strain-based and stress-based continuum damage models .2. computational aspects. *Int. J. Solids Struct.*, 23(7):841–869, 1987. 1.2, 4.1, 4.4.6

[182] A. Simone. *Continuous-Discontinuous Modelling of Failure*. PhD thesis, Delft University of Technology, 2003. 3.2, 4.1, 4.4.2

[183] A. Simone. Partition of unity-based discontinuous elements for interface phenomena: computational issues. *Comput. Methods Appl. Mech. Engrg.*, 20(6):465–478, 2004. 1.2, 4.1, 4.4.2, 4.5.1

[184] J.H. Song, P.M.A. Areias, and T. Belytschko. A method for dynamic crack and shear band propagation with phantom nodes. *Int. J. Numer. Methods Engng.*, 67(6):868–893, 2006. 3.1, 3.3.1, 7.2

[185] A.J.M. Spencer. *Continuum Mechanics*. Dover Publications, New York, 1 edition, 1980. 2.1, 2.5

[186] I. Stakgold. *Green's Functions and Boundary Value Problems*. John Wiley & Sons, LTD, 1 edition, 1979. 3.2

[187] F.L. Stazi, E. Budyn, J. Chessa, and T. Belytschko. An extended finite element method with higher-order elements for curved cracks. *Comput. Mech.*, 31(1-2):38–48, 2003. 3.1, 3.3.1

[188] E. Stein and F.J. Barthold. *Elastizitätstheorie in "Der Ingenieurbau"*. Ernst & Sohn, 1 edition, 1996. 2.1, 2.2, 2.5, 2.5, 2.6.2

[189] P. Steinmann. Application of material forces to hyperelastostatic fracture mechanics. I. Continuum mechanical setting. *Int. J. Solids Struct.*, 37(48-50):7371–7391, 2000. 1.2, 7.2

[190] P. Steinmann. On boundary potential energies in deformational and configurational mechanics. *Journal of the Mechanics and Physics of Solids*, 56(3):772–800, 2008. 4.1

[191] P. Steinmann and P. Betsch. A localization capturing FE-interface based on regularized strong discontinuities at large inelastic strains . *Int. J. Solids Struct.*, 37(30):4061–4082, 2000. 4.1, 4.2

[192] M. Stolarska, D.L. Chopp, N. Moës, and T. Belytschko. Modeling crack growth by level sets in the extended finite element method. *Int. J. Numer. Methods Engng.*, 51(8):943–960, 2001. 1.2, 5.1, 5.3.6, 5.3.14

[193] N. Sukumar, D.L. Chopp, E. Béchet, and N. Moës. Three-dimensional non-planar crack growth by a coupled extended finite element and fast marching method . *Int. J. Numer. Methods Engng.*, 76(5):727–748, 2008. 1.2, 3.4.4, 5.1, 5.3.6, 5.3.15

[194] N. Sukumar, N. Moës, B. Moran, and T. Belytschko. Extended finite element method for three-dimensional crack modelling. *Int. J. Numer. Methods Engng.*, 48(11):1549–1570, 2000. 1.2, 3.1, 3.4, 5.1, 5.3.14

[195] N. Sukumar and J.H. Prevost. Modeling quasi-static crack growth with the extended finite element method Part I: Computer implementation. *Int. J. Solids Struct.*, 40(26):7513–7537, 2003. 1.2, 3.1, 3.4, 3.4.4, 5.3.1

[196] D.V. Swenson and A.R. Ingraffea. Modeling mixed-mode dynamic crack propagation using finite elements: Theory and applications. *Comput. Mech.*, 3(6):381–397, 1988. 1.2

[197] T.Belytschko, W. K. Liu, and B. Moran. *Nonlinear Finite Elements for Continua and Structures*. John Wiley & Sons, LTD, 1 edition, 2000. 2.1, 2.5, 2.6.3

[198] D.L. Turcotte and G. Schubert. *Geodynamics*. Cambridge university press, 2 edition, 1982. 6.3, 6.3.1

[199] J.F. Unger, S. Eckhardt, and C. Könke. Modelling of cohesive crack growth in concrete structures with the extended finite element method. *Comput. Methods Appl. Mech. Engrg.*, 196(41-44):4087–4100 , 2007. 4.1, 4.4, 4.4.3

[200] J. Utzinger. *Analysis and Computation of Solid Interfaces on the Meso scale*. PhD thesis, Kaiserslautern University of Technology, 2008. 4.3.2

[201] G. Ventura, E. Budyn, and T. Belytschko. Vector level sets for description of propagating cracks in finite elements. *Int. J. Numer. Methods Engng.*, 58(10):1571–1592, 2003. 1.2, 5.3.15

[202] G. Ventura, J.X. Xu, and T. Belytschko. A vector level set method and new discontinuity approximations for crack growth by EFG. *Int. J. Numer. Methods Engng.*, 54(6):923–944, 2002. 1.2, 5.3.15

[203] A. Vervuurt, J.G.M. van Mier, and E. Schlangen. Analyses of Anchor Pull-Out in concrete. *Materials and Structures*, 27(169):251–259, 1994. 6.2.2

[204] G.N. Wells. *Discontinuous modelling of strain localisation and failure*. PhD thesis, Delft University of Technology, 2001. 1.2, 3.1, 3.2, 4.1, 4.2, 4.3.3, 4.4.2, 4.6.1, 4.6.2

[205] G.N. Wells and L.J. Sluys. A new method for modelling cohesive cracks using finite elements. *Int. J. Numer. Methods Engng.*, 50(12):2667–2682, 2001. 1.2, 4.1, 4.4, 4.4.2, 4.4.4, 5.1, 5.3.2, 5.3.2

[206] G.N. Wells, L.J. Sluys, and R. de Borst. A consistent geometrically non-linear approach for delamination. *Int. J. Numer. Methods Engng.*, 54(9):1333–1355, 2002. 4.1, 4.2, 4.3.3

[207] G.N. Wells, L.J. Sluys, and R. de Borst. Simulating the propagation of displacement discontinuities in a regularized strain-softening medium. *Int. J. Numer. Methods Engng.*, 53(5):1235–1256, 2002. 1.2, 5.1, 5.3.2

[208] B. Winkler, G. Hoffstetter, and G. Niederwanger. Experimental verification of a constitutive model for concrete cracking. *Proceedings of the Institution of Mechanical Engineers Part L-Journal of Materials-Design and Applications*, 215(L2):75–86, 2001. 6.2.1

[209] B.J. Winkler. *Traglastuntersuchungen von unbewehrten und bewehrten Betonstrukturen auf der Grundlage eines objektiven Werkstoffgesetzes für Beton*. PhD thesis, Innsbruck University, 2001. 6.2.1

[210] P. Wriggers. *Nichtlineare Finite-Element-Methoden*. Springer Verlag, Berlin, 1 edition, 2001. 2.1, 2.5, 2.5, 2.5, 2.6.3, 2.6.5

[211] E. Wyart, M. Duflot, D. Coulon, P. Martiny, T. Pardoen, J. F. Remacle, and F. Lani. Substructuring FE-XFE approaches applied to three-dimensional crack propagation . *Journal of Computational and Applied Mathematics*, 215(2):626–638, 2008. 7.2

[212] X.P. Xu and A. Needleman. Numerical simulation of fast crack-growth in brittle solids. *Journal of the Mechanics and Physics of Solids*, 42(9):1397–1405, 1994. 1.2, 4.1, 4.4, 4.4.4

[213] X.P. Xu and A. Needleman. Numerical simulations of dynamic crack growth along an interface. *International Journal of Fracture*, 74(4):289–324, 1996. 1.2, 4.1, 4.4, 4.4.4

[214] X.P. Xu and A. Needleman. Numerical simulations of dynamic interfacial crack growth allowing for crack growth away from the bond line. *International Journal of Fracture*, 74(3):253–275, 1996. 1.2, 4.1, 4.4

[215] G. Zi and T. Belytschko. New crack-tip elements for XFEM and applications to cohesive cracks. *Int. J. Numer. Methods Engng.*, 57(15):2221–2240, 2003. 3.4.4, 4.1, 4.4

[216] G. Zi, J.H. Song, E. Budyn, S.H. Lee, and T. Belytschko. A method for growing multiple cracks without remeshing and its application to fatigue crack growth. *Modelling and simulation in materials science and engeneering*, 12(5):901–915, 2004. 7.2

[217] O.C. Zienkiewicz. *Methode der finiten Elemente*. Carl Hanser Verlag, Wien, 2 edition, 1971. 2.1, 2.6.3

Curriculum Vitae

Name:	Philippe Jäger
Geburtsdatum:	01.12.1977
Geburtsort:	Hattingen
Nationalität:	deutsch
Familienstand:	ledig

1984 – 1993	Rudolf-Steiner Schule, Witten
1993 – 1999	Hardenstein-Gesamtschule, Witten Abschluss: Allgemeine Hochschulreife
1999 – 2000	Wehrersatzdienst, Kulturzentrum Werkstadt, Witten
2000 – 2005	Studium des Bauingenieurwesens, Ruhr-Universität Bochum Vertiefungsrichtung: Konstruktiver Ingenieurbau Abschluss: Diplom-Ingenieur
2005 – 2007	Promotionsstudent als Stipendiat im DFG Graduiertenkolleg GRK 814: *Ingenieurmaterialien auf verschiedenen Skalen: Experiment, Modellierung und Simulation*, Lehrstuhl für Technische Mechanik, Technische Universität Kaiserslautern
seit 2007	Wissenschaftlicher Mitarbeiter, Lehrstuhl für Technische Mechanik, Technische Universität Kaiserslautern